

# **ENABLING TECHNOLOGIES FOR ULTRASOUND IMAGING IN COMPUTER-ASSISTED INTERVENTION**

by

**Emad M. Boctor Mikhail**

A dissertation submitted to Johns Hopkins University in  
conformity with the requirements for the Doctor of Philosophy

Baltimore, Maryland  
**October 2006**

© Emad M. Boctor 2006  
All rights reserved

#### INFORMATION TO USERS

The quality of this reproduction is dependent upon the quality of the copy submitted. Broken or indistinct print, colored or poor quality illustrations and photographs, print bleed-through, substandard margins, and improper alignment can adversely affect reproduction.

In the unlikely event that the author did not send a complete manuscript and there are missing pages, these will be noted. Also, if unauthorized copyright material had to be removed, a note will indicate the deletion.



---

UMI Microform 3240673

Copyright 2007 by ProQuest Information and Learning Company.  
All rights reserved. This microform edition is protected against  
unauthorized copying under Title 17, United States Code.

ProQuest Information and Learning Company  
300 North Zeeb Road  
P.O. Box 1346  
Ann Arbor, MI 48106-1346

# Abstract

There has been an increasing interest in minimally invasive US-guided interventions that require precise placement of a surgical tool (needle, tissue ablator, etc.) to the anatomical target. To address this problem, I have developed a collection of novel technologies and integrated those in prototype systems.

I introduce multiple system embodiments that involve robotics, tracking, anatomical modeling, ultrasound image processing, and elasticity monitoring. The underlying themes in these systems are (1) simultaneous tracking of surgical tool with respect to the US images and (2) monitoring physiological changes, specifically tissue coagulation, throughout the procedure.

My main contribution to the first theme is inventing a robust method for 2D and 3D ultrasound probe calibration with a closed-form solution. As a result, one can discern the unknown spatial transformation between image pixels and tracker coordinates in real-time, in-vivo while the patient is being scanned. I also introduced a novel methodology for in-vivo quality control of tracked US systems, by capturing system errors that manifest in changes of calibration parameters. The concept, mathematical formulation, and experimental evaluation are presented and demonstrated in-vitro experiments.

With respect to the second theme, I presented a rapid US-based approach to monitor ablative therapy by optimizing shape parameters. My method involves the integration of a biomechanical computational model of the tissue, a correlation approach to estimate and track tissue deformation, and an optimization method to solve the inverse problem of recovering the shape parameters in the volume of interest. I demonstrate convergence and reliability on simulated data and present successful monitoring of tissue ablation of ex-vivo bovine liver samples.

- Primary advisor: Gabor Fichtinger, Ph.D.  
Associate Research Professor of Computer Science,  
Mechanical Engineering, and Radiology,  
Center for Computer Integrated Surgical Systems and Technologies,  
Johns Hopkins University
- Co-advisor: Gregory D. Hager, Ph.D.  
Professor and Deputy Director  
Center for Computer Integrated Surgical Systems and Technologies,  
Department of Computer Science,  
Johns Hopkins University
- Co-advisor: Russell H. Taylor, Ph.D.  
Professor and Director  
Center for Computer Integrated Surgical Systems and Technologies,  
Department of Computer Science,  
Johns Hopkins University

# Acknowledgements

This thesis is the result of five years of work, during which I received invaluable support from many people. It has been an extraordinary intellectual journey, one that is similar to climbing a high mountain. It was a teamwork that got me there, to enjoy the beautiful scenery at the top of this mountain. Words can not express my gratitude to all those who helped me, but I would like to give my thanks to all of them.

First and foremost, I would like to thank my thesis supervisor, Prof. Gabor Fichtinger, for instilling in me the qualities of a good researcher. His mentorship was paramount in providing a well-rounded experience consistent with my long-term career goals. He continually stimulated my independent thinking and nurtured my leadership skills.

Similarly, I would like to extend my special thanks to my thesis co-advisors, Professors Gregory D. Hager and Russell H. Taylor. Their generous attention and dedication have shaped my career in innumerable ways. Their incessant enthusiasm, integral view on research, and dedication to high-quality research have formed the way I conduct research.

I am grateful for the assistance, generosity, and advice of Prof. Michael A. Choti at the Department of Surgery. Likewise, my thanks go to Michelle DeOlivera, MD, for her valuable input to the clinical aspects of my research.

I sincerely appreciate the help that I received from Drs. Roger Ghanem, Allison Okamura, Gregory Chirikjian, Ron Kikinis, and Jerry Prince. I am also grateful to Dr. Stanislav Emelianov for his expert advice in the field of elasticity imaging.

I had the fortunate of working with a group of brilliant and motivated researchers in the laboratories of the Engineering Research Center. I truly enjoyed every moment of our work together, even the endless nights we so often spent in the lab. To many former and present lab members, I express my heartfelt thanks for their friendships and collective encouragement: Anton Deguet, Csaba Csoma, Ankur Kapoor, Ameet Jain, Ofri Sadowsky, Greg Fischer, Anand Viswanathan, Ming Li, Josh Leven, Robert Webster and Hassan Rivaz. I especially thank Dr. Iulian Iordachita for his brilliant mechanical designs and unrelenting support.

My work was financially supported by a number of organizations, including The National Science Foundation through the Engineering Research Center, the National Institute of Health through a collaborative grant with Burdette Medical Systems, Inc. The final two years of my dissertation research was financed by a fellowship from Siemens Corporate Research. My heartfelt thanks go to Drs. Frank Sauer, James Williams and their entire staff at Siemens, especially Dr. Ali Khamene, and Wolfgang Wein.

My research would not have been possible without love and support of my whole family. I dedicate my thesis to my mother, Amal Khella, and to my late father, Moussa Boctor, for their love, encouragement, and unwavering faith and confidence in my abilities.

Last but definitely not at least, I am forever indebted to my wife, Eman. Her love, constant encouragement and support without any complaint have enabled me to complete this work.

Finally, my expression of gratitude would not be complete without praising my Lord whose words have always guided and enlightened my way: “I will instruct you and teach you in the way you should go; I will counsel you and watch over you” (*PSALM 32-8*).

# Contents

<b>Abstract</b>	ii
<b>Acknowledgements</b>	iv
<b>List of Abbreviations</b>	xii
<b>List of Tables</b>	xiv
<b>List of Figures</b>	xv
<b><u>Part-I Ultrasound-guided Intervention Systems</u></b>	
<b>1 Motivation and Prior Art</b>	1
1.1 Robot-Assisted Needle Placement Systems .....	3
1.2 Instrument Tracking .....	4
1.3 3D Ultrasound (3DUS) .....	5
1.4 Thermal Therapy: RF Liver Ablation .....	7
1.5 External Beam Radiation Therapy .....	9
1.6 Our Contributions .....	12
<b>2 Ultrasound-guided Intervention Systems</b>	14
2.1 Introduction .....	14
2.2 Our Approaches and Methods .....	17
2.2.1 Passive/Passive System .....	18
2.2.1.1 Tracked RF ablator and passive arm .....	20
2.2.1.2 Freehand tracked 3D ultrasound .....	21
2.2.1.3 Planning and visualization software .....	24
2.2.2 Active/Passive System .....	26
2.2.2.1 Robotic 3DUS system (LARS-US) .....	28
2.2.3 Passive/Active System .....	31
2.2.3.1 Virtual RCM needle insertion robot control .....	33
2.2.4 Active /Active System .....	35

2.3	Experiments and Results .....	37
2.3.1	Initial Phantom Experiments with Passive Needle Insertion .....	37
2.3.1.1	Passive/Passive Experimental Procedures and Results ...	37
2.3.1.2	Active/Passive Experimental Procedures and Results ....	40
2.3.2	Ex-vivo Experiments with Active Needle Insertion .....	42
2.3.2.1	Experimental Procedures for the Dual-Arm System .....	42
2.3.2.2	Results and Discussions .....	45
2.3.3	Comparative Study .....	47
2.3.4	In-vivo Animal Study .....	51
2.4	Conclusions .....	52
<b>3</b>	<b>Virtual Remote Center of Motion Control for Needle Placement Robots</b>	<b>54</b>
3.1	Introduction .....	55
3.2	Materials and Methods .....	58
3.2.1	System overview .....	58
3.2.2	The Virtual RCM: A Heuristic Search .....	61
3.2.3	Analysis of Candidate Heuristic Functions .....	62
3.3	Simulation Results .....	65
3.4	Experimental Implementation .....	67
3.4.1	Results and Discussion .....	69
3.5	Conclusions .....	70
<b>4</b>	<b>CISUS: An Integrated 3D Ultrasound System for IGT Using a Modular Tracking API</b>	<b>72</b>
4.1	Introduction .....	73
4.2	Architecture of the CISUS System .....	76
4.2.1	System Overview .....	76
4.2.2	Functions Implemented in CISUS .....	78
4.2.3	System Design .....	80
4.2.3.1	Development environment .....	80
4.2.3.2	Architecture .....	81
4.2.3.3	Implementation .....	83
4.2.3.4	Extension to CISUS .....	85
4.2.3.5	Rapid prototyping interface .....	86
4.3	Current IGT Application .....	87
4.4	Conclusions .....	88

<b>Part-II Ultrasound Calibration</b>	
<b>5 Ultrasound Calibration Using the Hopkins Phantom</b>	<b>90</b>
5.1 Introduction .....	90
5.2 Prior-Art .....	92
5.3 Materials and Methods .....	95
5.3.1 Theory and mathematical framework .....	95
5.3.2 The multisided tank and the Hopkins phantom .....	97
5.3.3 Experimental setup and workflow .....	99
5.3.4 Feature extraction .....	101
5.3.5 Verification on synthetic data .....	103
5.3.6 Initial guess .....	103
5.4 Results and Discussion .....	105
5.4.1 Results with the multisided tank .....	108
5.4.2 Comparison of the Hopkins and the cross-wire phantoms .....	110
5.4.3 Hopkins automatic calibration toolkit (UltraCal) .....	113
5.5 Conclusions .....	114
<b>6 Ultrasound Calibration Using Closed-form Formulation</b>	<b>115</b>
6.1 Introduction .....	115
6.2 Closed-form Formulation .....	117
6.3 Calibration Methods and Protocols .....	121
6.3.1 The modified Hopkins phantom .....	121
6.3.2 The thin plate phantom .....	123
6.3.3 Double-wedge phantom .....	129
6.3.3.1 Double-wedge geometry and imaging .....	131
6.3.3.2 Bootstrapped US calibration using $AX=XB$ .....	135
6.4 Experiments and Results .....	138
6.4.1 The modified Hopkins phantom .....	138
6.4.2 The thin plate phantom .....	140
6.4.3 Double-wedge phantom .....	142
6.5 Conclusions .....	145
<b>7 Real-time Quality Control (QC) and Ultrasound Self-Calibration</b>	<b>146</b>
7.1 Introduction .....	146
7.2 Mathematical Formulations .....	148
7.2.1 Translation Motion .....	152
7.2.2 Planar Motion .....	154
7.2.3 Rotation about an axis .....	157
7.2.4 Out-of-plane motion estimation .....	158
7.3 Methods and System Integration .....	159
7.3.1 Experimental system .....	159
7.3.2 Algorithm workflow .....	159
7.3.3 Real-time tracker .....	161
7.4 Experiments and Results .....	162
7.5 Conclusions and Future work .....	164

<b>Part III Elasticity Imaging</b>	
<b>8 Monitoring Ablative Therapy</b>	<b>166</b>
8.1 Introduction .....	166
8.2 Strain Imaging and Prior Art .....	169
8.3 Liver Elasticity Study .....	171
8.3.1 Materials and methods .....	172
8.4 Robotic Strain Imaging System .....	176
8.4.1 3D Strain acquisition system .....	183
8.5 Experiments and Results .....	186
8.5.1 Liver elasticity study .....	186
8.5.2 Monitoring Radionics ablation .....	189
8.5.3 Initial feasibility of 3D strain acquisition .....	194
8.6 Conclusions .....	195
<b>9 Elasticity-based Segmentation</b>	<b>197</b>
9.1 Introduction .....	197
9.2 Strain Image Segmentation .....	199
9.3 Elasticity Model based on Tissue Deformations .....	202
9.3.1 Tissue Displacement Estimation .....	203
9.3.2 Theoretical Displacement Estimation .....	204
9.3.3 Shape Optimization .....	205
9.4 Experiments and Results .....	206
9.5 Future work and Conclusions .....	209
<b>10 Conclusions</b>	<b>211</b>
10.1 Ultrasound Guided Intervention Systems .....	211
10.2 Ultrasound Calibration and Online Quality Control .....	213
10.3 Elasticity-based Segmentation .....	214
<b>A Robotic Ultrasound Image Based Servoing</b>	<b>216</b>
A.1 Approach .....	216
A.2 Experiments and Results .....	219
A.3 Conclusions .....	222
<b>B CIS-UltraCal: An Open-Source Ultrasound Calibration Toolkit</b>	<b>223</b>
B.1 Approach .....	223
B.2 Interface Design and Implementation .....	225
<b>C Error Propagation Analysis of <math>AX=XB</math></b>	<b>227</b>
C.1 Sensitivity Analysis of Linear System .....	227
C.2 Error Propagation Analysis of $AX=XB$ .....	231
C.3 Covariance Propagation Method .....	236
<b>D Toward Accurate Out-of-plane Motion Estimation</b>	<b>238</b>
D.1 Approach Introduction .....	239

D.2	Simulation Methods .....	240
D.3	Optimizing $v_R$ and $v_S$ .....	245
D.4	Experimental Results .....	246
D.5	Discussion and Conclusion .....	248
	<b>Bibliography</b>	249
	<b>Vita</b>	267

# List of Abbreviations

AI	:Artificial Intelligence
API	:Application Programming Interface
BFS	:Breadth First Search
B-mode	:Brightness-mode
CBCT	:Cone Beam Computed Tomography
CIS	:Computer Integrated Surgery
CISUS	:Computer Integrated Surgery with Ultrasound
CNR	:Contrast-to-Noise Ratio
CT	:Computed Tomography
CTF	:CT Fluoroscopy
DFS	:Depth First Search
DICOM	:Digital Imaging and Communications in Medicine
DOF	:Degree-of-Freedom
EBRT	:External Beam Radiation Therapy
EM	:Electromagnetic
ERC	:Engineering Research Center
FEM	:Finite Element Method
FOB	:Flock of Birds
GUIs	:Graphical User Interface
HCC	:Hepatocellular Carcinoma
HIFU	:High Intensity Focused Ultrasound
ICC	:Intra-Class Correlation
IGS	:Image Guided Surgery
IGT	:Image-Guided Therapy
IMRT	:Intensity-Modulated Radiotherapy
IOUS	:Intraoperative Ultrasonography
LARS	:Laparoscopic Assistance Robotic System
LSQSE	:Least Squares Strain Estimator
MIS	:Minimally Invasive Surgery
MRC	:Medical Robot Control
MRI	:Magnetic Resonance Imaging
NCC	:Normalized Cross Correlation

PNN	:Pixel Nearest Neighbor
PRF	:Pulse Repetition Frequency
QC	:Quality Control
RBF	:Radial Basis Functions
RCC	:Robot Control Computer
RCM	:Remote Center of Motion
RF	:Radiofrequency
RFA	:Radiofrequency Ablation
ROI	:Region of Interest
SNR	:Signal-to-Noise Ratio
ST-RCM	:ST Remote Center of Motion
TDE	:Time Delay Estimation
URI	:Ultrasound Research Interface
US	:Ultrasound
USEI	:Ultrasound Elasticity Imaging
VNN	:Voxel Nearest Neighbor
VOI	:Volume of Interest
VRCM	:Virtual Remote Center of Motion
VTK	:Visualization Toolkit
STD	:Standard Deviation
3D	:Three dimension
2DUS	:2D Ultrasound
3DUS	:3D Ultrasound

# List of Tables

3.1	Experimental results. ....	70
5.1	Multisided tank analysis. The upper table shows estimated calibration matrices and pixel ratios by Hopkins and cross-wire methods under different trials. These trials are based on spatial coverage of scanning (top side vs. multiple sides). The lower table shows the error statistics with the 1.0 and 2.0 cm inter-distance reflectors in the Hopkins phantom (Figure 8). ....	109
5.2	Comparison between the Hopkins phantom and the cross-wire phantom based on reconstruction accuracy measures. ....	111
5.3	Comparison between the Hopkins and cross-wire phantoms, based on reconstruction precision measures. ....	112
6.1	The above table lists average error and standard deviation in mm the recovered translation vector for different calibration sequences. The sequences were generated using synthetic data with added noise of 0.5%, 1%, 5%, 10% respectively. ....	138
6.2	The above table lists average pose values and average deviation in mm and degrees of recovered transformation matrix using actual ultrasound and optical tracking device data. ....	139
6.3	Average pose and deviation of the recovered calibration matrix using the thin plate calibration phantom with the AX=XB method. ....	140
6.4	Standard deviation of position reconstruction accuracy (R-STD) in mm, for three calibration methods. ....	142
7.1	QC system report on rotation and scale. ....	148
8.1	Ultrasound and strain measurements for the 15 ablated liver samples. ....	191
8.2	The intra-class correlation study between the observers' measurements. ....	192
8.3	Observer "A" measurements from gross-pathology, ultrasound, and strain images. ....	193

# List of Figures

1.1	Computer integrated surgery system (courtesy of Prof. R. Taylor.) .....	2
1.2	Restitu™ system from Resonant Medical Inc. where tracked 3DUS is used to guide EBRT for prostate. ....	12
2.1	Typical radiofrequency ablation of liver tumor guided by freehand 2DUS(Courtesy of Dr. M. Choti.) .....	16
2.2	Flow diagram for the four different proposed ultrasound guided liver ablation systems. ....	18
2.3	Components of the proposed system with tracked passive arm and tracked freehand ultrasound. ....	19
2.4	Pivot calibration method to define the 2 end-points of the RF ablator in the tracker coordinate system. (Courtesy of Prof. Russell H. Taylor.) .....	20
2.5	Tracked passive arm that shows part of the 6 DOF passive arm and the whole 5-bar RCM linkage. ....	21
2.6	Generic freehand tracked 3DUS system. (Courtesy of R. Prager to use part of his original figure.) .....	22
2.7	Dual 3D view interface based on 3D Slicer for planning and visualization.	25
2.8	System components of the proposed system with tracked passive arm and fully encoded 7 DOF robotic arm to handle US scanning. ....	26
2.9	The LARS Robot. ....	29
2.10	System components of the proposed system with tracked US probe and robotic arm to handle ablator insertion. ....	33
2.11	System components of the proposed Active/Active system. ....	36
2.12	Rubber ball phantom experiment. LR: experimental setup. L: path planning with 2D and 3DUS data. UR: confirmatory 2DUS snapshot. ...	38
2.13	Triangle phantom experiment. LR: experimental setup. L: screen captures from planning and monitoring. UR: confirmatory 2DUS snapshot. ....	39
2.14	Top: Triangle based phantom used for reconstruction verification. Left: Thresholded reconstruction from freehand scan showing the ripples on the top edge. Right: Reconstruction from robotic scan showing smoother and uniform edge. ....	40

2.15	Prototype and system integration. A: shows the robotic 3DUS acquisition system. B: shows the physical system integration. C: the dual 3D view interface based on 3D Slicer for planning and visualization. ....	41
2.16	Left: Experimental setup for the dual-armed robotic system. Right: Close-up of biopsy experiment. ....	43
2.17	Mechanical phantom with 4 pins. ....	43
2.18	Orthogonal slices of 3DUS reconstruction of an olive in calf liver phantom. ....	44
2.19	Ultrasound is used to assess needle placement with respect to the olive target embedded in calf liver. ....	45
2.20	This is a snap shot for the CISUS interface under the 3D Slicer. Tracked 3DUS volume is shown from two different angles and at the bottom there are the three 2D-sections. Actual needle location is shown in real-time as thick cylinder registered to the US volume and a thin line is emanating from it as a virtual extension. There are two overlaid balls one for planning an insertion point and the other for targeting. The targeting ball is centered at the hypoechoic lesion that represents one of the three embedded lesions in this study. One can notice the good quality of the freehand tracked 3DUS volume. ....	48
2.21	Two perpendicular X-ray projections showing needle targeting (solid circle) with respect to known geometry object. ....	50
2.22	Comparison chart showing the average targeting accuracy/STD components in both projections with freehand and 3DUS systems. ....	51
2.23	The Passive/Active system with fluoroscopy X-ray to assess the targeting accuracy of this trial. Notice the C-arm is oriented to acquire AP x-ray projection. ....	52
3.1	Experimental setup. ....	59
3.2	Slicer graphical user interface. ....	60
3.3	Heuristic functions. ....	63
3.4	Illustration of frames and vectors necessary for building a simulation of candidate heuristic functions. ....	64
3.5	Above are 360 rotations of $\alpha$ for two particular $\beta$ angles to show the dependency between $\alpha$ and $\beta$ . Note: on the left we have better alignment as it is shown in the cross product value 0.3, while on the right the cross product value is 0.55. ....	66
3.6	Plot of distance (left) and the cross product (right) heuristic functions for all angular values. ....	66
3.7	Needle insertion scenarios flow chart. ....	68
4.1	The synergic integration of CISUS and 3D Slicer. ....	77
4.2	Graphical user interfaces (GUIs) for the system settings From left to right: Capture Device, Tracker, Reconstruction, and Robotic/Freehand US. ....	79
4.3	GUI for the execution phase. ....	80
4.4	An overview of the CISUS module architecture illustrating the class	82

hierarchy as well as the relationship between the C++ and the Tcl layers. . .	
4.5 The inheritance graph of the cisTracker library. ....	84
4.6 A sample of medical robots with which the mrc software library can interface. ....	85
4.7 The rapid software development pipeline. ....	86
4.8 Robotically assisted 3DUS liver ablation system; system layout (left), and experimental setup (middle), and a typical planning screen with CISUS-3D-Slicer interface (right). ....	88
5.1 Calibration Phantoms and their corresponding US images; Left: Cross-wire phantom. Middle: Three-wires phantom, and Right: Single-wall phantom. ....	94
5.2 The chain of transformations is from pixel frame $P$ , to the receiver frame $R$ , to transmitter frame $T$ , and finally to construction frame $C$ . The $(u, v)$ pixel coordinates are multiplied by $(S_x, S_y)$ scale factors. The resulting transformed point $C_x$ has the $(0, 0, 0)$ coordinate values [crosswire phantom]. (The upper figure is courtesy of R. Prager.) ....	95
5.3 The matrix on the top illustrates the general form of one of the six degrees of freedom transformation matrices (Three translations [ $x$ , $y$ , and $z$ ] and Three rotations [ $\alpha$ , $\beta$ , and $\gamma$ ]). The equation in the bottom represents the Levenberg-Marquardt optimization method. ....	96
5.4 The Multisided tank is shown with five sides (top and four rubber windows). At the bottom, there is a piece of Lego to attach different phantoms. ....	97
5.5 The Hopkins phantom (left) and a typical image of it (right), illustrating the large number of data points that can be collected, in a potentially automated manner. ....	98
5.6 Shows how the Hopkins phantom is built to maintain well-visible feature points. ....	102
5.7 Finding the initial guess for ${}^R T_P$ . ....	105
5.8 A: Points from Hopkins phantom extracted and placed in the construction-space. B: reconstruction of 5 reflectors in the Hopkins phantom's xy space. C: US image for these 5 reflectors. ....	108
5.9 The vertical-axis is the condition number while the horizontal-axis is the number of points dropped from the optimization (total are 720 in this case). It shows that the condition number remains stable to the 600 level, which means 80-100 points is enough to make the system well conditioned. ....	111
5.10 "A" shows the reconstruction of the Hopkins phantom by using the calibration matrix of the cross-wire method. "B" shows the reconstruction based on Hopkins calibration parameters. It is obvious that Hopkins method leads to more reconstruction accuracy as it is shown in Table 5.1 as well. ....	112
6.1 The formulation of transformations in the cross-wire phantom. The chain	117

goes from pixel frame P, to receiver frame R, to transmitter frame T, and to construction frame C. The (u,v) pixel coordinates are multiplied by (Sx,Sy) scale factors. The transformed point Cx is (0,0,0). (Courtesy of R. Prager.) .....	
6.2 The coordinate systems formulation for the proposed AX =XB method. ..	118
6.3 The Calibration setup shows the multi-sided tank with the modified Hopkins phantom. .....	121
6.4 The N-shape phantom helps in extracting the pose between the US image plane and the phantom space, “A <sub>1</sub> transformation”. .....	122
6.5 The calibration setup shows the optically tracked probe, which images the three thin plates. .....	123
6.6 Optical pointer is used to digitize 3D points prior to calibration on the three clear plastic plates forming the phantom (R), and an ultrasound image of one of the plates (L). .....	125
6.7 CAD design showing US probe attachment held in-place by the dual flat-spring fiducial (R) Actual implementation for the dual flat-spring fiducial holding a linear array US probe with optical rigid-body and a typical US image (L). .....	127
6.8 Offline calibration to adjust the thin-plate in the middle of the elevation width of the US beam (L) Optical pointer is used to digitize 3D points and estimate the transformations (A's) between different dual flat-spring fiducials. .....	128
6.9 The three double-wedge fiducials arranged on an acrylic board to maximize the accuracy according to the observations mentioned in section 6.3.2. .....	129
6.10 Coordinate definitions in the AX=XB closed form solver. .....	130
6.11 Double-wedge phantom used for calibrating Siemens VF 10-5 linear array (L) and Aloka laparoscopic long stick probe where the optical rigid-body at the very end. .....	131
6.12 Double-wedge US image shows clouds moving in opposite directions (L) The cloud pairs are inline and with equal size indicating good alignment with double-wedge plane (R). .....	132
6.13 Double-wedge US image shows cloud separation due to pure translation offset in the elevation direction (L). Typical US image for equal size cloud pair with separation in axial direction (R). .....	134
6.14 Illustrates how double-wedge resolves beam angle. .....	134
6.15 Conventional calibration. .....	135
6.16 Bootstrapped calibration. .....	135
6.17 Reconstruction accuracy setup, acquiring 52 cross wire images from different angles (L), The reconstruction precision framework (R, Top) and the resultant standard deviation in mm (R, Bottom.) .....	141
7.1 Coordinate definitions in the closed form AX=XB. .....	148
7.2 Experimental system and an illustration for the two suggested special motions. ‘Motion I’ indicates a planar motion, and ‘Motion II’ indicates a	155

rotation about an axis. ....	155
7.3 Illustration showing the unknown $\zeta$ . ....	156
7.4 The real-time self-calibration workflow. ....	160
7.5 Relation between the recovered scale and number of images & step size. .	164
7.6 Similar convergence for the three rotation angles ( $\alpha, \beta, \gamma$ ) under 4 different small steps $d=(1,2,4,5)$ . ....	165
 8.1 2D representation of strain based imaging. Before compression: the overlay represents 1D cascaded particles with uniform spacing. After compression: the overlay represents two groups of particle spacing. Small spacing indicates soft tissues that moved more (high strain) than the hard tissue (low strain). ....	170
8.2 RITA Model 1500 Radio Frequency generator and the Windows95 laptop (Left), An ablator device is inserted and deployed in a liver block (Right).	173
8.3 The initial linear region corresponds to the heating of the liver tissue with the RF probe from near room temperature to the target temperature (in this case 70°C). The target temperature was maintained for 10 minutes. The RITA RF probe had an array of 5 thermisters and the generator averaged the individual readings and used the average value in a feedback loop to maintain the constant average temperature. After the 10 minute target interval, the RITA generator entered a brief cool down cycle as seen in the graph at the steep drop off point. Similar temperature outputs were obtained for each temperature grouping. ....	174
8.4 It shows the 35 liver samples taken from seven different livers, using six different ablation protocols (50°, 60°, 70°, 80°, 90°, and 100° C) and arranged in five independent samples per temperature group. Note the weight of each sample was measured before and after ablation. ....	174
8.5 Shows Rheometric Scientific RFS III rheometer and a zoomed picture to demonstrate how specimens were placed in the center of the rheometer tray. ....	175
8.6 The 35 samples kept in formalin solution for histological examinations and arranged from left to right according to temperature, starting from room temperature to 100° C. ....	176
8.7 The overall robotic strain based imaging system (L) and schematic drawing of the robot's end-effector holding the US probe (R). The large probe serves as a compression plate. ....	177
8.8 Illustrates the oval/ellipsoidal ablation shape along the needle axis, which tolerates the need of gross-pathology cutting sub-millimeter accuracy (Left), we can see the ablator tip in the B-mode and expect the ablation to build up around it (Right). Also due to cooling cycle induced vibration, the tip can be seen using color Doppler mode during aggressive ablation.	180
8.9 Illustrates LARS robotic system holding the US probe with a compression plate. It also shows the liver sample embedded in a transparent gelatin phantom, while active ablation is carried on using a Radionics ablation device (Left). To the right, the picture illustrates another setup using	181

passive robotic system and the US Antares unit is shown. ....	180
8.10 Illustrates the US probe with the compression plate; and it also shows the needle that is used to introduce multiple fiducials in the transparent gelatin on both sides. ....	181
8.11 The first row shows the first three liver samples with 4 min ablation; the second row shows the first three liver samples with 6 min ablation; the third row shows the first three liver samples with 8 min ablation. ....	182
8.12 The calibration procedure is done on two steps. First, we locate the pointer at the center of the rotating stage by the help of a micrometer (Left). If the micrometer gives the same reading for the 360° rotation that means that the pointer is in the center of the rotating stage. Second, we adjust the location of the US probe using the 3DOF Cartesian stage and the US image feedback to center the array on the pointer head (Right). ...	185
8.13 Illustrates the 3D elastography acquisition setup for the 10 Cm <sup>3</sup> phantom with isoechoic spherical inclusion. The B-mode US image doesn't delineate the location of the enclosed lesion. ....	185
8.14 Illustrates the mean stress distribution vs. time for the seven temperature groups. ....	186
8.15 Illustrates the stress-strain relationship for the seven temperature groups.	187
8.16 Illustrates the dynamic elastic shear modulus (G') with frequency for the seven temperature groups. ....	188
8.17 Top: histological images of the 20 and 100 reticulin stains, Bottom: histological images of the 20 and 100 H&E stains. ....	188
8.18 The first row shows the first three strain images with 4 min ablation; the second row shows the first three strain images with 6 min ablation; the third row shows the first three strain images with 8 min ablation. ....	190
8.19 Above are depicted 3D cross sections of a lesion. The left is a B-Mode image in which it is difficult to determine the location of the lesion because of the isoechoic appearance. The right is a displacement image in which the lesion is more easily seen. ....	194
8.20 Clockwise from the top-left are displacements images for rotational 1°, 2°, 3°, and 4° datasets. ....	195
 9.1 B-mode image shows ex-vivo liver boundaries embedded in gel based medium. It is not possible to differentiate the ablated area from B-mode. Strain is generated from differentiating a displacement map in the axial direction. Strain provides clear evidence of the presence of hard lesion, which is in agreement with the gross pathology picture. ....	198
9.2 Conventional straightforward image segmentation pipeline for Strain images. ....	201
9.3 Iterative tracking and segmentation pipeline. ....	203
9.4 Correlation in the displacement map, thresholded at different correlation levels. ....	204
9.5 Shows both strain and displacement an image that reflects tissue deformations. Model displacement image represents FEM theoretical	207

deformation. Also it illustrates a small circle to the top, left corner as an initial guess and another small circle after 8 iterations approaching to the final ellipse. Gross pathology picture is included to the right. ....	208
9.6 Scale convergence of the ellipse. ....	208
9.7 Location convergence of the ellipse. It also shows the effects of K on optimizing shape parameters. K is the ratio of Young's modulus of ablated lesion to normal liver. ....	209
A.1 Experimental setup using LARS and CART robots. ....	218
A.2 The results above present the action of the robot when a step in the positive Z direction is introduced. ....	219
A.3 Offline servoing results showing actual and desired locations in X, Y, and Z. ....	220
A.4 Using ACM to segment the feature of interest in the US. ....	220
B.1 The Hopkins phantom features extraction algorithm. ....	223
B.2 Flowchart of the calibration process in the Ultra-Cal toolkit. ....	224
B.3 GUI at different levels in the calibration process. ....	225
D.1 Speckle decorrelation concept. ....	237
D.2 The procedure for acquiring the elliptical discriminant function for all values of $0 < v_R < 3$ and $0 < v_S < 3$ . Each data sample A is calculated by a random walk. Each one of the 30000 sets of A has 5000 samples as indicated. The A values inside a set all share the same $\mu$ and k values. For each set, R and S values are calculated for all combinations of $v_R$ and $v_S$ between 0 and 3. Using the 30000 R and S pairs obtained for a specific $v_R$ and $v_S$ , we calculate the FDS discriminant ellipse by PCA and the covariance method. ....	240
D.3 The elliptical discriminant function and 100 points corresponding to 100 sets with different $v_R$ and $v_S$ values as labeled (each set has 5000 sample data A). In the two top figures, the sets are not FDS, since they have few scatterers. Therefore, ideally they all have to be placed outside the elliptical discriminant function. The two bottom figures the sets are FDS and the ellipse is expected to encompass them. ....	241
D.4 The regions with $\mu < 10$ and $k > 1$ are labeled by FS (few scatterers) and C (coherent) respectively. ....	242
D.5 Top left: summation of pFDS over the area C in Figure D.4 as a function of $v_R$ and $v_S$ . The bigger number indicates bigger false acceptance and therefore should be avoided. Top right and bottom left and right: The R – S values of 100 sets of coherent data (each set has 5000 sample data A) for different $v_R$ and $v_S$ values as labeled. A more reliable discriminant function will classify less percentage of the points as FDS (bottom right.)	243
D.6 Top left: summation of pFDS over the area FS in Figure D.4 as a function	

of $v_R$ and $v_S$ . The bigger number indicates bigger false acceptance and therefore should be avoided. Top right and bottom left and right: The R-S values of 100 sets of few scatterers data (each set has 5000 sample data A) for different $v_R$ and $v_S$ values as labeled. A more reliable discriminant function will classify less percentage of the points as FDS (bottom right.)	244
D.7 Top left: summation of pFDS over the area FDS in Figure D.4. The bigger number indicates better acceptance of the FDS. Top right and bottom left and right: The R-S values of 100 sets of FDS data (each set has 5000 sample data A) for different $v_R$ and $v_S$ values as labeled. All three cases perform well in accepting FDS. ....	246
D.8 Bovine liver B-scans at three different $v_R$ and $v_S$ values as labeled. The numbers at the center of each patch indicates how close the R and S of the patch is to the FDS ellipse. Big numbers are assigned to the patches that clearly are not FDS (marked by a circle around the number) in the bottom image. ....	246

## **Part-I: Chapter 1**

### **Motivation and Prior Art**

Image-guided surgery can be defined as a surgical procedure where the surgeon uses indirect visualization to operate, i.e., by employing imaging instruments in real time, such as fiber optic guides, internal video cameras, flexible or rigid endoscopes, ultrasonography, etc. Most image-guided surgical procedures are minimally invasive.” IGS systems allow the surgeon to have more information available at the surgical site while performing a procedure. In general, these systems display 3D patient information and render the surgical instrument in this display with respect to the anatomy and a preoperative plan. The 3D patient information can be a preoperative scan such as CT or MRI to which the patient is registered during the procedure, or it can be a real-time imaging modality such as ultrasound or fluoroscopy. Such guidance assistance is particularly crucial for minimally invasive surgery (MIS), where the procedure is performed through small openings in the body. MIS techniques provide for reductions in patient discomfort, healing time, risk of complications, and help improve overall patient outcomes; however, the sensory information available to the surgeon is greatly limited as compared with the open approach.

Minimally invasive surgery has improved significantly with computer integrated surgery (CIS) systems and technologies. Computer integrated surgery systems assist surgical interventions by providing pre- and intra-operative information, such as surgical plans, anatomy, tool position and surgical progress to the surgeon, helping to extend his or her capabilities in an ergonomic fashion. A CIS system combines engineering, robotics and computer technology for an improved surgical environment [Taylor-1996]. These technologies offer mechanical and computational strengths that can be strategically invoked to augment surgeons' judgment and technical capability. They enable the fusion of information with action, allowing surgeons to extend minimally invasive solutions into more information-intensive surgical settings. Figure 1.1 shows the overview structure of computer integrated surgery. Surgical assistant system is a variety of CIS system [Taylor-2002], which focuses on intraoperative decision support and skill enhancement. In next sections will summarize some of the CIS tools pertaining to robotic surgical interventions under ultrasound guidance.

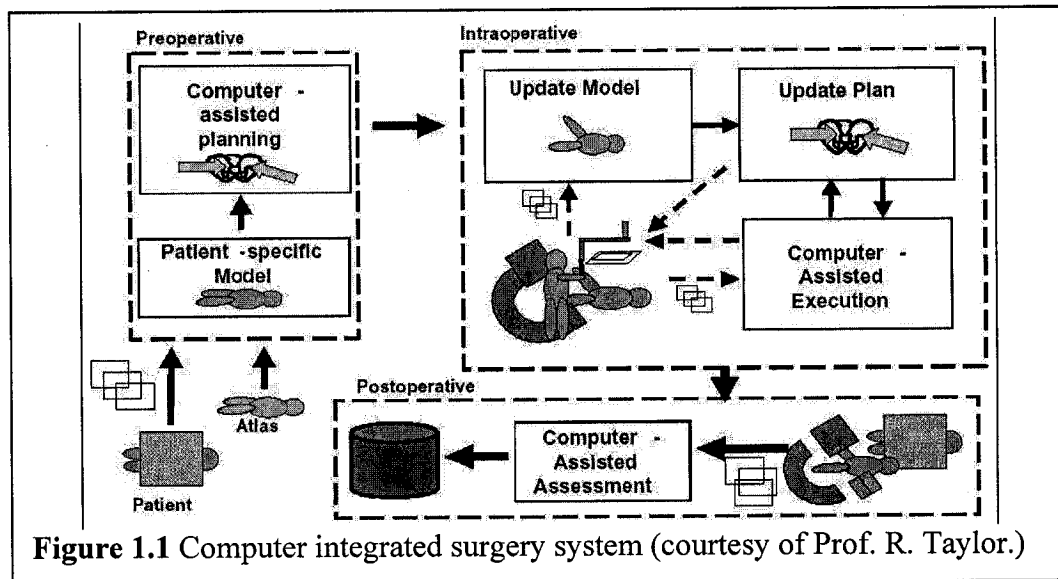


**Figure 1.1** Computer integrated surgery system (courtesy of Prof. R. Taylor.)

## **1.1 Robot-Assisted Needle Placement Systems**

Various image-guided needle placement robots have been used in non-liver applications. The applicants have published extensively in this domain, especially Taylor et al. who was the first to apply the remote center of motion concept to surgical instruments and developed the first such robot [Taylor-1995]. The “remote center of motion”, (RCM), concept refers to the ability to perform a pivoting motion around a fix point in space. This invention has laid the groundwork for the development of many modern needle placement and laparoscopic robots known today, including such a well known system as the daVinci™ (Intuitive Surgical, Inc.). Masamune et al. developed an MRI-compatible pivoting structure for stereotactic neurosurgery procedures [Masamune-1995]. In the search for lightweight RCM structures, Loser et al. reported on a 5-bar RCM linkage for needle insertion under visual servo control in a fluoro-CT imager [Loser-2000]. At Johns Hopkins, Stoianovici et al. (including Taylor) developed a chain-drive RCM robot (ST-RCM), conjunctly with a radiolucent needle driver for percutaneous renal access under joystick control and also used the system with C-arm fluoroscopy [Su-2002, Stoianovici-1998, Stoianovici-1997]. This robot later was applied under computational image guidance with C-arm fluoroscopy [Patriciu-2000], computer tomography [Patriciu-2001], and CT fluoroscopy [Solomon-2002]. Fichtinger et al. investigated the utility of the ST-RCM robot inside a CT scanner for transperineal intraprostatic needle placement [Fichtinger-2002c], as well as for general purpose injections [Masamune-2001]. Fichtinger and Burdette also applied a 6 degrees-of-freedom (DOF) variant of the ST-RCM robot for transperineal brachytherapy under real-time transrectal US guidance, where they integrated the robot with Burdette’s FDA approved US-based surgical guidance system [Fichtinger-2002a]. Choti et al. reported on the use of the ST-RCM device with CT guidance in a series of six patients undergoing percutaneous liver tumor radiofrequency ablation [Choti-2002b].

Attempts to develop alternative (non-RCM) kinematic approaches for percutaneous needle placement have included use of several non-medical industrial robots. For example, Yanof et al. used a Kawasaki FS-02 robot under CT guidance [Yanof-2001] and Rovetta et al. employed a SR 8438 Sankyo Scara robot under US guidance [Rovetta-1999]. Several non-RCM custom made robots have been developed for needle insertion. Chinzei et al. achieved 5 DOF needle placements with coupled Cartesian motion of two rigid arms [Chinzei-2001]. Li et al. tested the FDA approved NeuroMate™ robot (by Integrated Surgical Systems, Davis, CA) under CT guidance in stereotactic needle-based neurosurgery [Li-2002]. Fichtinger et al. demonstrated intraprostatic needle placement through the rectum wall with a 3 DOF in MRI robot that was guided in a cylindrical frame of reference inside the rectum [Fichtinger-2002b, Susil-2002].

For the sake of completeness, we also mention that stereotactic automated breast biopsy systems also perform some sort of mechanically assisted needle placement. In these systems, however, the target is stationary and effectively immobilized, so lightness and dexterity were not among the critical design factors. Furthermore, biopsy needles are typically inserted and retracted by a fast-action spring-loaded gun, which is not a suitable approach in liver surgery.

## 1.2 Instrument Tracking

Because ultrasound imaging cannot show the trajectory of the needle before it is inserted, simultaneous spatial tracking of both the US probe and the needle is the only option that will show where the needle is oriented with respect to the target. Therefore, spatial tracking is a fundamentally important aspect of the proposed systems.

Spatial tracking has become a straightforward task in computer assisted surgery during the recent years. Several thousand tracking systems are currently being used in a wide variety of medical applications in the United States and worldwide, typically utilizing some form of optical or electromagnetic technique. A few applications of encoded mechanical linkages, such as the BAT® system by Nomos Corp. (<http://www.nomos.com>) for US-guided target setup for external beam radiotherapy, are also known. A new frameless stereotactic system for radiotherapy guidance is presently being developed by CMS-IGD. As the engineering literature of spatial tracking is very extensive, we do not cite specific works here. Among a number of research systems, a few commercial solutions also exist for combining 2D ultrasound with tracked surgical instruments, including Sononav® by Medtronic Sofamor-Danek (<http://www.sofamordanek.com>).

### **1.3 3D Ultrasound (3DUS)**

At present, no commercial surgical navigation system exists which applies volumetric compounding and visual analysis of spatially registered 2D ultrasound images. Such systems only exist in the academic domain [Rohling-1997, Gobbi-2002], including preliminary work by our laboratory [Boctor-2003a, Boctor-2003b, Boctor-2001]. In order to achieve 3DUS volume, one can apply encoded carriers to move a 2DUS probe along a predefined trajectory, which is, for example, the basis of contemporary transrectal ultrasonography. Transrectal needle placement under 3D spatially registered image guidance resulted from the addition of Burdette's digitally encoded transrectal probe positioning system [Burdette-1997, Burdette-1998, Doggett-2000]. A closed-loop point-and-click surgical system was created by adding robotically assisted needle placement and online dosimetry calculation with updates based upon actual needle and source locations in the target tissue. [Fichtinger-2002a]. There has been recent interest in the

industry toward specific 3D ultrasound probes, but these devices provide limited field of view and they will probably need to be tracked in order to be widely used in image-guided surgery.

Several active robots have also been developed for consistent and repeatable telemanipulation of transcutaneous ultrasound probes. Pierrot et al. applied a Mitsubishi PA-10 industrial robot with a force controller to assist ultrasound technicians moving a US probe against the patient's body [Pierrot-1999]. Salcudean et al. built a five-bar counterbalanced RCM linkage [Salcudean-1999, Abolmaesumi-2002] to perform tele-echography of the carotid artery. At Johns Hopkins, Goldberg and Taylor developed a miniature robot for 5 DOF telemanipulation of a transcutaneous ultrasound probe [Goldberg-2001]. While telemanipulation may be helpful in diagnostic ultrasonography, surgery is an inherently hands-on process where cooperative manipulation would be a more suitable scenario. We envision the robot and surgeon both holding the US probe simultaneously and sharing control of the device. When it is appropriate, the robot complies with human action, while in certain situations the robot initiates an action that the human can accept or override. The robot and human communicate through a haptic interface built into the handle of the device. Taylor developed the first cooperatively manipulated force-controlled surgical robot, the Robodoc™ for total hip replacement surgery [Taylor-1994]. He adapted the method for laparoscopic assistance in the LARS (Laparoscopic Assistance Robotic System) robot [Taylor-1995], and most recently applied a similar method to microsurgical needle placement with the Steady Hand robot [Taylor-1999]. In this thesis, we explore possible scenarios which integrate robotic components to help with surgical intervention under US guidance. Our main driving clinical application is liver ablation either in open surgery, laparoscopic, or percutaneous scenarios.

## **1.4 Thermal Therapy: RF Liver Ablation**

In spite of recent advances in cancer therapy, treatment of primary and metastatic tumors of the liver remains a significant challenge to the health care community worldwide. Hepatocellular carcinoma is one the most common malignancies encountered throughout the world, and is being seen with increasing frequency in Western countries due to the changing prevalence of hepatitis C. This disease affects over 1 million people per year with dismal overall survival rate. In selected patients, potentially curative therapies including surgical resection and liver transplantation can be offered, but unfortunately most patients are not candidates for these treatments. With regard to metastatic liver cancer, colorectal cancer remains the most frequent hepatic malignancy in the United States. Liver resection is also potentially curative in these patients, with 5 years survival rates between 25 and 55%. Unfortunately, most patients with primary or secondary liver cancer are candidates for resection. Moreover, many patients' tumors recur within the liver following resection and few of these are candidates for re-resection. For these reasons, increasing interest has been focused on ablative approaches for the treatment of unresectable liver tumors. Radiofrequency ablation (RFA) is becoming the most commonly used and perhaps most promising modality for tumor ablation.

The rationale for RFA of liver tumors is evident. To begin, this approach often allows for greater preservation of uninvolved hepatic parenchyma, directing the treatment specifically to the tumor location. This feature is particularly beneficial for patients with hepatocellular carcinoma in the background of cirrhosis, where hepatic reserve is often limited. In cases of metastatic disease, tumors which are multiple, bilobar, centrally located, or in areas not technically resectable are potentially well suited for this approach. Additionally, RFA may be applicable for some patients with isolated hepatic recurrence

following liver resection, perhaps resulting in lower morbidity than repeat hepatic resection.

RFA has been developed partially in response to the limitations of other ablative approaches such as cryotherapy. Overall, reported complications have been rare with RFA. The principle limitation of ablation size, seen in earlier models, has been largely eliminated with the newer 5cm electrodes. In most major liver centers, RFA has become an integral component of the tools available to the hepatic surgeon as well as the interventional radiologist for the treatment of liver cancer.

An additional benefit of RFA is that it can be applied through minimally invasive approaches. Length of hospital stay, costs, and morbidity may be reduced using these approaches. These benefits add to the appeal of widening the application of local therapy for liver tumors to other tumor types, perhaps in combination with more effective systemic therapies for minimal residual disease. Improvements in the control, size, and speed of tumor destruction with radiofrequency will begin to allow us to reconsider treatment options for such patients with liver tumors. . Consideration for randomized trials comparing resection to RFA may be warranted in the future, if evidence emerges demonstrating that perhaps positive outcomes from use of local control with RFA approaches that of liver resection.

Although surgical resection remains the “gold standard” potentially curative therapy for primary and metastatic liver tumors, it is clear that radiofrequency ablation will begin to play an increasingly expanding role in the treatment options for the physician treating liver cancer. Improvements in treatment devices, imaging modalities, and minimally invasive tools all contribute to the future promise of this approach. The work in this

thesis provides number of enabling technologies to leverage the use of ultrasound and to help solve the main challenges facing the current practice of ablative therapy.

## **1.5 External Beam Radiation Therapy**

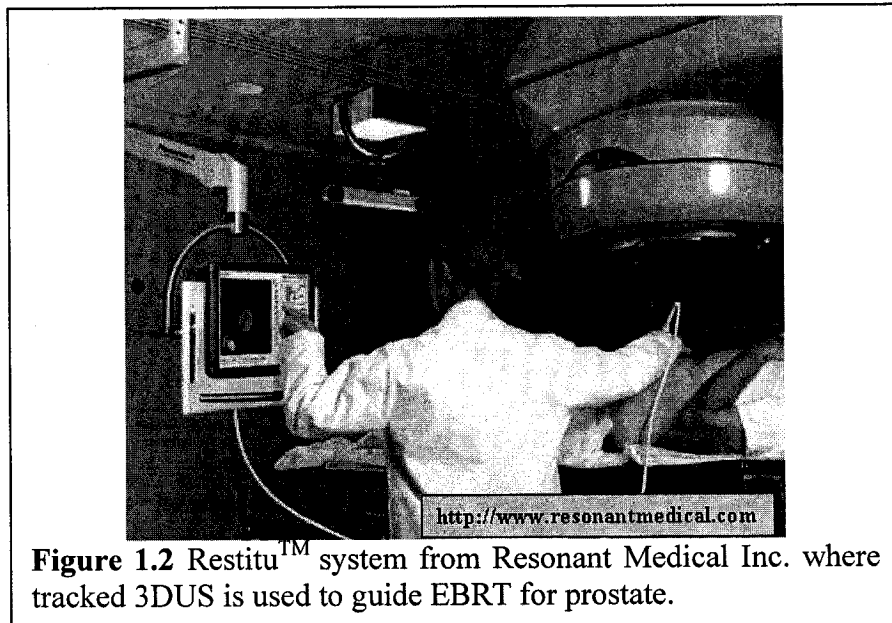
External beam radiation therapy (EBRT) is routinely used in the definitive management of patients with both clinically localized and locally advanced adenocarcinoma of the prostate [Cooperberg-2004a, -2004b, -2004c]. The total radiation dose is typically delivered in 35 to 42 treatment fractions over the course of about 8 weeks. Despite advancements in delivery techniques, the unsolved problem accounting for the motion of the prostate between and during treatment fractions remains. Literature shows mounting evidence that the prostate migrates substantially between treatment fractions, primarily due to variation in the contents of the bladder, bowel, and rectum. Among many who studied the problem early on, Lattanzi found the magnitude of field misalignments to be larger than 5mm in 51% of cases and larger than 10mm in 21% of cases [Lattanzi-2000]. Hundreds of papers since then have documented the problem. At the time of this writing, a PubMed search on prostate motion or localization in radiation therapy brought 304 references, with over 200 written in the past 5 years alone. Further adding to the problem, the prostate may migrate during the treatment fraction, which makes repeated or real-time localization desirable. McNair et al. used a urethral catheter containing radio-opaque markers which were visible on electronic portal imaging, enabling verification of prostate position [McNair-2004]. The mean intrafraction movement was found to be 0.2mm (SD 1.2mm), 2.9mm (SD 3.1mm) and 0.7mm (SD 2.3mm) in the RL, CC and AP direction, respectively. While the independent prostate movement was identified, the catheter was poorly tolerated.

Treatment margins are increased to account for prostate motion, causing adverse side effects from radiation. Clinically significant gastrointestinal and genitourinary complications occur in about 46% and 56% of patients respectively, and are treatment volume dependent [Peeters-2005]. Erectile dysfunction appears in up to 80% of patients [Siegel-2001] and has been associated with dose to the nearby penile bulb [Roach-2004]. Most importantly, geographic miss has been clearly associated with increased risk of treatment failure and complication [De Crevoisier-2005]. Several approaches have been investigated to attempt to stabilize and/or localize the prostate for radiation therapy. Dietary control of the contents of rectum and bladder is universally practiced, but alone is insufficient. Wang et al. prospectively assessed the setup accuracy with a stereotactic body localizer in immobilizing patients for stereotactic intensity-modulated radiotherapy (IMRT) for prostate cancer [Wang-2004], but the residual placement error (based on implanted gold fiducials) remained substantial, because this approach did not address independent motion of subsurface soft tissues. Stabilization with an inflatable rectal balloon [Patel-2003, Teh-2002] is invasive, uncomfortable, and does not allow for prostate visualization. Implanted passive metal markers [Nederveen-2001, Nederveen-2002, Kitamura-2002] and active beacons by Calypso Medical Systems ([www.calypsomedical.com](http://www.calypsomedical.com)) require surgical implantation and are vulnerable to edema induced motion and intraprostatic migration over the 8 weeks therapy. Flat panel cone beam computed tomography (CBCT) [Smitsmans-2005, Letourneau-2005] has been investigated, but this approach has limitations in soft tissue contrast [Nikolaou-2005, Vences-2005], requires that specialized hardware be added to the therapy machine [Jaffray-2002], and most significantly, it exposes the patient to excessive radiation dose especially if CBCT performed multiple times during each treatment session. Most recently, multiple researchers have looked at predictive statistical models to account for both systematic and random organ motions [Sohn-2005, Booth-2005, Chu-2005, Yang-

2005], but these statistical methods have not been popular because irrefutable direct position measurement is a more generally preferred method, with the goal of reducing setup errors.

Tracked transabdominal B-mode ultrasound has shown promise in prostate localization (Figure 1.2), and is non-invasive, non-toxic, inexpensive, and widely available. Four commercial systems are currently available. In all of these, the prostate is localized in the B-mode ultrasound image whose coordinate space is spatially registered with the coordinate space of the linear accelerator. When the prostate is localized in the ultrasound image, its location becomes known in the coordinate space of the linear accelerator, and the therapeutic beam can be aimed at the prostate, as planned. While most investigators have found B-mode transabdominal prostate localization generally helpful, its clinical performance fluctuates and depends strongly on the skill level of the personnel acquiring and interpreting the images [Jani-2005, Langen-2003, Trichter-2003, Little-2003, Chandra-2003, Serago-2002, Morr-2002, Lattanzi-2000]. EBRT is performed in radiation oncology facilities where the radiation technology staff is usually not well trained and experienced in sonography. The primary source of error is that prostatic contours are often indistinct in transabdominal B-mode images, and most technologists reflexively increase probe pressure in an effort to improve image quality. Higher abdominal pressure, however, causes increased posterior dislocation of the prostate, whereas when the probe is removed from the abdomen prior to treatment the prostate “bounces” back anteriorly [McGahan-2004]. The average prostate motion due to probe pressure has been found to be 3mm in depth, and results in a systematic error of dose being targeted in the direction of the rectal wall which lies posterior to the prostate [Artignan-2004]. Furthermore, in current clinical practice US-based localization is performed in the beginning of the

session, and there is no safeguard against prostate migration (target dislocation) during the fraction, which, as we said earlier, is a known problem [McNair-2004].



Despite initial enthusiasm, contemporary freehand B-mode transabdominal US has clearly reached its practical limits. It is therefore a logical imperative to improve on ultrasound imaging and make it capable of robust and rapid tracking of the prostate transabdominally. In this thesis, we will describe enabling technologies to leverage the current use of tracked US, with the goal of improving external beam radiation therapy outcomes to the level where it can fulfill its clinical promise.

## 1.6 Our Contributions

There has been an increasing interest in minimally invasive US-guided interventions that require precise placement of a surgical tool (needle, tissue ablator, etc.) to the anatomical target. To address this problem, we have developed a collection of novel technologies and integrated those in prototype systems.

We introduce multiple system embodiments that involve robotics, tracking, anatomical modeling, ultrasound image processing, and elasticity monitoring. The underlying themes in these systems are (1) simultaneous tracking of surgical tool with respect to the US images and (2) monitoring physiological changes, specifically tissue coagulation, throughout the procedure. These systems and test-beds are described in Part-I of this thesis in Chapter 2, 3, and 4.

With respect to the first theme, we invented a robust method for 2D and 3D ultrasound probe calibration, which uses a closed-form solution to discern the unknown spatial transformation between image pixels and tracker coordinates. A novel methodology will be introduced for real-time in-vivo quality control of tracked US systems, by capturing system errors that manifest in changes of calibration parameters. The process runs transparently while the subject is being scanned during the procedure. The concept, mathematical formulation, and experimental evaluation are presented and demonstrated in-vitro experiments in Part-II of this thesis in Chapters 6 and 7.

With respect to the second theme, we invented a rapid US-based approach to monitor ablative therapy by optimizing shape and elasticity parameters. Our method involves the integration of a biomechanical computational model of the tissue, a correlation approach to estimate and track tissue deformation, and an optimization method to solve the inverse problem of recovering the shape parameters in the volume of interest. Convergence and reliability will be demonstrated on simulated data. Successful monitoring of tissue ablation will be presented from 18 ex-vivo bovine liver samples. Finally, we describe extension of the framework for partial and full reconstruction of elasticity parameters. The details are presented in Part-III of this thesis.

## **Part-I: Chapter 2**

# **Ultrasound-guided Intervention Systems**

### **2.1 Introduction**

Hepatocellular carcinoma is one of the most common malignancies, and accounts for more than 1 million HCC cases per year worldwide [Choti-2000a]. Metastatic disease to the liver, primarily from colorectal cancer is the most frequently found hepatic malignancy in the United States. The principal potentially curative treatment for these patients is liver resection, resulting in 5 years survival rates between 25 and 55%. Liver resection, which results in 5 year survival rates of between 25% and 55%, is the primary potentially curative treatment for patients with this condition. Unfortunately, most patients with primary and secondary liver cancer are not candidates for resection, primarily due to tumor location or underlying liver disease. For these reasons, increasing interest has been focused on interstitial ablative approaches for the treatment of unresectable liver tumors. Local tissue ablation is performed with lower morbidity than resection and can be employed as a minimally invasive approach, including percutaneously and laparoscopically, and hence more patients are eligible for this curative therapy for liver cancer. Studies have demonstrated the efficacy of interstitial ablative approaches for the treatment of hepatic tumors, including chemical ablation, cryoablation, and thermal ablation using energy sources like radiofrequency, laser, microwave, or focused ultrasound. Thermal ablation using radiofrequency energy is the most frequently used modality [Choti-2002a, Choti-2000b] (Figure 2.1), but other

techniques are also used, including ethanol injection, cryotherapy [Fishman-2000], microwave [Enomoto-2001], and interstitial photon radiation [Choti-2000c].

Although ablative therapies are more effective for treating hepatic tumors, there are still problems due to the need for precise placement of the ablator devise and the need to monitor the zone of necrosis. The precise location of hepatic tumors is usually determined by a preoperative imaging modality such as computed tomography or magnetic resonance imaging. However, the preoperative planning information cannot be used actively or solely during surgery to guide resections or probe placements for ablative therapies. Moving or using these scanners (CT, MRI) to the surgery room would assist intraoperative guidance. However there are deterrents to using these scanners in the operating room. First, they are expensive, based on the unit cost, installation cost, cost per operation and cost of compatibility (i.e. MRI should be placed in a magnetic free interference environment). Second, MRI and CT scanners are large machines, and the space they occupy could make standard operations more difficult. Third, these imaging devices are not real-time, and depending on actual system architecture, their latencies may be quite significant.

Intraoperative ultrasonography (IOUS) may be the ideal imaging modality, because it provides excellent anatomical imaging, which is real-time and interactive; it is widely popular in diagnostic and therapeutic procedures [Caratozollo-1999]. Because of its specificity and sensitivity, its use is particularly significant when diagnosing and treating disorders of the pancreas, biliary tree, and liver [Choti-2002a], especially in early stages of the disease. Alternative techniques, such as preoperative imaging (angiography, scintigraphy, CT, US), and surgical exploration, is less than 60-80% [Bazan-1989]. Intraoperative ultrasonography, however, allows for early diagnosis and precise

localization of many diseases, and is an excellent guidance tool for accurate and radical surgical treatment.

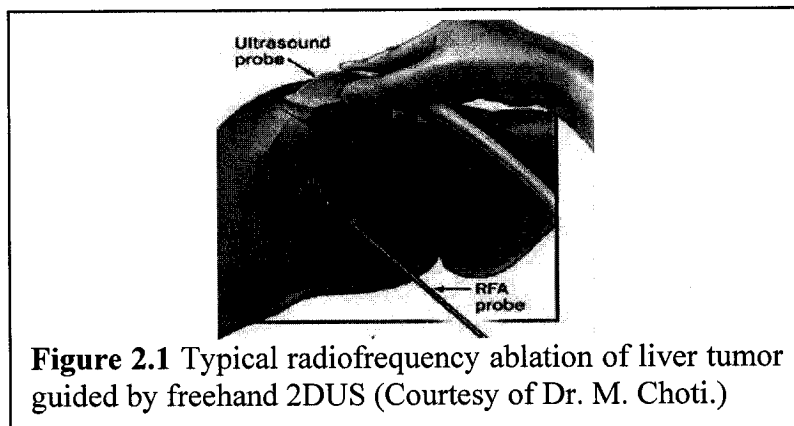


**Figure 2.1** Typical radiofrequency ablation of liver tumor guided by freehand 2DUS (Courtesy of Dr. M. Choti.)

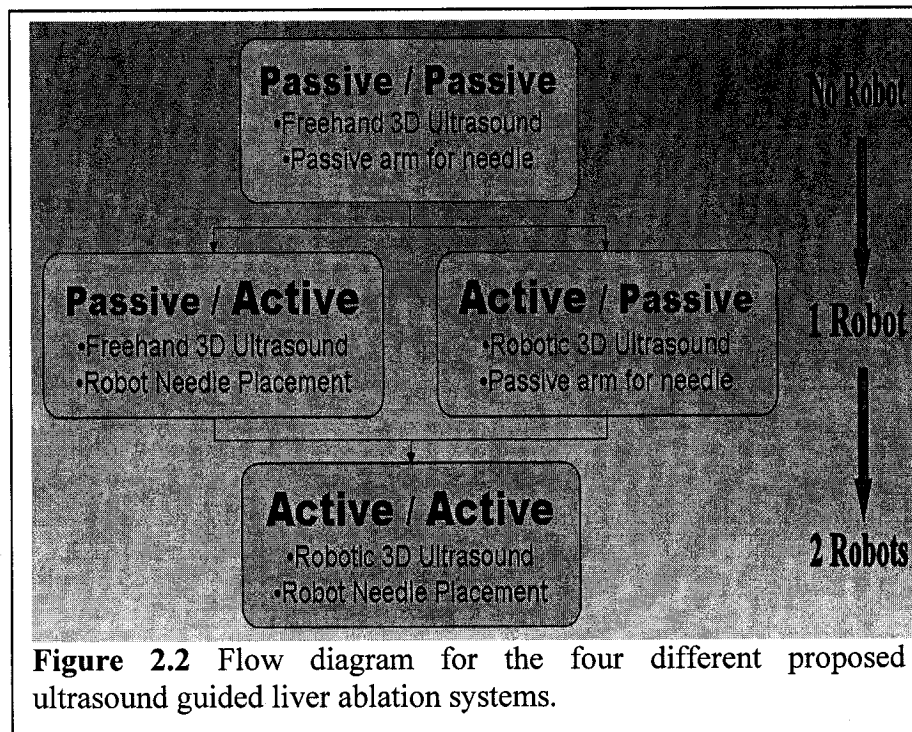
In current surgical practice, intraoperative US-guided liver ablation is generally performed in two major steps. First, targets (i.e. tumors) are identified by preoperative imaging, chiefly CT and MR. Second, these tumors are intraoperatively or laparoscopically localized by IOUS. Current methodology requires manual IOUS in conjunction with free hand positioning of the ablation probe under ultrasound guidance (Figure 2.1). Simultaneous manual handling of the B-mode ultrasound probe and the ablator device is a challenging task that is prone to significant errors in the hands of even the most experienced physicians [Boctor-2003a]. IOUS imaging provides perhaps the best imaging modality for targeting, but its current two dimensional format leads to significant interuser variation in results. It is extremely difficult to place the ablator device precisely into the target, due to tissue deformation and target motion. In addition, irregularly shaped target volumes typically require multiple insertions and several overlapping thermal lesions, which are even more challenging to accomplish in a precise and timely manner without causing excessive damage to surrounding normal tissues.

US-guided liver ablation is an ideal setting to make use of tracked ultrasound technologies. Improving real-time guidance for planning, delivering, and monitoring ablative therapy would provide the tool that would allow accurate and effective application of this promising therapy. It is believed that image-guided tracked ablation can make these procedures significantly more accurate, more effective, safer, and less expensive. In response to the clinical issues outlined above and the promise embedded in both medical robotics and tracking technologies, we have developed a collection of innovative US-guided interventional systems and have thoroughly tested their accuracy and efficacy using simulation, phantom, and ex-vivo animal studies. In the following sections we will describe the details of these novel interventional systems, and examine the improvements in targeting accuracy and performance efficacy we believe they will provide.

## 2.2 Our Approaches and Methods

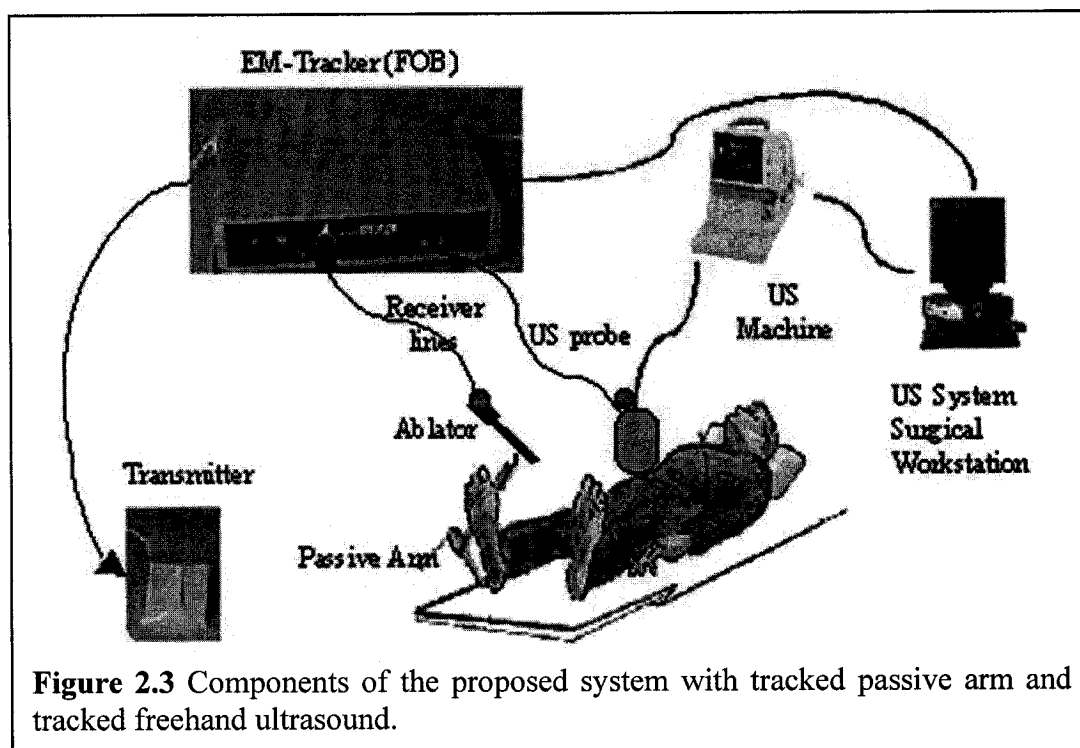
The key feature of our prototype system is real-time spatial tracking of both the ultrasound probe and RF ablator. This scenario applies to all forms of ultrasonography: transcutaneous, laparoscopic, and intraoperative; in this thesis, we explore the last two. Figure 2.2 illustrates the four possible alternatives for intraoperative US-guided liver ablation, depending on how the ablator and ultrasound transducer are handled with respect to one another. The first alternative is to have a passive/passive system where the ablator is guided by a passive arm and the US transducer is used in freehand scanning[Boctor-2003a]. In a passive/active system, an active arm guides the ablator while the ultrasound transducer is still held manually [Boctor-2004a]. In an active/passive system, the US probe is guided and controlled by a robotic arm while the ablator is attached to a passive articulated mechanical linkage [Boctor-2003b]. Consequently, in an active/active system both the ablator and US probe are under robotic control [Boctor-

2004b]. It is also possible to categorize these innovative solutions according to the degree of robotic control involvement (Figure 2.2), reflecting important cost effectiveness issues.



### 2.2.1 Passive/Passive System

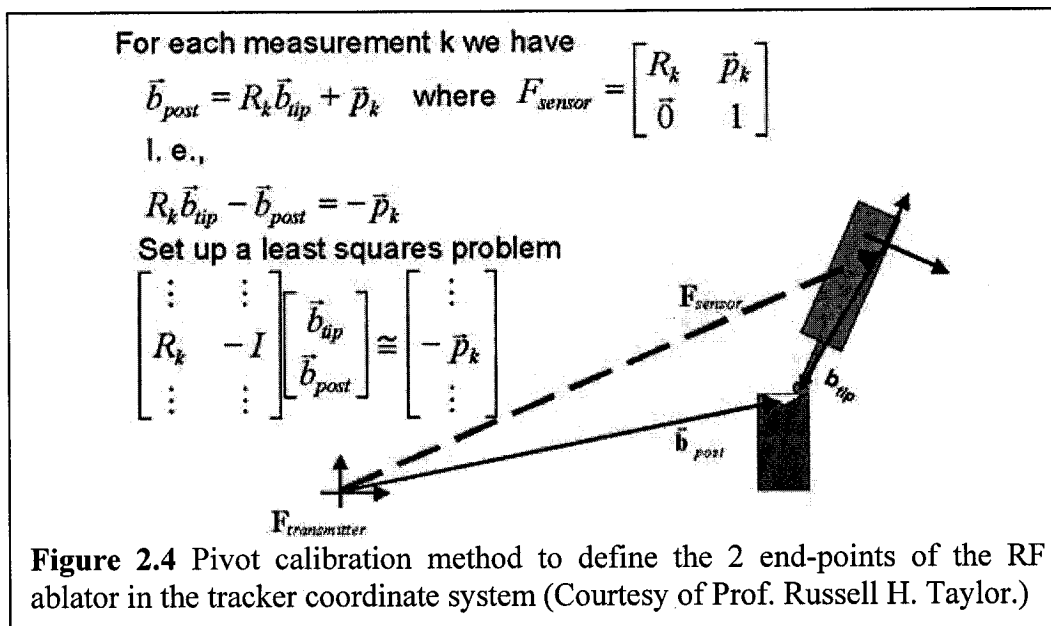
The key component in the proposed solution is tracking both US and RF probes for better accuracy in targeting the tumor, reducing the time required for the operation, and minimizing the dependency of the surgical experience. This proposed solution would be applicable for all three different liver ablation approaches: percutaneous, laparoscopic, and intraoperative. However, in this project, we test the concept in open intraoperative setting. In our proof-of-concept study, an adjustable passive arm (with 6 degrees-of-freedom) holds the RF ablator and a tracked freehand B-mode ultrasound probe provides data for computer-reconstructed 3D ultrasound (Figure 2.3).



The components we use are: (1) a commercial B-mode ultrasound scanner (Aloka SSD1400, Japan), (2) a pulsed magnetic field position and orientation measurement system (Flock of Birds, model 6D FOB, Ascension Technology Corp., Burlington, VT, USA); (3) an RF ablation probe (XL, RITA Medical Inc.), an adjustable mechanical support arm developed at Johns Hopkins, and (4) a graphic workstation for capturing ultrasound images, recording data from the FOB tracker, building the 3DUS volume and performing the analysis, planning and monitoring of the delivered treatment. The particular US probe used in this study is a 3.5MHz curved array transducer. Full ultrasound images from the video output of the ultrasound scanner are digitized by a frame grabber board (Matrox, MeteorII) attached to the graphic workstation. The system shown in Figure 2.3 avoids expensive robotic components and utilizes an affordable – compared to other expensive tracking technologies– electromagnetic tracking device.

### 2.2.1.1 Tracked RF ablator and passive arm

It is of utmost importance to identify the location of the ablator tool before insertion and to plan for highly accurate and minimum invasive targeting. Because ultrasound imaging cannot show the trajectory of the needle before it is inserted, simultaneous spatial tracking of both the US probe and needle is the only alternative to let us know where the needle is oriented with respect to the target. Therefore, spatial tracking is of fundamental importance to the proposed system.



Tracking the ablator device and identifying its end points with respect to the tracker frame (FOB) is called calibration of the RF ablator. The location and orientation ( $F_{Sensor}$ ) of the FOB's sensor with respect to the base frame or FOB's transmitter ( $F_{Transmitter}$ ) are captured real-time. In order to get the unknown position vectors for the two end points, a Pivot Calibration method was used as shown in Figure 2.4.

In addition, the process of ablation through one entry point demonstrates the need for

pivoting support. To provide this support, the RF probe is supported by an adjustable rigid mechanical structure comprising the following components (Figure 2.5): (1) A 6 DOF passive arm provides moving the needle to the point of insertion. (2) A 5-bar remote center of motion linkage, attached to the passive arm, provides two independent rotations for the needle to pivot around the point of insertion. (3) A passive unencoded linear stage holds the ablator needle and provides insertion into the liver. (4) Friction brakes hold the rotation and linear motion stages in place. (5) A Lego attachment holds interchangeably the Flock of Bird and Polaris sensors. (6) A plastic extension for the RF probe allows for accurate pivoting calibration around both ends of the needle.

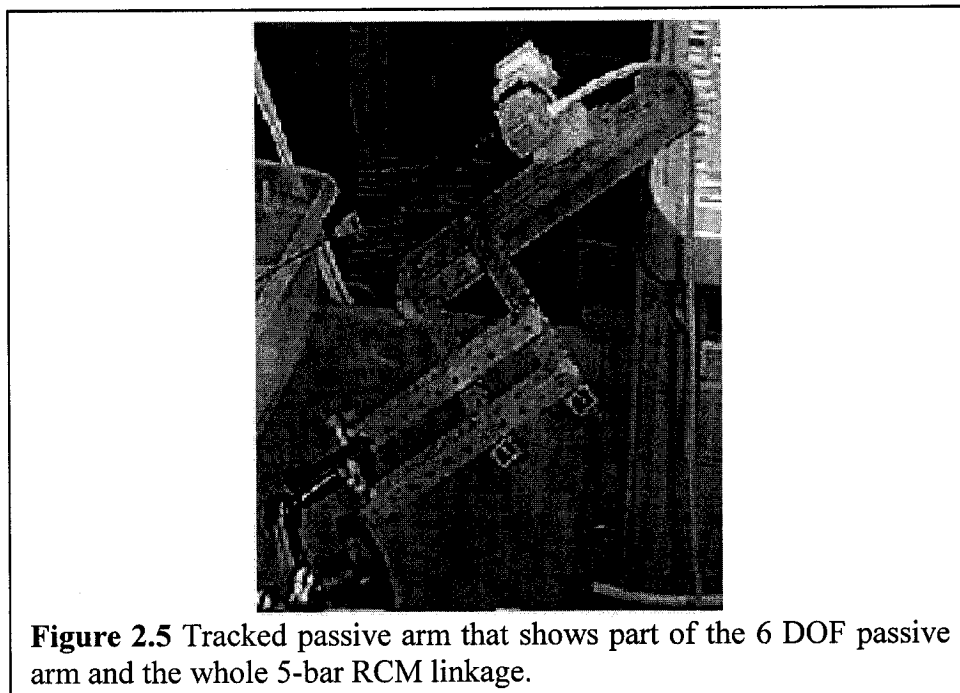


**Figure 2.5** Tracked passive arm that shows part of the 6 DOF passive arm and the whole 5-bar RCM linkage.

### **2.2.1.2 Freehand tracked 3D ultrasound**

The freehand tracked ultrasound system entails compounding the acquired 2DUS images into a 3D volume, which is considered to be an excellent tool for intraoperative planning. Tracking is the essential element of this system; it identifies location and orientation for

every scanned US image into the reconstructed 3D volume. Generic tracked US system utilizes freehand scanning and a tracking device, typically optical or electromagnetic. Figure 2.6 depicts the basic idea behind such generic tracked US system.

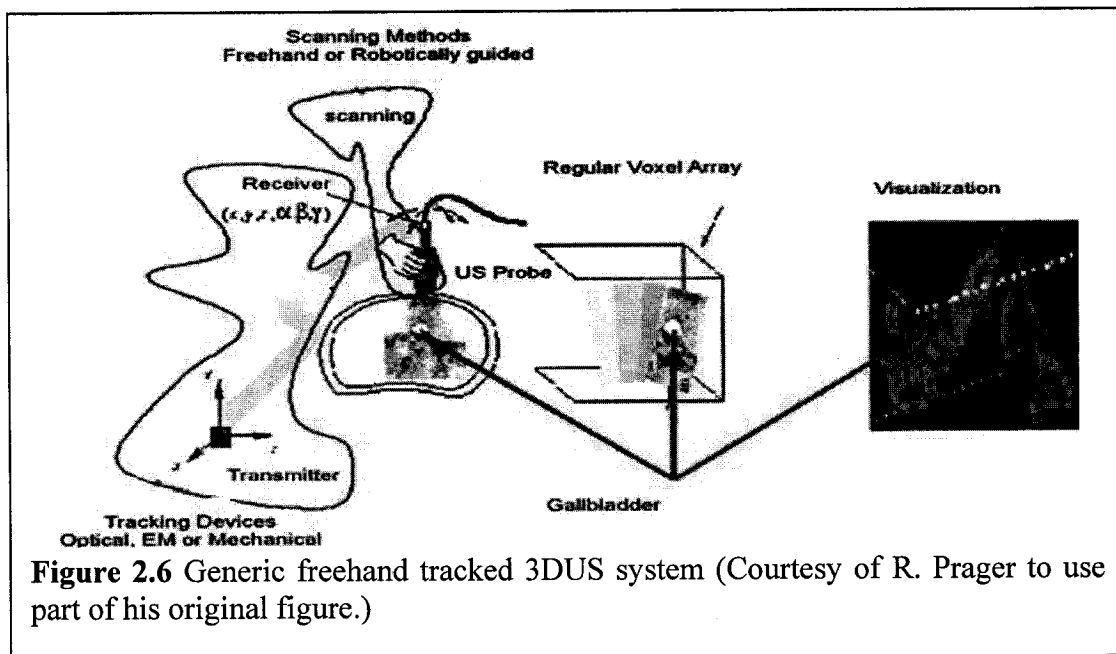


**Figure 2.6** Generic freehand tracked 3DUS system (Courtesy of R. Prager to use part of his original figure.)

The following modules represent the main components of the Tracked US system:

- **Acquisition and Synchronization Module:** Captures the two streams of US data and tracker information in a synchronized way and sets the parameters of both units.
- **Reconstruction Module:** Converts the scattered arrays of images into a structured 3D voxel array for the scanned organ by selecting the appropriate algorithm (Voxel Nearest Neighbor (VNN), Pixel Nearest Neighbor (PNN), Distance Weighted methods (examples include the Shepard and Gaussian methods), and Radial Basis Functions (RBF)).
- **Processing and Visualization:** Enhances the US images by applying smoothing, anisotropic diffusion and/or morphological operators.

- **Calibration Module:** Calibrates the US beam to determine the transformation between the US image frame and the tracker coordinate system or the world coordinate system.

The two calibration processes that are central to the accuracy of the 3D ultrasound System (3DUS): temporal calibration and spatial calibration are both discussed below.

**Temporal Calibration.** This task involves estimating the latencies between the tracking device and the video signal from the ultrasound machine. The goal is to synchronize both streams; one process acquires US images and places them in reserved memory and the other acquires readings from the tracker and stacks them in memory. Synchronization calibration is performed once per hardware/software configuration. We have adopted two methods for handling this one time task.

The first method was originally introduced in the Cambridge tracked US system, Stradx [Berman-1999]. The basic idea is introducing a sudden movement of the US probe (moving 5-10cm in less than 100-200ms), which will be rendered in both tracker readings and US image appearance. By careful examination of both streams, one can estimate the latency offset between the two processes. However, if US images are acquired every  $t$  secs, and tracker readings every  $T$  secs, then the latency offset can be recovered to an accuracy of  $+/- (T+t)/2$  secs. Therefore, performing several calibrations and averaging the resulting offset is recommended.

Our second method is a novel hardware-based method. A series of experiments reading the two signals of US capture and position sensor reading on an oscilloscope helped to

design the optimal and minimal settings for these two synchronized processes. They also helped determine the inner delay of the measurement cycle of the position sensor device. A fundamentally important feature of this calibration process is the use of a real-time monitoring and debugging tool. When either a US capture or tracker reading occurs, a signal is generated to indicate where the reading begins and ends through the use of a parallel port. The time taken to output to the parallel port by the help of low level assembly commands is on the order of a few processor cycles (4-6 Machine Cycles). Reading these two signals during normal operation mode on a real-time digital oscilloscope assists in estimating the latency offset and determining optimal design for this real-time module.

***Spatial Calibration.*** The spatial calibration process involves determining the 6 DOF rigid body transformation between the position sensor and the corner of the B-scan plane, and also the scale ratios in x and y dimensions (typically in mm/pixel units). This task is considered to be the critical task of any image-guided interventional system. Spatial calibration is usually performed by scanning and reconstructing some known object and then, using the discrepancy between the reconstructed shape and the known shape, re-estimating the calibration parameters. Knowing this transformation matrix, one can place every pixel in the image coordinate system into the reconstruction space. Our 3DUS interventional systems utilize novel calibration methods that range from conventional offline phantom-based methods to real-time phantomless patient specific calibration methods. Due to the importance and potential impact of these innovations, these methods will be covered separately in Part-II of this thesis.

### ***2.2.1.3 Planning and visualization software***

For our graphical user interface, we adapted the 3D Slicer medical data visualization

package [Gering-2001]. This is a public domain open source system primarily developed by the Surgical Planning Laboratory at the Brigham and Women's Hospital (<http://www.slicer.org>), with sustained contribution from our group. The strength that we added to Slicer is a generic 3DUS processing module, providing synchronized real-time capture of 2DUS data and position information, and robust assembly of a spatially registered 3D volume from sparse and irregular 2D information. The software also provides a customizable real-time overlay display of the US volume, RF ablator tip with its current ablating range, and the current 2D ultrasound slice. Tumor coverage can be planned with single-spot and overlapping multiple ablations. In addition to the aforementioned visual overlay, other visual and metric tools help the user to place the ablator. The system reposts the current insertion depth that can be double-checked against the ruler on the passive unencoded insertion stage, shows the distance between the actual and the planned RF ablator, and also provides coordinate systems and landmarks to ease navigation in the virtual space, as shown in Figure 2.7. Detailed software implementation and synergetic integration will be presented in Chapter 4.

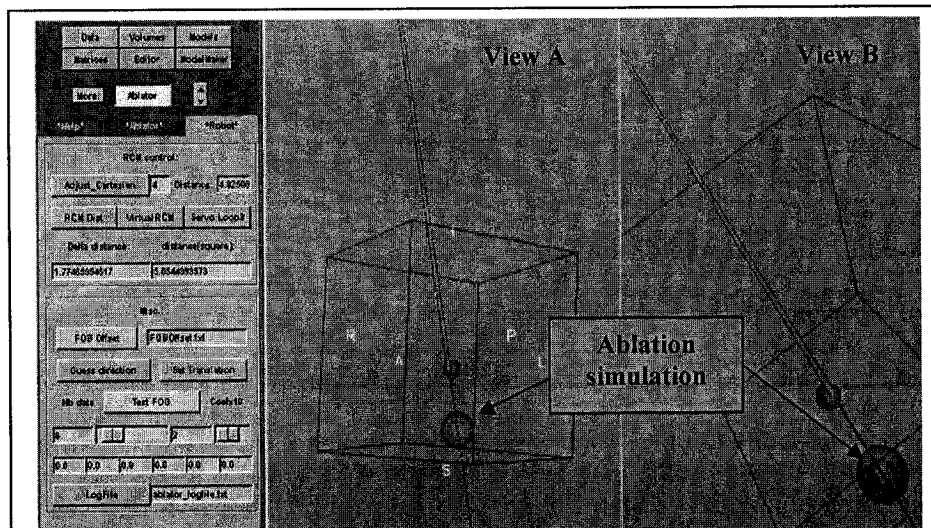


**Figure 2.7** Dual 3D view interface based on 3D Slicer for planning and visualization.

## 2.2.2 Active/Passive System

Simultaneous manual handling of the B-mode ultrasound probe and the ablator device is a challenging task that is prone to significant errors in the hands of even the most experienced physicians [Boctor-2003a]. We realized that freehand manipulation of the US probe critically lacks the level of control, accuracy, and stability required for guiding liver ablation. Volumetric reconstruction from sparse and irregular 2D image data is suboptimal. Variable pressure from the sonographer's hand also causes anatomic deformation. Finally, maintaining optimal scanning position with respect to the target lesion is crucial, but virtually impossible with novice hands to achieve with freehand guidance. To address these problems, we propose to integrate robot assisted three dimensional intraoperative ultrasound with a passive lightweight arm to facilitate precise placement of a thermal ablator into the liver and to monitor the progress of tissue ablation with real-time ultrasound (Figure 2.8).

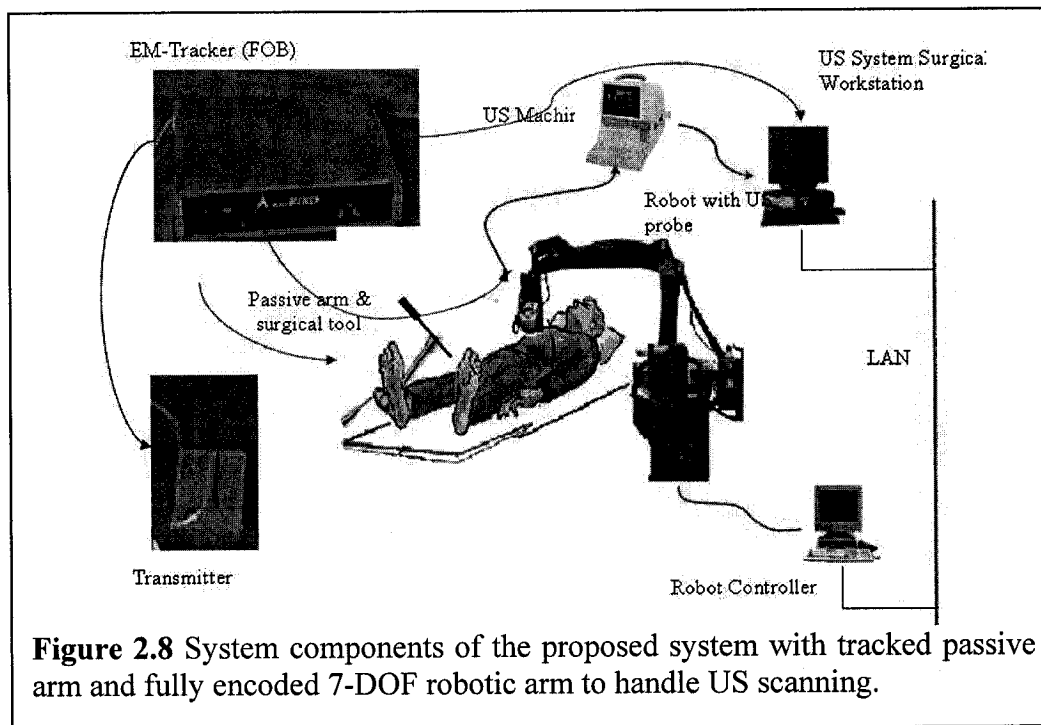


**Figure 2.8** System components of the proposed system with tracked passive arm and fully encoded 7-DOF robotic arm to handle US scanning.

Regardless of whether the ablation is delivered in transcutaneous, laparoscopic, or open surgical setting, the process always involves moving the tip of the device to a preselected entry point, then entering the device into the tissue till it reaches a preselected target point only then the actual tissue ablation can take place. Real-time ultrasound imaging has an active role throughout the entire procedure, hence precise, predictable, and repeatable control of the US probe is critically needed. A robot assisted ultrasound system would provide many benefits: enabling more structured and optimized 3D ultrasound datasets, providing consistent reliable guidance to interventions, help registering multimodality images, and avoiding fatigue and occasional musculoskeletal injury to the sonographer [Harms-1993]. In liver ablation surgery, robot assisted ultrasound can maintain the pressure profile induced by the US probe, thus minimize tissue deformation and motion artifacts. Telesurgery and teleradiology are also potential beneficiaries of robotic ultrasound.

The integration of robot assisted ultrasound with spatial co-registration of the ablator device promises to make these procedures more accurate, faster, more effective, and less expensive in the long run. Robotic assistance may also reduce the dependency of outcome manual skill of the surgeon, leaving actual medical knowledge and experience the decisive factor of the surgery. The actual system embodiment of this paradigm features (Figure 2.8): (1) The LARS robot developed previously by Taylor et al. [Taylor-1995], (2) a commercial ultrasound scanner (Aloka SSD1400, Japan), (3) a pulsed magnetic field position and orientation measurement system (Flock of Birds, model 6D, Ascension Technology Corp., Burlington, VT, USA), (4) an RF ablation probe (XL, RITA Medical Inc.) supported by a passive arm; and (5) a central workstation to provide overall control, data management, and graphical user interface. The hub of the system is the central workstation that provides capturing of ultrasound images, recording data from

the FOB tracker, building the 3DUS volume, and planning and monitoring of the delivered treatment. The particular US probe used in this study is a 3.5MHz curved array transducer from Aloka. A real-time image capture board (Matrox, MeteorII) is installed in the central computer to acquire the US images through the video output interface.

### **2.2.1 Robotic 3DUS system (LARS-US)**

Taylor was the first to propose use of the remote center of motion concept in medical robotic systems [Taylor-1995], which denotes the ability to provide angular orientation about a fixed point in space. Taylor's invention has become the foundation for many modern laparoscopic and needle placement robots known today, including such well known systems as the DaVinci (by Intuitive Surgical Systems). The LARS robot is a kinematically redundant manipulator composed of a proximal translation component, along with a distal remote center of motion component that provides three rotations and one controlled insertion motion that passes through the RCM point. The LARS, as shown in Figure 2.9, consists of a three-axis linear Cartesian motion stage, a two-axis parallel four bar linkage which provides two rotations ( $R_x$  and  $R_y$ ) about the remote center of motion, and a two-axis distal component providing an insertion motion,  $s$ , and rotation  $R_s$  about the instrument axis, which passes through the remote center of motion.

A unit called RCC (Robot Control Computer) controls the LARS and essentially acts as a server. A dedicated computer runs the robot server and it is accessed by a client application running on the central planning/monitoring workstation. The communication takes place via TCP/IP connection over a local network. The client application is sealed off from the robot server; they communicate with the use of a small library of functions, such as InitializeRobot, MoveRotationalStage, and so forth. Procedure, error, and status

codes are also communicated to the client application. The robot software infrastructure has been developed at our Center, under the name of Modular Robot Control (MRC) library. The MRC library is a generalized set of portable C++ classes for distributed and modular robot control; it covers forward and inverse kinematics, joint level control, force sensors and peripheral support.

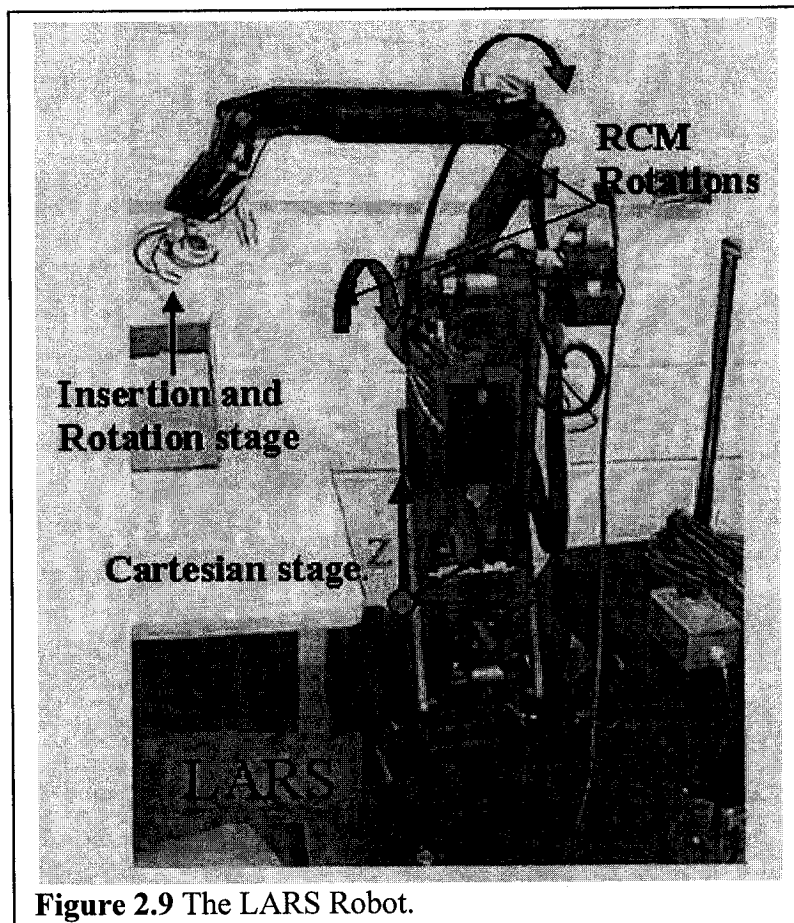


**Figure 2.9** The LARS Robot.

In this project, we have adopted the LARS robot to acquire 3DUS data in preliminary studies for our minimally invasive robot assisted liver ablation research program. In order to achieve the coupling between the US and the LARS, the following steps had to be completed: (1) Calibrate a 6 DOF force sensor resident on the LARS and integrate it with

the MRC library. (2) Design and build end-effectors to hold the US probe in the RCM point. (3) Integrate the LARS in the 3DUS software. The integration of LARS requires the implementation of several image acquisition scenarios. One scenario is to move the robot in a steady way, covering the volume of interest and in the same time capture dynamically the US images along with their tracker readings. Another way is to move the robot incrementally to capture statically the US images and the tracker readings. The steadiness of the robot is one of the prominent features, allowing for static tracking. In general, static tracking is more accurate than dynamic tracking in freehand tracked ultrasound, because here one does not have to calibrate the system for the delay between the image and the tracker reading [Lavallée-1998].

The force sensor is incorporated into the system to serve two purposes. First, the imaging protocol starts with an exploration phase, when the user guides the arm around the volume of interest. This is accomplished by using a multi-dimensional force-sensor that interprets the intentions of the user and allows the robot to comply and learn this path. The robot can thus acquire a 3DUS volume by capturing position/force tagged 2DUS images according to a predefined scanning profile. Second, maintaining the same pressure profile allows accurate scan repeatability. This not only helps improve management of data gaps but also produces high quality and reproducible volume reconstruction. Once the volume is available, we can plan the treatment and execute it with the use of the passive arm, monitored in repeat scans performed the robot assisted ultrasound.

The overall accuracy of reconstruction in a freehand 3DUS system is dependent, to a certain extent, on the following factors. First, good synchronization (temporal calibration or accurate tagging between the captured image and the tracker reading) is required to

overcome the uncertainties of dynamic tracking and the unknown internal delays of the tracking device (which is in the order of 20-80msec). Second, optimal spatial reconstruction and, to some extent, motion artifact compensation is required. This is a significant challenge, considering the sparse and irregular 2D image data, variable pressure from the sonographer's hand causing variable deformation of the imaged tissues. Third, preprocessing and gap filling algorithms are required because there is no fixed gap pattern for every freehand scan.

A robotically assisted 3DUS system, overcomes these challenges. In a robotic US system, there is no need for synchronization to tag the captured US image with the tracker reading, because scanning is performed in a well controlled incremental fashion. In other words, the robot can be gated to start the next movement only after having captured the US image and reading the tracker has been completed. In addition, the robotic system provides more favorable management of data gaps, which in turn leads to faster and more efficient data preprocessing.

The passive component of this system is the same one used in the Passive/Passive paradigm, which is an adjustable 6 DOF arm connected to RCM linkage as discussed in Section 2.2.1.1.

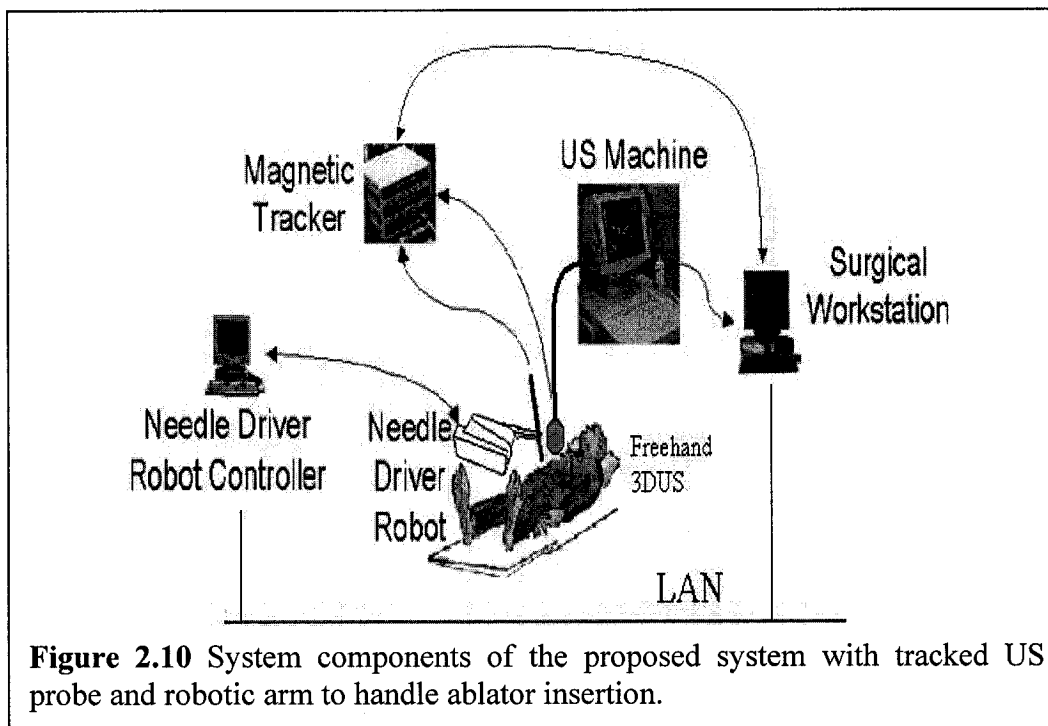
### **2.2.3 Passive/Active System**

In this system, the configuration of the previous system – Active/Passive – is swapped and the ablator insertion task is augmented with a robotic hand, while US acquisition is handled manually. US scanning does not require sharp precision; another reason to pursue this configuration. A US probe as a camera has a wide angle and good penetration depth (up to 20cm), which makes it easy for even a novice user to capture the volume of

interest. Inserting an ablator tool requires considerable precision and accuracy (0.5 – 3mm), and using a robotic hand can improve the accuracy of image-guided needle placement over traditional freehand techniques. While many research groups have demonstrated this concept, clinical adoption of needle placement robots has not immediately followed, because 1) Robots are generally expensive and 2) they are difficult to calibrate and register to the patient in a manner fast and user-friendly enough to be practical in the operating room. We address these considerations with a novel, clinically applicable, low-cost system consisting of a robot which manipulates the needle through a surgeon specified trajectory, guided by tracked freehand 3DUS. We address cost by algorithmically enabling the robot to be unencoded, uncalibrated, and mechanically simple. We address ease of use by eliminating preoperative registration, and nearly eliminating calibration. The surgical tool is tracked and thereby registered imager intraoperatively. A structured 3DUS volume, created using a tracked conventional 2DUS probe, provides the basis for accurate and reliable volumetric visualization, simulation, and planning. The system components are integrated using a 3D Slicer-based software package.

Figure 2.10 demonstrates the schematic architecture of our experimental system. Major system components include: 1) a PC-based surgical workstation providing overall application control, 2D and 3D ultrasound processing and surgeon interfaces; 2) a conventional 2D ultrasound system (SSD-1400 ultrasound machine, Aloka Inc.); 3) a five degrees-of-freedom robot, composed of 3 prismatic and 2 rotational joints, for positioning a needle; and 4) an electromagnetic (EM) tracking system (Flock of Birds, model 6D, Ascension Technology, Inc). We utilize the EM tracking system rather than robot encoders to provide positional reference. The EM base unit is fixed to the operating table and individual sensors are attached to the ultrasound probe and needle holder. In the

following section I will briefly describe the utilization of an inexpensive robot arm to accurately position the needle at the selected target. The robot is controlled with a special control algorithm, which we call Virtual RCM. This algorithm requires minimal calibration and removes the need for encoding, complex mechanical design, and preoperative registration, resulting in decreased system cost and setup time.



### 2.2.3.1 *Virtual RCM needle insertion robot control*

The Virtual RCM [Boctor-2003d, Boctor-2004g] is an algorithm that aligns the needle with the directional vector from the body entry point to the target within the liver; the key performance criteria are accuracy, robustness, and fast convergence within very few cycles. To accomplish this without inverse kinematics, encoding of joints, or mechanical RCM enforcement, an incremental adaptive motion cycle algorithm is used

In addition to the 6 DOF pose of the needle, which is readily available from the tracker reading, this procedure requires the relative orientation between the robot base and the tracker base station. This is easily and quickly determined by moving the Cartesian stage arbitrarily (maintaining a safe distance from the patient) while recording sensor readings. Direction cosines yield the rotation matrix.

The 2 DOF motorized rotational “wrist” stage [Stoianovici-2001], can be used to provide a mechanically constrained fulcrum. However, in our experimental demonstration, the tool holder purposely removes the mechanical remote center of motion property of the wrist by holding the needle off the RCM point. This demonstrates that the Virtual RCM algorithm outlined here can eliminate the need for an expensive, difficult to calibrate RCM wrist. Because the tool is not on a mechanically constrained RCM, the yaw and pitch DOF ( $\alpha$  and  $\beta$ ) of the wrist are not decoupled, and thus cannot be optimized individually, as is done in mechanically constrained RCM systems.

To optimize the needle alignment, a blind search of all possible  $\alpha$  and  $\beta$  angles would eventually yield the correct alignment. However, it would be impractical (and perhaps impossible in the operating room) to repeatedly rotate the two joints a full  $360^\circ$  until the best alignment is determined from all possible discrete combinations of the two variables. To rapidly optimize  $\alpha$  and  $\beta$  simultaneously, we draw upon heuristic search techniques developed in the field of artificial intelligence (AI). We discretize each rotational DOF and partition our search space into two subspaces, one for each angle. A heuristic function guides the search to optimal needle alignment. In practical terms, this means that the robot makes incremental motions, and after each it checks to determine whether the needle is becoming more aligned or less so. This tells us which direction is likely to cause

better alignment. By continually moving both angles, the robot is able to rapidly hone in on the proper alignment.

Selecting a heuristic function that quantifies improvement in needle alignment is not trivial. Good functions must not have local minima that may trap the algorithm before alignment is achieved, nor should they be sensitive to noise in tracker readings. Further, the function must not compound noise error. Based on these considerations, the cross product was determined to be a good choice for the heuristic function. To create the heuristic the cross product of vector from the needle base to the needle tip and the vector from the insertion point to the target is taken. Minimizing the magnitude of the result yields a needle aligned with the desired entry path. Further details of various control algorithms and accuracy of different heuristic functions are described in Chapter 3.

The passive component of this system is the same one used in the Passive/Passive paradigm, which is a freehand tracked 3D ultrasound system as discussed in Section 2.2.1.2.

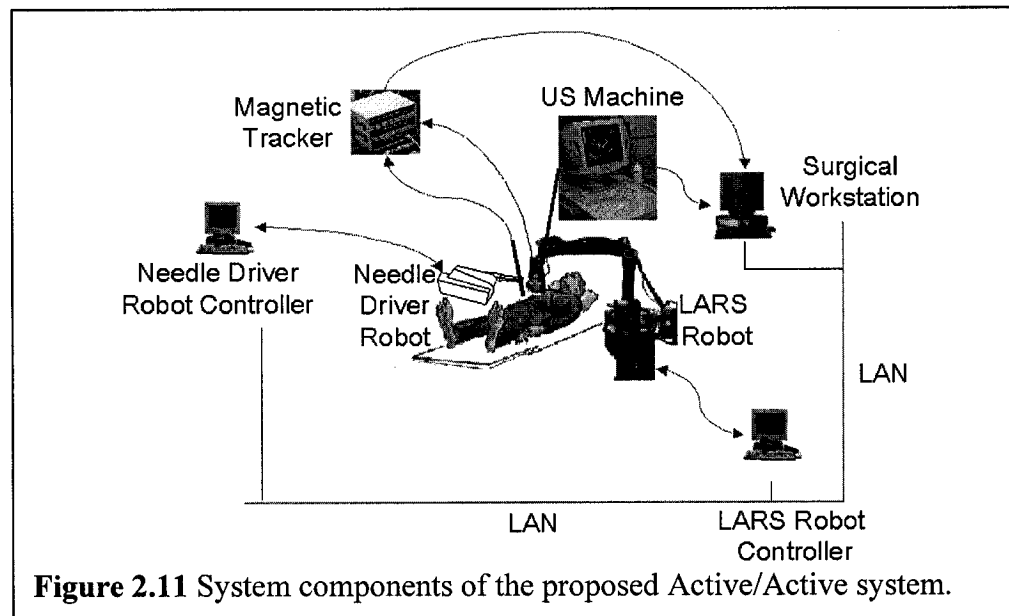
#### **2.2.4 Active /Active System**

In the previous sections, we discussed the Passive/Passive system where there is no robot involved. We also discussed the systems evolving from incorporating single robot hand, as seen in Passive/Active and Active/Passive systems. Accordingly, in this section we describe a “two handed” system in which robot arms manipulate both the ultrasound and the needle placement devices, in the surgical contexts of liver cancer biopsy and ablation. This system may allow for superior US imaging and placement of the tool tip, compared with freehand ultrasonography and needle placement. The dual-arm configuration assists the surgeon with device manipulation and hand-eye coordination, so that more effort can

be concentrated on planning and monitoring the procedure. By promoting more accurate imaging and targeting of the lesions, we potentially improve the therapeutic coverage of those cancerous regions and reduce the number of needle insertions required, reducing the likelihood of spreading cancer along a needle path.

Figure 2.11 shows the overall architecture of our experimental system. Major system components include:

- A PC-based surgical workstation providing overall application control, 2D and 3D ultrasound processing and surgeon interfaces.
- A conventional 2D ultrasound system (SSD-1400 ultrasound machine, Aloka Inc.) interfaced to the surgical workstation.
- A robot (the LARS) holding the ultrasound probe.
- A second robot for positioning a needle guide.
- An electromagnetic tracking system (Flock of Birds, model 6D, Ascension Technology, Inc.) interfaces to the surgical workstation.



In providing positional reference and co-registration between the ultrasound and ablator needle, we rely on an electromagnetic tracking system rather than the robot encoders. The tracker base unit is fixed to the operating table, and individual sensors are attached to the ultrasound probe and needle guide. The main advantages of this approach are: (1) it permits quick reconfiguration of the experimental setup to use 0, 1, or 2 robots, and (2) it simplifies modular replacement of end effectors. With this approach, we need only calibrate the tool tips (ablator or needle) to the tracker, and the motion of both robots is based entirely on sensed tool location [Boctor-2003d, Boctor-2004g]. As neither robot accomplishes motion through inverse kinematics, the robots do not need to be precalibrated to tracker space.

The active components of this system are the same as described in both Passive/Active and Active/ Passive systems, discussed in Sections 2.2.3.1 and 2.2.2.1.

## **2.3 Experiments and Results**

Chronologically, systems development began with the Passive/Passive system, followed by both Active/Passive and Passive/Active systems, and ended with the expensive “two handed” Active/Active system. Concurrent to the development of these systems, experimental testing began with phantom (mechanical subjects), then moved to ex-vivo tissue testing, and concluded with one animal study. The forthcoming sections will show the development of these systems and the progression of experimental testing.

### **2.3.1 Initial Phantom Experiments with Passive Needle Insertion**

#### **2.3.1.1 *Passive/Passive Experimental Procedures and Results***

We report the results from initial experiments using mechanical phantoms to verify and determine the accuracy of the system. Two different phantoms were used. The first

phantom was a 1.0cm rubber ball immersed in a transparent water tank. 2DUS images incorporating the region of interest were captured in order to build the 3D volume, with methodology discussed earlier in Section 2.2.1.1. The reconstructed 3D volume was then combined with the real-time tracked RF ablator in the dual 3D view visualization windows to help in planning and targeting, as discussed in Section 2.2.1.3. After planning, we moved the ablator to target, as seen in Figure 2.12. The method of verification was visual observation in the tank under water, on graphical display, and in

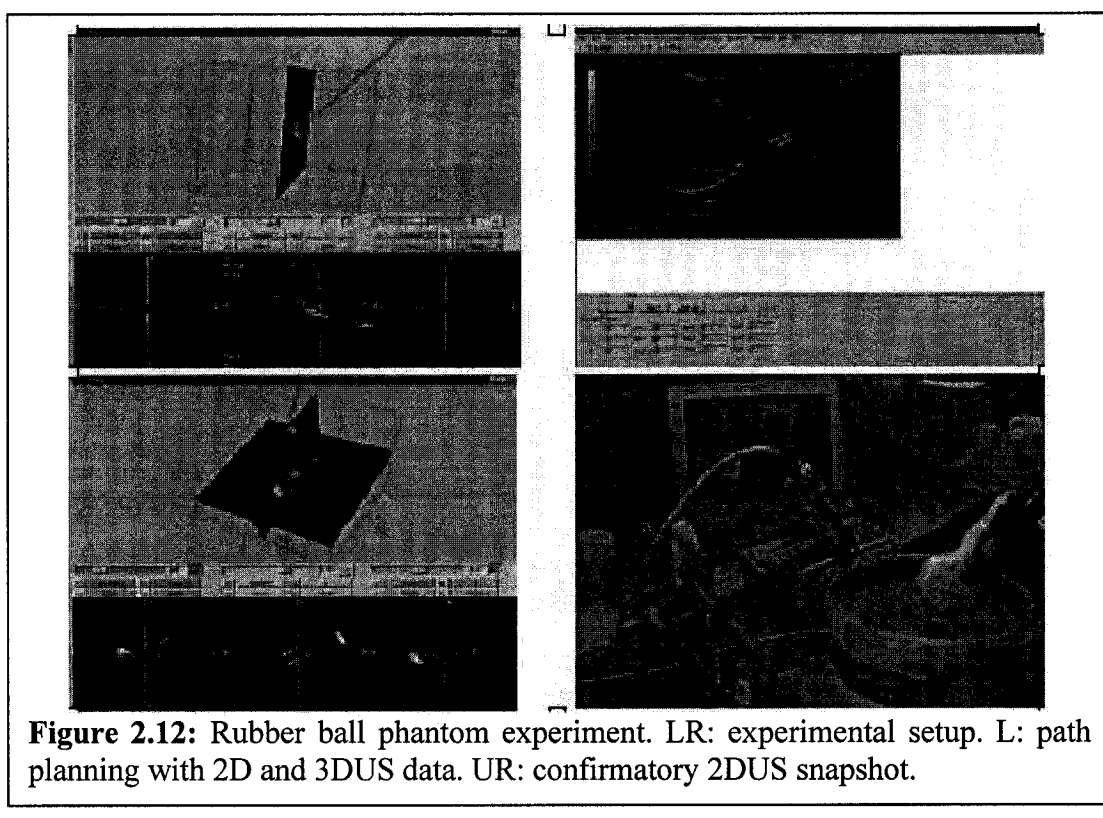


**Figure 2.12:** Rubber ball phantom experiment. LR: experimental setup. L: path planning with 2D and 3DUS data. UR: confirmatory 2DUS snapshot.

live 2DUS. We evaluated whether (1) the ablator correctly touched the rubber ball in the tank, (2) the system correctly overlaid the rubber ball in the reconstructed 3DUS with the real-time picture of the tracked ablator, (3) the rubber ball and ablator show up correctly

in live 2DUS images. Potential target motion was assessed by finding the dislocation of the image of the rubber ball between the preinsertion 3DUS volume and the live 2D image. As no target motion was noted, the experiment was indeed appropriate to assess absolute accuracy of our system. (Note: in the actual needle placement, we set the insertion depth 0.5cm shorter, in order to avoid dislocating the 1.0cm rubber ball.) The accuracy of targeting ranged from 4 to 5mm. The measurement procedure was rather complex method and susceptible to error due to poor visibility of the rubber ball in live 2DUS images.

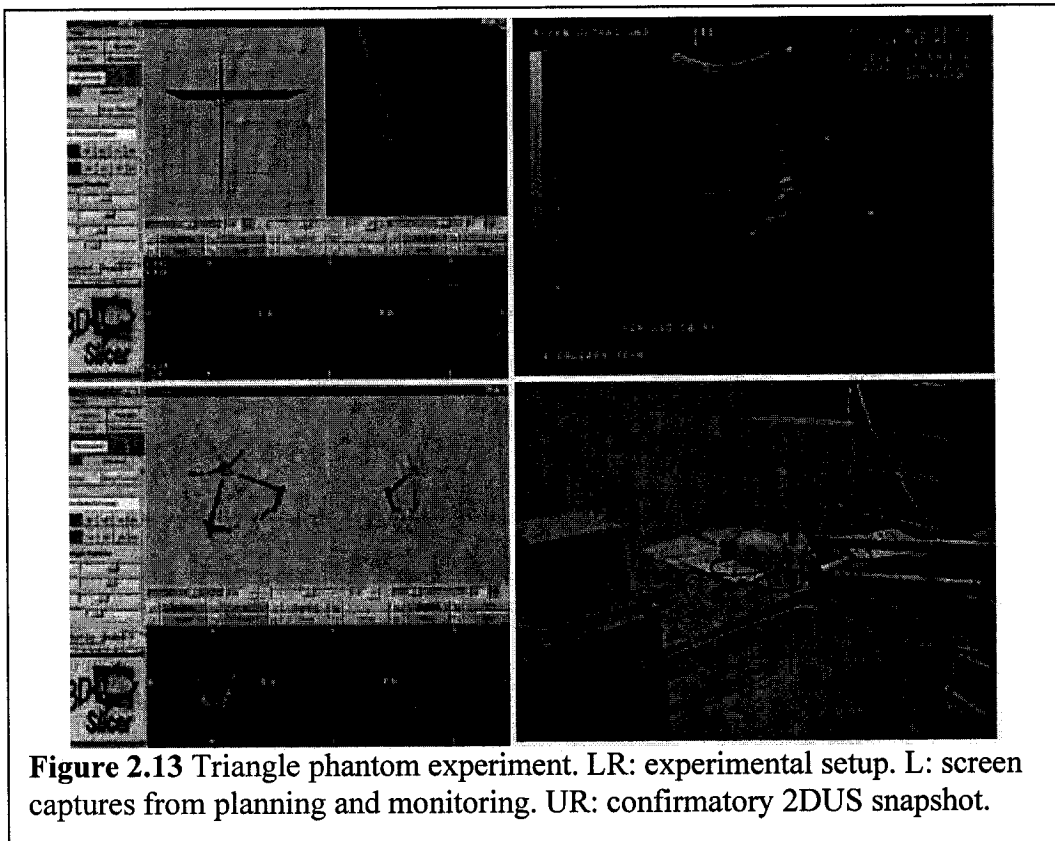


**Figure 2.13** Triangle phantom experiment. LR: experimental setup. L: screen captures from planning and monitoring. UR: confirmatory 2DUS snapshot.

A second series of experiments were performed using a triangle phantom with which targeting accuracy ranges from 1 - 2mm in both axial and lateral directions. However, we could not measure the targeting accuracy in the elevation direction due to the symmetry

of the triangle phantom. Figure 2.13 depicts the experimental arrangement and shows images taken for these experiments. This experiment was repeated five times as shown in the left images of Figure 2.13. The same verification scheme was applied here, using visual observation to check the targeting of single point rather than 1cm rubber ball, using US verification, as shown in the right images of Figure 2.13.

### **2.3.1.2 Active/Passive Experimental Procedures and Results**

We have conducted comparative in-vitro experiments between the robotic ultrasound system and the freehand 3D system. The robotic system provided better quality and accuracy of the 3D reconstruction as shown in Figure 2.14. This is afforded by regular step scanning, better management of the predefined gap distribution, and provision for static tracking.

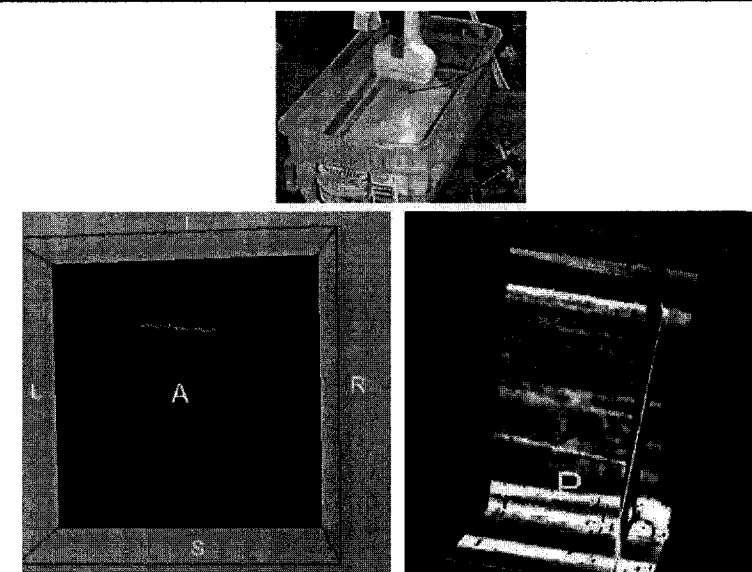


**Figure 2.14** Triangle based phantom used for reconstruction verification (Top.) Thresholded reconstruction from freehand scan showing the ripples on the top edge (Left.) Reconstruction from robotic scan showing smoother and uniform edge (Right.)

Figure 2.15-A shows a snapshot of the robotic US S/W with real time US capturing, tracking information and robot control parameters. Figure 2.15-B is a typical scene of the integrated system during one of the testing experiments using the triangle-shaped phantom shown in top panel of Figure 2.14. 3D Slicer visualization software for planning, simulating and supervision the ablation with dual 3D views appears in Figure 2.15-C. Results from these experiments show the ability of the method to accurately

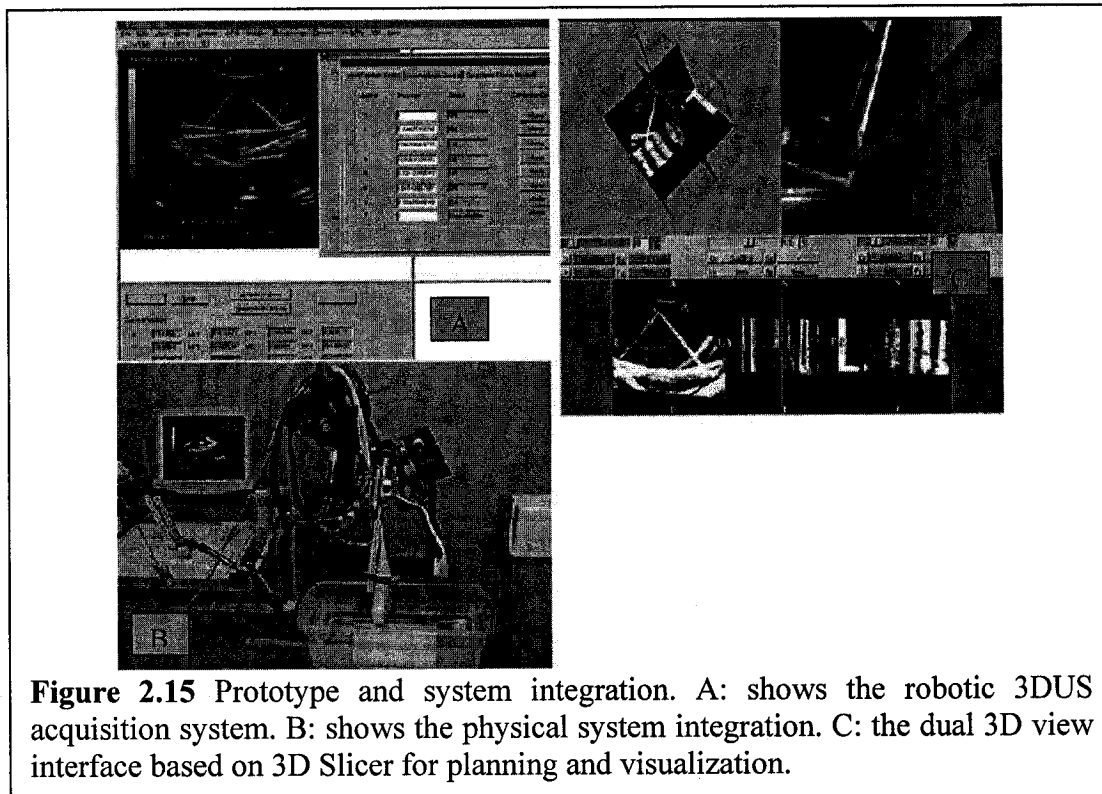


**Figure 2.15** Prototype and system integration. A: shows the robotic 3DUS acquisition system. B: shows the physical system integration. C: the dual 3D view interface based on 3D Slicer for planning and visualization.

reach a target. Both 2D and 3DUS guiding schemes proved to be able to hit the target (verified by visual and US confirmation); however ablation planning based on single 2DUS was not always sufficient in covering the target volume, which was always achieved with 3DUS planning. The comparison between planning based on 2DUS vs. 3DUS data will be further examined on Section 2.3.3. The method of verification was

visual observation in the tank under water, on graphical display, and in live 2DUS. The average targeting accuracy was 1.5mm in both axial and lateral directions. We could not, however, measure the targeting accuracy in the elevation direction due to the symmetry of the triangle phantom.

From this limited phantom study with both systems, one cannot draw any statistically significant claims about superior accuracy of one method over the other, freehand 3DUS vs. Robotic 3DUS. Both methods have the same range of accuracy, which is mainly a function of the system calibration accuracy. Intuitively, one should not expect prominent differences between both methods, since we have the following: 1) A stationary target and no presence of any motion artifact, 2) Both systems' accuracy depends on the same tracking device and the same calibration procedure, 3) The target is an observable feature, the triangle edge of the phantom, which can be easily detected with freehand 3DUS. In the coming two sections we pursue more experimentations using active needle insertion. Because, it is a well researched claim [Rovetta-1999, Su-2002, Wei-2004] that robot's precision is critical for needle interventions.

### **2.3.2 Ex-vivo Experiments with Active Needle Insertion**

#### ***2.3.2.1 Experimental Procedures for the Dual-Arm System***

We conducted needle placement experiments using two different phantoms. The first phantom was a calf liver with pitted olives embedded in the liver at depths ranging from 5mm to 40mm, to simulate cancerous lesions. Figure 2.16-Left shows the experimental setup, and Figure 2.16-Right shows close-up of the apparatus with the liver phantom. In order to assess the geometric accuracy of the system a second, mechanical phantom, with no symmetry feature in the elevation direction, was introduced. This phantom, shown in Figure 2.17, consists of several plastic pins (8mm OD) immersed in a water tank. We

also used this phantom to compare the performance of our dual-arm system to the single-arm scenario performing needle insertion. Next we will describe the workflow for the liver phantom, noting that the procedure was almost identical for the mechanical phantom.

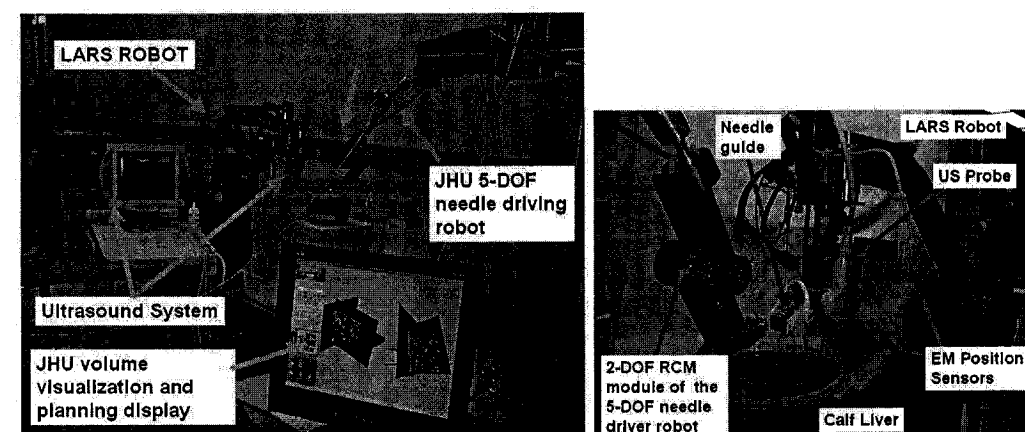


**Figure 2.16** Left: Experimental setup for the dual-armed robotic system. Right: Close-up of biopsy experiment.

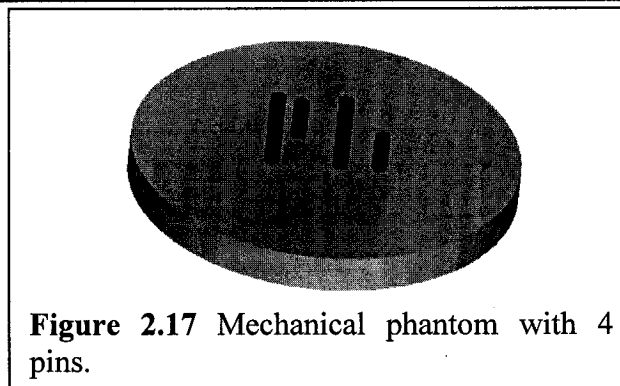


**Figure 2.17** Mechanical phantom with 4 pins.

**Step 1: Exploration.** We use the LARS robot in either force compliant or teleoperation mode to move the US probe over the liver. Concurrently, we observe the live 2DUS images to approximate target volume of interest (VOI) containing target lesions. Then we command the LARS to move the US probe between the start and end points of the VOI. In essence, we “teach” the LARS controller the scanning protocol for the given VOI.

**Step 2: Volume Scanning.** The LARS autonomously moves the US probe from the start to the end points in a step-and-repeat fashion, with 20ms pauses at each step. At each position, a 2DUS image is acquired along with the EM pose information. Our system is also capable of acquiring images with a continuous motion scan, but we preferred step-and-repeat mode to make the synchronization between the EM tracker and the US unit more accurate. The 2DUS images are then compounded into a 3DUS volume. Figure 2.18 depicts three orthogonal slices passing through the center of an olive target.

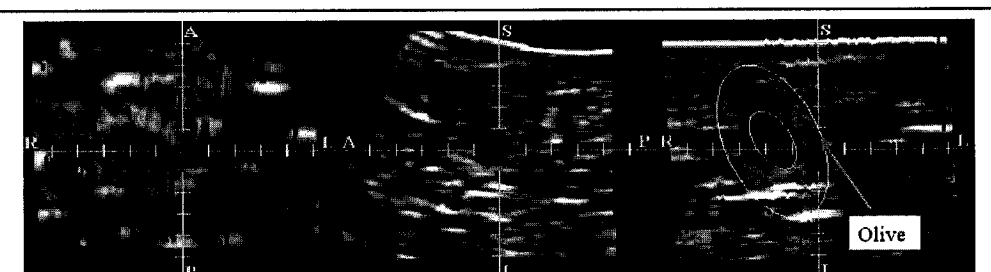


**Figure 2.18** Orthogonal slices of 3DUS reconstruction of an olive in calf liver phantom.

**Step 3: Planning.** The interactive 3D Slicer interface is used to identify the target and entry points. The display shows the trajectory of the needle and the predicted region of ablation. The computer also determines the insertion depth for the needle.

**Step 4: Moving the robot.** A depth marker is placed on the needle at the appropriate distance from the tip, and then the needle is placed into the guide. The 5 DOF needle placement robot moves the needle tip over the entry point and aligns the needle in the desired path in three steps: (1) orient the needle approximately while the robot is still in some safe distance from the subject; (2) move the needle tip to the entry point; and (3) align the needle precisely using the RCM stage.

**Step 5: Insertion.** The needle is driven manually to the predetermined depth, monitored by the depth marker and in the real-time computer display. During both insertion and

assessment, either the US probe on the LARS or a standalone probe (Figure 2.19) is used to monitor and confirm placement of the needle.

**Step 6: Assessment.** We record (1) whether we hit the target and (2) the insertion depth at which the needle actually hits the target. We also use a second ultrasound probe to observe the needle tip, and to target and measure the distance between them with the standard operator's interface on the ultrasound console. Figure 2.19 shows the procedure and a typical US image.

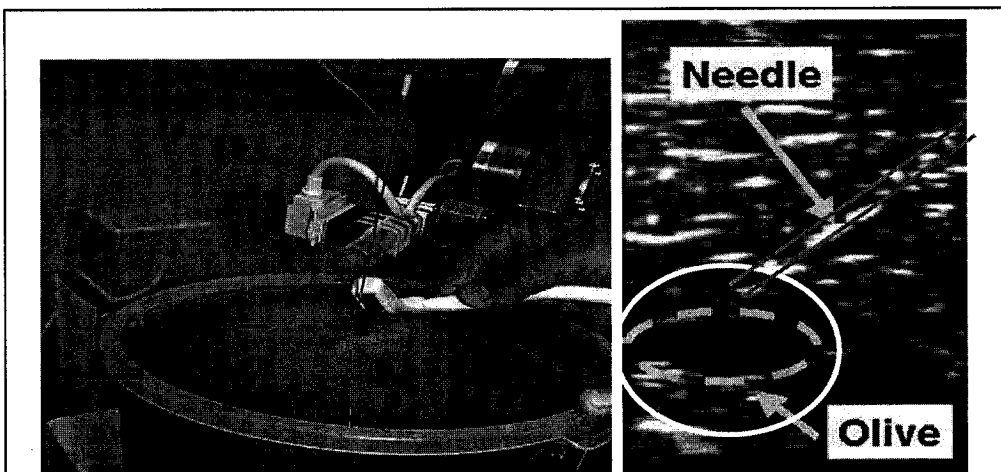


**Figure 2.19** Ultrasound is used to assess needle placement with respect to the olive target embedded in calf liver.

### **2.3.2.2 Results and Discussions**

We have conducted three successful experiments for the liver/olive phantom procedure described before. Qualitative verification was performed in two of them by feeling the resistance of the olive and in the last one by observing the US image, Figure 2.19. Based on three measurements, the average mismatch between real and planned insertion depths was of 1.2mm.

We collected three robotic scans and three freehand scans from the mechanical phantom shown in Figure 2.17, in order to compare the performance of robot assisted needle insertion with and without robotic US scan. First, we selected a VOI containing the targets and reconstructed the VOI into a 3DUS volume for needle insertion planning. The ratio of the number of raw 2DUS pixels within the VOI to the number of voxels in the VOI was compared. For reconstructions from a single robotic sweep, this ratio was consistently about 1.5-1.6, while the ratio for a single freehand sweep was between 0.3-0.8, an inconsistent value which fluctuated in a wide range. After increasing the number of freehand sweeps to three, the ratio still remained approximately only 0.9, which is still considerable variability. A ratio greater than 1.0 may imply that we either have relatively little gap between the slices, or we try to place multiple pixels in the same voxel, either case leading to better 3D image quality. In our experiments for freehand scanning, this ratio was found to be less than 1.0 and rather inconsistent, implying that we had many empty voxels in the volume, either because of scanning gaps or because of the orientation of the scan plane within the reconstructed volume. In either case, a lower image quality can be observed, compared to robot assisted scans, and there is also a strong indication that repeated scans cannot be consistently acquired freehand.

To determine the systemic error of the dual-arm system on the mechanical phantom, we placed the tracked needle at the artificial target (plastic pin) and recorded the distance between the needle tip and the target in the Slicer screen. From 10 trials, the average measure was ~3.0mm. This measurement of error comprised the all elements of the system's error, except the error of the robot control algorithm and needle deflection in real tissue: US calibration, calibration error of needle tip to tracker, sensor uncertainty, floating point truncation, and US image resolution. For termination criterion, the robot control algorithm (which is described in detail in Chapter 3) used the system error we

found above. Using robotic needle insertion with robotic US data, the success rate in hitting the head of the pin was 7 out of 7 trials. Using robotic insertion with freehand US data, the success rate was only 3 out of 4 trials. This could be explained because of: 1) the presence of gaps that degrade planning accuracy, 2) bad planning, due to poor visualization, and/or 3) synchronization inaccuracy due to dynamic tracking of freehand system.

In conclusion, with regard to the use of an active needle in ex-vivo and phantom experiments, there are no substantial efficacy or accuracy differences between tracked and robotic 3DUS. In fact, with a bit of training on how to use tracked US probe, one can generate manually 3DUS volumes sufficient to target static or quasi-static objects. Also, we have observed significant time reduction using robot hand to control needle insertion task compared to the manual tracked passive arm. There are an increasing number of research groups, including my lab and companies advocating the use of robotic control to enhance targeting accuracy [Rovetta-1999, Su-2002, Wei-2004] in addition to the time reduction benefits mentioned above. Thus, we decided to conduct a comprehensive comparative study between current practice of targeting ablative therapy and the proposed Passive/Active prototype.

### **2.3.3 Comparative Study**

All our previous experiments were designed to evaluate the targeting accuracy and to compare the practical feasibility of various test-bed integrations, which include Passive/Passive, Passive/Active, Active/Passive, and Active/Active systems. These experiments can not help us to assess the effectiveness of the enabling technologies we introduced, including tracking 3DUS and robotics guidance, to the current practice of liver ablation procedure. It was imperative to conduct another experimental study where

we carefully compared the differences in performance between one of our proposed systems and liver intervention as it is currently practiced.

The two components of our comparative study are freehand targeting based on manual 2DUS guidance (the current practice) and a robotic needle assistant based on tracked 3DUS guidance. Our study is applied on ex-vivo bovine liver with embedded lesions, where respiratory motion artifacts are not present. This led us to speculate that the quality of freehand tracked 3DUS acquisition is comparable to that of the rapid robotic 3DUS system (Figure 2.20). In this study, we chose our system to have freehand US handling

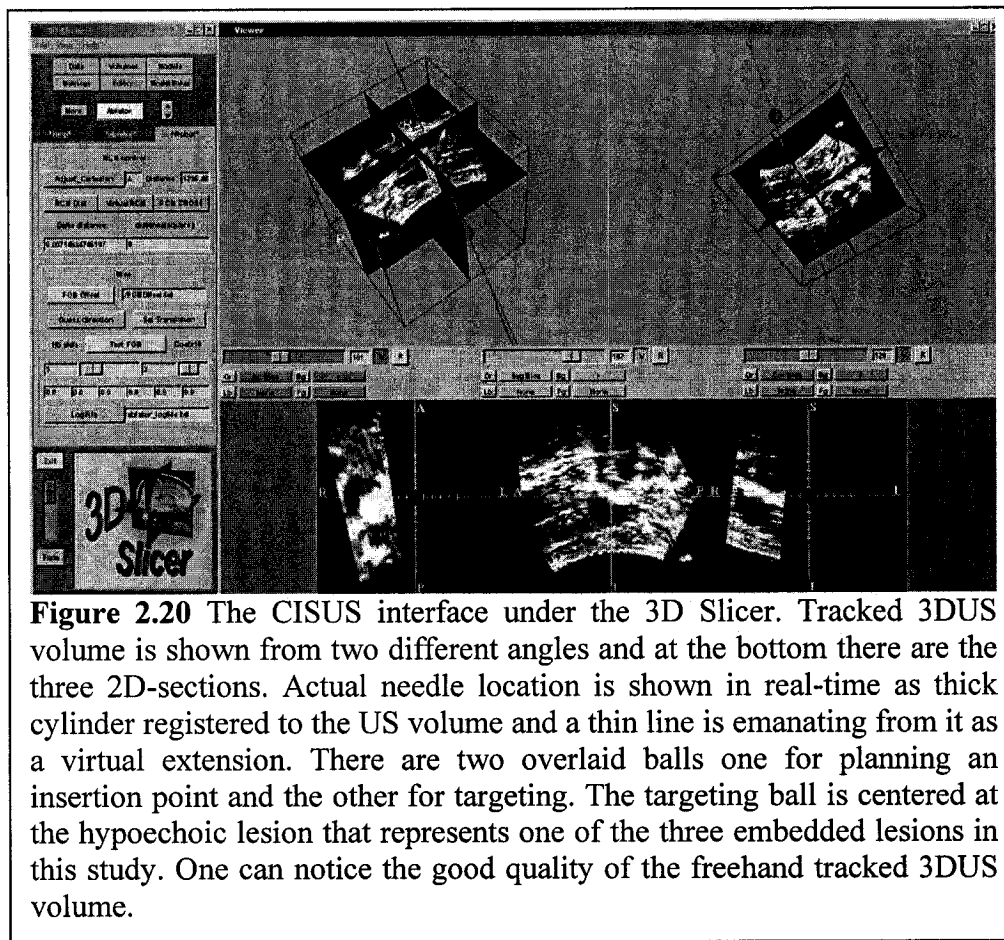


**Figure 2.20** The CISUS interface under the 3D Slicer. Tracked 3DUS volume is shown from two different angles and at the bottom there are the three 2D-sections. Actual needle location is shown in real-time as thick cylinder registered to the US volume and a thin line is emanating from it as a virtual extension. There are two overlaid balls one for planning an insertion point and the other for targeting. The targeting ball is centered at the hypoechoic lesion that represents one of the three embedded lesions in this study. One can notice the good quality of the freehand tracked 3DUS volume.

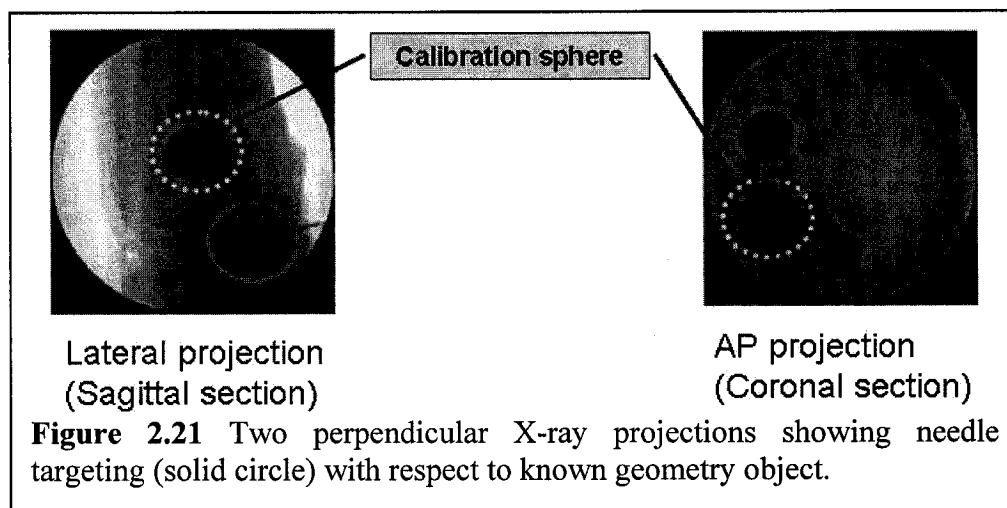
over robotic 3DUS, and we kept robotic guidance for needle placement task. Initially, we prepared three lesions to be embedded as targets (artificial tumors) in the ex-vivo bovine liver. These lesions were composed of agar 2%, alcohol 7%, contrast agent 20% and distilled water for the remaining 71% by volume to ensure visibility under US and X-ray. The placement of these three lesions was selected to give different targeting complexity, with one shallow lesion (about 3cm from surface) and two deep lesions (about 8 and 14cm.)

The experimental procedure for the Passive/Active system in this study is similar to the one described for the dual-arm robotic system in Section 2.3.2.1 with one difference in the assessment procedure. Instead of relying on a second US probe to assess the accuracy of targeting in 2D, we are using encoded, fluoroscopic C-arm to give us targeting accuracy in 3D from two perpendicular projections. After observing liver ablation procedures a few times, we realized that the surgeon can not orient the US probe arbitrarily due to space limitations, especially in laparoscopic scenarios. Even with an ex-vivo scenario where the whole liver is exposed, the expert surgeon<sup>†</sup> tried to apply a realistic scanning motion. We noticed that most of the time it is easy to orient the US probe in lateral or sagittal projections and it is hard to get coronal or anterior-posterior projections. This inspired us to design the fluoroscopic X-ray assessment phase to collect two perpendicular projections where the coronal projection is one of them (Figure 2.21). Our hypothesis is that planning based on 2DUS data and omitting one projection (the coronal section) might suffer from biased targeting error. To check this hypothesis, we compare these targeting error components with our tracked 3DUS system. In addition to the targeting accuracy components we look at the execution time, i.e. number of trials. We design the study to allow one execution to the Passive/Active system and up to six

---

<sup>†</sup> Dr. Michael A. Choti, he is a surgeon professor at the department of surgery in Johns Hopkins.

trials for the manual 2DUS protocol. Next we compare the targeting accuracy of the manual 2DUS at the first and last trials with our tracked 3DUS single trial.



We have nine trials for the manual 2DUS protocol and six trials for the Passive/Active system. Figure 2.22 shows the accuracy results comparing freehand 2DUS vs. robotic needle guided by tracked 3DUS system. For the first trial of the freehand procedure, error components in the AP projection are substantially larger than those of lateral projection ( $p<0.05$ ). At the same time, error components from applying the tracked 3DUS system are comparable in both projections and substantially lower than those of the first trial of the freehand system. By allowing the surgeon to correct his trials up to 6 times (3 times on average), one can observe comparable average error components in both projection. The average errors of the 3DUS system in both projections are still lower than those of the last trial of the freehand procedure. We attribute our system performance mostly to the utilization of tracked 3DUS data that is related to the accuracy of tracking and system calibration. At the same time, real-time tracking of the needle and its virtual extension overlaid on the 3DUS volume helped to precisely define the targeting path and penetration from the first trial. The role of the robot in guiding the needle consistently

facilitated the execution of the intervention, but it is not obvious from this study that it contributed additional accuracy.

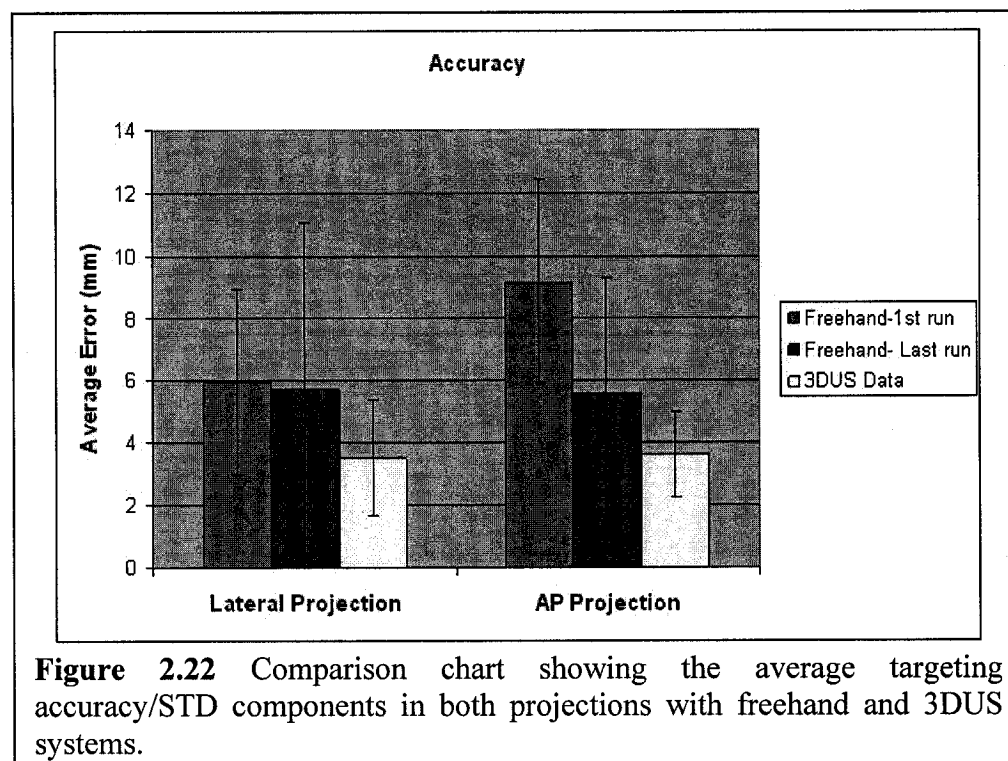


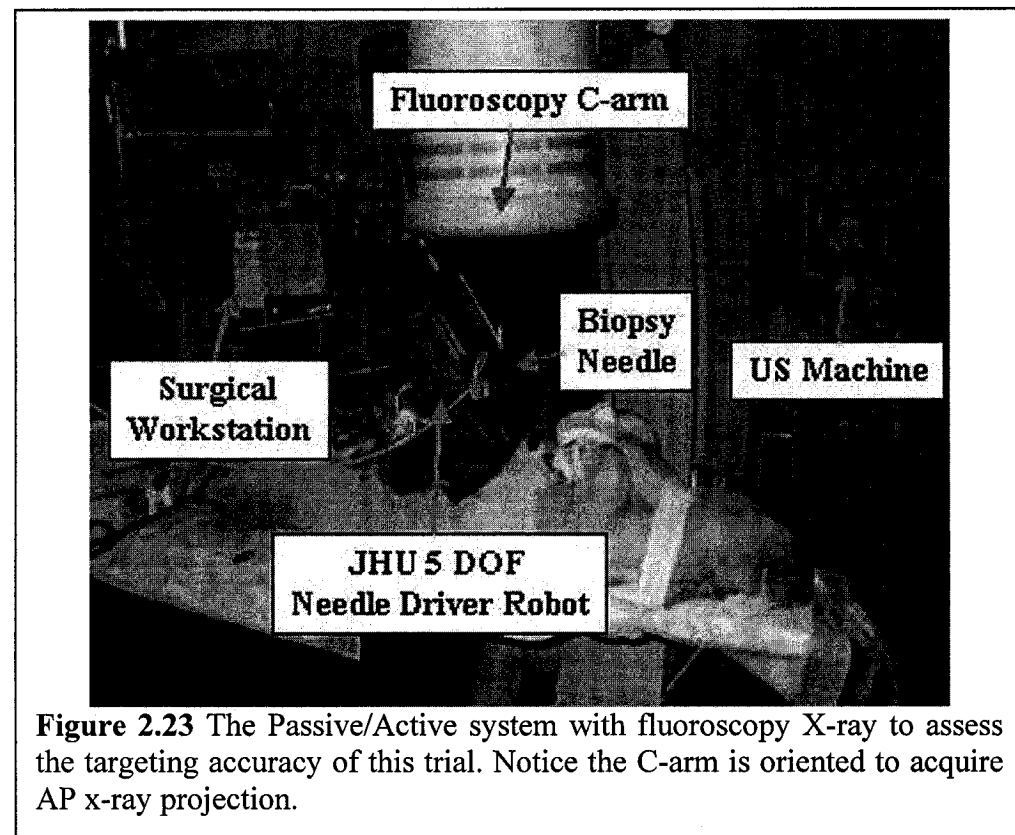
**Figure 2.22** Comparison chart showing the average targeting accuracy/STD components in both projections with freehand and 3DUS systems.

The STD of our system targeting accuracy is about 1mm, which is 3 to 4 times less than those of the manual 2D method. Overall, the proposed interventional tracking system provided more accuracy and consistency compared to the conventional interventional method.

### 2.3.4 In-vivo Animal Study

The Passive/Active system, tracked freehand 3DUS and active needle insertion, was tested on an in-vivo animal model as shown in Figure 2.23. Spherical lesion was implanted by a balloon catheter in the pig's liver. The lesion was composed of agar 2%, alcohol 7%, contrast agent 20% and distilled water for the remaining 71% by volume to

ensure visibility under US and X-ray. We ran the system twice to target the lesion. In the first trial we missed the planned target (center of the lesion) by more than 10mm. This is because we did not compensate for the rapidly moving target due to heart motion. In the second trial, using controlled anesthesia, we managed to acquire US, plan, and target within 20 seconds with 5.5mm accuracy. The trial shows a promise to apply these enabling technologies to liver intervention procedures.



## 2.4 Conclusions

In conclusion, there are no substantial efficacy or accuracy differences between tracked 3DUS and robotic 3DUS, with regard to the active needle ex-vivo and phantom experiments. In fact, with a bit of training on how to use tracked US probe, one can generate good enough quality 3D reconstruction to target static or quasi-static objects.

Targeting rapidly a moving object is not part of our systems' design specifications and is out of our research scope. This is because our driving clinical applications, either liver ablation in an open surgery scenario or prostate EBRT, do not encounter substantial motion artifact. An important use of robotic US is to provide rapid 3D acquisition from 2D images, such as with the current mechanical 3DUS wobbler probes, or to ensure US acquisition with repetitive and known boundary conditions for creating elasticity images, as shown in Part-III of this thesis. Furthermore, the use of robotic US has the potential to create a steady image of the target by automatically tracking the region of interest and moving the US probe to focus on the target. Appendix-A presents the work done on robotic US servoing in CIS-II project<sup>†</sup>. Similarly, using robots to guide needle insertion is an important addition to these systems, particularly when a moving target is encountered.

From the comparative study, we find that these interventional systems hold a promise to assist liver interventional procedures as in ablative treatment. Figure 2.22 shows superior performance of the tracked 3DUS over the conventional manual method. However, this performance is mainly attributed to system's the calibration accuracy and integration. This led the author to investigate the US calibration problem and to study it thoroughly, as it is shown in Part-II of this thesis.

---

<sup>†</sup> This project was undertaken in the spring of 2004, in collaboration with Gregory S. Fischer, with Prof. Taylor as supervising faculty.

## **Part-I: Chapter 3**

# **Virtual Remote Center of Motion Control for Needle Placement Robots**

Using robots, we can improve the accuracy of image-guided needle placement over traditional freehand techniques. While many research groups have demonstrated this, widespread clinical adoption of needle placement robots has not immediately followed, because 1) Robots are generally expensive and 2) they are difficult to calibrate and register to the patient in a manner fast and user-friendly enough to be practical in the operating room. Our solution to these considerations is a novel, clinically applicable, low-cost system consisting of a robot, which manipulates the needle through a surgeon specified trajectory, guided by tracked freehand (3DUS). We address cost by algorithmically enabling the robot to be unencoded, uncalibrated, and mechanically simple. We address ease of use by eliminating preoperative registration, and nearly eliminating calibration. The surgical tool is tracked and thereby registered imager intraoperatively. A structured 3DUS volume, created using a tracked conventional 2DUS probe, provides the basis for accurate and reliable volumetric visualization, simulation, and planning. The system components are integrated using a 3D Slicer-based software package.

### 3.1 Introduction

Recent advances in medical imaging have encouraged a rapid increase in such minimally invasive image-guided interventions as biopsy and needle-based local therapies. The success of these procedures hinges on the accuracy of needle placement. Conventional unassisted freehand techniques depend primarily on the physician's hand-eye coordination and often suffer from inaccuracy and inconsistency in needle placement. As an appealing alternative, medical robots offer the potential to manipulate surgical instruments more precisely and consistently than is possible by hand. At the same time, contemporary medical robots introduce a prohibitively complex engineering entourage into otherwise rather straightforward needle placement procedures.

Manual needle placement typically includes the following three decoupled tasks: (1) move the needle tip to the preselected entry point with 3 DOF Cartesian motion, (2) orient the needle by pivoting around the entry point using 2 DOF rotation, and (3) insert the needle into the body using 1 DOF translation along a straight trajectory. The technical challenge for robot assisted needle placement has been to reproduce this sequence of motions robotically in a safe, practical, and affordable manner.

One possibility that addresses technical challenges is to use serial linkages and coordinate the joints mathematically under computer control, as is done in the commercial Zeus™ and Aesop™ laparoscopic robots (Intuitive Surgical, Inc.). Similar solutions were used in the IGOR [Cinquin-1992], PUMA [Davies-1991, Kwoh-1988], Neuromate [Varma-2003, Li-2002], Kawasaki [Yanof-2001], and Sankyo Scara [Rovetta-1999]. However, serial linkages present two fundamental problems. First, the robot kinematics introduce mathematical singularities in the active workspace, which is prohibitive in most medical applications. Another difficulty with conventional serial robots is that their use requires a

fully described and precisely encoded kinematic chain. It is rather difficult to calibrate these arms, and loss of calibration accuracy during clinical use is a critical risk. Because their trajectory and range of motion is solely controlled by software, lack of human control increases operative risks when these devices are used.

A decidedly more appealing and safer alternative to using the systems described above is the family of kinematically decoupled robots. These devices contain separately controlled and sequentially operated Cartesian, rotational, and insertion stages, thus they appear to be a more natural fit for the process of needle placement. They are also safer because the range of motion of each individual stage can be independently constrained and if needed, mechanically blocked, preventing overdriving of any individual axis. The least straightforward action for a decoupled needle placement robot is orienting the needle toward the preselected target. One approach is to use a 2 DOF design that mechanically constrains the fulcrum point at the needle tip. Goniometric arcs have been proposed to perform this function [Harris-1997], but these are impractical for needle placement because the fulcrum point has to be in the center of the arcs, which blocks access to the patient. Taylor implemented the remote center of motion point concept in a laparoscopic robot [Taylor-1995], where the fixed fulcrum point is produced farther away from the mechanism, which leaves room for surgical instruments and allows the physician access to the patient. The RCM concept has been applied in several laparoscopic and needle placement robots, including commercial systems such as the da Vinci™ (Intuitive Surgical, Inc.). At the Johns Hopkins University, Stoianovici, et al. developed a chain-drive RCM robot that is used in conjunction with a radiolucent needle driver for percutaneous access [Stoianovici-2001]. Variants of this robot have been tested under image guidance using fluoroscopy [Su-2002], computed tomography [Fichtinger-2002c], ultrasound [Boctor-2004b], and CT-fluoroscopy [Solomon-2002]. The workflow in these

systems is usually the following: (1) register robot to imager, (2) select target and entry points, (3) solve inverse kinematics, (4) move needle to entry, (5) line up needle with target, and (6) insert needle. Some steps may be executed manually, depending on the number of actuated degrees of freedom available, but the workflow remains the same. While the RCM paradigm has made significant impact on the field, it also has some disadvantages: (1) precise construction must guarantee the existence of a known fulcrum point within acceptable range depending on the use requirements, (2) a tool holder must be carefully designed for each new tool, placing it exactly on this fulcrum point, and (3) each joint must be fully encoded.

An appealing alternative to mechanically constrained fulcrum point would be generating programmed or “virtual” RCM software, which still takes advantage of decoupled and uncalibrated Cartesian, rotational, and insertion stages. This problem is the focus of our research here.

Contemporary MRI, fluoroscopy and CT-fluoroscopy allows for real-time visualization, which allows for real-time tracking of surgical instruments. Three dimensional US-guided interventional systems [Boctor-2004b, Wei-2004] also include a real-time tracker in the field of interest. In these systems, one can track the end-effector of a surgical robot and manipulate the device under visual servo control. It has been known in general robotics that operational space formulation [Khatib-1987] and partitioned control [Craig-1992] can be used to alter the behavior of the system to appear, kinematically and dynamically, to be an RCM device. Unfortunately, existing kinematic and dynamic models need to be precise, so the joints need be fully encoded and calibrated. Extensive research has also been devoted to visual servo control [Corke-1996], but work applied to uncalibrated and/or unencoded robots has focused on estimating the robot’s Jacobian

rather than generating a virtual Remote Center of Motion. Artificial intelligence-based algorithms for robot motion have also been investigated, but have not yet been applied to the task of needle placement. These algorithms have been used to control uncalibrated mobile robots which explore unknown environments and navigate familiar environments [Donald-1987]. Related research has also examined the effect of uncertainty in robot sensors and/or the environment [Rivest-1995] in an attempt to generate a collision free map of the space.

Our present contribution is to compose an uncalibrated needle placement robot from three linear stages, two rotational stages, one linear insertion stage and an AI-based motion algorithm to create a Virtual RCM robot that does not require either encoded joints or complete knowledge of the robot kinematics. Unlike classic RCM robots, the Virtual RCM method does not require (1) the existence of a physically fixed fulcrum point, (2) a priori knowledge of the kinematic chain, or (3) encoding of the joints. This relaxes many requirements previously imposed on RCM needle placement robots. For example, the axes of the prismatic stages do not need to be orthogonal, the axes of rotation stages do not need to intersect, and kinematically unknown passive linkages are permitted anywhere along the chain. This allows robots using the Virtual RCM algorithm to be simple and inexpensive to construct, eliminates laborious calibration, and permits testing of new robots or parts of robots to proceed rapidly without affecting the accuracy of image guidance.

### **3.2 Materials and Methods**

#### **3.2.1 System overview**

Our proof-of-concept system (Figure 3.1) is comprised of a 3 DOF motorized Cartesian stage (NEAT, Inc.), a passive unencoded adjustable arm, a 2 DOF motorized rotational

stage designed by Stoianovici, et al.[Stoianovici-2001]. The Virtual RCM algorithm requires measurement of the pose of a point on the robot with a known transformation to the tool frame. In clinical practice, fiducials attached to the robot can provide this information directly from computed tomography [Chirikjian-2002] or MRI images. When using ultrasound (US) as the imaging modality, magnetic tracking can provide the pose of both the image and the tool [Boctor-2004a]. In our system, we attach a magnetic tracker to the tool holder (Flock of Birds, model 6D, Ascension Technology, Inc.). The passive arm shown in Figure 3.1 helps gross initial positioning of the needle tip and also purposely introduces an unknown linkage in the kinematic chain, demonstrating that the Virtual RCM does not require known kinematics. The tool holder also purposely removes the RCM property of the Stoianovici rotation stage by holding the needle off the RCM point, demonstrating that the Virtual RCM does not require careful construction of the fulcrum constraining mechanism or the tool holder.

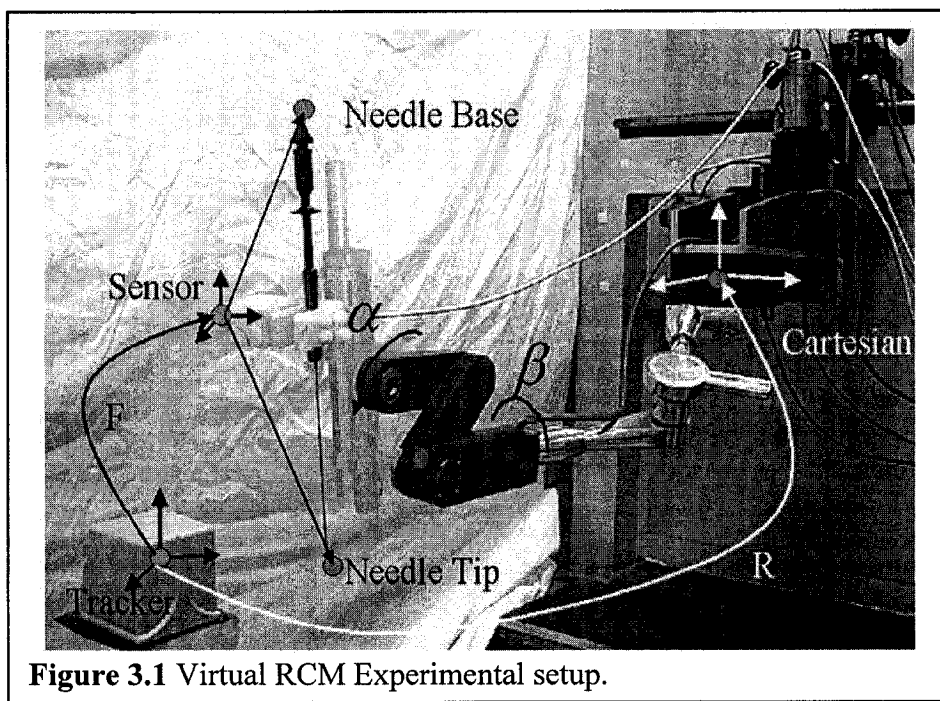


**Figure 3.1** Virtual RCM Experimental setup.

Low-level control of the robot is achieved using a motion control card (MEI, Inc.), driven with the Modular Robot Control library, developed at the Johns Hopkins University [Kumar-2003]. The readings of the FOB tracker are reported to a PC running the 3D Slicer medical data visualization package [Kikinis-2003], which is a public domain open source program primarily developed by the MIT AI Lab and the Surgical Planning Laboratory at the Brigham and Women's Hospital, with sustained contribution from Johns Hopkins. In Slicer, we create a 3D virtual environment (Figure 3.2) where objects are represented in the FOB tracker coordinate frame.

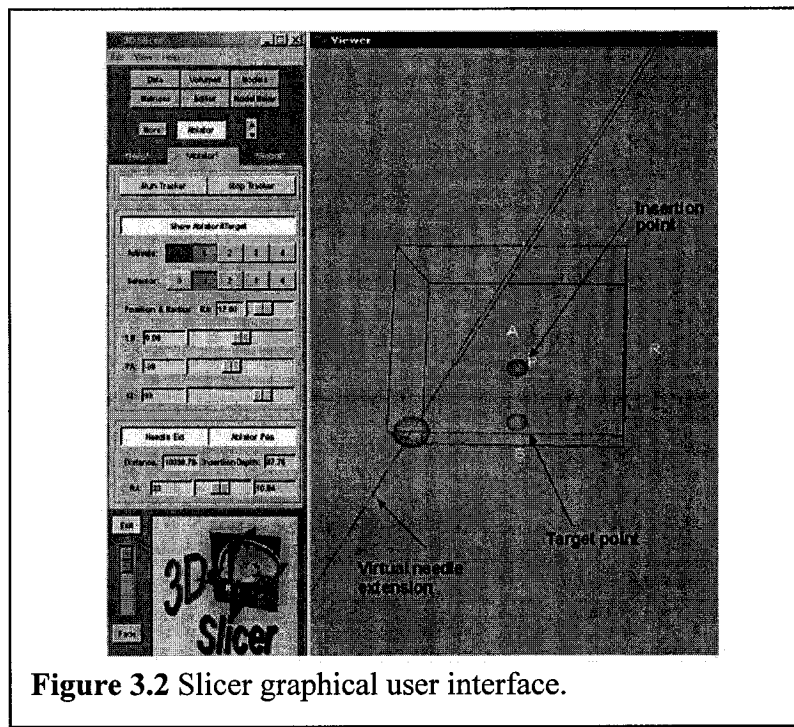


**Figure 3.2** Slicer graphical user interface.

The incremental adaptive motion cycle of the Virtual RCM algorithm (Developed in Sec. 3.2.2 and 3.2.3 and tested in Sec. 3.3) that aligns and translates the needle (experimentally verified in Sec. 3.4) requires transformation between the magnetic sensor and the tool frame. Using readings from the FOB tracker, this transformation is

determined offline by a version of the pivot calibration [Boctor-2003a]. Orientation of the Cartesian stage, expressed in the coordinate frame of the tracker, is also required. This is obtained by moving the Cartesian stage arbitrarily (maintaining a safe distance from the patient) while recording sensor readings. Direction cosines yield the orientation of the Cartesian stages with respect to the tracker.

### 3.2.2 The Virtual RCM: A Heuristic Search

In addition to accuracy and robustness, a key performance criterion for the Virtual RCM needle placement algorithm is fast convergence within very few cycles. In systems where the Virtual RCM algorithm is implemented (where the tool tip is not mechanically constrained to an RCM point), the roll and pitch DOF ( $\alpha$  and  $\beta$ ) are no longer decoupled, and therefore cannot be optimized individually. A blind search of all possible  $\alpha$  and  $\beta$  combinations is not useful for these coupled variables, because it would be impractical to repeatedly rotate the two joints a full 360 degrees until the best alignment is determined from all possible discrete combinations of the two variables. To rapidly optimize these two variables simultaneously, we draw upon artificial intelligence techniques, such as a heuristic-based Breadth First Search (BFS) or Depth First Search (DFS). We discretize each rotational DOF and partition our search space into two subspaces, one for each angle. A heuristic function guides the search to optimal needle alignment rapidly by deciding where to search next at each state.

In practical terms, this means that the robot makes incremental motions, and after each motion it uses the heuristic function to observe whether the needle is becoming more or less aligned. This enables the algorithm to determine which direction of motion is likely to cause better alignment. By continually moving both angles, the robot is able to rapidly home in on the proper alignment.

Selecting a heuristic function that quantifies improvement in needle alignment is not a trivial matter. A desirable function would not have local minima that may cause the final alignment to converge at an incorrect solution. Another consideration is that the magnetic tracker (or any device that provides the pose of the needle) introduces some uncertainty. Therefore, a good heuristic function must have a low sensitivity to noise. It is also important to conduct an error propagation analysis of candidate heuristic functions. This can be done by applying Equation (3.1), where  $z$  represents a heuristic function measure. The quantity  $z$  is a function of measurements, denoted by  $x$  and  $y$ , subject to sensor uncertainty. The standard deviations ( $\sigma_x$  and  $\sigma_y$ ) represent the uncertainties in measurement. The total uncertainty of the heuristic function  $z$  is then given by:

$$\sigma_z^2 = \frac{\partial f(x, y)}{\partial x} \sigma_x^2 + \frac{\partial f(x, y)}{\partial y} \sigma_y^2 \quad (3.1)$$

This indicates that heuristic functions where sensor readings are multiplied/divided are much more sensitive to sensor noise than heuristic functions that involve only addition and subtraction.

### 3.2.3 Analysis of Candidate Heuristic Functions

One potential heuristic function is the cross product between the needle vector and the entry path vector. The needle vector is defined from the needle base to the needle tip and entry path vector is defined from the entry point to the target position. Minimizing the magnitude of the cross product between these two vectors yields a needle aligned with the entry path.

Another potential heuristic function to move and align the needle is first to minimize the distance between the needle tip and the entry point ( $d$  in Figure 3.3), and then to align by minimizing  $d_{normal}$  while maintaining the needle tip at the entry point. We will see in simulation that each of these is a poor candidate heuristic function because they have local minima that can cause the needle to become misaligned.

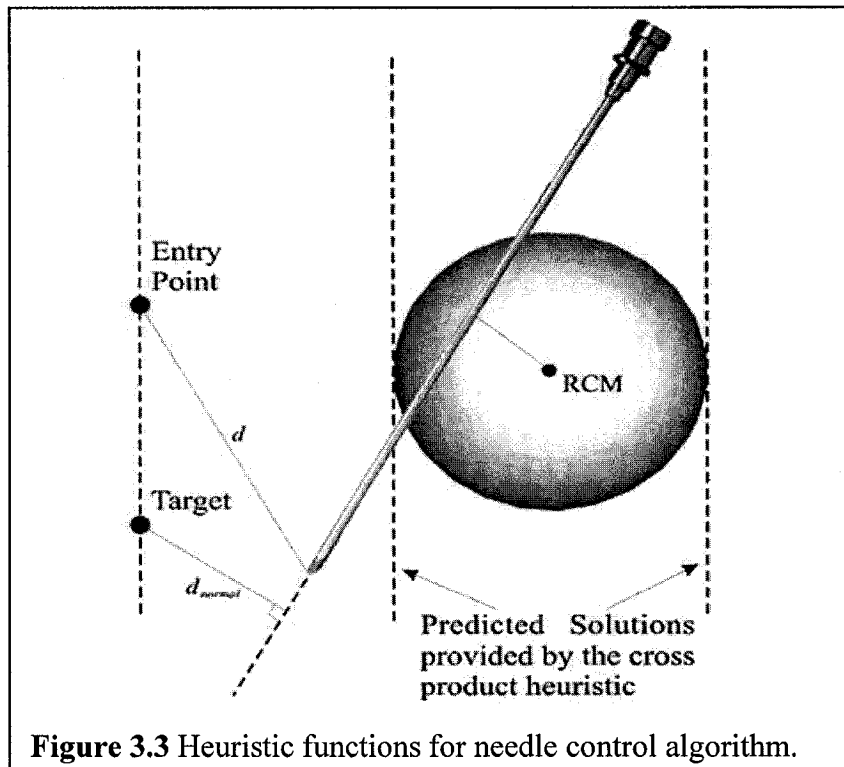


**Figure 3.3** Heuristic functions for needle control algorithm.

In order to compare different heuristic functions, we build a simulator reflecting our robot configuration. As shown in Figure 3.4, we have an RCM frame at the RCM point and two rotational DOF ( $\alpha$  and  $\beta$  around  $x$  and  $y$  axes respectively). We also have a tracker frame, where the planned “entry” and “target” points are defined. Most importantly, the transformation between these two frames is  $F_{rcm}^{tracker}$ , which is not required in the physical system (no calibration step necessary) but is assigned a value for simulation purposes.

The needle coordinates in the RCM frame (note: needle tip is not at the RCM point) can be transformed to tracker frame as follows:

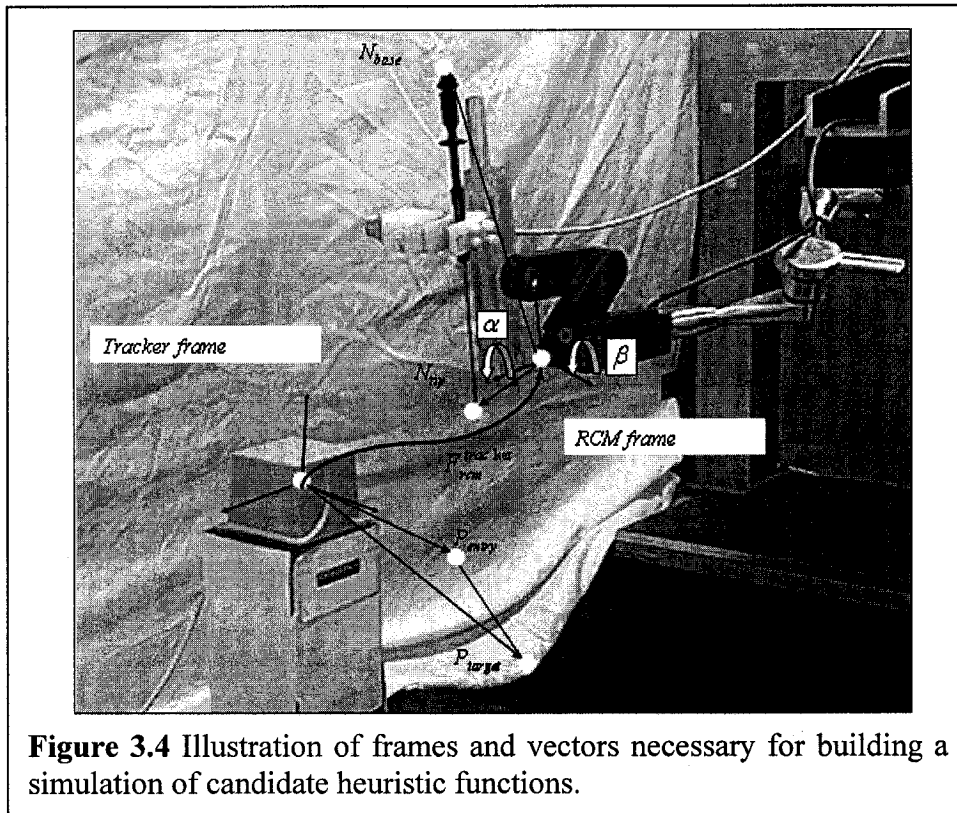
$$\vec{n}_{tip}^{tracker} = F_{rcm}^{tracker} R(\vec{x}, \alpha) R(\vec{y}, \beta) \vec{n}_{tip}^{rcm}$$

$$\vec{n}_{base}^{tracker} = F_{rcm}^{tracker} R(\vec{x}, \alpha) R(\vec{y}, \beta) \vec{n}_{base}^{rcm}$$

Where  $R(\vec{x}, \alpha)$  is a rotation around the  $x$ -axis by  $\alpha$  degrees and  $R(\vec{y}, \beta)$  is a rotation around the  $y$ -axis by  $\beta$  degrees. Now, we have the needle base and tip points in tracker space where the planned entry-target points are defined. The following will illustrate the different heuristic functions we simulated to check the applicability of each one.

$$cross - product = \|(\vec{n}_{base}^{tracker} - \vec{n}_{tip}^{tracker}) \times (\vec{p}_{entry}^{tracker} - \vec{p}_{target}^{tracker})\|$$

$$dist.metric = dist(\vec{n}_{base}^{tracker}, \vec{n}_{tip}^{tracker}, \vec{p}_{entry}^{tracker}, \vec{p}_{target}^{tracker})$$



Comparison between the distance heuristic function and the cross product heuristic function illustrates why the cross product function is the preferred choice for creating a Virtual RCM. The distance heuristic function requires that the needle tip be placed at the insertion point, while the cross product heuristic function search can take place with the needle anywhere in space. The cross product function will also be subject to less alignment error, as is illustrated in the simulation in the next section.

### 3.3 Simulation Results

In our simulation, all possible discrete combinations of  $\alpha$  and  $\beta$  can be plotted with respect to the scalar value of a given heuristic function. This yields visual and intuitive understanding of the heuristic functions. Figure 3.5 shows the simulated needle as  $\alpha$  is rotated a full 360 degrees while  $\beta$  is held constant at  $5^\circ$  and  $50^\circ$ . This procedure is repeated for each  $\beta$  value. Plots of two heuristic function results across the entire  $\alpha$ - $\beta$  space can be seen in Figure 3.6. As can be seen from the figure, the cross product heuristic function has a higher specificity than alternate heuristic functions. Its deep minima will yield a more accurate alignment result in the presence of sensor noise or other real world uncertainties than the shallow minima of the distance heuristic will yield.

At first glance, it may not be obvious which of the minima on the cross product function are acceptable solutions. Two of the four minima can be discarded immediately, because they represent the needle oriented with the base toward the target, which is the wrong way. The other two minima are equally good solutions, representing the needle aligned on either side of the actual RCM point as shown by the dashed lines on Figure 3.3. Application-specific workspace constraints would provide the only reason for choosing one minima over the other, since both represent equally good alignments of the needle. If no such workspace constraints exist, this interesting multiple solution property of the

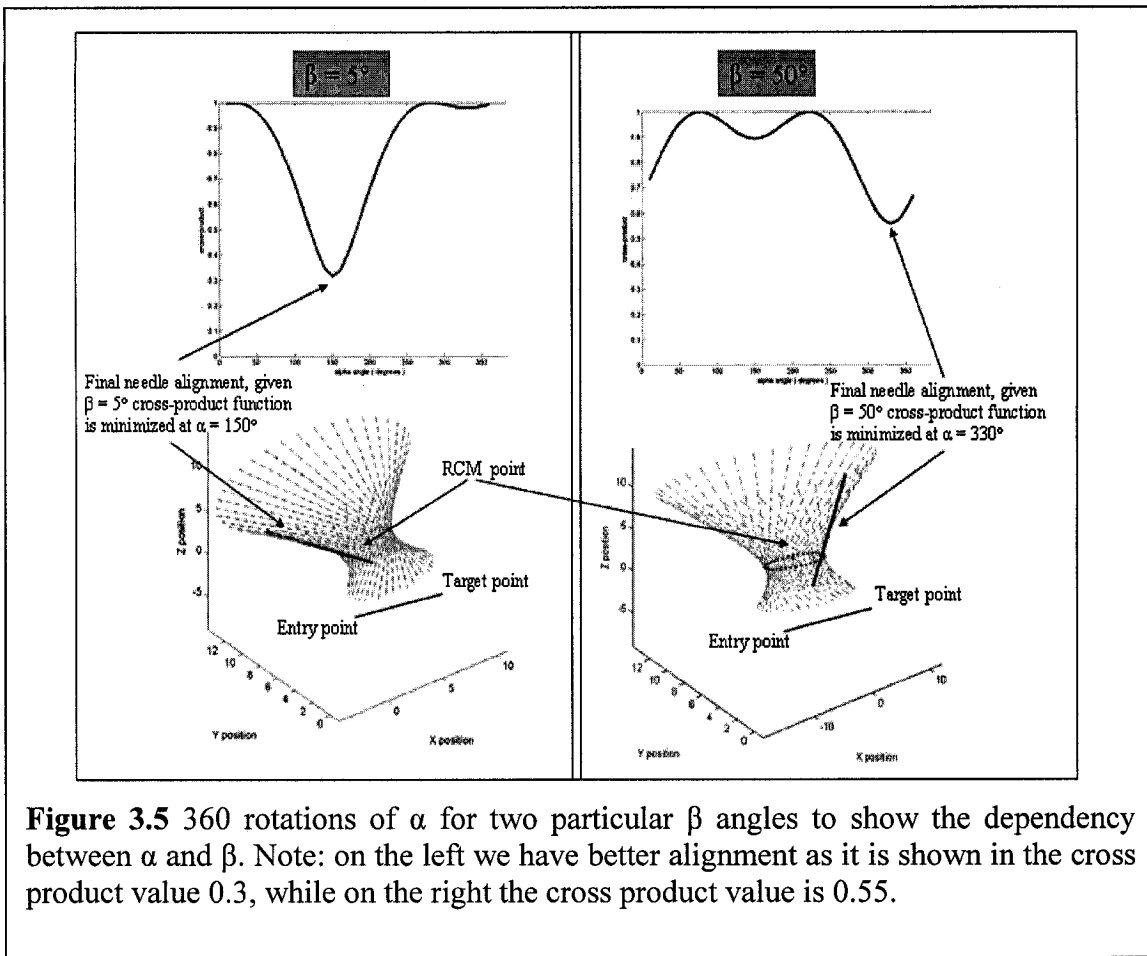


**Figure 3.5** 360 rotations of  $\alpha$  for two particular  $\beta$  angles to show the dependency between  $\alpha$  and  $\beta$ . Note: on the left we have better alignment as it is shown in the cross product value 0.3, while on the right the cross product value is 0.55.

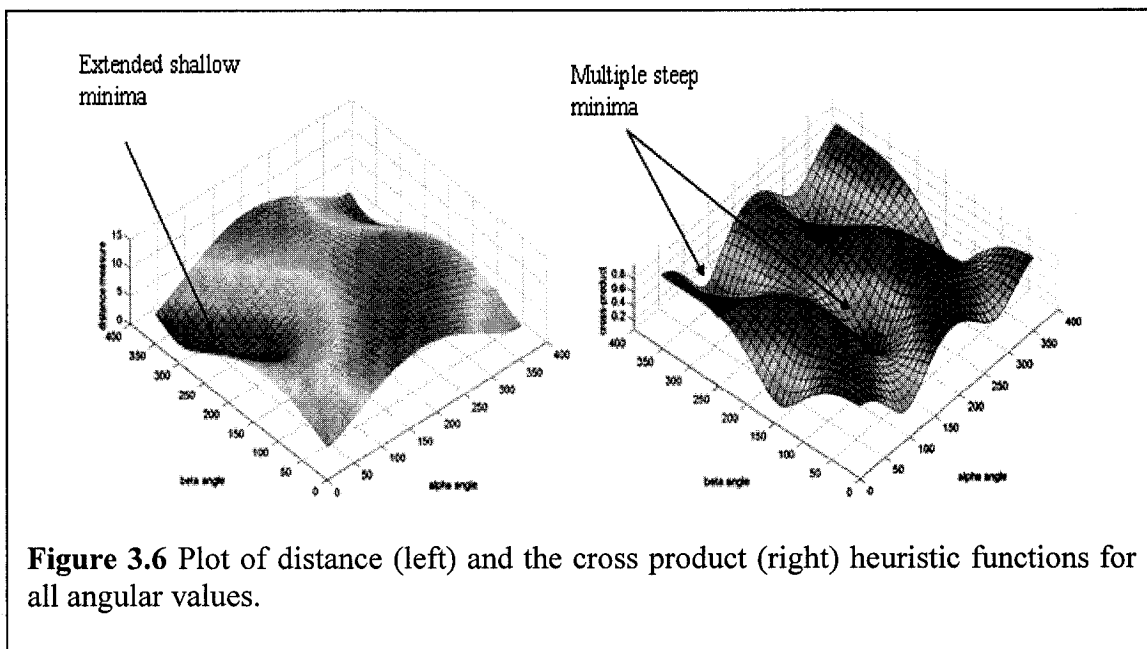


**Figure 3.6** Plot of distance (left) and the cross product (right) heuristic functions for all angular values.

cross product heuristic function is beneficial to the speed of the algorithm. A search of a multiple solution space can generally converge more quickly than a search with a single solution.

The most compelling advantages of the cross product function are its spatial invariance and its low overall error in alignment. The magnitude of a spatially invariant function does not change with Cartesian motion. This has important practical implications for patient safety, as is described in the next section. Even more important to practical application, the cross product will have lower final error than the distance heuristic function because the former requires only summation of error, while the latter requires both multiplication and square root functions.

### **3.4 Experimental Implementation**

The two rotational joints of the robot perform needle alignment using the previously described cross product heuristic function. The joints are moved in small increments. Since the tool tip is not on the mechanical fulcrum point, it will be displaced a small amount during each rotation. However this displacement is immediately compensated for by the Cartesian stages, based on the tracker reading. Thus the needle tip remains on a Virtual RCM point. The robot continues to move through the search tree by moving the rotational joints alternately in incremental motions that decrease the value of the heuristic function.

There are several ways to apply this algorithm to needle placement (Figure 3.7). The most obvious is to perform needle placement using the same sequence of motions as would be used manually (Virtual RCM Method), where the robot first moves the needle tip to the entry location, and then aligns it along the insertion vector. Humans do not

orient the needle first and then move it to the entry point, although this is an equally good order of operations. (Perhaps the reason for this is that humans are able to discern smaller differences in vector alignment between nearby vectors than those separated by a distance of many centimeters. It may also be easier for humans to control the alignment more accurately by pivoting the needle on a fixed point.)

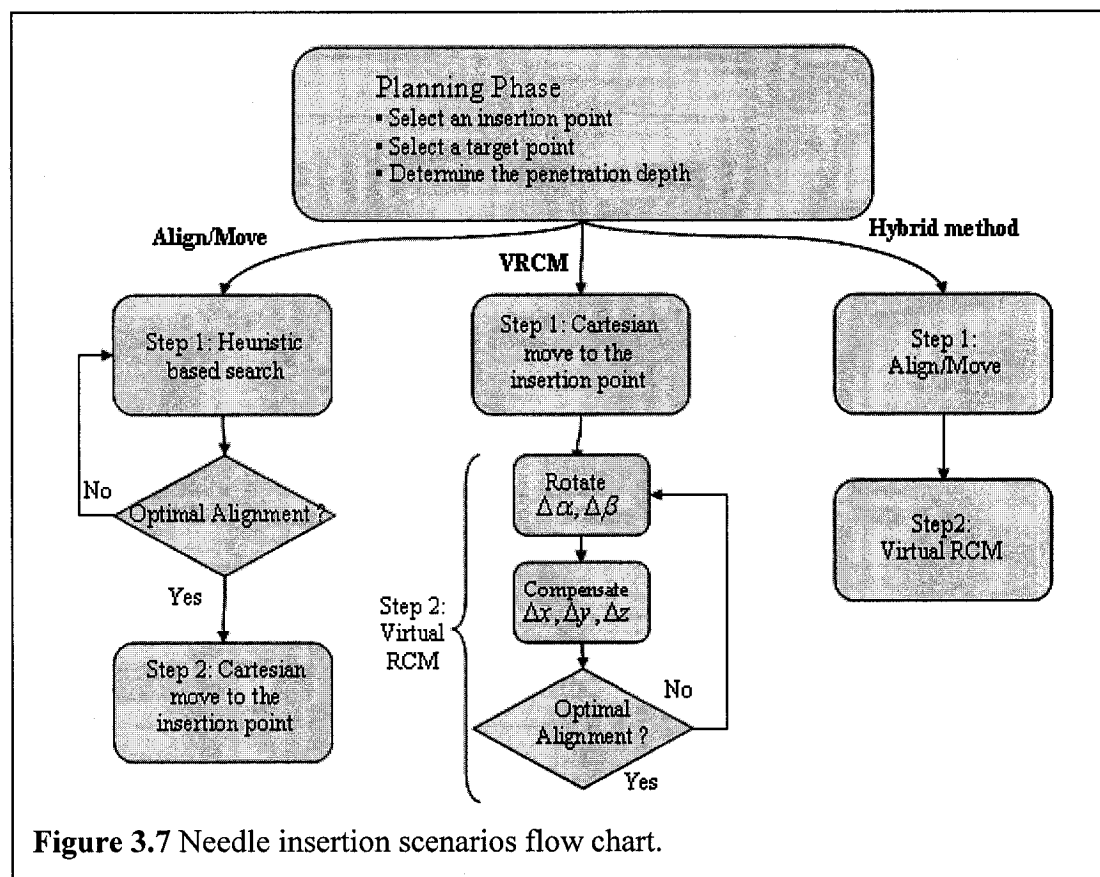


Figure 3.7 Needle insertion scenarios flow chart.

Since robots suffer from no such limitations, there is no intrinsic reason why a robot could not perform an alignment before moving the needle to the surgical site (Align/Move Method). The advantage to this for the robot is speed. Since the robot is located at a safe distance from the patient, we can eliminate use of the Cartesian

correction portion of the Virtual RCM algorithm and find the correct alignment more rapidly.

A third alternative is to use a combination of the first two methods (Hybrid Method). The robot can rapidly make a quick rough alignment of the needle away from the patient, then move to the insertion point (Align/Move Method), and finally fine-tune the alignment with Virtual RCM motion (Virtual RCM Method). Figure 3.7 presents a flow chart of all three methods, (Align/Move, Virtual RCM, and Hybrid.)

### 3.4.1 Results and Discussion

We performed needle placement according each of the three methods, and the results are summarized in Table 3.1. In our experiment, the number of steps required (regardless of the method used) was nearly linearly proportional to the initial misalignment. This was because we used a fixed initial (largest) step size. If the initial step size were large and adaptively modified as the solution was approached, the algorithm could reach a solution in fewer steps. However, for reasons of safety, this would only be practically feasible in Align/Move or the Hybrid Methods, where the needle tip is aimed away from the patient, or the alignment is already nearly correct. In our experiments it was possible, given a wide range of initial conditions, to get an optimized solution within few (20-30) steps requiring a total time of only 0.8-1.2sec, since each step takes an average of 40ms.

As can be seen from the Table 3.1, Align/Move is the fastest (it has the fewest steps required) of the three methods, because no Cartesian motion is needed to compensate for tip displacement. The results for Virtual RCM show that this method alone is essentially equivalent to Align/Move in both rotational and displacement accuracy, yet it is much slower. The Hybrid method is much more accurate than the first two, yet the algorithmic

Method	Experiment Sets		Set I	Set II	Set III
	Initial angle deviation (deg)		15.6	28.7	51.4
	Initial target displacement (mm)		21.2	41.8	118.2
Align/Move	# of steps	Rotation		17	35
		Translation		1	1
	Angle error (deg)		2.2	2.8	2.1
	Target displacement (mm)		1.05	2.81	3.40
Virtual RCM	# of steps	Rotation		17	35
		Translation		17	35
	Angle error (deg)		2.8	2.2	2.8
	Target displacement (mm)		1.68	3.02	5.15
Hybrid Tech.	# of steps	Rotation	Method I	17	35
			Method II	2	2
		Translation		2	2
	Angle error (deg)		1.4	1.7	1.9
	Target displacement (mm)		0.78	2.44	3.99

**Table 3.1** Virtual RCM experimental results.

complexity has the same order of magnitude as Align/Move. It is important to note that the accuracy presented in the table is severely limited by the tracker accuracy, which is reported by the manufacturer to be 2.54mm RMS (this is a first generation FOB tracker).

### 3.5 Conclusions

In this work, we have provided algorithms that allow needle placement robots to operate without having a mechanically constrained fulcrum point, and also without calibration, encoding, and a complete knowledge of the kinematic chain.

The proof-of-concept prototype system achieved 0.78mm translation and 1.4 degrees rotational accuracy with the VRCM method. Further more, the Virtual RCM control algorithm was used in all experiments mentioned in Chapter 2, including the comparative study and the one animal trial with system accuracy of about 4 to 5mm.

As a future goal of this work, I would like to replace the magnetic tracker with a CT Fluoroscopy scanner. We will gather the pose of the needle tip directly from the CTF images using the method described in [Chirikjian-2002]. Our ultimate goal is to accurately place needles using inexpensive, uncalibrated, and unencoded robots in intraoperative imagers (CTF, MRI, and X-ray fluoroscopy), using purely image-based spatial registration of the tool holder alone. In terms of algorithmic enhancements, we will incorporate target uncertainty into our model.

## **Part-I: Chapter 4**

# **CISUS: An Integrated 3D Ultrasound System for IGT Using a Modular Tracking API**

Ultrasound has become popular in clinical/surgical applications, both as the primary image guidance modality and also in conjunction with other modalities like CT or MRI. Three dimensional ultrasound (3DUS) systems have also demonstrated usefulness in image-guided therapy (IGT). At the same time, however, current lack of open-source and open-architecture multi-modal medical visualization systems prevents 3DUS from fulfilling its potential. Several standalone 3DUS systems, like Stradx or In-Vivo, exist today. Although these systems have been found to be useful in real clinical settings, it is difficult to augment their functionality and integrate them into versatile IGT systems. To address these limitations, a robotic/freehand 3DUS open environment called (CISUS) is being integrated into the 3D Slicer, an open-source research tool developed for medical image analysis and surgical planning. In addition, the system capitalizes on generic application programming interfaces (APIs) for tracking devices and robotic control. The resulting platform-independent open-source system may serve as a valuable tool for the image-guided surgery community. Other researchers could easily integrate the generic CISUS system along with other functionalities (e.g., dual view visualization, registration, real-time tracking, segmentation, etc...) to rapidly create their medical/surgical applications. Our current driving clinical application is robotically assisted and freehand

3DUS-guided liver ablation, which is fully being integrated under the CISUS<sup>†</sup> within 3D Slicer. Initial functionality and preclinical feasibility are demonstrated earlier in Chapter 2 on phantom and ex-vivo animal models.

## 4.1 Introduction

Image-guided therapy, the use of medical imaging for guidance of therapy, is not a new concept. Since the discovery of x-rays, various imaging methods such as CT, MRI and US have been used to localize normal anatomical structures and pathologic lesions, as well as to guide surgical instruments. The core components of IGT usually involve image analysis, segmentation, registration, and visualization. IGT uses cutting edge engineering and medical imaging research to change the current practice of surgery. The implementation of IGT will allow the surgeon to use medical image analysis as a surgical navigation tool through the patient's anatomy via visualization of the anatomical changes during surgery. IGT has already led to such improvements in surgical procedures as accuracy, speed, shorter hospitalization and improved overall outcomes. These trends are expected to continue on an accelerated path in the foreseeable future.

In addition to medical imaging devices, other hardware such as tracking devices and medical robots may also be useful for IGT. A tracking device is an apparatus that shows the location of objects in 3D space and returns "real-time" information concerning the position and orientation of those objects relative to a given frame of reference. These devices can also play a substantial role in building 3DUS data from series of tracked 2DUS images. A robot or mechanical arm allows for steady positioning and precise

---

<sup>†</sup> The work presented in this chapter is a collaborative effort with Mr. Anand Viswanathan and it was published on SPIE Medical Imaging 2004 [Boctor-2004f]. Source code in C++ classes, Tcl-tk planning and robotic control module, and architecture design were provided by the author; Tcl-Tk programming, vtkCISUScontainer classes, rapid developing pipeline, GUI design and programming were provided by Mr. Viswanathan.

manipulation of surgical instruments in and around the target anatomy and it can also be used to manipulate US scanners.

The surgeon can choose the best course of action to treat the patient using the information provided by preoperative images. Medical images can be used not only for the purposes of diagnosis and surgical planning before surgery, but also for visualizing the anatomical Region of Interest (ROI), which may be fully embedded in the organ and cannot be directly visualized, during surgery. During both acquisition of medical images and surgery, the target and surrounding anatomy are susceptible to motion and deformation, typically caused by respiration and mechanical contact with the surgical instruments. Therefore, it is a logical imperative to track the 3D location of the anatomy of interest in interventions concerning sensitive or vital structures. Through IGT systems one should be able to detect organ motion as well as organ deformation by using real-time imaging (in our case US) to track and monitor the dislocation and deformation of anatomy.

Another aspect of IGT is the synthesis of different imaging modalities, or multimodality registration. Typically, by acquiring preoperative 3D volumes in a high resolution imaging modality such as CT or MRI, we can register another imaging modality that is real-time such as fluoroscopy and US, to provide accurate and updated visualization information to the surgeon during the procedure. This would provide a minimally invasive and precise approach to treatment of a wide array of organ systems and diseases. As minimally invasive surgical applications gain prominence, the role of IGT will increasingly become more significant for capturing intraoperative surgical changes and for providing integrated visualization.

Ultrasound imaging has emerged as a widely popular guidance modality for medical interventions, since it is portable, interactive, real-time, safe, cost-effective and convenient to use in outpatient clinics and sometimes even in an office setup, in contrast to other modalities such CT and MRI. Consequently, US machines have become predominant in the operating room and have started to fill the X-ray's niche in intraoperative guidance, especially when soft tissues are involved. Significant research has been dedicated to using US, but significant technical improvements are needed before the full potential of US can be realized, particularly in applications involving IGT. Individual 2DUS images or volumes must be assembled into extended 3D volumes [Fenster-2001] and then the position of surgical tools must be related to the reconstructed 3DUS volume. These tasks also critically require a reliable calibration framework.

In the current field of US image-guided therapy applications, there are very few commercial/research US systems, such as Stradx [Prager-1998a] and In-Vivo [Sakas-1992], which are proprietary and closed. Augmenting the functionality of these closed systems and integrating them into an IGT environment entails formidable technological, logistical, and legal challenges. There have been successful attempts at integrating US in IGT applications as can be seen in MISON [MISON-web], an intraoperative imaging system, which integrates 3D ultrasound and navigation, and prostate brachytherapy systems also routinely use US [CMS-web, Varian-web].

Although the systems above illustrate the feasibility and importance of US in the IGT context, a standard and open environment for the development of US-guided therapy is still missing. The work we present here is intended to fill in this gap by introducing an open source platform to develop various specialized US IGT therapy systems using real-time 2D and/or 3DUS imaging. To address these limitations, a robotic/freehand 3DUS

open environment [CISST-web] Computer-Integrated Surgery guided by US imaging, a.k.a. (CISUS) is being integrated into the 3D Slicer (Surgical Planning Lab, Brigham and Women's Hospital and Harvard medical school) [3D Slicer-web], an open source research tool intended for diagnostic visualization and surgical planning.

## 4.2 Architecture of the CISUS System

In this chapter, we present the following sections: (1) an overview of the CISUS system, (2) its functional requirements, and (3) system design. The last includes description of the development environment, CISUS architecture, implementation details, system extensibility, and the rapid prototyping interface.

### 4.2.1 System Overview

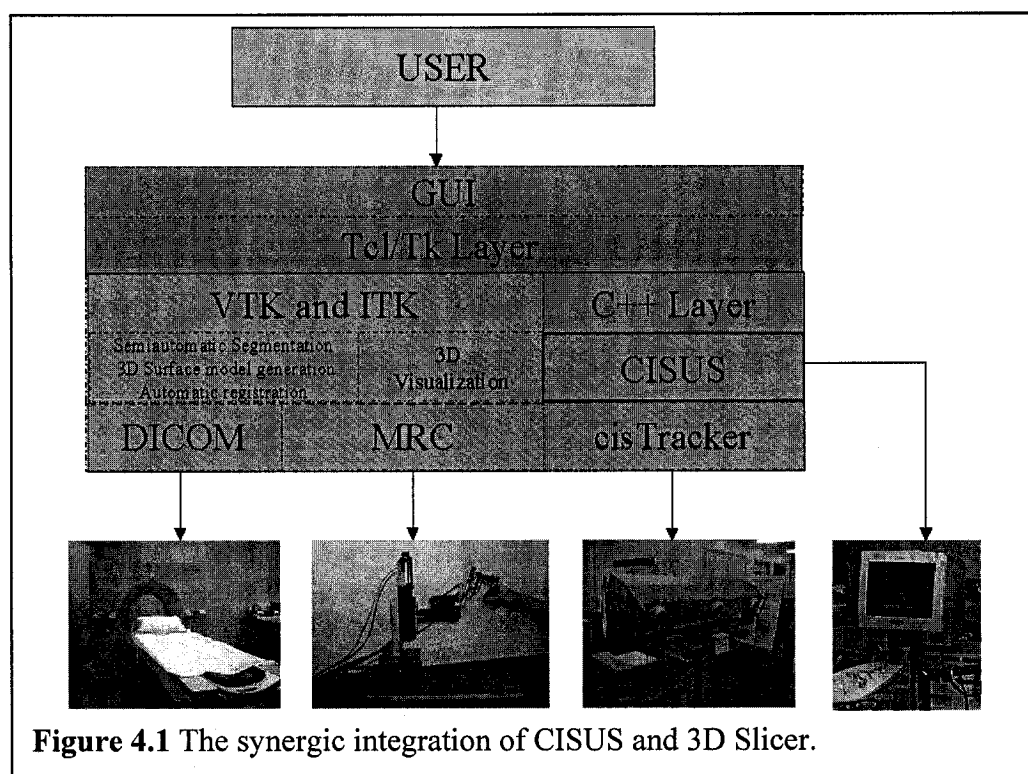
The home environment for the CISUS software package is the 3D Slicer [Gering-1999, 3DSlicer-web], which is a development environment designed for open source analysis and visualization of medical data. The 3D Slicer utilizes an underlying open source software package, Visualization Toolkit (VTK), to handle the rendering and visualization pipeline while using Tcl/Tk for the user interface. Essentially 3D Slicer is a set of VTK-based C++ classes and a structured user interface in Tcl/Tk designed to be used in IGT applications. These libraries are both compiler and operating system independent. 3D Slicer offers an array of useful features, including:

- A multi-plane reformatting plane algorithm to display an arbitrarily oriented slice of a 3D volume.
- The ability to display multiple volumes on the same slice.
- Display windows that show the axial, sagittal, and coronal 2D slices as well as a 3D graphical view.
- The ability to create, edit, and render surface models.

- A trajectory assistance module that can display virtual objects in the 3D view and assist in planning the trajectory path of the object.

Other significant elements of 3D Slicer's core functionality are multi-modal registration to semi-manually align two or more 3D volumes, and a volume editor that contains a variety of segmentation tools. 3D Slicer provides functionality to create rendered surface models from the 3D volume and use a decimation algorithm to reduce the number of triangles needed to represent those models. Using the features listed above, it is relatively straightforward to extend 3D Slicer into IGT applications for both preoperative and intraoperative surgical planning, which makes 3D Slicer an ideal host for the proposed open 2D and or 3DUS system, which we call CISUS.

The synergic integration of CISUS and 3D Slicer is shown in Figure 4.1, 3D Slicer can be extended to include external libraries, such as the cisTracker and mrc modules for



tracking devices and robotic control, respectively. CISUS can take advantage of all the features of 3D Slicer and use the DICOM format to read imaging modalities. CISUS was designed to be integrated into the 3D Slicer environment along with libraries for controlling medical robots and tracking devices (mrc and cisTracker respectively.)

#### **4.2.2 Functions Implemented in CISUS**

The functions of CISUS offer sufficient flexibility to instantiate an array of specific clinical/surgical applications. The functions provide flexible configuration of the specific application and the means to control the execution of interventions. There are separate graphical user interfaces (GUIs) to configure the image capture device, tracking device, image reconstruction parameters, and robotic/freehand US capture settings, as shown in Figure 4.2.

- The “Capture GUI” allows for setting the parameters for the image acquisition device as configured by vtkVideoSource. These parameters can be saved or loaded from an input configuration file.
- The “Tracker GUI” configures the parameters for the tracking device as configured by cisTracker. There is a button selection to test whether the tracking device is properly configured. There is also a selection to load the US probe calibration matrix for a specific calibrated probe.
- The “Reconstruction GUI” sets both the options for building the volume and the postprocessing options to be applied on the volume. The user can choose from Voxel Nearest Neighbor, Pixel Nearest Neighbor, and Distance Weighted Interpolation methods [Rohling-1998]. The user can load a configuration file which describes the ROI and another which specifies the filling algorithm and its tuning parameters.

- The “Freehand/ Robotic GUI” allows the user to select the type of system based on the existing available hardware. The user can then choose options such as use of speckle correlation (in the case of an untracked freehand system), as well as the type of sweeping motion to be used. In the presence of a medical robot, the user can choose to configure the robot using a configuration file and specify force compliance mode. The user will have a button selection to test the configuration of the robot.

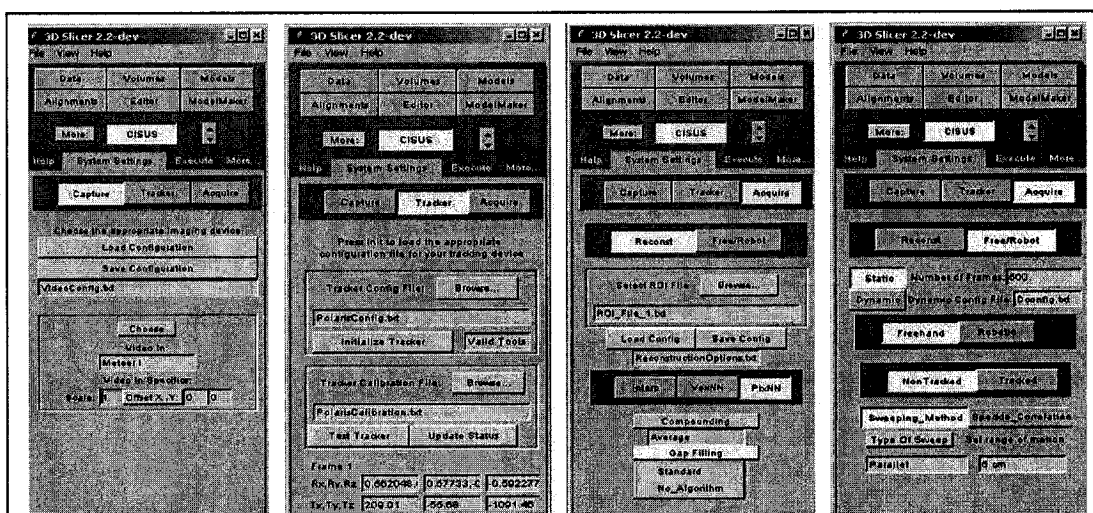


**Figure 4.2** Graphical user interfaces (GUIs) for the system settings. From left to right: Capture Device, Tracker, Reconstruction, and Robotic/Freehand US.

For the Execution phase, the user has a GUI to initialize the system and start data acquisition and 3DUS reconstruction (Figure 4.3.) The user can decide whether to save the 3DUS volume and/or the 2DUS images with the corresponding 3D position provided by the tracker. The user also has the option to load and save the above configuration parameters in files, for a rapid convenient configuration of the system.

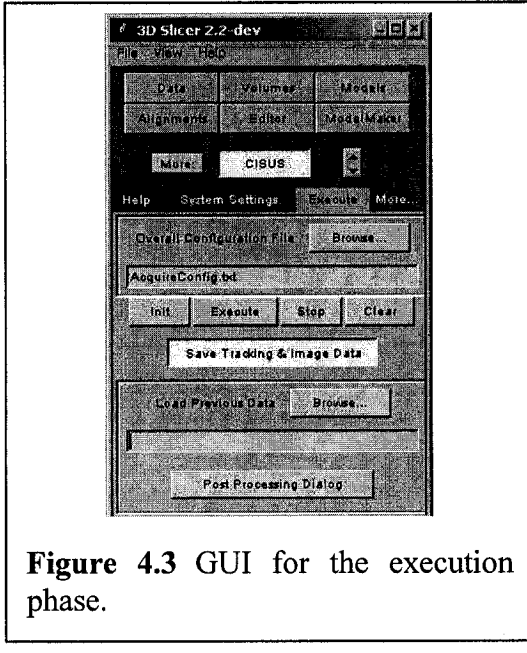


**Figure 4.3** GUI for the execution phase.

### 4.2.3 System Design

#### 4.2.3.1 Development environment

The development setup of the CISUS module requires the following software: CMake 1.8.3 [[www.cmake.org](http://www.cmake.org)], Tcl/Tk 8.3/8.4 [[www.activestate.com](http://www.activestate.com)], VTK 4.2 [[www.vtk.org](http://www.vtk.org)], 3D Slicer 2.x [3D Slicer-web] and the cis-2 and mrc-2 libraries [CISST-web]. CMake is a cross-platform makefile generator. 3D Slicer uses Tcl/Tk for the GUI layer. The SWIG 1.3.19 [[www.swig.org](http://www.swig.org)] software is also needed for an optional Tcl wrapped version of the cis-2 library.

A number of steps are required for using the CISUS libraries. First, using CMake, we build the makefiles for VTK with the WRAP\_TCL, USE\_ANSI\_STDLIB, and BUILD\_SHARED\_LIBS options all set to ON, the last to generate dynamic libraries as the output of the makefile. After compiling the generated makefiles, we use CMake again to generate the makefiles for the 3D Slicer code in the base directory. (It is advisable to check if vtkSlicerBase.dll and vtkSlicerBaseTCL.dll were indeed generated.) Next, we

use CMake on the `{SLICER_HOME}/Modules/vtkCISUS` directory to generate the makefiles that are responsible for compiling and linking against precompiled cis-2, mrc-2, and VTK dynamic libraries. Finally, we build the CISUS module using the generated makefiles and set the proper path settings, and lastly add “`vtkCISUS`” to the `SLICER_MODULES_TO_REQUIRE` environment variable.

#### **4.2.3.2 Architecture**

US-guided therapy may be used in a wide variety of clinical configurations, which CISUS addresses in two major steps: in a configuration and an execution phase. In the execution phase, the system performs the surgical intervention based on the settings derived in the configuration phase. As shown in Figure 4.2, the “System Settings” tab has been divided into three categories: (1) “Capture Device” to configure a video input source for US equipment or to use 3D Slicer’s DICOM reader. (2) “Tracking Device”, if one is present, to configure a tracking device using the modular cisTracker library [CISST-web] that currently supports Polaris, Optotrak, Aurora, Flock Of Birds, and Flashpoint. (3) “Acquisition” to specify a multitude of operational parameters, such as scanning configuration, freehand vs. robotic; acquisition mode, static vs. dynamic. There is also a tab for serialization of the acquired data (images, tracking information, and force sensor readings, and possibly more information). Robotic control is provided by the separate module named Modular Robot Control [CISST-web] a.k.a. mrc.

CISUS consists of VTK-based C++ classes and a Tcl/Tk script for the GUI. The overview of the CISUS module architecture illustrating the class hierarchy is shown in Figure 4.4. There is a class named `vtkCISUSContainer` that interfaces with the GUI and contains configuration variables. This class was designed to be the sole interface to the Tcl layer, by limiting the generation of Tcl wrappers to just the `vtkCISUSContainer` class.

This scenario ensures that all GUI interactions take place through `vtkCISUSContainer` and all other classes rely on it to handle their own GUI traffic. After generating a `vtkCISUSContainerTCL` library, one can directly load the library from Tcl. This `vtkCISUSContainer` class also serves as the entry point for all other related classes. The `vtkCISUSContainer` class is also responsible for the execution phase of the system and to serialize (and de-serialize) the entire system setup as well as the acquired 2DUS image data along with the computed 3D volume. There are three classes, each responsible for the configuration of the “Tracking” device used, for the “Acquisition” phase, and for the “Reconstruction” phase, respectively. These classes are serialized such that data (both positional and ultrasound images) and configuration options can be saved into a file and loaded from a file.

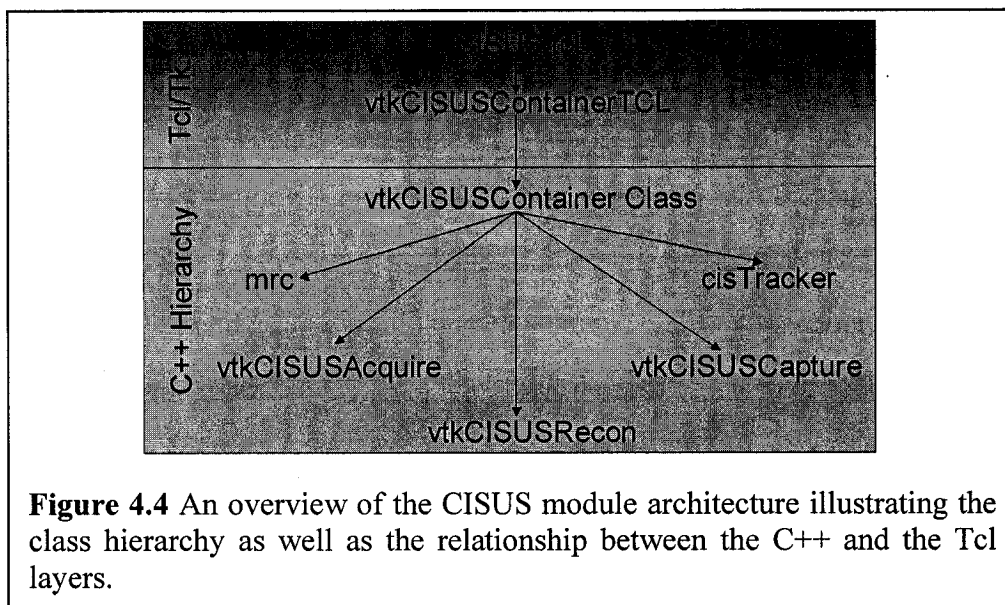


**Figure 4.4** An overview of the CISUS module architecture illustrating the class hierarchy as well as the relationship between the C++ and the Tcl layers.

The Tcl/Tk script loads the `vtkCISUSContainerTCL` library and displays a GUI within the 3D Slicer with which the user can interface. Working in this window management environment, the user can configure and operate the system and also seamlessly switch to

other 3D Slicer modules and back without losing any of CISUS data.

#### **4.2.3.3 *Implementation***

The vtkCISUSCapture class handles the video input device and allows for setting the scale and offset of the US image. VTK is a powerful open source visualization package that handles the rendering pipeline of visual programming. Since our host application was 3D Slicer, which relies on VTK, we chose to use VTK's VideoSource libraries to handle the video input from the US machine. This class uses a pointer to a vtkVideoSource object. By using vtkVideoSource, one can immediately use one of the preexisting derived classes for Matrox frame grabbers and generic windows acquisition cards. If support of another card is needed, one can simply add the appropriate derived class for vtkVideoSource. Since the base class of vtkVideoSource defines standard generic interface for video inputs, only superficial modifications are needed to make a new class of vtkVideoSource be used in the CISUS module.

The vtkCISUSAquire class handles the acquisition and configuration of the US image and tracking data. This class is responsible for the synchronization between the hardware components and for determining the type of operational mode the system is using. This class contains the US images along with related data (tracking data, encoder values, and force sensor readings).

The vtkCISUSRecon class handles the ROI parameters as well other options to configure the volumetric US reconstruction algorithm. This class uses the input of the configuration file or the input from the user interface to determine which types of algorithms are available.

The CISUS module uses the Engineering Research Center (ERC)'s libraries [CISST-web] to handle tracking devices and medical robotic hardware. `cisTracker` is used for the tracking device. This generic tracker class defines a basic outline of what actions tracking devices should be able to perform. The class is independent of the particular tracking device and operating system used. Classes derived from this general class must be tailored to the hardware specifications of a given tracker. This library is to be used for standalone systems, where the application using the tracker library is run on the computer to which the tracking device is physically attached. The `cisTracker` class also contains a simulated tracking device class to allow use of a virtual tracking device to aid developers with testing their code without actually having a physical tracking device connected to the system. Figure 4.5 illustrates the inheritance tree of the base class `cisTracker` and the specialized derived classes.

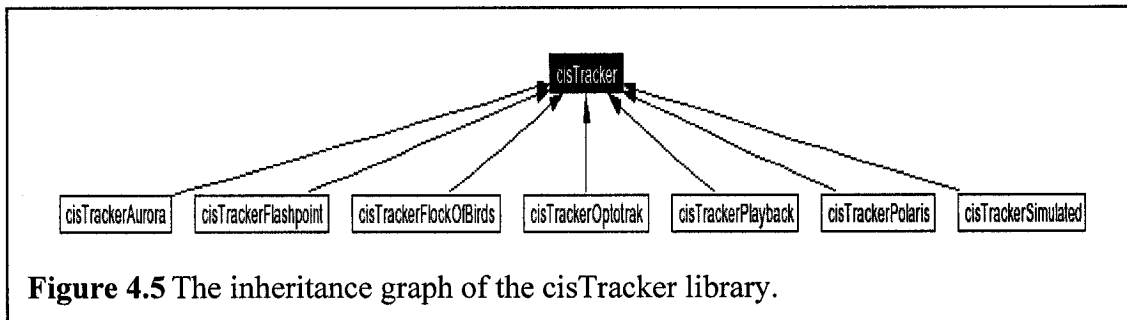
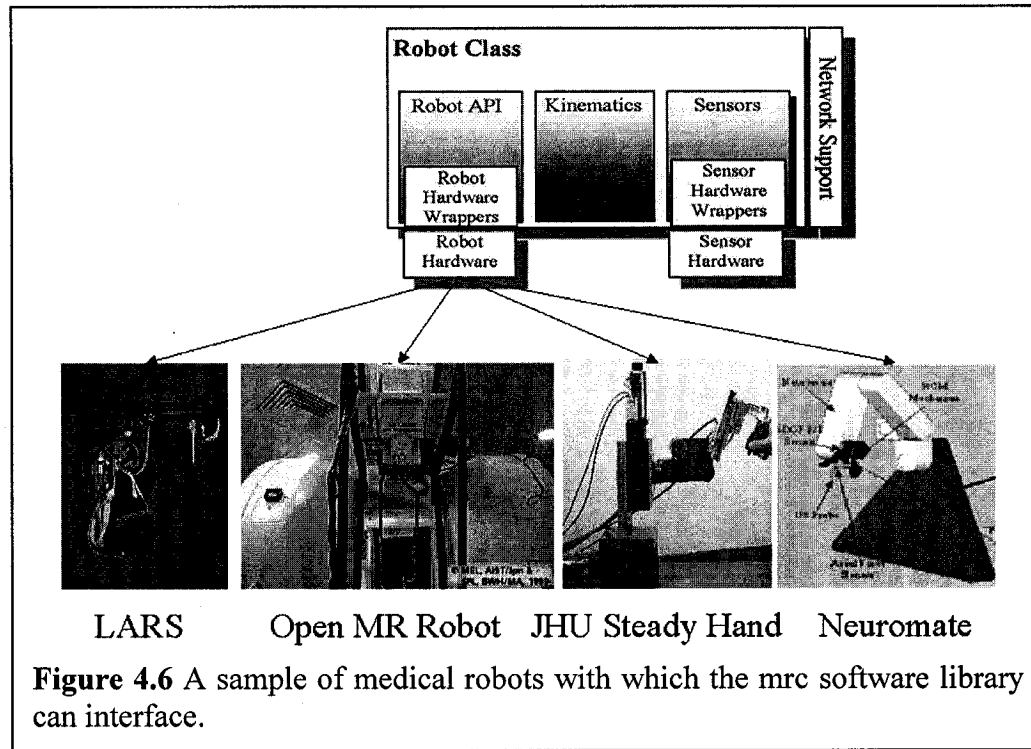


**Figure 4.5** The inheritance graph of the `cisTracker` library.

For Robot control, the CISUS module uses the modular robot control library, or `mrc`. The purpose of `mrc` is to provide a standard interface for distributed modular medical robots for computer integrated surgery robot applications while providing a standard usage of C/C++ libraries provided by robot hardware vendors. The `mrc` library allows for seamless use of multiple robot platforms in CIS applications, without hard coding any of the robot's particulars in the application's source code. As shown in Figure 4.6, the `mrc`

library was designed specifically to control a variety of robots including the LARS [Taylor-1995], the Brigham open-MR robot [Chinzei-2000], the Steady Hand[Taylor-1999], and the Neuromate [Neuromate-web], among several others [ISIS-web]. For force compliant control of surgical assistants, the mrc also supports various force sensors.



#### 4.2.3.4 Extension to CISUS

The architecture of the CISUS module was designed to allow for flexible extension with a minimum amount of new code added. To add a new algorithm or method to the CISUS, the following steps are followed:

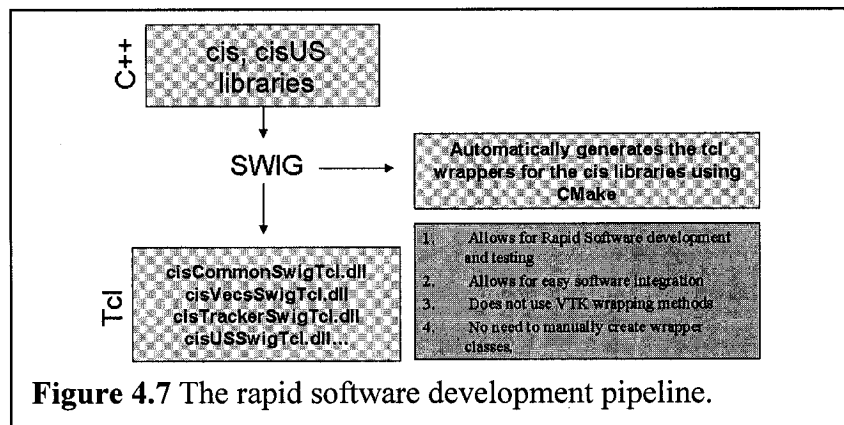
1. Add the code to the appropriate class {Acquire, Capture, Reconstruction}.
2. Add the methods to wrap the inserted function in the `vtkCISUSContainer` class.
3. Edit the GUI interface in the `CISUS.tcl` file to make the new function appear in the GUI.

To add new classes to the CISUS module, the following simple process is followed:

1. Place the classes in the {SLICER\_HOME}\Modules\vtkCISUS\cxx directory and edit the CMakeListsLocal.txt to add the new .cxx files to the LOCAL\_NO\_WRAP\_SRCS variable.
2. Use the vtkCISUSContainer class as an entry point for the new class and add the appropriate Tcl code to the GUI in the CISUS.tcl file.
3. Run CMake to regenerate the vtkCISUS makefiles and then recompile the library.

#### 4.2.3.5 Rapid prototyping interface

In the process of developing the CISUS system, we explored the possibility of integrating wrapped C++ libraries into Tcl using the interface compiler, SWIG (Figure 4.7). By combining the powerful makefile generator CMake with the SWIG development tool, we were able to implement an automatic generation of the Tcl wrapped libraries. This Tcl layer was very helpful in providing a foundation for rapid software development and testing. Normally VTK uses the Tcl interface generator Cable to wrap classes into other



languages. Initially our automatic wrapping strategy was based on using CMake and Cable. Due to limited support of the C++ STL libraries as well as advanced templated

code in the Cable package, the SWIG package was utilized instead. In the development of our algorithm, we realized that the synchronization between the tracking device, the video input and if present, a robotic device to be performed in the C++ layer to reduce any temporal delays. After coming to this decision, we instead chose the path of using VTK inheritance to wrap only the vtkCISUSContainer class to interface to the Tcl layer. However, we left the implementation of using the SWIG route of the Tcl interface for the ERC libraries in order to facilitate faster software development for other CISUS developers. The SWIG interface for the CISUS module also allows easier software integration. In addition to Tcl wrapped libraries, SWIG is also able to produce Perl and Python wrapped libraries.

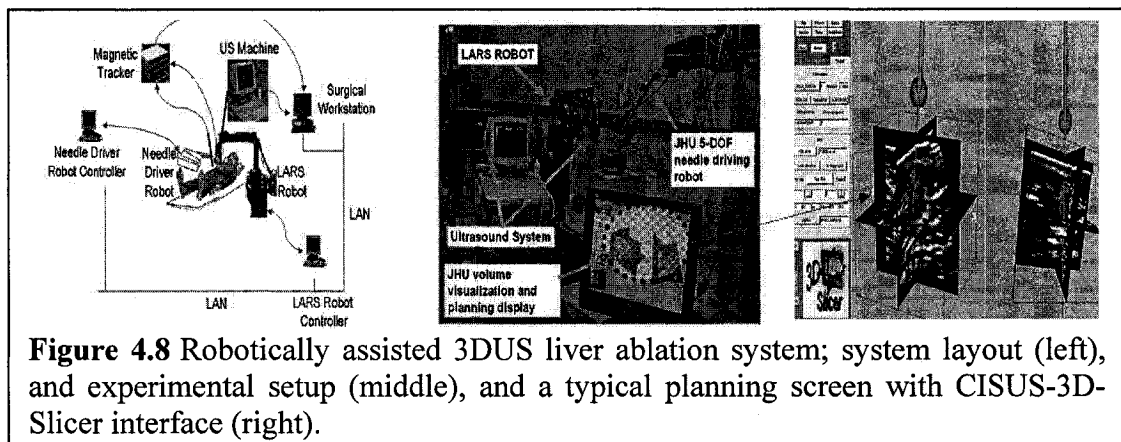
One important consideration is that although 3D Slicer contains the functionality of multimodality imaging, semiautomatic segmentation, 3D surface model generation, automatic registration, and 3D visualization, the CISUS system code solely relies on VTK and can be transplanted into a GUI environment outside of 3D Slicer.

### **4.3 Current IGT Application**

Based on the clinical application requirement specifications gathered during the setup phase, there might be four possible operational modes. The first configuration mode, “Tracked Freehand US” is utilized for any generic 3DUS application. The second configuration mode, “Image-Based Freehand US Tracking” is a cost-effective 3DUS system without the usage of a physical tracking device [Prager-2002, Smith-2003]. The third operational mode, “Robotic Scanning without a Tracking Device” utilizes the robot’s encoder position instead of a tracking reading; this configuration can be demonstrated by the ultrasound positioning robot developed at the University of British Columbia [Abolmaesumi-2002]. Finally, the last operational mode, “Robotic Scanning +

Tracking Device” illustrates a synergistic 3DUS system that incorporates both the tracking device and robotic control. The CISUS system previously developed in the ERC-CISST lab is an example of this operational mode by utilizing the LARS robot and a magnetic tracking device [Boctor-2004b, Boctor-2003b].

The authors have utilized a preliminary version of the CISUS system to develop different US-guided liver ablation prototypes. These prototypes vary from freehand to robotic 3DUS guidance, also from manual to robotically assisted needle insertion, and utilize a homogeneous user interface through the use of CISUS-3D Slicer. Figure 4.8 shows a snapshot for the integrated CISUS-3D Slicer system in an ex-vivo liver experiment.



#### 4.4 Conclusions

It is difficult both to augment the functionality of the available 3DUS systems and to integrate them into a clinical application {or clinical applications}. The robotic/freehand 3DUS open environment (CISUS) and 3D Slicer as an open source research tool intended for diagnostic visualization and surgical planning has demonstrated the potential to solve these limitations. The integrated 3DUS system, “CISUS for IGT”, uses a modular

tracking API and provides the following salient features:

- A generic 3DUS visualization workstation that could be used in different clinical applications.
- A flexible system that supports or can be extended to support any type of US image acquisition (through frame grabber cards or other video input.)
- A flexible system that incorporates external hardware to allow for specialized configurations (i.e. a tracking device or a robot.)
- Rapid clinical/surgical US-based applications developing tool for researchers.
- This new open, cross- platform compiler independent architecture will serve as a valuable tool to the medical imaging community.
- Most importantly, an unprecedented open synergistic environment for US-guided therapy.

The CISUS-3D Slicer open system substantially assisted in rapidly developing different research tools and prototype systems in our laboratories. The primary beneficiary of CISUS is the previously mentioned 3DUS-guided liver ablation (Figure 4.8) project. The lab's future agenda is to fully integrate the CISUS system with medical robot control, to test it under different operational modes (e.g., static vs. dynamic), and to integrate new hardware. A challenge we currently face is to improve on the available documentation and code maintenance, thereby encouraging the IGT research community to participate in the CISUS project, either as users or as developers. One of the drawbacks of the system is that the US beam calibration module exists as a standalone MATLAB-based toolkit and is currently not part of the CISUS system under 3D Slicer.

## **Part-II: Chapter 5**

# **Ultrasound Calibration Using the Hopkins Phantom**

### **5.1 Introduction**

The development of Computer Integrated Surgery over the past two decades has been a revolutionary change in surgical procedures. The introduction of various imaging modalities, such as MRI, CT, and US, has been an advancement in all stages -- pre-, post-, and -intraoperative -- of surgical procedures. True 3D imaging modalities, like MRI and CT, have extremely potent rendering capabilities, but are cumbersome to use for intraoperative procedures, mainly due to obstructive hardware and imaging latency. Ultrasound, however, has been emerging as a widely popular image guidance modality, since it is real-time, convenient to use in the operating room, and readily inexpensive compared to CT and MRI.

Unfortunately, conventional ultrasound is predominantly a 2D imaging methodology. A significant amount of research has been conducted to convert this technology into something that can provide the physicians with a 3D real-time visualization of the internal anatomy [Thomas-1998]. There are two basic methods to achieve this. The first, an intrinsically 3D method, is to either employ a fixed two dimensional array transducer or a uniformly moving single array of sensors. With this approach, scanning range is constrained by the hardware, quite often bulky, limiting its efficacy. The second

technique, an indirectly 3D method, is to let the surgeon manually acquire spatially co-registered 2D image slices, compound those into a contiguous 3D volume [Boctor-2001], then refresh the volume with real-time slices. This approach is highly applicable to tracking surgical tools and compensating for organ motion. Significant research has been geared towards the more generally useable second method. The quality and speed of volumetric compounding greatly depends on how well spaced and controlled the individual slices are; robotic assistance greatly enhances this spacing and control. [Boctor-2003b, Salcudean-1999]. A common way to co-register the individual 2D ultrasound slices is to track the imaging probe with a magnetic or optical tracker. In this case, a fixed transformation between the US beam and the tracker needs to be determined, so that arbitrary image pixels can be referenced in a global frame. Obtaining this fixed transformation is referred to as “ultrasound calibration”. After calibration, a 3D volume is reconstructed by some surface- or voxel-based method, and then the data is visualized with some appropriate combination of surface extraction [Boctor-1998], volume rendering, re-slicing, panoramic viewing, or multi-planar techniques. The accuracy of calibration appears to greatly influence the quality of the reconstructed volume and visualization, and through these the accuracy and reality of surgical planning and monitoring.

A widely popular way of calibration is imaging a precisely machined phantom of a priori known geometric properties. These properties are then identified in the images and their volumetric reconstruction is formulated in a mathematical framework that contains free variables for the unknown transformation. Solving for the unknown variables provides us with the calibration parameters. There is error associated with each stage of the process (phantom fabrication, image acquisition, spatial co-registration, image processing,

formulation, and numerical optimization solution), the combined total of which may easily amount to a prohibitively large degree of error.

Most existing publications related to 3D ultrasound are concerned with volume measurements, reconstruction issues, image compounding, and accuracy of US scanning, while they treat calibration as a marginal necessity to achieve their main objective. Only few papers have been devoted solely to the investigation of probe calibration [Carr-1996, Prager-1998b, Muratore-2001], while existing calibration methods critically need improvements in accuracy, ease of use, and performance time; some of them also need precise manufacturing of phantoms.

This calibration work focuses on enhancing the current methodology by introducing a novel calibration hardware, the Hopkins phantom and the multisided tank, with an associated mathematical framework. In contrast to prior methods, the Hopkins phantom is inexpensive, easy to construct and scan, yields significantly more data points per image than previously known designs, and easy to automate. We review the existing calibration methods (cross-wire, three-wire, and single-wall) in terms of their physical design, achievable accuracy, the number of images required, and the potential for full automation. The discussion continues with the Hopkins phantom and general mathematical framework used to solve the problem, and then we describe experimental validation and results.

## 5.2 Prior Art

Figure 5.1 shows three classic calibration phantoms that can be placed inside any tank for scanning from the top of the tank. The cross-wire method [Prager-1998b] (Figure 5.1-left) is based on scanning the intersection of two crossing wires or some small object, like

a bead or a pinhead. The target is suspended in a water bath, is scanned from different directions, and then the crossing point (or pinhead) is detected manually in each image afterwards. The accuracy of this method depends, to a large degree, on the accuracy of the manual detection in the images. Each image provides only one data point that is extremely laborious to determine manually. The process is hard to automate because it is extremely difficult to differentiate a single target from imaging artifacts.

The three-wire phantom [Carr-1996, Prager-1998b] (Figure 5.1-middle) involves scanning three-wire submerged in a water bath and crossed in such a way that they constitute an orthogonal coordinate system. Like the cross-wire technique, the wires here also need to be marked manually. The accuracy of this method also depends on whether the wires are precisely orthogonal and whether they are truly straight. The primary advantage of this method over the cross-wire method is that it is easier to scan the length of the wire than to keep the image focused at single point, while scanning from multiple directions.

The single-wall method [Prager-1998b] (Figure 5.1-right), as its name suggests, features a planar surface immersed in a water bath. This plane is viewed from various directions in the US images, each of which contains lines that lay in the plane. One problem with this method is that specular reflection causes low returning intensity at oblique scan angles. Furthermore, it is difficult to determine the true position of the floor in the images based solely on reflected signal intensity. This is due to the strong reverberations from the bottom, which appear like a “comet tail” in the reflected intensity signal. The Cambridge phantom method, essentially, is an enhanced version of the single-wall method. It overcomes both previously mentioned problems, but introduces dependencies on a precision-made phantom and clamp that is custom made for every US probe.

Cross-wire, three-wire, and single-wall techniques are all well known, and appreciated US calibration methods, specially the cross-wire. They are all, however, share the same fundamental basis, which is that they are all based on geometrical models. From the literature, geometrical model based phantoms include points [Carr-1996, Prager-1998b,

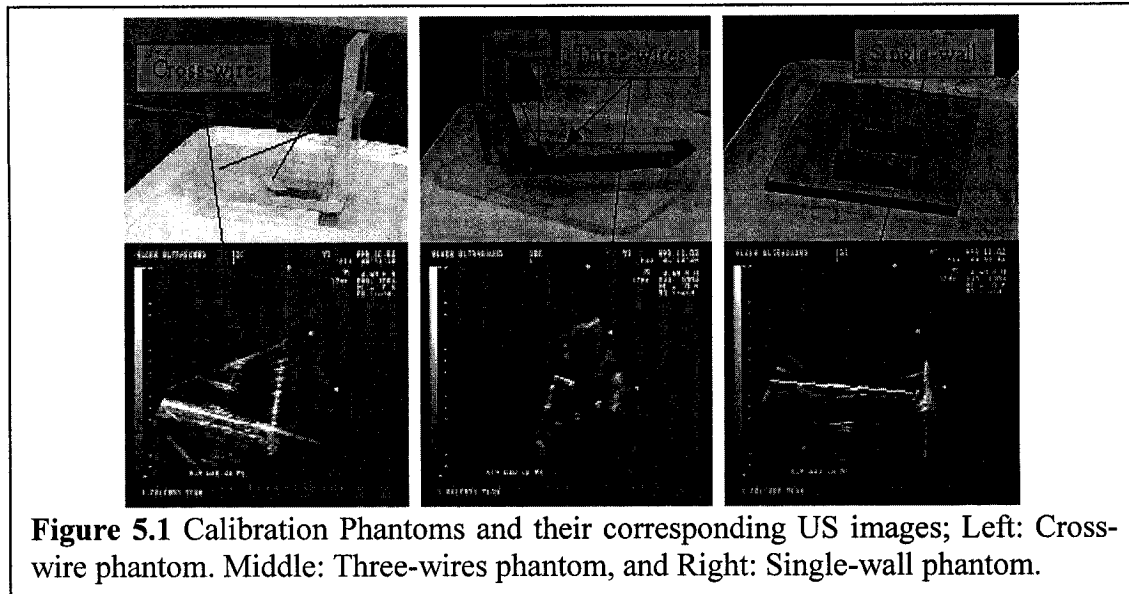


**Figure 5.1** Calibration Phantoms and their corresponding US images; Left: Cross-wire phantom. Middle: Three-wires phantom, and Right: Single-wall phantom.

Pagoulatos-2001, Detmer-1996, Boctor-2003c], and planes [Prager-1998b, Rousseau-2002, Boctor-2003c] Figure 5.2 shows a typical formulation for the coordinate systems required for the fore mentioned phantoms.

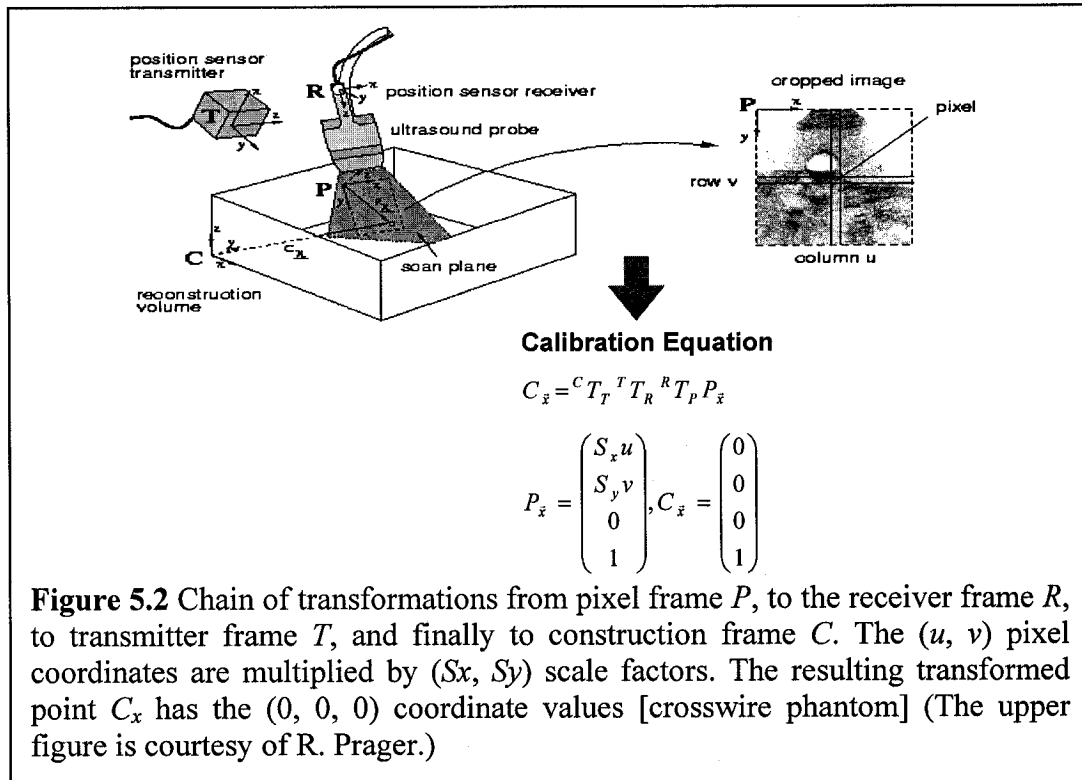
Others, such as Galloway et al. [Muratore-2001] use pointer-based methods, which simplify the non-linear optimization problem. However, these methods require pointer calibration and careful data collection. One variation of the point-based method was introduced by Pagoulatos [Pagoulatos-2001], where the phantom is a collection of N-shaped fiducials that are defined in the tracker frame. We will make use of this N-shaped phantom in our method.

Blackall et al. [Blackall-2000] presented a voxel based registration method for US calibration. Registration is achieved by the maximization of normalized mutual information. This occurs when accurate calibration parameters give optimal similarity between the US images of the phantom and the 3D voxel based model. Mercier et al. recently published [Mercier-2005], an excellent review paper for US calibration methods that described all the mentioned methods including our Hopkins method.

### 5.3 Materials and Methods

#### 5.3.1 Theory and mathematical framework

Figure 5.2 explains the mathematical framework of the calibration process, including the catenation of transformations between the coordinate frames. Our goal is to calculate  ${}^R T_P$  transformation matrix between pixel frame  $P$  and receiver frame  $R$ . The calculation must be as accurate as possible, ideally within the order of error of the tracker. Knowledge of



this unknown transformation matrix would allow us to place every image pixel in the construction coordinate system, which can be conveniently affixed to the operation room or to the patient's body.

The calibration phantom helps us to determine the unknown transformation by providing fixed points in space, which appear clearly in the ultrasound images and at the same time can be localized in the construction frame. There are three frame transformations: (1)  ${}^R T_P$  matrix between the pixel frame and the receiver frame, (2)  ${}^T R$  matrix between receiver frame  $R$  and transmitter frame  $T$ , and (3)  ${}^C T_T$  matrix between the transmitter frame and the construction frame. The equation involves 14 unknown variables: for  ${}^C T_T$  and  ${}^R T_P$ , with three translations and three rotations each, and the  $(Sx, Sy)$  scale factors for the  $(u, v)$  pixel coordinates. The  ${}^T R$  matrix is known and this is the reading from the FOB tracker. Figure 5.3 shows the general form for of the unknown six degrees of freedom

$${}^T T_I(x, y, z, \alpha, \beta, \gamma) =$$

$$\begin{pmatrix} \cos \alpha \cos \beta & \cos \alpha \sin \beta \sin \gamma - \sin \alpha \cos \gamma & \cos \alpha \sin \beta \cos \gamma + \sin \alpha \sin \gamma & x \\ \sin \alpha \cos \beta & \sin \alpha \sin \beta \sin \gamma + \cos \alpha \cos \gamma & \sin \alpha \sin \beta \cos \gamma - \cos \alpha \sin \gamma & y \\ -\sin \beta & \cos \beta \sin \gamma & \cos \beta \cos \gamma & z \\ 0 & 0 & 0 & 1 \end{pmatrix}$$

$$\mathbf{0} = \mathbf{f}(\theta, \phi) \approx \mathbf{f}(\theta, \phi_i) + \frac{\partial \mathbf{f}(\theta, \phi_i)}{\partial \phi} (\phi - \phi_i)$$

$$\Rightarrow \Delta \mathbf{f} = \mathbf{J}(\phi - \phi_i) = \mathbf{J} \Delta \phi$$
  

$$\phi_{i+1} = \phi_i + (\mathbf{J}^T \mathbf{J} + \varepsilon \mathbf{I})^{-1} \mathbf{J}^T \Delta \mathbf{f}$$

**Figure 5.3** The general form of one of the six degrees of freedom transformation matrices (Three translations [ $x, y$ , and  $z$ ] and Three rotations [ $\alpha, \beta$ , and  $\gamma$ ]). The equation in the bottom represents the Levenberg-Marquardt optimization method.

transformation matrices, as they are composed from the three rotations and three translation components. As the equations reflect, this problem is not a linear optimization that is usually straightforward to solve, but a non-linear optimization problem of large residual error type, which calls for the application of the Levenberg-Marquardt method.

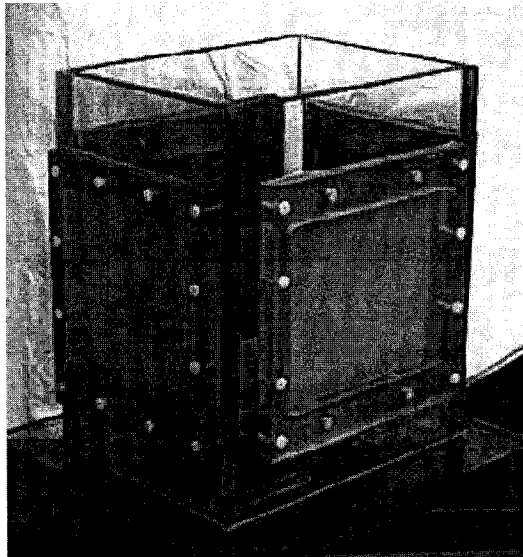


**Figure 5.4** The Multisided tank with five sides (top and four rubber windows). At the bottom, a piece of Lego is used to attach different phantoms.

### 5.3.2 The multisided tank and the Hopkins phantom

For comparative analysis, we built a cross-wire, a three-wire, and a single-wall phantom (Figure 5.1). Our experience showed that their designs and associated methods of data collection were not efficient and that it was hard, if not impossible to automate the image segmentation phase of the calibration process. These observations inspired us to add two new ideas to the methodology. The first innovation was to build a transparent plastic water tank, in which we can scan the submerged phantom not just from the top, but also

from all four sides of the tank through rubber windows (Figure 5.4). The second innovation was to build a new phantom (called the Hopkins phantom) that consists of two parallel plastic plates with parallel nylon lines stretched between the plates, in a pattern to form two orthogonal planes of a Cartesian coordinate system (Figure 5.5- left). The phantom is oriented in the multi-window tank in an oblique position, so that the structure can be scanned through the two opposite windows and through the top, with a plurality of nylon lines visible in each image (Figure 5.5- right). In every image, there is a set of parallel nylon lines near to and far from the probe, which can enhance the accuracy and

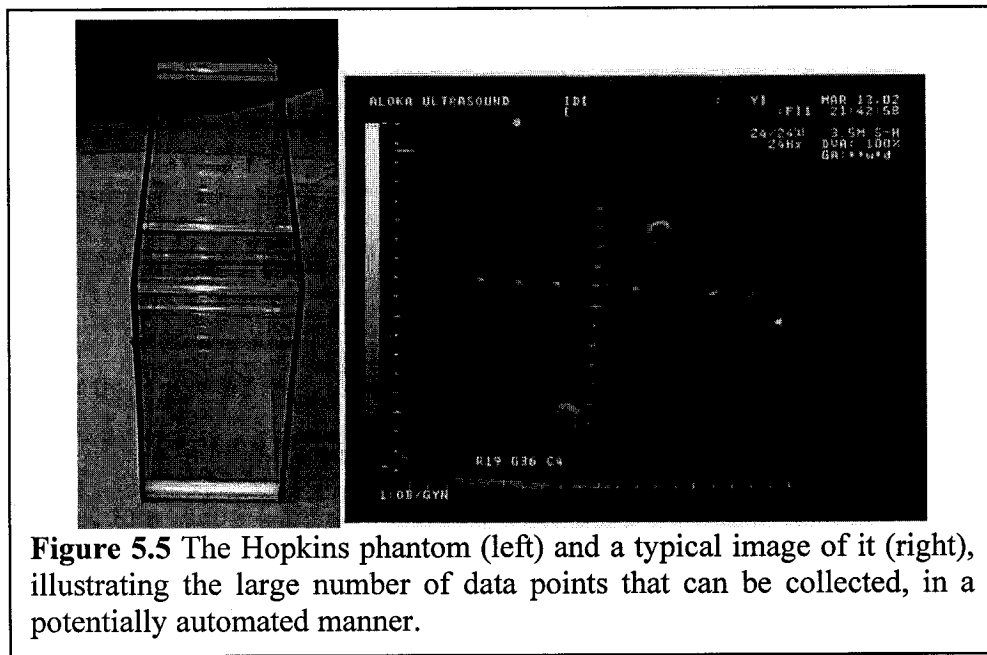


**Figure 5.5** The Hopkins phantom (left) and a typical image of it (right), illustrating the large number of data points that can be collected, in a potentially automated manner.

repeatability of calibration, as Galloway pointed out [Muratore-2001]. The Hopkins phantom provides a large number of highly recognizable features collected from small number of images, allowing us to automate the task of image processing. Typically, only few images are sufficient for accurate calibration, a considerable reduction, compared to the typical 200 images with cross-wire phantom or 400 images with three-wire phantoms [Prager-1998b]. In summary, the Hopkins phantom in conjunction with the multisided

tank gives us the following advantages:

- It reduces the number of necessary images by a factor of 20, conservatively.
- It increases the number of data points in each image.
- It reduces the “beam width” problem that it is a constant problem with the single-wall phantom.
- It is easy to construct, and no there are special design requirements for any US probe used, which distinguishes it from the Cambridge phantom.
- The clarity of the calibration images enables easy automation of the calibration process.
- Images can be collected in a wide range of scanning motion.

### **5.3.3 Experimental setup and workflow**

The experiment was conducted on a fixed laboratory bench. The Flock of Birds transmitter was mounted at a height providing ample workspace of the sensor. Each of the phantoms was fixed inside the plastic tank by pieces from a Lego toy set. This was very important preventive measure, because any movement of the phantom relative to the transmitter during the experiment would render the whole calibration attempt void. For the same reason, tank was also fixed with respect to the transmitter.

The issue of speed of sound in water was carefully considered. The ultrasound machine does not let us input the speed of sound as a variable. Instead, it assumes an average velocity of sound for human flesh, 1540m/s in our case, and then calculates its image pixel values accordingly. It is known that the speed of sound in water at room temperature is 1480m/s. Therefore, for precise calibration it is necessary to dope the water in some fashion, so that the speed of sound in the tank would match the machine’s hardwired constant. The simplest solution was to heat the water to 50°C, where the sound

of speed in it is 1542m/s. Another constraint is that the glue holding the rubber windows on the tank loses strength at 59°C. Thus, the temperature had to be tightly regulated at around 50°C. We used the 112-point variant of the Bilaniuk and Wong formulas to obtain the speed of sound in pure water below, where  $c$  is the speed and  $T$  is the temperature in degrees of Celsius:

$$c = 1.40238742 \times 10^3 + 5.03821344 T - 5.80539349 \times 10^{-2} T^2 + \\ 3.32000870 \times 10^{-4} T^3 - 1.44537900 \times 10^{-6} T^4 + 2.99402365 \times 10^{-9} T^5$$

The preheated water was poured into the tank until the phantom was fully immersed in the water. The calibration process was performed twice with each phantom. First, the tank was placed adjacent to the transmitter, and then the calibration was repeated after the tank was moved farther away from the transmitter. When all the FOB readings are close to the transmitter, the absolute distances are small. Therefore, the tracking percentage error is relatively high, but the uncertainty (error) of the reading is low. Moreover, when the readings are all farther out, percentage error must be smaller. However, the reading uncertainty is high. For comparative analysis, both datasets were taken.

In all sessions, the phantom was scanned from the top of the tank and from three of its four sides, while the fourth side of the tank conveniently faced the transmitter. (For example, for the cross-wire and Hopkins phantoms, data was taken from three far sides and from top.) On each scanned side, 6 to 10 runs were performed at different angles between the probe and the tank. The US probe was moved slowly, in order to acquire a high number of scans in each run. Depending upon the type of phantom scanned, each run had the number of images ranging from 50 to 200. (In case of the cross-wire phantom, an especially large number of images were needed, because the intersection of

wires is not clearly visible in every image. Typically, we had to combine about 25 consecutive images to yield one reliable intersection point.)

### 5.3.4 Feature extraction

Once the large amount of raw data was collected, we needed to extract all useful information from it. Within each frame, an FOB reading was also taken at that very instant and was stored, providing us with time-stamped, spatially correlated ultrasound images. By careful examination of all these images, the points of interest were segmented out, the pixel coordinates were noted, and a link was created between the pixel values and the corresponding FOB reading. These bundles were collected into a single file and later fed to the numerical optimization program. For example, in the case of the cross-wire phantom, over 4400 images were processed manually for usable wire intersection points. This phase alone took about over 100 person-hours to complete. In order to aid this tedious and inherently error-prone process, a semi-automated method was created which automatically stored and logged the feature points that were manually selected with a mouse click. This seemingly minor infrastructural enhancement significantly reduced the amount manual labor and work time, decreasing in turn the likelihood of human operator error. Ideally, we would like to achieve fully automated image processing, when all feature points are segmented out by software without human intervention. In this approach, one would apply a chain of filters to remove speckle and other artifacts as much as possible, and then geometric constraints would guide the segmenter to the true feature points. Unfortunately, the cross-wire, three-wire, and single-wall phantoms do not allow for automated image processing, because the simple geometry of the phantom does not provide sufficient constraint for the feature tracker. Taking the crosswire image as an example (Figure 5.1- left), the feature does not have consistent echogenicity. This happened mainly because of the beam width effect. In other words, the appearance

(echogenicity) of the crosswire depends on many parameters, such as US power, time gain control settings, depth, US probe type, lateral resolution, axial resolution, and most importantly beam width. If the crosswire happens to be in the middle of the beam width, there should be more confined echo compared to the case at the beam edges.

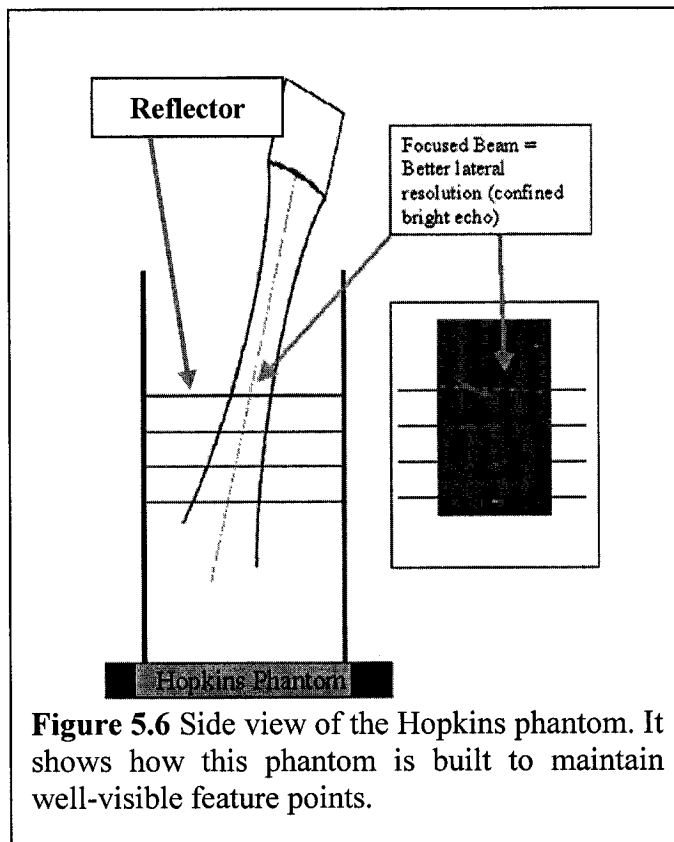


**Figure 5.6** Side view of the Hopkins phantom. It shows how this phantom is built to maintain well-visible feature points.

In order to overcome this problem, the Hopkins phantom is designed in such a way that each reflector would cross the width of the beam from side to side with any angle of insonation (Figure 5.6). This will form a brighter spot for each reflector, where the size of this spot depends primarily on the width of the beam (the amount of focusing), and later on resolution as a function of depth. Figure 5.6 shows that the upper reflector produced a small bright echo because we have a good focusing zone (small beam width), and usually

better lateral resolution at the shallow depth. On the other hand, the lower reflector produced a larger spot in the axial direction due to the larger beam width and in the lateral direction mainly because of poor lateral resolution at the far zone. This is one of the prominent features of the Hopkins phantom that allows for fully automated feature extraction in a reliable and repeatable way.

### 5.3.5 Verification on synthetic data

After the feature points were extracted from the images, the data was processed by running a numerical optimization algorithm to obtain the values of the unknown calibration matrix. As the problem is inherently non-linear in behavior with a large residual error, we decided to use the Levenberg-Marquadt method for non-linear least squares optimization. The code was written in Matlab, where the basic numerical functions were directly available. The authors generated synthetic input to check whether the optimization code was working correctly. They roughly estimated the value of  ${}^R T_P$  and  ${}^C T_T$  matrices with a common ruler. Then they extracted about 50 images from the precollected dataset with their corresponding  ${}^T T_R$  transformation matrices. Utilizing  ${}^R T_P$ ,  ${}^C T_T$ , and  ${}^T T_R$  into the  $P_x = [{}^C T_T \ {}^T T_R \ {}^R T_P]^{-1} C_x$  formula yielded a set of  $P_x$  points, the synthetic input data, in the image pixel frame. Using this input and the corresponding known  ${}^T T_R$  matrices into the optimization code the result was almost the same  ${}^R T_P$  and  ${}^C T_T$  as those used for generating the synthetic data. The difference between these transformations was a negligible residual error left at the end of the optimization.

### 5.3.6 Initial guess

Non-linear optimization works the best if the algorithm starts from a good initial guess of the final solution, otherwise the algorithm may get trapped in a mirror solution or in a local minimum. A good initial estimate typically turns the optimization into a low

residual error problem, which then glides quickly and smoothly to its true solution. It is therefore quite important to have a good initial guess for the 14 unknowns incorporated in  ${}^R T_P$ ,  ${}^C T_T$ ,  $S_x$ , and  $S_y$ .

The simplest case was  $S_x$  and  $S_y$ , because the approximate pixel scale factor was a priori known for the given Aloka SSD1400 US machine within a given set of scanning parameters, such as beam penetration depth. The value of the scale factors was 21 pixels per one centimeter uniformly in both directions, resulting  $0.04878\text{cm}^{-1}$  for both  $S_x$  and  $S_y$ .

The orientation of the FOB transmitter has no bearing on the experiment, so we were free to align it in a way that was convenient with respect to the construction frame, so that the  ${}^C T_T$  would have a known rotational component or no rotation at all. Then the approximate values of the translational component of  ${}^C T_T$  could be measured with a ruler or a calibrated tracked pointer.

There is also a similarly simple way to estimate the six values in  ${}^R T_P$ . Early in the construction phase of the system, we tried to align the FOB receiver symmetrically on the probe and without rotation. Therefore, the estimated  ${}^R T_P$  has only three translation components and no rotation. We were able to measure with a ruler the position of the FOB receiver from the ultrasound transducer, and then the position of the transducer with respect to the origin of the image pixel frame could be approximately determined from the images.

Another alternative to get an estimate of  ${}^R T_P$  is shown in Figure 5.7. Vector ‘ $a$ ’ is determined by using a calibrated tracked pointer to touch down the crosswire and record the reading. Then, capture any US image that contains the crosswire, and record the  ${}^T T_R$

as shown in Figure 5.7. The  $(u, v)$  image pixel coordinates of the crosswire were read out from the image. From here, using  $S_x$  and  $S_y$  pixel scale factors, the  $(u, v)$  image pixel coordinates, and the plane normal, the  $P$  origin of the image pixel frame could be determined in the FOB transmitter frame. This resulted in a closed-loop of transformations, from which obtaining  ${}^R T_P$  was insignificant.

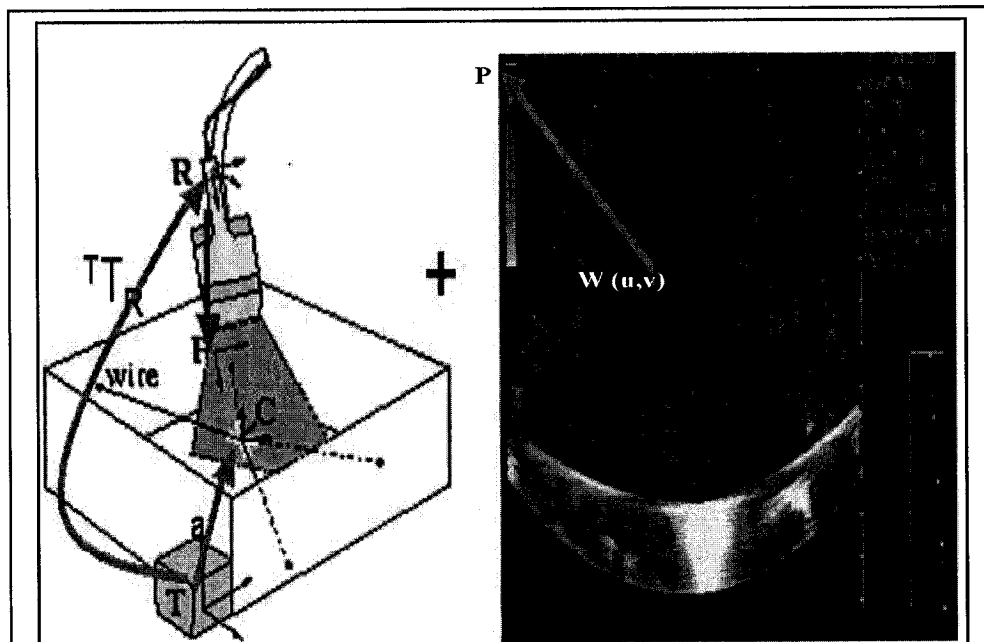


**Figure 5.7** Finding the initial guess for  ${}^R T_P$ .

## 5.4 Results and Discussion

We first investigated whether the multisided tank can provide significant improvements using both current calibration methods and the new Hopkins phantom. The results were analyzed to measure the extent of improvements in terms of accuracy of the calibration process and/or the needed number of images to maintain that level of accuracy. Next, we compared the Hopkins phantom and calibration method to the cross-wire phantom that is one of the most commonly used methods. The cross-wire method has been documented

to be more accurate than the also popular three-wire and single-wall methods [Prager-1998b].

As we have previously mentioned, accuracy and precision measures are needed to analyze all these results and draw conclusions. A straightforward way to measure precision is to compute a number of calibration matrices with a given method and then to calculate descriptive statistics (mean, standard deviation, and range) for each variable in the calibration matrix. Ideally, the experiments should produce an identical calibration matrix with each repetition. Using this method of measuring the precision would require significant time, repeating the same calibration method many times. A more realistic measure of the precision method would be to map a fixed point in space from its position in the US image space to the receiver's space using the derived calibration matrix, then to analyze the variability of this point in receiver space, in terms of mean, standard deviation and range of motions. Ideally, the point in receiver space should remain stationary with zero error, regardless of the position and insonation angles of the phantom. The cross-wire phantom is used for this precision test by insonating the crosswire point (fixed point) from different views, using a previously obtained  ${}^R T_P$  calibration matrix. We obtained  ${}^R T_P$  from either the Hopkins or the cross-wire phantom.

In each reconstruction, the crosswire point appeared as a cloud of at least 36 views (one crosswire point per view) collected from at least three sides of the tank, with 12 images on each side. The precision of reconstruction is then measured by evaluating the "tightness" of this cloud. The difference in position is calculated as observed from all possible combinations of two views out of all views, at least 630 combinations in each case, as follows:

$$\Delta^T \vec{x} = {}^T T_R^{view\ 1\ R} T_p^P \vec{x}^{view\ 1} - {}^T T_R^{view\ 2\ R} T_p^P \vec{x}^{view\ 2},$$

$${}^P \vec{x}^{viewi} = \begin{pmatrix} S_u \times u^{viewi} \\ S_v \times v^{viewi} \\ 0 \\ 1 \end{pmatrix}.$$

Where,  $S_u$  and  $S_v$  are the pixel ratios and  $(u, v)^{viewi}$  is the crosswire position in the US space. Therefore, the magnitude of  $\Delta^T \vec{x}$  reflects the precision of reconstructing the crosswire point. We have calculated this measure from all possible combinations of the 36 views.

Direct measurement of calibration accuracy is not as straightforward as of precision measurement, because the true calibration matrix is not known. One possible approach is to use synthetic sequences based on a known calibration and to generate synthetic images with speckle noise for calibration [Rousseau-2002]. This method checks the accuracy of the calibration process compared to a known matrix, however, it is a simulated process and it does not use real US images that have different lateral and axial resolutions, beam width, side lobes, and speckle noise. In our approach, the Hopkins phantom plays a dual role, serving as a calibration phantom and as a reconstruction accuracy measurement tool at the same time. The nylon reflectors in the Hopkins phantom are separated by 1cm in one axis and 2cm in the other axis with 0.01mm machining accuracy and possible 100μm for assembling accuracy. The idea is to scan these reflectors with different insonation angles from different sides of the tank, and then to reconstruct them in tracker space. The next step is to measure the inter-distances between these reflectors to see the extent of deviation from the trusted 1cm and 2cm values (Figure 5.8).

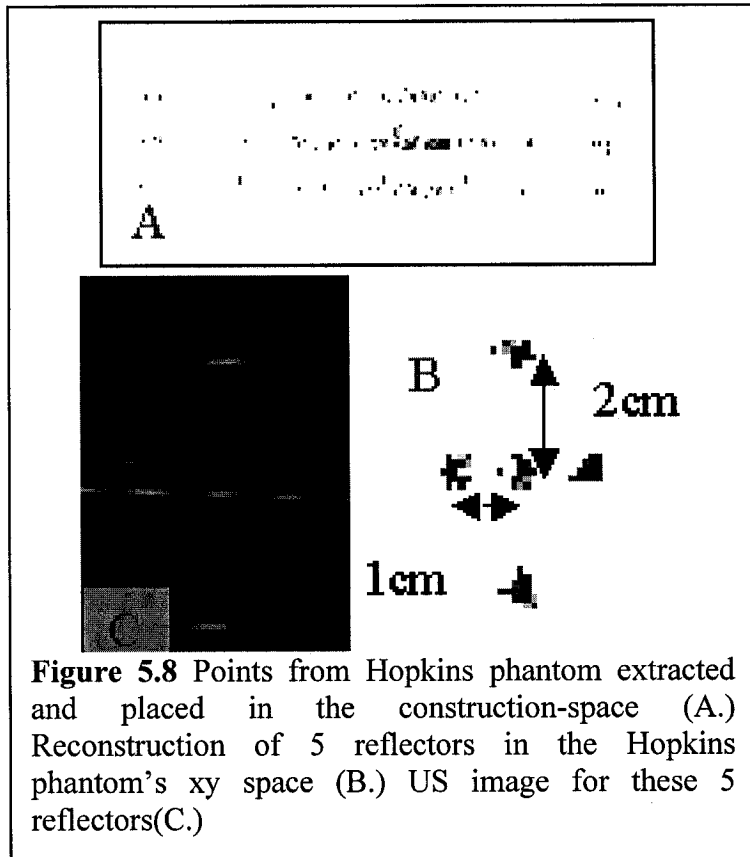


**Figure 5.8** Points from Hopkins phantom extracted and placed in the construction-space (A.) Reconstruction of 5 reflectors in the Hopkins phantom's xy space (B.) US image for these 5 reflectors(C.)

#### 5.4.1 Results with the multisided tank

To quantify the suspected benefits of the multisided tank, we have conducted series of experiments on both the Hopkins and cross-wire phantoms. For both, three different solutions have been extracted based on the following datasets:

- Top side only, including 227 points for Hopkins phantom and 36 points for cross-wire phantom.
- All sides with three times the data acquired from the top side, as shown in Figure 5.4, yielding 704 points for the Hopkins phantom and 119 points for the cross-wire phantom.
- All sides with the same number of data points as the single top side case.

Table 5.1 shows the resulting calibration matrices using both phantoms for the acquisition scenarios listed above. The lower portion of the table discusses the reconstruction accuracy analysis that we conducted on every calibration matrix. The table includes numbers for reconstruction accuracy, within mean value, standard deviation and min-max range. The mean value is the average difference between the true (1cm and 2cm as shown in Figure 5.8) and the calculated inter-distances of the two reflectors taken from all possible views, representing the amount of misregistration in reconstruction space.

Unknowns	Hopkins phantom				cross-wire phantom			
	Topside (n=227)	All sides (n=220)	All sides (n=230)	All sides (n=704)	Top side (n=36)	All sides (n=36)	All sides (n=119)	
X (cm)	9.3387	9.4771	9.6347	9.7104	9.8440	9.4190	9.5385	
Y (cm)	13.0277	12.6659	12.6267	12.9159	12.6467	13.1486	12.8696	
Z (cm)	12.5079	11.7709	11.3023	11.4596	11.1253	11.1541	10.8402	
A (rad)	-1.6505	-1.6374	-1.6465	-1.6516	-1.6614	-1.6598	-1.6572	
B (rad)	0.0883	-0.0387	-0.0022	-0.0105	0.0255	-0.0127	0.0018	
$\Gamma$ (rad)	0.0109	0.0010	0.0181	0.0190	0.0628	0.0025	0.0514	
S <sub>x</sub> mm/pxl	0.0480	0.0479	0.0476	0.0482	0.0473	0.0492	0.0483	
S <sub>y</sub> mm/pxl	0.0476	0.0479	0.0477	0.0479	0.0471	0.0496	0.0488	
Reconstruction accuracy analysis applied with 1cm and 2cm inter-distance reflectors								
	1cm	2cm	1cm	2cm	1cm	2cm	1cm	2cm
Mean mm	-1.38	-0.40	-0.279	-0.184	-0.185	-0.083	-0.200	-0.259
STD mm	3.496	5.215	1.7847	2.0772	1.7631	1.9306	1.6790	1.5829
Min mm	6.804	10.46	5.7621	5.6484	3.7141	5.3666	4.6066	6.5533
Max mm	-10.8	-10.6	-6.602	-6.194	-5.764	-6.863	-5.360	-5.179
	1cm	2cm	1cm	2cm	1cm	2cm	1cm	2cm

**Table 5.1** Multisided tank analysis. The upper table shows estimated calibration matrices and pixel ratios by Hopkins and cross-wire methods under different trials. These trials are based on spatial coverage of scanning (top side vs. multiple sides). The lower table shows the error statistics with the 1.0 and 2.0cm inter-distance reflectors in the Hopkins phantom.

The standard deviation represents the uncertainty of reconstruction accuracy. Observing all, but especially the mean and STD values, it is obvious that calibration with the

multisided tank substantially enhances accuracy of calibration, regardless of whether the Hopkins or the cross-wire phantom is used. For example, the standard deviation in the Hopkins phantom dropped from 5.2 to 1.5 between the “Top side N=227 points” and “All-sides N=704 points” cases. Using the same number of data points, collected evenly from multiple sides of the tank, produces very good and reliable results. Taking the cross-wire phantom as an example with 1cm reflector distance, the STD is in the order of 2.1-2.2mm using data from all sides of the tank, as opposed to 3.2mm using for the top side data only and even regardless to dropping the number of points from 119 to 36.

An average image of the Hopkins phantom yields 20 data points. This means that a highly reasonable set of 220 points could be collected from just 10 to 12 images, which is sufficient to produce a very accurate calibration matrix if the images are collected from all sides of the tank. Altogether, using the Hopkins phantom with the multisided tank, just 3 to 4 images collected from each side can produce a very accurate calibration matrix. Furthermore, the optimization framework remains stable even with fewer images and data points. For example, the condition number of the Jacobian matrix in Levenberg-Marquardt method near to the solution remains bounded at about 150 while using only 80 points (3 to 4 images) collected from all sides combined, as shown in Figure 5.9.

#### **5.4.2 Comparison of the Hopkins and the cross-wire phantoms**

We have applied two different analytical techniques to compare the accuracy of the Hopkins and cross-wire phantoms. These techniques improve precision accuracy of the reconstruction accuracy, as we alluded to in the beginning of the “Result and Discussion” section. For normalization, we used manual feature extraction for both methods, and acquired multisided data for both phantoms.

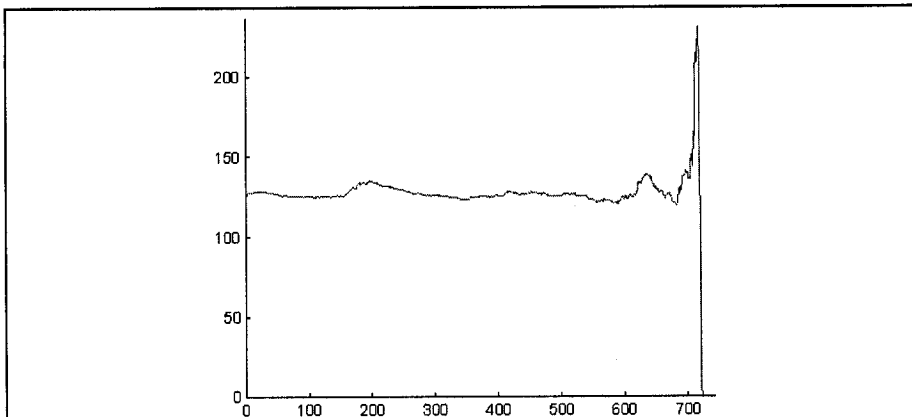


**Figure 5.9** Condition number stability. The vertical-axis is the condition number while the horizontal-axis is the number of points dropped from the optimization (total are 720 in this case). It shows that the condition number remains stable to the 600 level, which means 80-100 points is enough to make the system well conditioned.

Table 5.2 shows two reconstruction accuracy analysis trials for Hopkins and cross-wire phantoms, both indicating the superiority of the Hopkins method in terms of the mean error of reconstruction accuracy, while the standard deviation is almost the same for both.

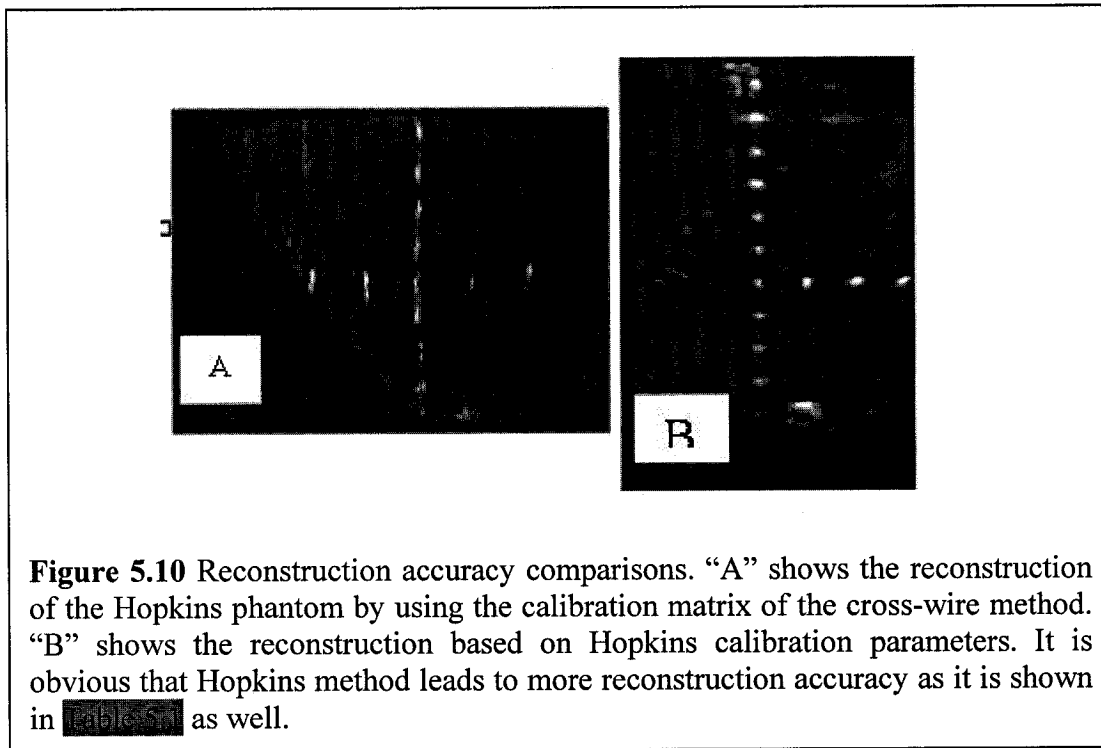
	Trial #1				Trial #2			
	Hopkins		cross-wire		Hopkins		cross-wire	
	1cm	2cm	1cm	2cm	1cm	2cm	1cm	2cm
Mean(mm)	-0.1472	0.0041	-0.1726	-0.1038	-0.2000	-0.2585	-0.3102	-0.4083
STD (mm)	1.0806	2.1857	1.2437	1.9010	1.6790	1.5829	2.1764	1.7811
Min (mm)	3.7318	8.5480	5.3191	5.5081	4.6066	4.6066	5.0594	4.4829
Max (mm)	-3.2152	-5.1998	-4.4075	-6.3755	-5.3604	-5.1786	-6.8606	-7.2443

**Table 5.2** Comparison between the Hopkins phantom and the cross-wire phantom based on reconstruction accuracy measures.

Table 5.3 shows the results of reconstruction precision experiments and illustrates that both phantoms are in the same order of precision. Figure 5.10 is a visual realization of reconstruction accuracy tests. It can be seen clearly that Hopkins method reconstructs the acquired data and registers them in the construction space more accurately.

	<b>Trial #1</b>		<b>Trial #2</b>	
	<b>Hopkins</b>	<b>cross-wire</b>	<b>Hopkins</b>	<b>cross-wire</b>
<b>Mean(mm)</b>	0.8376	0.7732	0.6053	0.4681
<b>STD (mm)</b>	0.3950	0.3451	0.2828	0.2260
<b>Min (mm)</b>	0.0287	0.0332	0.0180	0.0195
<b>Max (mm)</b>	2.4228	2.0373	1.7882	1.3744

**Table 5.3** Comparison between the Hopkins and cross-wire phantoms, based on reconstruction precision measures.



### **5.4.3 Hopkins automatic calibration toolkit (UltraCal)**

Several different methods of ultrasound calibration have been presented over the years. Most methods which are commonly used today consist of a non-linear least squares problem, which results from the registration of the ultrasound image with one of a number of different phantoms. Though the methods of calibration are well understood, details of implementation are often left up to the individual researcher. For example, outliers are a persistent obstacle to an accurate ultrasound calibration, but defining which data points are outliers is not necessarily straight forward.

Certain packages exist that provide an interface for ultrasound calibration, but these systems are not open to be modified or extended. Thus, a researcher intending to perform a new calibration procedure would have to program one from scratch, presenting a problem to those who are not inclined to do such programming.

In an effort to counter this, and to stimulate further research using ultrasound, we have built CIS-UltraCal<sup>†</sup>, a toolkit that incorporates many of the current ultrasound calibration methods. Ultrasound calibration typically requires a development of a complicated software component that can be a hindrance to researchers. By providing a highly-modular open-source system, we hope to make ultrasound calibration research more accessible, preventing researchers from having to start from scratch.

CIS-UltraCal toolkit can semi-automatically process cross-wire, single-wall, and fully automatically Hopkins phantoms. The tool-kit also has an easy to use GUI interface

---

<sup>†</sup> This project started from my work on cross-wire, single-wall and Hopkins calibration methods. Then, Kishore Kothapalli conducted a qualifying project under supervision of Prof. Hager to segment automatically Hopkins phantom features. Next, I supervised an CIS-II project done by Ryan Kon and Joshua Leven to integrate all the work done in a matlab-based toolkit for US calibration, called CIS-UltraCal [Kon-2005].

where one can add or modify to the results given by the built-in segmentation. Details of this package can be found in Appendix B.

## 5.5 Conclusions

Our experiments proved that the introduction of a multisided tank improves the speed and accuracy of the calibration process in several aspects. The new Hopkins phantom provides a large number of data points from only a few images. The calibration matrix can be obtained accurately after collecting only 10 to 12 images, even without a good initial guess. Due to its design and construction, the Hopkins phantom allows for static tracking. The content and quality of images allow for fully automated calibration [Kon-2005].

Despite the manifold advantages of this method, we were left with several questions including; how to define the type of motions and to estimate the necessary number of poses that maximizes the accuracy. These questions steer our research utilizing novel closed-form formulations that will be discussed in details in Chapters 6 and 7.

## **Part-II: Chapter 6**

# **Ultrasound Calibration Using Closed-form Formulation**

### **6.1 Introduction**

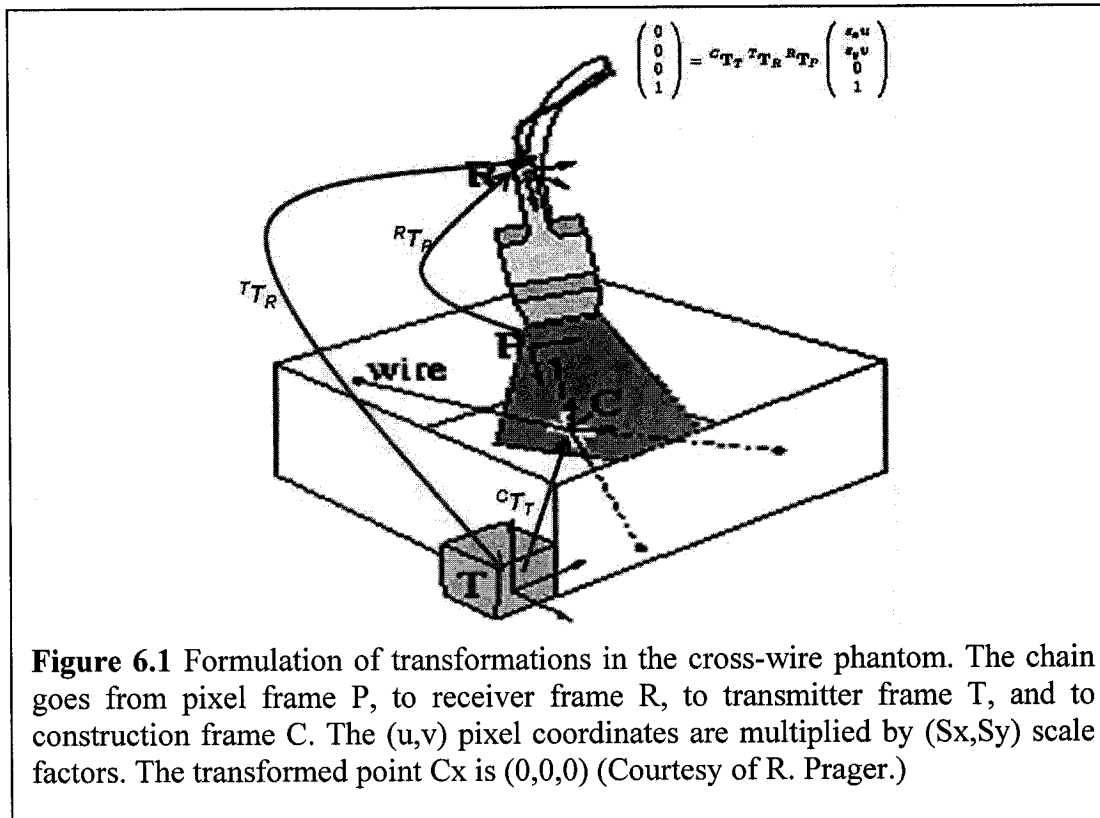
As we mentioned earlier, significant research has been dedicated to quantitative tracked ultrasound which requires tracking the US probe in 3D space with respect to a stationary frame of reference. Tracking is typically achieved by rigidly attaching 3D localizers to the US probe. . The spatial transformation between the US image pixels and the tracking body attached to the US probe must be evaluated through calibration process. Hence, calibration is ubiquitously present in all systems where ultrasound is used for quantitative image guidance. Accuracy of calibration is the most significant factor for accurate tracked US systems and therefore it is a logical imperative to minimize calibration error.

In all currently known calibration processes, including Hopkins method presented in Chapter 5, an object of known geometrical properties (a.k.a. phantom) is scanned by the tracked US probe and then various mathematical procedures are applied to determine the unknown transformation that maximizes the similarity between the US images and the actual phantom. Geometrical phantoms based on points [Detmer-1996, Carr-1996, Prager-1998b, Pagoulatos-2001, Boctor-2003c, Boctor-2004d, Viswanathan-2004, Muratore-2001] and planes [Rousseau-2002, Boctor-2003c, Prager-1998b, Viswanathan-2004] have been developed and compared to each other to determine optimal accuracy

and performance [Prager-1998b, Boctor-2003c]. The cross-wire and three-wire phantoms require a large number of images and are hard to automate, while the single-wall phantom, such as the Cambridge phantom [Prager-1998b] and the Hopkins method [Kon-2005] are more automatic, repeatable methods. Typically however, all of these phantoms are very complex to create and to use in calibration. These complex phantoms also require segmentation of numerous points per each individual US image. Figure 6.1 shows a typical formulation for the coordinate systems required for the most of the previously mentioned phantoms. There is error associated with each stage of the calibration process (typically phantom fabrication, image acquisition, spatial co-registration, image processing, formulation of transformations, and numerical optimization solution) which aggregate and may induce a prohibitively large final error in the calibration by landing unavoidable non-global minimum. According to Hsu and Prager [Hsu-2006], convergence to global minimum only takes place more than 50% of the time. Thus, they repeat the optimization 50 times at different starting points and pick the solution with the lowest residual error. This would make the probability of getting a non-global minimum about 1 in  $10^{15}$ . In addition to this limitation, there are few questions we could not answer easily given the aforementioned non-linear optimization (Figure 6.1) method:

- 1) What are the minimum number and type of motions that maximizes the accuracy?
- 2) Is it easy to find a closed-form equation that relates directly the accuracy of the calibrated parameters to the uncertainty of the tracker and US imaging? In other words, finding a direct asymptotic accuracy measurement, instead of the indirect reconstruction accuracy methods.
- 3) Is it possible to perform the calibration immediately, in one second?
- 4) Is it possible to perform the calibration online during the intervention?

Because of these and other questions, we steered our research in this area to utilize a closed-form formulation, which we discuss in the following section.



## 6.2 Closed-form Formulation

Our closed-form formulation was inspired by mapping the US calibration problem to the well known Hand-Eye calibration problem in the fields of robotics and computer vision [Tsai-1989, Shiu-1989, Chou-1991, Chen-1991, Wang-1992, Horaud-1995, Daniilidis-1996]. In our closed-form formulation, we still image a calibration phantom submerged in water bath. We will demonstrate that the complexity of the phantom is minimal and the number of images required for calibration is remarkably low (3-6 frames) compared with standard calibration phantoms. Figure 6.2 presents the coordinate systems for

mathematical formulation.  $A_1$ ,  $A_2$  are the transformations of the US image coordinate system ( $P$ ) with respect to the fixed reconstruction coordinate system ( $C$ ) at poses 1 and 2, respectively.

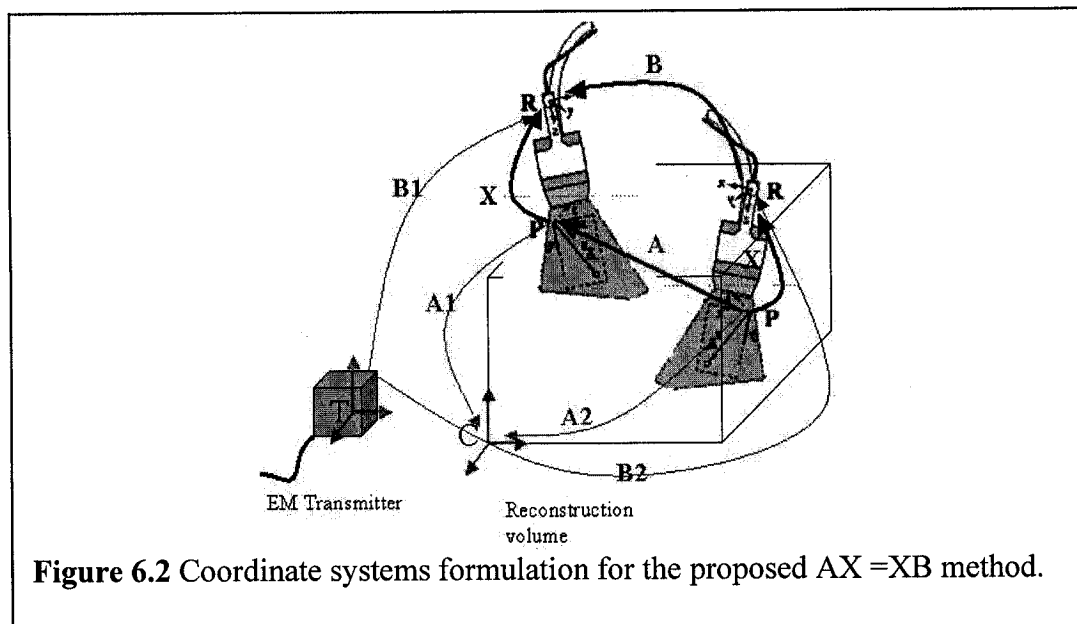


**Figure 6.2** Coordinate systems formulation for the proposed  $AX = XB$  method.

2, respectively. The actual selection of  $C$  is arbitrary and the only requirement is that it must be rigidly fixed during the calibration process.

Using  $A_1$ ,  $A_2$ , we obtain the transformation between poses 1 and 2, as  $A = A_2 A_1^{-1}$ . At the same time, the transformation between the two poses can be recovered by using a calibration phantom or phantom or recovered directly by matching the 2D ultrasound images acquired in these poses to a prior 3D model of the phantom object. To determine the matrix  $A$ , we focused on a strategy that minimized the complexity of our imaging phantom.  $A_1$ ,  $A_2$  are the relative transformations between each of our imaging phantoms.  $B_1$ ,  $B_2$  are the tracking device readings for the sensor frame ( $R$ ) with respect to tracker reference frame ( $T$ ) at poses 1 and 2 respectively. Again, the relative pose between sensor frame ( $R$ ) at pose 1 and 2 is given by  $B = B_2^{-1}B_1$ . This yields the following homogeneous matrix equation:

$$AX = XB \quad (6.1)$$

Where  $A$  is estimated from images,  $B$  is assumed to be known from the external tracking device, and  $X$  is the unknown transformation between the US image coordinate system and the sensor frame ( $R$ ). The estimated US image frame motion in general is given by:

$$A(\lambda) = \begin{pmatrix} & & \lambda_x \cdot u_{ax} \\ R_a & & \lambda_y \cdot u_{ay} \\ 0 & 0 & 0 \\ & & \lambda_z \cdot u_{az} \\ & & 1 \end{pmatrix} \quad (6.2)$$

Where  $R_a$  is the rotation of the US image frame between pose 1 and 2,  $\lambda$  is the unknown scale factor vector that relates the translation vector  $u_a$  in voxel space (3DUS, CT, or MRI) to the US image frame translation vector  $t_a$  (in mm) such that:

$$t_a = \begin{pmatrix} \lambda_x u_{ax} \\ \lambda_y u_{ay} \\ \lambda_z u_{az} \end{pmatrix} = \begin{pmatrix} u_{ax} & 0 & 0 \\ 0 & u_{ay} & 0 \\ 0 & 0 & u_{az} \end{pmatrix} \cdot \begin{pmatrix} \lambda_x \\ \lambda_y \\ \lambda_z \end{pmatrix} = D_{ua} \lambda. \quad (6.3)$$

It is important to account for the most general case where the scale factor  $\lambda$ , which converts from voxel space to metric coordinates, is not known. Such a scenario could happen if “ $A$ ” is recovered by registering the US image to a prior acquired model in voxel space. From the homogeneous equation (6.1) and using (6.2), one obtains:

$$R_a R_x = R_x R_b \quad (6.4)$$

$$R_a t_x + D_{ua} \lambda = R_x t_b + t_x \quad (6.5)$$

In the linear formulation of the problem we will use the linear operator  $vec$  and the *Kronecker product* ( $\otimes$ )[Brewer-1978]. Using the following fundamental property of the Kronecker product:

$$\text{vec}(CDE) = (C \otimes E^T) \text{vec}(D) \quad (6.6)$$

One can rewrite (6.4) and (6.5) into:

$$(R_a \otimes R_b) \text{vec}(R_x) = \text{vec}(R_x), \quad (6.7)$$

$$(I_3 \otimes t_b^t) \text{vec}(R_x) + (I_3 - R_a)_x - D_u \lambda = 0 \quad (6.8)$$

From (6.7) and (6.8), we can transform the whole problem ( $AX=XB$ ) into a single homogeneous linear system:

$$\begin{bmatrix} I_9 - R_a \otimes R_b & 0_{9*3} & 0_{9*3} \\ I_3 \otimes t_b^t & I_3 - R_a & -D_u \end{bmatrix} \begin{pmatrix} \text{vec}(R_x) \\ t_x \\ \lambda_{3*1} \end{pmatrix} = \begin{pmatrix} 0_{9*1} \\ 0_{3*1} \end{pmatrix} \quad (6.9)$$

The solution for this homogeneous linear system could be given by finding the null space, which is a subspace in  $R^{15}$ . Then the unique solution could be extracted from the null space using the unity constraint to the first 9 coefficients representing the  $R_x$ . However, another approach can be achieved by solving the system in two steps: first extract the rotation and scales, and then solve for the translation. The complete algebraic analysis for the “Hand-Eye” problem (where the scale factor is assumed to be constant in three direction) is given in [Andreff-2001, Tsai-1989], where it is proved that two independent motions with non-parallel axes are sufficient to recover a unique solution for  $AX=XB$ . We have extended this solution method to account for inhomogeneous scale in the three coordinate axes. Detailed algebraic analysis for the general scale factor is included in Chapter 7.

In addition of identifying the set of motions that are necessary and sufficient to calibrate the system, one can easily conduct error propagation analysis and finds direct asymptotic accuracy measures, as shown in Appendix C. In the coming section, we will describe three different experimental embodiments based on this formulation.

### 6.3 Calibration Methods and Protocols

#### 6.3.1 The modified Hopkins phantom

The calibration setup, shown in Figure 6.3, consists of a transparent plastic water tank, in which we can scan the submerged phantom not just from the top, but also from all four sides of the tank through rubber windows [Boctor-2003c]. We use a linear array (7.5 MHz) US probe with a rigid attachment containing optical markers tracked by an

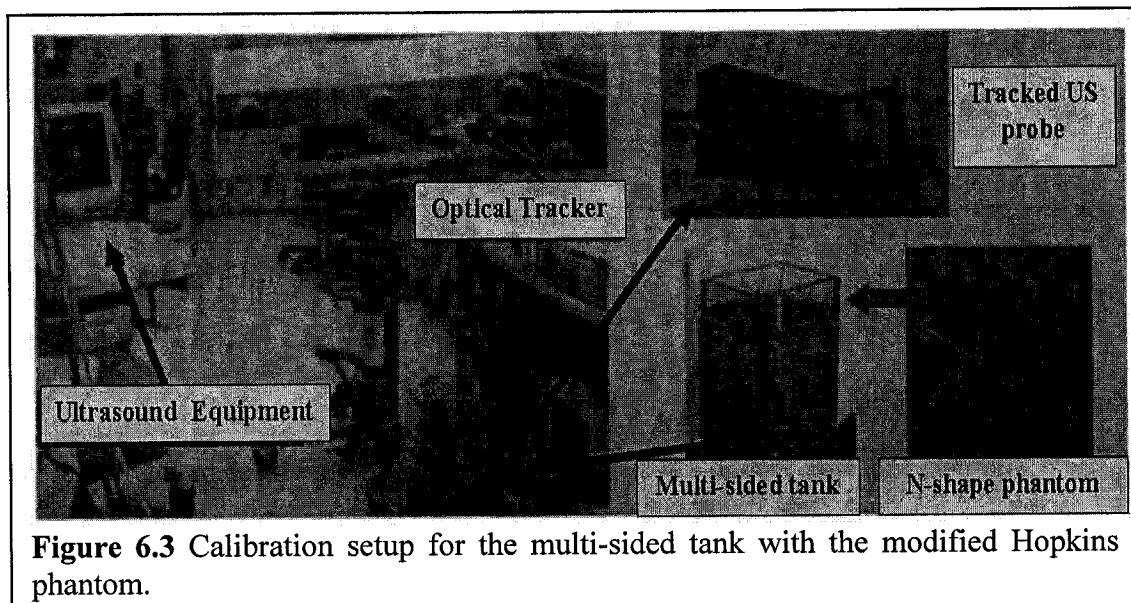


**Figure 6.3** Calibration setup for the multi-sided tank with the modified Hopkins phantom.

Optotrak. The actual phantom is the Hopkins phantom described in Chapter 5 with an additional matrix of N-shape wires stretched between two parallel plates. The phantom is oriented in the multi-window tank in an oblique position so that the structure can be

scanned through two opposite windows and the top, with a plurality of wires visible from each image. Similar to the work of Pagoulatos [Pagoulatos-2001], an additional group of vertical N-shape fiducials has been added to his original design and utilizes an algorithm to select the image points and to relate them to points on the physical phantom space.

In relating the phantom space coordinate system to the ultrasound image space, the N-shape wires provide 3 points (ellipses) for each N-shape fiducial. In Figure 6.4, E, K and Z are the 3 points that would be seen in the ultrasound image while points A,C and B,D represent points where the wire intersects the parallel plates. Using triangle similarity and a priori knowledge of the vertices in phantom space, the x and y coordinates of the center image point of the N-shape fiducial can be computed. The location of this point K in phantom space is extracted as follows:

$$x_k = x_b + \left( \frac{KE}{EZ} \right) * (x_c - x_b)$$

$$y_k = y_b + \left( \frac{KE}{EZ} \right) * (y_c - y_b)$$

The transformation between the ultrasound image space and phantom space is then determined by using Horn's quaternion rigid registration method [Horn-1987].

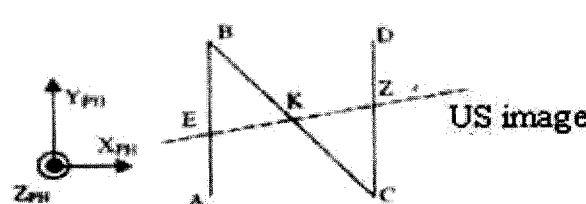


**Figure 6.4** The N-shape phantom helps in extracting the pose between the US image plane and the phantom space, “A<sub>1</sub> transformation.”

The aforementioned phantom and method is a direct implementation of the  $AX=XB$  formulation. The modified Hopkins phantom, however, is not easy to build and also requires careful data collection and processing. This prompts us to build another phantom that is effortless to assemble, maximizes accuracy with a minimum number of poses, and requires negligible image processing, reporting the calibration immediately. The next Sections 6.3.2 and 6.3.3 will describe a new phantom called the thin-plate phantom and a modified version of this phantom based on double-wedge fiducials.

### 6.3.2 The thin plate phantom

Originally, we introduced the above closed-form formulation using a modified N-shape phantom [Boctor-2004d], called modified the Hopkins phantom, which is tedious to build and to process. Therefore, we have replaced the z-phantom with an easier design, build, and process as shown in Figure 6.5 [Viswanathan-2004]. In our experimental setup, we used the SONOLINE Antares US scanner (Siemens Medical Solutions USA, Inc. Ultrasound Division, Issaquah, WA) with a Siemens VF 10-5 linear array probe held in a rigid attachment mounted on an adjustable arm. The adjustable arm is used to adjust the

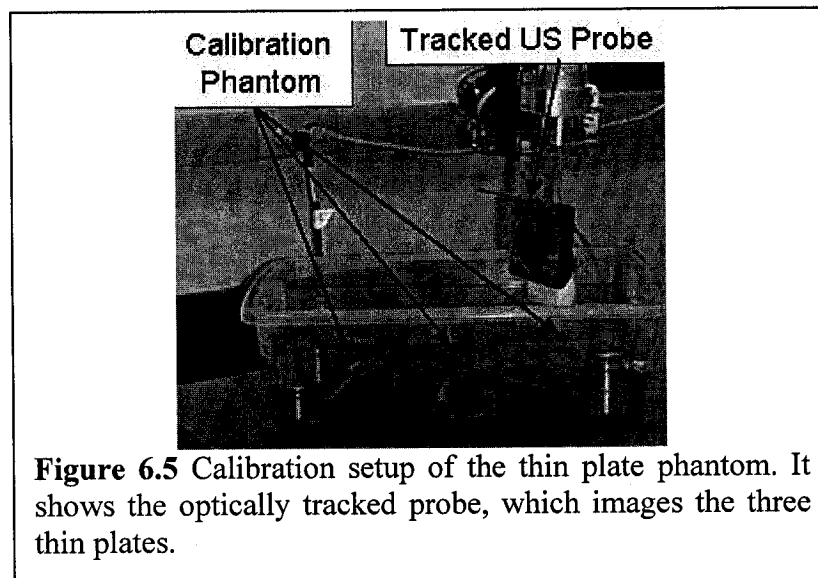


**Figure 6.5** Calibration setup of the thin plate phantom. It shows the optically tracked probe, which images the three thin plates.

spatial position of the tracked US probe to image the calibration phantom. Multiple optical markers were attached to the probe holder, which then were tracked by an OPTOTRAK device (Northern Digital Inc.). The calibration phantom was submerged in a transparent plastic water tank. The calibration phantom consisted of three identical thin (4mm) plastic plates of irregular shape. The candidate feature from this phantom is simply a single point on a line that can be easily detected by a wide variety of probes and depth settings. The plastic plates were machined together to ensure their congruency. The plates were positioned on a flat surface and fixed in place using Lego blocks and permanent glue for support, as seen in Figure 6.6. Using an optical pointer, we collected 3D points of each of the plates for offline processing. The pointer was pivoted about each digitized point in order to obtain an accurate estimate of the desired 3D point as shown earlier in Figure 6.4. These 3D points are registered to provide a local coordinate system for each of the thin plates. From the local coordinate systems, one can calculate the relative transformations between each pair of plates.

The poses of the three plates were carefully arranged in order to give optimal results for the two motions required by the  $AX=XB$  formulation, based on previous simulations and supporting literature [Tsai-1989, Shi-2005]. According to the following observations in [Tsai-1989]:

*Observation 1.* The RMS error of rotation from gripper (Sensor) to camera (US probe) is inversely proportional to the *sine* of the angle between the interstation (motion) rotation axes (denoted by  $\sin(\alpha)$ ).

*Observation 2.* The rotation and translation error are both inversely proportional to the interstation (motion) rotation angle (denoted by  $\beta$ ).

From these observations and a numerical simulation, we built the thin-plate phantom to allow big angular motion ( $\beta = 60\text{-}90$  degrees) and large motion axes separation ( $\sin(\alpha)=1$ , hence  $\alpha=90$  degrees.)

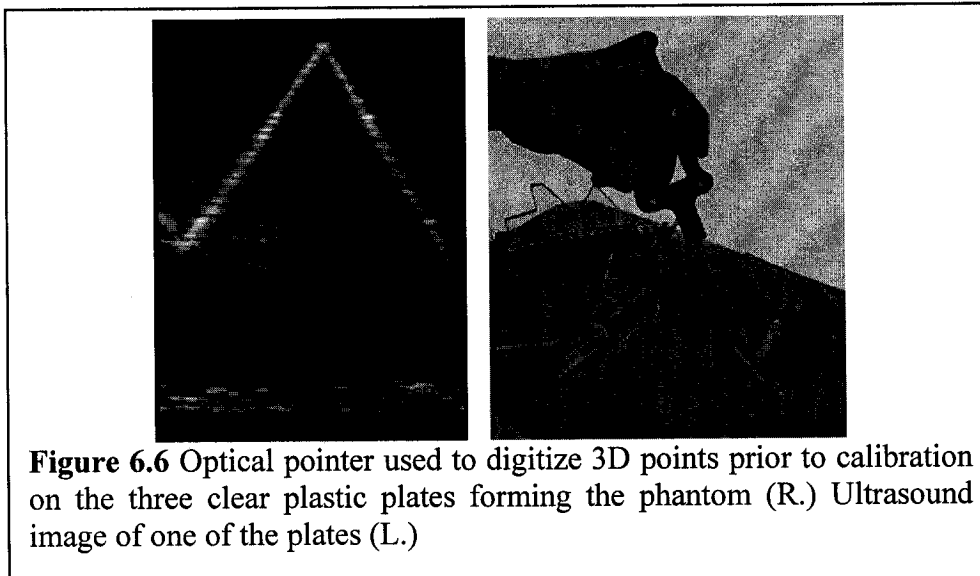


**Figure 6.6** Optical pointer used to digitize 3D points prior to calibration on the three clear plastic plates forming the phantom (R.) Ultrasound image of one of the plates (L.)

In conventional US probe calibration research, arrays of wires have been used to establish the relationship between the coordinate systems of the US and the tracking device. This approach typically involves laborious segmentation to extract the wire points in the US images and then to relate these points to the tracking device coordinate system. In this work, we take a different approach by computing  $A_1$  and  $A_2$ , first by locating prominent feature points of the plates in the US images and then by using an optical digitizer (Figure 6.6) to compute the relative transformation between the plates. We tested two protocols for computing the  $A_1$  and  $A_2$  matrices for our thin plate calibration phantom:

- Move the US tracked probe so that the probe is parallel to the thin plate and the image plane of the US image shows the middle of the thin plate (showing all thin-plate features with consistent echogenicity).

- Apply the same protocol as above, but collect multiple tracking data from one end of the thin plate to the other end and use an averaging technique to find the “center” of the thin plate.

By using the adjustable arm, we receive good and consistent appearance of the thin plates in the US images. In Figure 6.6, An US image of a portion of the calibration phantom is shown. To acquire this image, the probe is placed according to the protocol to make sure that the entire plane of the plate appears in the US image at once. To ensure in-plane alignment of the US probe and of a plate being scanned, the contour of the plate is observed as the probe is moved over the plate. Having the probe and plate the same plane forms a constraint from which we assume that the  $A_1$  and  $A_2$  transformation matrices are the relative transformations between the plates of the calibration phantom with a positional offset based on the pixel coordinates of the phantom in the acquired US image. From the US image, we observe the sharp contours of the plates (Figure 6.6) from which we compute the rotation of the plate within the plane of the US.

Three sets of tracking and US image data are sufficient to solve the mathematical formulation with acceptable accuracy. An additional 3 sets of data can generate 48 calibration datasets (given two poses at each thin-plate, this leads to  $6*4*2$  combinations), which will ensure more precision and produce comparable results to previous calibration accuracies.

This method has many advantages, including minimal image processing, immediate calibration, and simple phantom assembly. However, it also has one disadvantage that requires careful data collection to ensure that the US plane is in-plane with the thin plates. As a practical alternative, we designed and built a simple probe holder that will dock into

the thin plates in a predefined manner, guaranteeing correct alignment between the probe and the plates. This phantom, a modified thin-plate as seen in Figure 6.7 provides immediate data collection due to its unique design. The objective is to use two flat springs to hold the US probe over the thin plate and allow for in plane motion, as in Figure 6.7. A similar concept (i.e. using a mechanical attachment to the US probe) has been used successfully in the Cambridge phantom [Prager-1998b]. To achieve good placement accuracy for this dual flat spring system, careful offline calibration is required to place these thin plates in the elevation center of the US beam. Offline calibration is

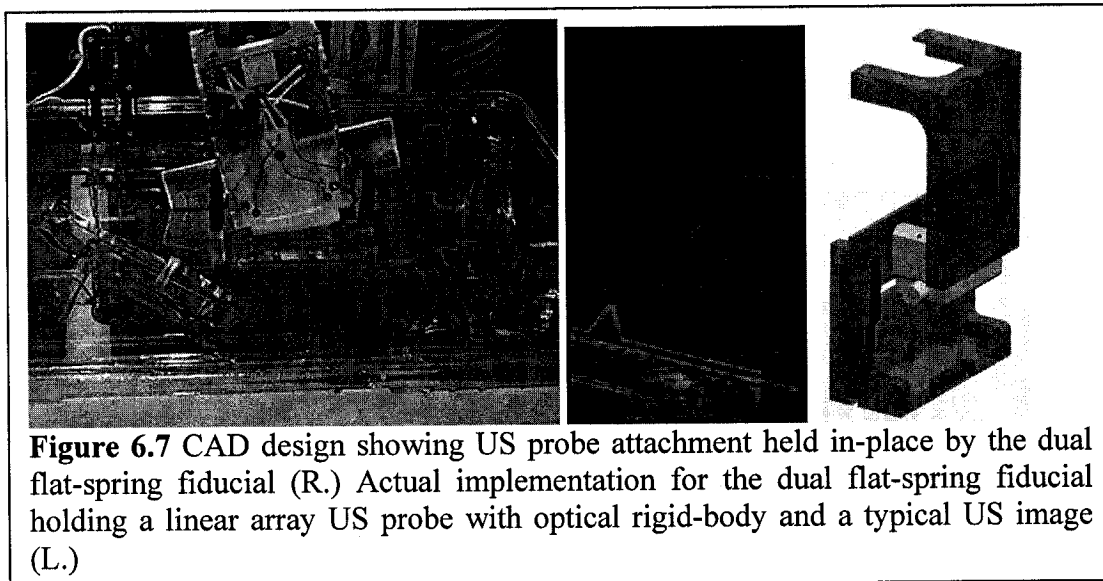


**Figure 6.7** CAD design showing US probe attachment held in-place by the dual flat-spring fiducial (R.) Actual implementation for the dual flat-spring fiducial holding a linear array US probe with optical rigid-body and a typical US image (L.)

done using an audible feedback system and an accurate micrometer stage (Figure 6.8). The output of this delicate procedure is a number of measurements that indicate the offset between the thin-plate and the middle of the US beam. Then we can correct this offset by adding or subtracting an appropriate number of metal pads with known thicknesses.

The consistent placement of the probe on the plates yields predictable and sharp US images that could be processed automatically (Figure 6.7-middle). Automatic image processing, however, might not promise a significant advantage, as we only use 3 to 6 frames and just a single feature point and line in each. The whole calibration setup can be sterilized and used for instantaneous intraoperative calibration.

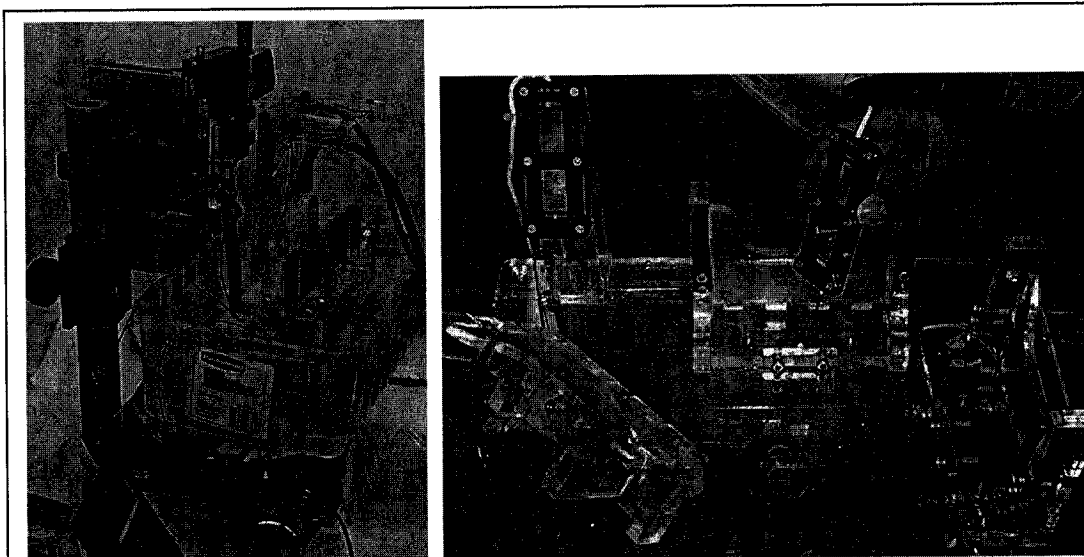


**Figure 6.8** Offline calibration to adjust the thin-plate in the middle of the elevation width of the US beam (L.) Optical pointer is used to digitize 3D points and estimate the transformations ( $A$ 's) between different dual flat-spring fiducials (R.)

In summary, we have demonstrated an immediate intraoperative US calibration method with substantial offline precalibration processing. Having a meticulous calibration method to align the US plane with the thin plate fiducial (Figure 6.8), we still suffer from a possible bias in the order of 200-400  $\mu\text{m}$  out-of-plane caused by the limitation of the calibration procedure. Also note that this offline calibration is tailored for one particular probe. If we decide to change the probe during intervention, we would probably first need to repeat this tedious procedure. In order to tackle this unavoidable uncertainty in

positioning any US probe on fixed fiducial, to reduce the amount of precalibration processing, and to build a generic phantom that can be used with any type of US probe, we propose a double-wedge phantom.

### 6.3.3 Double-wedge phantom

A novel three-piece phantom was designed to take full advantage of the  $AX=XB$  closed-form formulation and overcome the described limitations. Prior experience with  $AX=XB$  has revealed that robust and simple estimation of the  $A$  matrix is the key to simple calibration [Boctor-2004d, Viswanathan-2004]. We built three identical double-wedge fiducials (Figure 6.9), inspired by a recent work by Gee and Prager et al. [Gee-2005] and arranged them on an acrylic board in known relative poses similar to the thin-plate phantom. Figure 6.10 presents the coordinate systems for mathematical formulation in the closed-form solver.  $A$  is the relative transformation between the US image frame at pose  $k+1$  and  $k$ . Note that  $A$  can be recovered by using a calibration phantom or it can be recovered directly by matching the 2D ultrasound images acquired in these poses to a prior 3D model of the phantom object.  $B_k, B_{k+1}$  are the tracking device readings for the

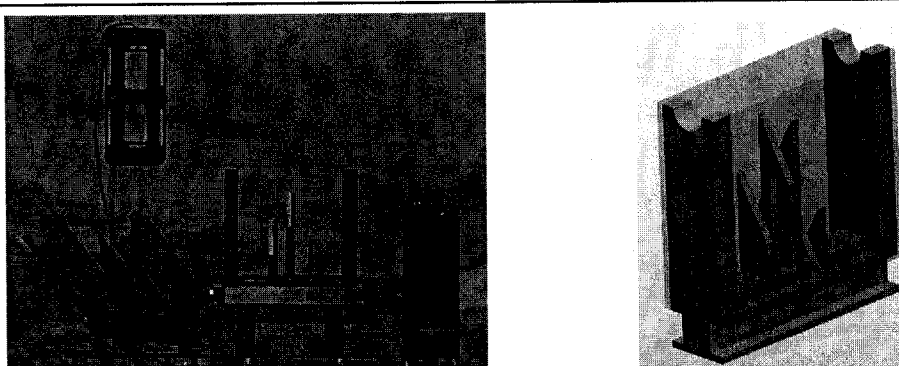
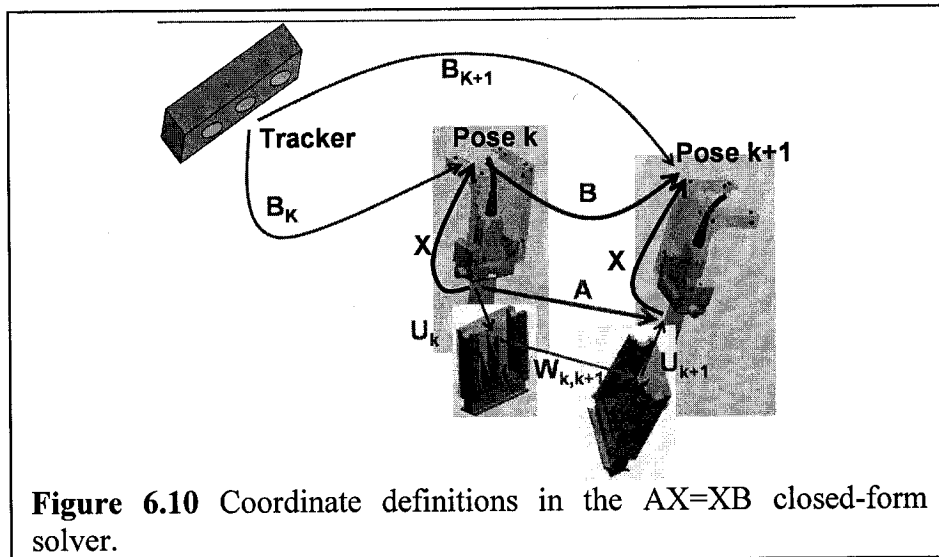


**Figure 6.9** Three double-wedge fiducials arranged on an acrylic board to maximize the accuracy.

sensor frame with respect to tracker reference frame at poses  $k$  and  $k+1$ , respectively. The relative pose between the sensor frame at pose  $k$  and  $k+1$  is given by  $B = B_k^{-1}B_{k+1}$ . This yields the following homogeneous matrix equation  $AX=XB$ , where  $A$  is estimated from images of a simple phantom,  $B$  is assumed to be known from the external tracking device, and  $X$  is the unknown transformation between the US image coordinate system and the sensor frame.



We were able to use the double-wedge phantom easily with different types of US probes including Siemens VF 10-5 linear array probe and Aloka laparoscopic probe (Figure 6.11). In the embodiment shown in Figure 6.11-right[Leven-2005], we used an Aloka US system (Aloka Ultrasound, Wallingford, Conn) with a laparoscopic probe. Multiple optical markers were attached to the probe holder, which then were tracked by an Optotrak device (Northern Digital Inc.). A rigid body marker is attached to the base plate of the phantom to serve as the common frame of reference set rigidly with respect to the phantom. We chose to demonstrate the double-wedge phantom calibration on tracked laparoscopic ultrasound that has been known to be the most challenging type of

calibration, due to the relatively large distance between the probe tracking markers and the US crystal, while there is relatively little separation between the individual probe tracking markers. We conjectured that if double-wedge calibration manages laparoscopic US, then it must work even better when using transcutaneous and intraoperative US probes. In the next sections we will discuss how the double-wedge method is capable of estimating the out-of-plane 3 DOF uncertainties,  $U_k$  as shown in Figure 6.10 using inherent features of the double-wedge design and also by introducing bootstrapped calibration on  $AX=XB$  framework.

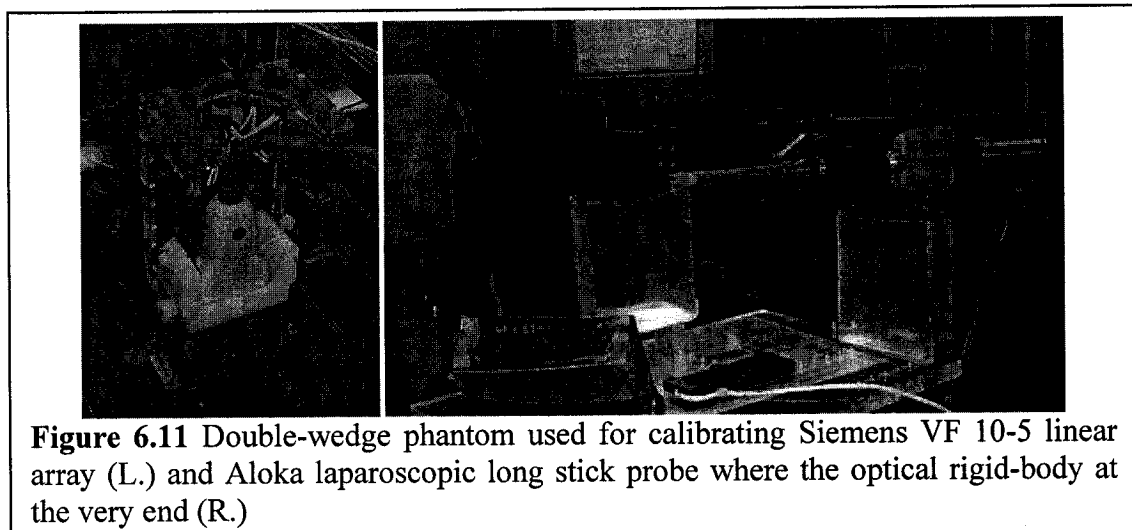


**Figure 6.11** Double-wedge phantom used for calibrating Siemens VF 10-5 linear array (L.) and Aloka laparoscopic long stick probe where the optical rigid-body at the very end (R.)

### 6.3.3.1 Double-wedge geometry and imaging

It is difficult to use the long stick laparoscopic US probe (Figure 6.11) to scan the double-wedge phantom in a water tank. Accordingly, we filled each double-wedge compartment with gel as shown in Figure 6.11. The US probe is brought to contact with this double-wedge gel sandwich as seen in Figure 6.11-right. We liberally apply coupling gel and twist the US probe on the edge of the sandwich, to collect a chunk of fan beams. As seen in Figure 6.12-left, the wedges provide sharp features in the US image that are easy to

segment. The goal is to place the probe so that the three wedges have equal size and inline clouds as shown in Figure 6.12-right. It is important to mention a few things that illustrate the leverage of double-wedge phantom design compared to thin-plate and modified Hopkins phantoms: 1) we did not use any special attachment to bring the US probe in plane with the phantom; placement was totally freehand<sup>†</sup>, and 2) we did not perform tedious offline precalibration specifically to accommodate one type of US probe.

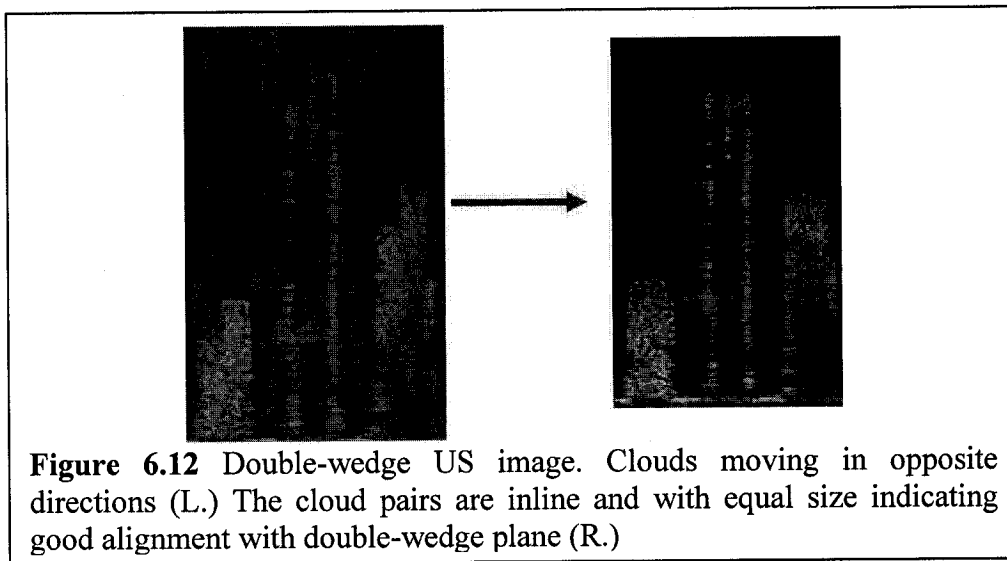


**Figure 6.12** Double-wedge US image. Clouds moving in opposite directions (L.) The cloud pairs are inline and with equal size indicating good alignment with double-wedge plane (R.)

We designed the double-wedge phantom to reveal more than answering the binary question if the US plane is aligned or not. In fact, by handling the descriptive geometry of these double-wedges and by analyzing the cloud pairs separation and size mismatch, the pose of the US image can be determined with respect to the sandwich. We can easily

<sup>†</sup> I did not collect the data myself; I trained my colleague, Josh Leven, to collect double-wedge US images in only a few minutes. He then sent me the data for analysis and calibration. The laparoscopic US calibration was part of the Josh's project on DaVinci telerobotic surgical system [Leven-2005].

estimate the relative pose between the US probe and a sandwich, thereby discerning the  $A$  matrix for the  $AX=XB$  equation, as explained earlier in relation to Figure 6.10.

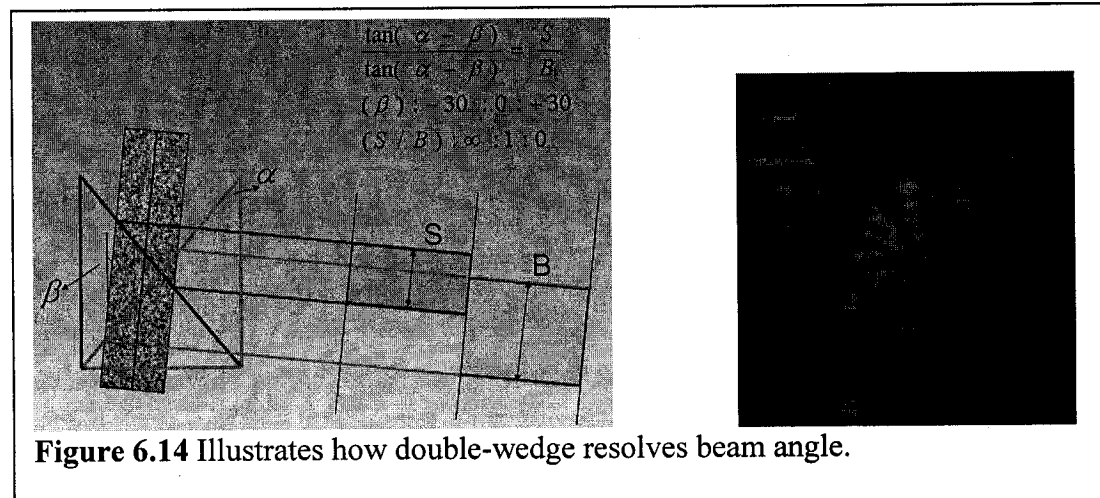
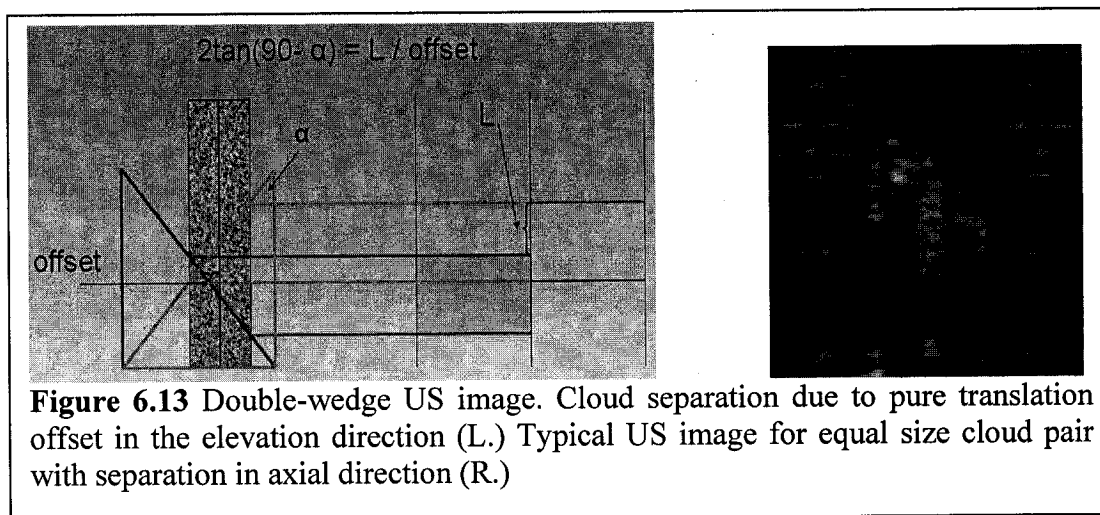
$$A = U_k W_{k,k+1} U_{k+1}^{-1}$$

Where  $U_k$  is the relative transformation between the US image frame and the double-wedge frame at pose  $k$ .  $W_{k,k+1}$  is the transformation between the double-wedge phantoms at poses  $k$  and  $k+1$ . Note that  $W_{k,k+1}$  can be estimated from a precise machining or by using a calibrated digitizing pointer, with an uncertainty below 100 $\mu\text{m}$ . However, the uncertainty of the  $U$  matrices is significantly higher. The accuracy of the calibration is predominately controlled by how well we can estimate the  $U$  matrices. From the US image of the double-wedge phantom we can estimate the following:

- 1) US beam offset from the double-wedge plane as shown in Figure 6.13. Note that in case of pure translational offset, the two clouds (echo of the double-wedge) will have the same size (axial distance) and will be separated with distance  $L$ . If we choose the double-wedge angle  $\alpha=60^\circ$ , this means that  $L = 2*\tan(30)*\text{offset} = 1.15*\text{offset}$ . So if the offset is 0.1mm, this will make the clouds separated by 115  $\mu\text{m}$  distance. Using an US scanner with 200 $\mu\text{m}$  axial resolution (a common value in many linear arrays) will fail to discern 115 $\mu\text{m}$  separations. However, we built the double-wedge with  $\alpha=30^\circ$ , which means  $L = 2*\tan(60)*\text{offset} = 3.46*\text{offset}$ . In this case, the double-wedge will act as a mechanical amplifier and transform any 0.1mm offset into 346 $\mu\text{m}$  cloud separation that can be discerned using 200 $\mu\text{m}$  axial resolution system.
- 2) US beam out-of-plane rotation as shown in Figure 6.14. Actually, the figure shows the out-of-plane rotation and translational offset at the same time. Both motions can be independently segmented with two geometry criteria:

- a. Translational offset is measured by L, as cloud separation.
- b. Out-of-plane rotation that is attributed to the size mismatch of the clouds.

In addition to this double-wedge US image method on the estimation of the  $U_k$  matrix (Figure 6.10), we can easily leverage the use of  $AX=XB$  by integrating a method that can bootstrap the calibration accuracy. The approach of our bootstrapped calibration is to perturb the out-of-plane motion parameters of the  $U$  matrices to compute a more accurate calibration, as shown in the next section.



### 6.3.3.2 Bootstrapped US calibration using $AX=XB$

In order to evaluate the overall accuracy of calibrated system, usually an object (typically cross-wire or single wall) is scanned from multiple directions and reconstructed in 3D space, and then the standard deviation of registration accuracy is reported as the measure of the quality of calibration. All current calibration methods, however, terminate at this point and fail to optimize the calibration toward minimum target reconstruction error (Figure 6.15). We propose to close the loop on reconstruction accuracy and use it for minimizing the calibration error. We refer to this iterative process as bootstrapped calibration (Figure 6.16) [Boctor-2005a].

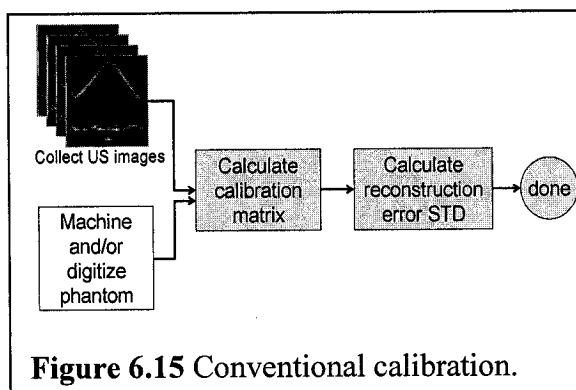


**Figure 6.15** Conventional calibration.

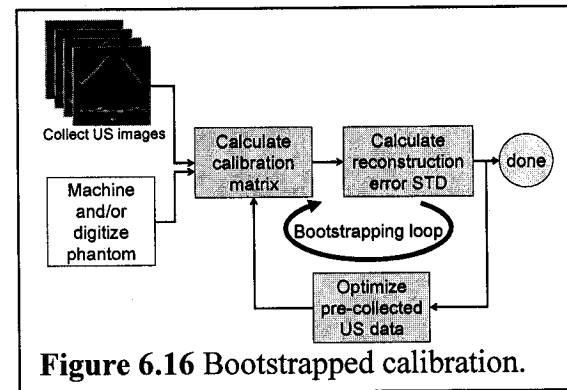


**Figure 6.16** Bootstrapped calibration.

In an attempt to improve target calibration accuracy, conventional methods simply increase the amount of input data and average the result of several calibration procedures. This brute force approach tends to improve on the precision of calibration, i.e. the expected uncertainty of a single calibration. For example, the mean of 100 calibrations will yield 1/10 of the variation of a single calibration. In addition to using this versatile tool, we also propose bootstrapping the conventional calibration process by adding an iterative feedback loop to minimize reconstruction error. There are two basic approaches to bootstrapping. The first approach takes new US data from both the phantom and evaluation targets (such as a cross-wire or single-wall) until the reconstruction error

remains below some sensible limit. This is not a true mathematical optimization, but it can be very effective if one can find the optimal pose for taking new US image data where the registration error decreases the fastest. Correlation analysis can reveal the link between probe motion and the likely improvement in reconstruction accuracy. Recent results based on the curvature of the criterion function at the solution were reported by Hsu et al. [Hsu-2006]. The second approach (Figure 6.16), which was implemented in this thesis, is based on correcting the already acquired tracked US data that we use to calculate the calibration matrix. In contrast to the first approach, we do not take new US images during the bootstrapping process. Instead, we iteratively reduce the error in the tracked ultrasound data that was collected before running the calibration process.

We recalculate the calibration matrix in the bootstrapping loop until minimum standard deviation of the position's reconstruction accuracy is achieved. This is a true numerical optimization that provides the best available result from the given data. If the residual reconstruction error remains high, additional US data need to be collected. However, this situation never occurred in our experiments. This might be attributed to the fact that we started with a good data set that maximizes the accuracy of calibration based on  $AX=XB$  framework.

**Bootstrapped Calibration Workflow.** Our bootstrapped calibration protocol is simple to execute. The double-wedge sandwich phantom and the US probe are brought to the field of the Optotrak tracker. The phantom is prepared by applying coupling gel to the edge of each sandwich. An image is collected from each sandwich, in the pose shown in Figure 6.11-right. Having the probe and the center plane of the sandwich in the same plane forms a constraint. In the  $k_{th}$  sandwich, we assume that the  $U_k$  transformation matrix is the relative transformation between the sandwich and the US image.  $U_k$  has an in-plane offset

and rotation that can be calculated from the of the wedges in the US image.  $U_k$  also has an out-of-plane motion component, which is supposed to be near to identity, when the probe is in the central plane of the sandwich. The US probe is rotated over the wedge until the left and right sides of the US image match. This can be achieved with freehand motion of the probe, due to the sharp features of the double-wedges in the US image. (Note that we could as well collect a fan beam of US images, process them numerically, and select the one closest to the center plane of the sandwich.) When the desired image is found to coincide with the center plane of the sandwich (when  $U_k$  has practically no out-of-plane components), we record the picture and the reading from the tracker. We determine the wedge points from the images, either by mouse click or image processing. Therefore we can compute the  $A$  and  $B$  matrices and then run the  $AX=XB$  module to estimate the full calibration matrix. (Also note that while 3 images are sufficient to recover the calibration matrix with acceptable accuracy, 6 additional images can generate  $9*6*3=162$  calibration datasets, and ensure significantly higher precision.) Having obtained a reasonable estimate of the calibration matrix, we can bootstrap the process, or refine the calibration. We can image a target from different directions with the tracked ultrasound probe. We reconstruct the expected target location in each image using the calibration matrix provided earlier by the  $AX=XB$  solver. Finally, we calculate the standard deviation between the observed and the reconstructed target points, denoted as  $R-STD$ . The value of  $R-STD$  is a good measure of the quality of the calibration, and it can also be used to drive a non-linear optimization loop. We apply such a non-linear optimization to change parameters in the  $AX=XB$  equation until  $R-STD$  settles in a minimum. In our experimental system, we used a common cross-wire target made of nylon filaments, submerged in a water tank at room temperature. We acquired 40 images, but we are also certain that significantly fewer images would still generously suffice. We can also scan the bottom wall of the phantom to try to reconstruct this plane.

In our prototype system, we can trust the result of the closed-form solver ( $X$  matrix), the Optotrak readings ( $B$  matrix), the machining of the phantom, the processing of US images of the sandwiches, and the segmentation of the cross-wire. The least trusted element of the calibration is our freehand maneuvering ability to bring the US image into the center plane of the sandwich, i.e. the out-of-plane component of the  $U_k$  and  $U^T_{k+1}$  in Figure 6.10. In each cycle, we modify these and then once we have a new  $A$ , we recalculate  $X$  using the original  $B$ , and finally recalculate  $R\text{-STD}$  for the presegmented cross-wire images.

## 6.4 Experiments and Results

### 6.4.1 The modified Hopkins phantom

Two different sets of experiments have been designed to test the calibration technique. The first set of experiments uses synthetic data where optimal parameters are exactly known. The second set of experiments use real ultrasound sequences as described in Section 6.3.1.

	Average Error (mm)			Standard Dev.(mm)		
Sequence I	0.0013	-0.00113	-0.0668	0.468	0.125	0.298
Sequence II	-0.002	0.00652	0.0356	0.382	0.195	-0.109
Sequence III	0.0657	-0.0357	-0.888	8.726	2.132	4.512
Sequence IV	0.0461	-0.0160	-0.895	13.89	3.459	6.058

**Table 6.1** Average error and standard deviation in mm of the recovered translation vector for different calibration sequences. The sequences were generated using synthetic data with added noise of 0.5%, 1%, 5%, 10% respectively.

Simulation trials were performed to provide insight into the numerical behavior of the linear formulation of  $AX = XB$ , as well as a means of testing the validity of the algorithm in a controlled environment. Ultrasound noise and beam width problem would affect the

accuracy of the estimated  $A$  matrix. Accordingly, the following protocol aims to simulate these disturbances. First, the missing transformation  $X$  is picked by a random choice. Second, a sequence of probe motions (sensor) is chosen. From the unknown transformation  $X$ , the ultrasound image motion can be deduced. Third, different levels of white noise are added to the ultrasound image motion frame “ $A$ ’s” to simulate a real environment as well as to the simulated tracking readings “ $B$ ’s”. The resolution of a tracking device is always in the order of 0.1% for EM devices and less than 0.001% for an optical based system. The algorithm was executed to recalculate the  $X$  transformation under different noise conditions, as shown in Table 6.1.

Real data was acquired at 7 poses. The algorithm was tested on all unique combination of 3 of these 7 poses (the minimum necessary to compute a solution.) Table 6.2 reports the average recovered pose values as well as the standard deviation. Much of the 1.54mm position error is attributed to the crudely prototyped of US probe attachment producing mechanical sag and limiting the angular range of tracking. However, we have proved that the novel closed-form formulation recovered both translation and rotation with repeatability in the order of 1.5mm and 1.63 degrees with only 3 poses. The estimated time from capturing these 3 poses, running the semi-automated extraction method and reporting the solution is less than 1min.

	Average			Standard Dev.		
Position (mm)	82.566	-87.89	35.929	0.76	1.15	1.54
Angles (deg)	5.139	1.727	-2.866	1.63	0.11	0.83

**Table 6.2** Average pose values and average deviation in mm and degrees of the recovered transformation matrix using actual ultrasound and optical tracking device data.

The modified Hopkins phantom, however, is not easy to build and requires careful data collection and processing. This prompts us to build another phantom that is effortless to assemble, maximizes accuracy with a minimum number of poses, and requires negligible image processing, and therefore reports the calibration immediately. The next sections 6.4.2 and 6.4.3 report results for new phantoms, one called the thin plate phantom and the other a modified version of this phantom based on double-wedge fiducials.

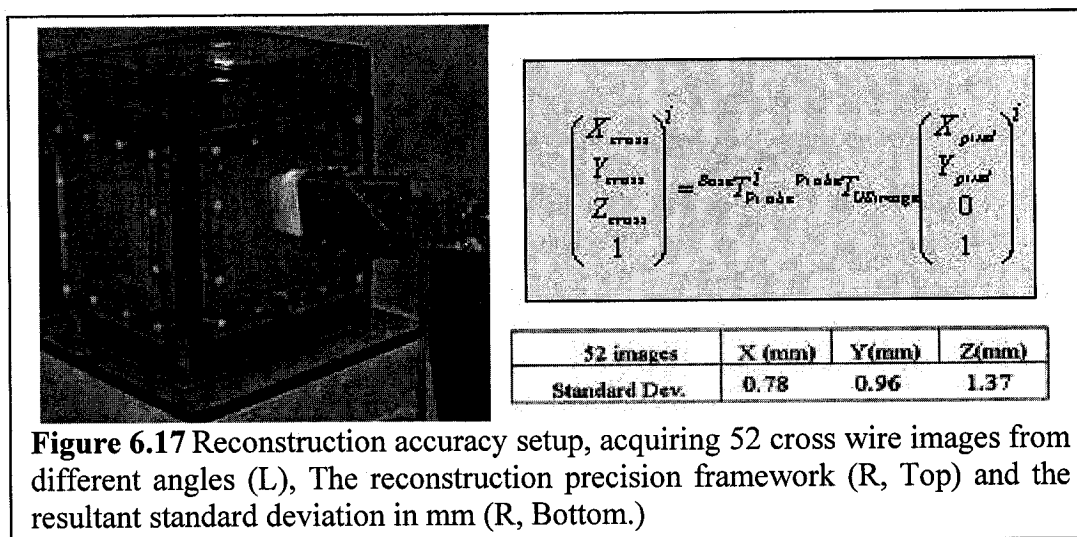
#### **6.4.2 The thin plate phantom**

In order to check the repeatability of our calibration setup and of our phantom's performance, we gathered data using a tracked ultrasound probe. US data was acquired in 2 poses for each of the calibration plates. The algorithm was tested on 48 unique combinations of 6 different poses (two poses per plate). Table 6.3 reports the average recovered pose values of these 48 combinations and the standard deviation, which reflect the repeatability of this method. These numbers are comparable to the previously reported repeatability analysis [Prager-1998b]. Right after data collection (tracking information and the offline processed data), the calibration algorithm executes almost immediately. The major source of expected error stems from the misalignment of the ultrasound probe to the plane of the thin plate. With the addition of the modified thin-plate phantom (Figure 6.7), this source of error can be removed from the system.

	Average			Standard Dev.(repeatability)		
Position (mm)	93.83	-38.50	38.21	1.31	2.08	2.41
Roll, Pitch, and Yaw Angles (degrees)	177.85	0.29709	2.7751	0.7 ~ 0.8		

**Table 6.3** Average pose and deviation of the recovered calibration matrix using the thin plate calibration phantom with the AX=XB method.

Next we performed precision assessment for the calibration, using one of the reported accuracy analysis methods [Prager-1998b]. Reconstruction precision was based on 3D reconstruction of the cross wire. The basic idea behind this test is to check how precise the calibration matrix would reconstruct all the cross wire points gathered from different insonification angles into a fixed point in space. The standard deviation of the point cloud reflects uncertainty in the calibration matrix as well as the manual extraction of the cross wire points, as shown in Figure 6.17. The resulting calibration precision is highly comparable to those reported in literature [Prager-1998b].



These preliminary results indicate that there is significant potential for using a simple calibration phantom in conjunction with the  $AX=XB$  closed-form formulation. The sharp features of the thin plastic plates of the calibration phantom appear markedly in US images and it is easy to locate these features based on pixel intensity and gradient. Compared to conventional wire-based calibration phantoms, the simplified design of our phantom and the use of optical digitization of 3D feature points reduced the amount of image processing required and still provided very accurate calibration results. Because conventional calibration methods relied on image information from an US machine,

registration accuracy, to a large extent, also depended on the resolution of the US imaging system and the accuracy of feature extraction. Ultrasound noise and beam width problem would normally affect the accuracy of the estimated  $A$  matrix. Therefore, if the modified thin-plate phantom were to eliminate the misalignment error between the US probe and the phantom, we should expect sub-millimeter reconstruction precision.

#### 6.4.3 Double-wedge phantom

Table 6.4 shows the standard deviation of position reconstruction accuracy in millimeters for three calibration methods: a pointer-based approach by Muratore and Galloway [Muratore-2001], the original  $AX=XB$  closed-form calculation using double-wedge phantom, and our bootstrapped calibration. The original  $AX=XB$  is more favorable than the pointer-based method, while the bootstrapped method is superior to both. The largest contributor to the residual  $R$ -STD that remains after bootstrapping is incorrect segmentation of the cross-wire targets and the temporal calibration. Ultrasound velocity also appears to be a significant factor. The calibration was performed on a gel phantom in which the speed of sound is 1,540m/sec, but the cross-wire was placed in room temperature water in which the speed of sound is only 1,420m/sec. From this problem

Pointer [Muratore-2001]			$AX=XB$ [double-wedge]			Bootstrapped		
x	y	z	X	y	z	x	y	z
3.6	2.8	2.1	2.5	3.3	2.2	2.5	2.5	2.0

**Table 6.4** Standard deviation of position reconstruction accuracy (R-STD) in mm, for three calibration methods.

alone we can suffer as much as 0.4mm error at 10cm penetration depth. One fundamental problem with reconstruction error based accuracy analysis is that it cannot separate calibration error from other factors of error. One could, however, obtain an estimate

based on the uncertainties of the independent variables feeding into the closed-form solver, which can be accomplished by propagating input uncertainties or by Monte-Carlo simulation.

In the pointer-based method, the increased deviation along the elevation direction ( $x$ ) is associated with the beam width problem. While the  $AX=XB$  provided a better estimate, bootstrapping did not improve  $R$ - $STD$  along that axis. The reason for this appears to be that the cross-wire target tended to fall in the center of the US images, roughly in the gravity center of the double-wedges. While bootstrapping fixes the out-of-plane rotation of the image with respect to the sandwich, it leads to relatively little out-of-plane motion in the image center where the cross-wire resided. Had we placed the cross-wire farther from the image center, bootstrapping would have shown more significant enhancement over the  $AX=XB$  method, in terms of residual  $R$ - $STD$ . A cross-wire target placed farther away from the gravity center of the three wedges would have driven bootstrapping more aggressively. In our system embodiment, perturbing the  $A$  matrix alone drives the overall calibration optimization effectively, but there is still residual  $R$ - $STD$  that could be further reduced. In other words, some parameters that we had trusted could also be perturbed to achieve a smaller  $R$ - $STD$ . The next obvious candidate is segmentation of the cross-wire targets. We performed this task manually, but the process could be aided by advanced image processing. Indeed, a significant advantage of bootstrapping is that the previously manual segmentation and correspondence process can be easily automated using the initial calibration estimate. Nevertheless, a simpler target structure, such as single-wall [Prager-1998b], may be more favorable. In our system, processing the US images of the sandwich phantom (i.e. in-plane portion of  $A$ ) and the readings from the tracker (i.e.  $B$  matrix) are very reliable and perturbing these does not promise further improvement on  $R$ - $STD$ .

We have also developed an image-based method to estimate the out-of-plane motion of the US probe by maximizing the similarity between the US image and the descriptive geometrical model of the sandwich. The calculated out-of-plane motion is in good agreement with the out-of-plane correction provided by the bootstrapping. Apparently, we can derive an estimate of out-of-plane motion based on image processing alone, but this takes time and is also prone to human error. On the other hand, we always need some form of accuracy assessment and once  $R$ -STD is calculated, bootstrapping is essentially free. Because the  $AX=XB$  closed-form solver works in real-time and the bootstrapping needs only a few iterations, the computational time required for a full calibration is negligible. In addition, we only need to use few images, the acquisition and processing of which is quick and easy. A further unique feature of the sandwich phantom is that, unlike all other phantoms, it does not reside in a water tank. The phantom could be covered with sterile plastic drape in the operating room, allowing for in-situ calibration. The cross-wire (or a single-wall) target could also be packaged with the sandwich phantom, thereby eliminating the earlier mentioned discrepancy in speed of sound between the sandwich and target phantom images.

Because conventional calibration methods relied on image information from an US machine, registration accuracy, to a large extent, also depended on the resolution of the US imaging system and the accuracy of feature extraction. These factors disappear in practice with bootstrapped calibration that can minimize R-STD effectively, even if the segmentation of features is somewhat incorrect. Thus the remaining significant sources of error left in the calibration matrix are the inaccuracy of the tracking and temporal synchronization; which is the ultimate limit for any calibration.

## **6.5 Conclusions**

This chapter summarizes a novel collection of US calibration methods based on a closed-form formulation. We were able to answer all the questions we had from Chapter 5, including the types of motion that maximize accuracy, and an adequate number of poses to perform full calibration. Further, we managed to overcome the axial and lateral resolution limits of the B-mode US image by introducing the double-wedge phantom as a “mechanical amplifier.” This phantom can magnify out-of-plane motion by 4 times the actual amount of displacement and orientation. Further more, we were able to easily run an iterative bootstrapped module on top of the  $AX=XB$  calibration.

Despite the effective use of this new method to calibrate a laparoscopic US probe, notoriously known to be the hardest type of probes to calibrate, we wanted to explore a truly phantomless calibration method. Special objects and phantoms are foreign to the operating room, where interrupting the procedure to calibrate the probe is not practical. What is required therefore is a paradigm shift in calibration technology to a phantomless self-calibration that is performed directly on the patient, intraoperatively, in real-time, and transparently to the physician (Chapter 7.)

## **Part-II: Chapter 7**

# **Real-time Quality Control (QC) and Ultrasound Self-Calibration**

### **7.1 Introduction**

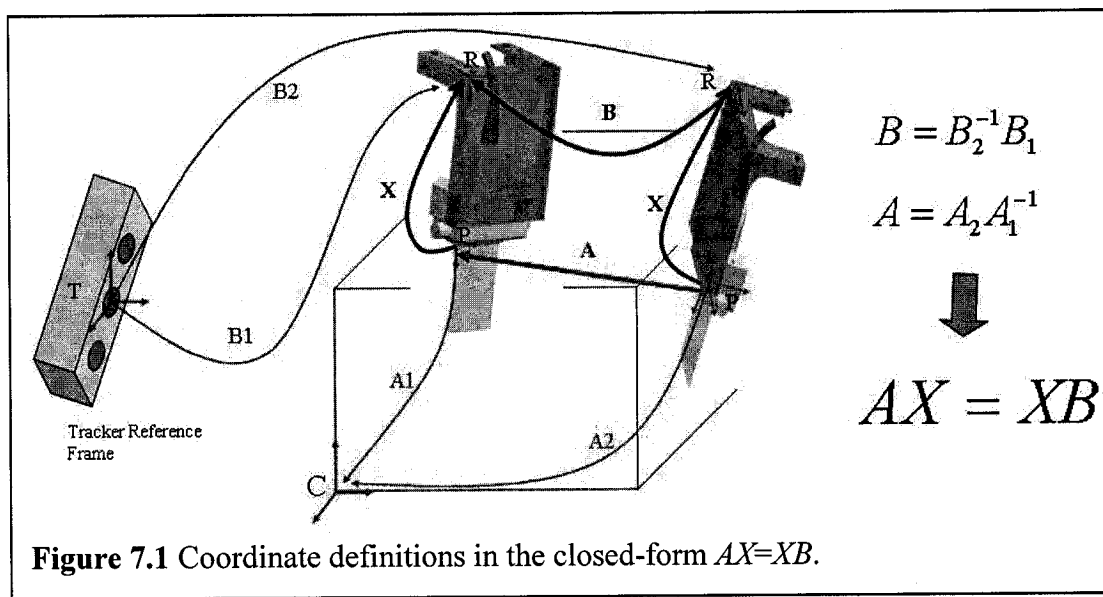
Significant research has been dedicated to quantitative tracked ultrasound, involving tracking the US probe in 3D space with respect to a stationary frame of reference. While tracked US originates from interventional applications, it recently has become an indispensable tool in external beam radiation therapy guidance [Langen-2003]. In fact, EBRT is expected to become the largest user of tracked ultrasound in the next couple of years. Each year in the United States 65,000 patients are treated for prostate cancer alone. Considering an average of 40 treatment fractions per patient, the total number of procedures is approximately 2.6 million a year. Tracked US guidance is also applicable to the EBRT of breast cancer, adding about 2 million more cases to the potential market.

Typically, tracking an US probe in 3D space with respect to a stationary reference is achieved by rigidly attaching 3D localizers to the US probe. A missing link, however, is the spatial transformation between the US image pixels and the 3D localizers on the probe, which requires calibration. Hence, calibration is ubiquitously present in all systems where ultrasound is used for quantitative image guidance. In our experience, the wide majority of intraoperative hazard situations in tracked US systems are caused by failure of registration between tracking and imaging coordinate frames, resulting in

miscalibration of the tracked US. The most typical form of error is a false reading of the tracker. This occurs quite often in electromagnetic tracking systems due to invisible field distortions caused by metal objects or electromagnetic noise. Another typical problem related to tracking is deformation or physical damage of the tracking body attached to the probe, causing a latent misreading of pose. These problems are exceedingly dangerous because they occur without apparent warning. Among human operator errors, inadvertent changes in lateral image polarity occur quite frequently and transparently to the clinical user. With regular offline recalibration some of the aforementioned errors can be caught prior to procedure. The process is called quality control (QC), and is a mandatory routine in any clinical department. Typically, QC is performed annually, monthly, or weekly, which places a heavy financial burden on the department. One of the major incentives of our work, in addition to increasing patient safety, is to reduce costs of QC to the department.

In all current calibration methods, a set of objects (often referred to as phantoms) with known geometrical properties are scanned and then various mathematical procedures are applied to estimate the unknown transformation in order to maximize the similarity between the US images and the phantom [Carr-1996, Prager-1998b, Pagoulatos-2001, Rousseau-2002, Boctor-2004d, Muratore-2001, Mercier-2005]. Special objects and phantoms are foreign to the operating room, where interrupting the procedure to calibrate the probe is not practical, and their use can be cumbersome. What is required therefore is a paradigm shift in calibration technology to a phantomless self-calibration that is performed directly on the patient, intraoperatively, in real-time, and transparently to the physician.

Generally, full calibration involves a six degree-of-freedom (DOF) rigid transformation and three or two dimensional scale factors when using 3DUS or 2DUS probes, respectively. However, on a practical level, the possibility of pure translational error in the calibration matrix is low. One atypical scenario would involve the rigidly attached sensor sliding without experiencing any relative rotation in the US image reference frame. Therefore, it is acceptable for the purpose of QC to recalibrate the system for the remaining rotational and scale degrees-of-freedom. The coming sections present the concept, mathematical framework, experimental implementation, and in-vitro evaluation of novel, unprecedented phantomless real-time method that detects intraoperative failures of the tracked US while recovering the calibration matrix.



## 7.2 Mathematical Formulations

As we showed earlier in Chapter 6.2, the key enabler of our self-calibration method is a closed-form mathematical formulation of the problem. Figure 7.1 presents the coordinate systems for the mathematical formulation.  $A_1, A_2$  are the transformations of US picture

coordinate system (P) with respect to the fixed construction frame (C) at poses 1 and 2, respectively. Note that the actual selection of C is arbitrary and the only requirement is that it must be rigidly fixed during the calibration process. Using  $A_1$  and  $A_2$ , we obtain the transformation between poses 1 and 2, as  $A = A_2 A_1^{-1}$ . At the same time, the transformation between the two poses can either be recovered using a calibration phantom or they can be recovered directly by matching the 2D ultrasound images acquired in these poses to a prior 3D model of the phantom object.  $B_1$  and  $B_2$  are readings from the tracker for the sensor frame ( $R$ ) with respect to tracker reference frame ( $T$ ), at poses 1 and 2 respectively. The relative pose between the sensor frame ( $R$ ) at pose 1 and 2 is given by  $B = B_2^{-1}B_1$ . This yields the following homogeneous matrix equation:

$AX = XB$ , which is :

$$\begin{aligned} R_a R_x &= R_x R_b, \text{ and} \\ R_a t_x + D(u_a) \bar{\lambda} &= R_x t_b + t_x \end{aligned} \quad (7.1)$$

Where  $A$  is estimated from images,  $B$  is assumed to be known from the external tracking device, and  $X$  is the unknown transformation between the US image coordinate system and the sensor frame ( $R$ ). Expanding this equation yields two separate constraints on translation and rotation, where  $R_a$  is the rotation of the US image frame between pose 1 and 2,  $\lambda$  is the unknown scale factor vector that relates the translation vector  $u_a$  in voxel space to the US image frame translation vector  $t_a$  (usually expressed in mm), such that:

$$t_a = \begin{pmatrix} \lambda_x u_{ax} \\ \lambda_y u_{ay} \\ \lambda_z u_{az} \end{pmatrix} = \begin{pmatrix} u_{ax} & 0 & 0 \\ 0 & u_{ay} & 0 \\ 0 & 0 & u_{az} \end{pmatrix} \cdot \begin{pmatrix} \lambda_x \\ \lambda_y \\ \lambda_z \end{pmatrix} = D(u_a) \bar{\lambda} \quad (7.2)$$

It is important to account for the most general case where the scale factor (which again converts from voxel space to image space) is not known. This scenario typically occurs

when  $A$  is recovered by registering the US image to some a priori known model including pre-acquired MRI or CT volume (or phantom) given in voxel space. In the linear formulation of the problem, we will use the linear operator  $\text{vec}$  and the *Kronecker product* ( $\otimes$ )[Brewer-1978]. Using the following property of the *Kronecker product*:

$$\text{vec}(CDE) = (C \otimes E^T) \text{vec}(D) \quad (7.3)$$

One can rewrite equation (7.1) as:

$$(R_a \otimes R_b) \text{vec}(R_x) = \text{vec}(R_x), \quad (7.4)$$

$$(I_3 \otimes t_b^t) \text{vec}(R_x) + (I_3 - R_a)t_x - D_u \lambda = 0 \quad (7.5)$$

From (7.4) and (7.5), we can transform the whole problem ( $AX=XB$ ) into a single homogeneous linear system:

$$\begin{bmatrix} I_9 - R_a \otimes R_b & 0_{9*3} & 0_{9*3} \\ I_3 \otimes t_b^t & I_3 - R_a & -D_u \end{bmatrix} \begin{pmatrix} \text{vec}(R_x) \\ t_x \\ \lambda_{3*1} \end{pmatrix} = \begin{pmatrix} 0_{9*1} \\ 0_{3*1} \end{pmatrix} \quad (7.6)$$

The solution for this homogeneous linear system could be given by finding the *null space*  $\Psi$ , which is a subspace in  $R^{15}$ . Then the unique solution could be extracted from the null space using the unity constraint to the first 9 coefficients representing the  $R_x$ . In the case of noise-free data, this method guarantees orthogonality but not normality of the recovered  $R_x$ , which can be easily fixed [Andreff-2001] as follows:

$$R_x = \frac{\text{sign}(\det(V))}{|\det(V)|^{1/3}} V$$

Where  $\text{sign}$  is a sign function that returns the sign of  $\det(V)$ ,  $V = \text{vec}^{-1}(v)$  and  $v$  is any vector in the *null space*  $\Psi$ . In the case of noisy data, one can project the estimated  $R_x$  into

$SO(3)$  manifold, and get a corresponding least squares solution. Obviously, one motion is not enough to recover all the parameters. In fact, two independent motions [Shiu-1989, Tsai-1989, Chen-1991, Shi-2005] (three poses) with non-parallel axes is sufficient to recover a unique solution for  $AX=XB$ . However, another solution can be described in where the system is solved in two steps: first extract the rotation as in (7.7), and then solve for the translation and scale as in (7.8).

$$\begin{pmatrix} I_3 - R_{a1} \otimes R_{b1} \\ I_3 - R_{a2} \otimes R_{b2} \end{pmatrix} \text{vec}(R_x) = 0 \quad (7.7)$$

$$\begin{pmatrix} I_3 - R_{a1} & -D_{a1} \\ I_3 - R_{a2} & -D_{a2} \end{pmatrix} \begin{pmatrix} t_x \\ \lambda_{3*1} \end{pmatrix} = \begin{pmatrix} -R_x t_{b1} \\ -R_x t_{b2} \end{pmatrix} \quad (7.8)$$

We have extended this solution method to account for inhomogeneous scale in the three coordinate axes [Boctor-2004d, Viswanathan-2004]. Prior to this work, as shown in Chapter 6, we have exploited this closed-form formulation to solve the calibration problem based on various mechanical phantoms including the double-wedge phantom [Boctor-2005a], the N-shape phantom [Boctor-2004d], and the thin wall phantom [Viswanathan-2004]. In all these methods, phantoms were built in order to assist estimation of  $A$ 's, which is the relative motion between successive US frames as shown in Figure 7.1. Our present task reduces to recovering  $A$ 's as we are scanning real tissue and collecting the corresponding  $B$ 's from the tracker, and then obtaining their calibration by solving the homogenous linear system in equation (7.6). Obviously, recovering  $A$ 's from real-time US sequences is a problem of tracking rather than a problem of feature segmentation from static US phantom images. Tracking the 6 DOF of  $A$ 's based on 3DUS data is considered a straightforward and easy to handle problem. The key challenge lies in the full recovery of the  $A$ 's based on 2DUS data. The in-plane motion parameters can be recovered with sub-pixel accuracy in real-time, using speckle based

tracking algorithms applied to the B-mode images. However, the out-of-plane motion parameters appear to be difficult to recover from 2DUS data. In this paper, we recover  $A$ 's through careful algebraic analysis of degenerate special motions utilizing the closed-form formulation in (7.6). In general, a special or degenerate motion does not lead to unique optimal total, 6DOF, calibration. However these special motions (translation, planar or rotation about an axis) as will be shown in the following Sections 7.2.1 through 7.2.3, can be used to partially calibrate the US system.

### 7.2.1 Translation Motion

This motion scenario is realized by moving the 2D or 3DUS probe in translational sweep (without rotation) to collect a nearly parallel stack of images and/or series of 3D slabs. It can also be shown in a panoramic scan where the images can be stitched together without introducing a relative rotation. Given this kind of motion,  $R_b = R_a = I_3$ , leading to,  $R_x * t_{bi} = t_{ai}$  where  $i$  denotes the motion. Using the property of the *Kronecker product* in (7.3):

$${}_{3*9} \left( I_3 \otimes t_{bi}^T \right) * {}_{9*1} \text{vec}(Rx) = t_{ai}, \text{ we have}$$

$$t_{ai} = \begin{bmatrix} \lambda_x * u_{ai}(x) \\ \lambda_y * u_{ai}(y) \\ \lambda_z * u_{ai}(z) \end{bmatrix} = \begin{bmatrix} u_{ai}(x) & 0 & 0 \\ 0 & u_{ai}(y) & 0 \\ 0 & 0 & u_{ai}(z) \end{bmatrix} \begin{bmatrix} \lambda_x \\ \lambda_y \\ \lambda_z \end{bmatrix} = D(u_{ai}) \vec{\lambda}$$

Three independent translations are sufficient to obtain a full-rank system. Solving for  $R_x$  and the three scale factors:

$${}_{9*9} \overbrace{\begin{bmatrix} (I_3 \otimes t_{b1}^T) \\ (I_3 \otimes t_{b2}^T) \\ (I_3 \otimes t_{b3}^T) \end{bmatrix}}^M * {}_{9*1} \text{vec}(Rx) = \begin{bmatrix} t_{a1} \\ t_{a2} \\ t_{a3} \end{bmatrix} = \begin{bmatrix} D(u_{a1}) \\ D(u_{a2}) \\ D(u_{a3}) \end{bmatrix} * \begin{bmatrix} \lambda_x \\ \lambda_y \\ \lambda_z \end{bmatrix}$$

$$vec(Rx) = \frac{1}{\Delta} \underbrace{\begin{bmatrix} I_3 \otimes \overbrace{(t_{b2} \times t_{b3})}^{v1} & I_3 \otimes \overbrace{(t_{b3} \times t_{b1})}^{v2} & I_3 \otimes \overbrace{(t_{b1} \times t_{b2})}^{v3} \end{bmatrix}}_{M^{-1}} * \begin{bmatrix} D(u_{a1}) \\ D(u_{a2}) \\ D(u_{a3}) \end{bmatrix} * \begin{pmatrix} \lambda_x \\ \lambda_y \\ \lambda_z \end{pmatrix}$$

Where  $\Delta = \det(t_{b1}, t_{b2}, t_{b3})$ , Using Khatri-Rao product [Brewer-1987] which defined as:

$$_{q \times u} F \circ _{t \times u} G = [F_1 \otimes G_1 \quad F_2 \otimes G_2 \quad \dots \quad F_u \otimes G_u] \text{ and the following fact}$$

$$vec(AB) = (B^T \circ A) vecd(V), \text{ where } vecd \text{ is } vec \text{ operator over diagonal elements.}$$

$$vec(Rx) = \frac{1}{\Delta} \left[ \underbrace{(I_3 \quad I_3 \quad I_3)}_D \circ \underbrace{(v_1 \quad v_1 \quad v_1 \quad v_2 \quad v_2 \quad v_2 \quad v_3 \quad v_3 \quad v_3)}_A \right] * \underbrace{\begin{bmatrix} D(u_{a1}) \\ D(u_{a2}) \\ D(u_{a3}) \end{bmatrix}}_V * \begin{pmatrix} \lambda_x \\ \lambda_y \\ \lambda_z \end{pmatrix}$$

$$vec(Rx) = \frac{1}{\Delta} vec(A * V * D^T), \text{ from linearity of vec operator}$$

$$Rx = \frac{1}{\Delta} A * V * D^T = \frac{1}{\Delta} \begin{bmatrix} \lambda_x(u_{a1}(x)v_1 + u_{a2}(x)v_2 + u_{a3}(x)v_3) \\ \lambda_y(u_{a1}(y)v_1 + u_{a2}(y)v_2 + u_{a3}(y)v_3) \\ \lambda_z(u_{a1}(z)v_1 + u_{a2}(z)v_2 + u_{a3}(z)v_3) \end{bmatrix}^T$$

We have obtained a closed-form solution that recovers an anisotropically scaled rotation matrix from three independent translations. We can recover the three scale factors by applying the unit constraint on each column vector, and we can then recover the underlying rotation by rescaling the columns into unit vectors. This proves that three independent motions are sufficient to recover the rotation and the three scale factors. However, the third motion is not even necessary. It can be shown that given two independent motions  $t_{b1}, t_{b2}$ , the third constraint comes from the cross-product between  $t_{b1}, t_{b2}$ .

In order to map this analysis to our application, several requirements must be considered. The ultrasound machine generates real-time 2DUS pixel-map, meaning that we have only two unknown scale factors in x and y, denoted as  $\lambda_x$  and  $\lambda_y$ . With sweeping probe motion we obtain multiple poses which suggests folding the closed-form representation into a least squares problem. Starting from the following equation:

$Rx * t_{bi} = t_{ai}$ , we have

$$t_{ai} = \begin{bmatrix} \lambda_x * u_{ai}(x) \\ \lambda_y * u_{ai}(y) \\ 0 \end{bmatrix} = \begin{bmatrix} \lambda_x & 0 & 0 \\ 0 & \lambda_y & 0 \\ 0 & 0 & \lambda_z \end{bmatrix} \begin{bmatrix} u_{ai}(x) \\ u_{ai}(y) \\ 0 \end{bmatrix} = D(\vec{\lambda}) u_{ai}$$

$$[t_{b1} \quad t_{b2} \quad \dots \quad t_{bn}] = Rx^T D(\vec{\lambda}) [u_{a1} \quad u_{a2} \quad \dots \quad u_{an}] \quad (7.9)$$

The solution of this equation can be achieved in many ways. One can solve non-linearly for the three rotations and the two scale factors ( $\lambda_x, \lambda_y$ ). Alternatively, one can solve linearly for the nine parameters of the scaled rotation and perform QR factorization with positive scale factor constraints. Or one can simply apply the norm constraint on (7.9) as follows:

$$\|Rx * t_{bi}\|^2 = \|t_{bi}\|^2 = \|D(\vec{\lambda})u_{ai}\|^2 = {u_{ai}}^T D(\vec{\lambda})^2 u_{ai}$$

This allows us to solve for both ( $\lambda_x, \lambda_y$ ). After recalculating the scaled  $u_{ai}$ , we obtain two sets of points governed by an  $SO(3)$  rotation matrix that can be recovered with Horn's method [Horn-1987].

### 7.2.2 Planar Motion

Planar motion is more general because in addition to translation, it allows in-plane rotation, referred to as 'Motion I' in Figure 7.2. This type of sweeping probe motion is commonly applied clinically. With this general motion, one can recover both rotation and

anisotropic scale factors as shown before, but this motion will not yield a full recovery of the position offset  $t_x$ . By applying (7.6) we obtain:

$$\begin{bmatrix} I_9 - R_{ai} \otimes R_{bi} & 0_{9*3} \\ I_3 \otimes t_{bi}^t & -D_{ui} \\ \vdots & \lambda_{3*1} \end{bmatrix} \begin{pmatrix} \text{vec}(R_x) \\ \vdots \end{pmatrix} = \begin{pmatrix} 0_{9*1} \\ 0_{3*1} \\ \vdots \end{pmatrix}, \text{ and} \quad (7.10)$$

$$\begin{bmatrix} (I_3 - R_{ai}) \\ \vdots \end{bmatrix}_{t_x} = \begin{bmatrix} D_{ui} \bar{\lambda}_{3*1} - (I_3 \otimes t_{bi}^t) \text{vec}(R_x) \\ \vdots \end{bmatrix} \quad (7.11)$$

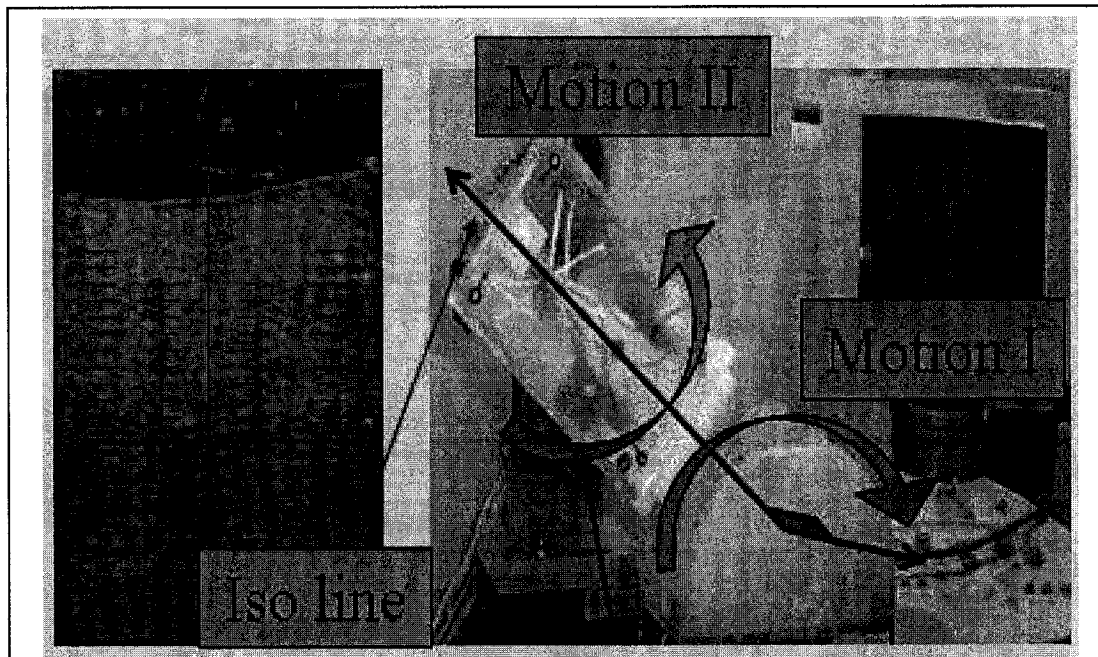


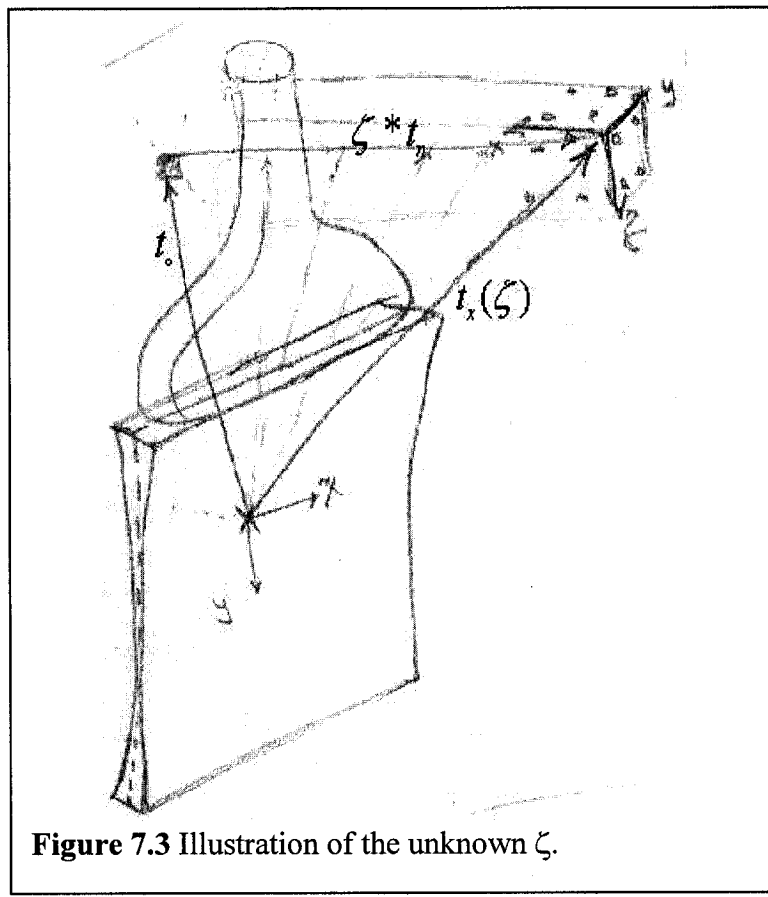
**Figure 7.2** Experimental system and an illustration for the suggested special motions. ‘Motion I’ indicates a planar motion, and ‘Motion II’ indicates a rotation about an axis.

Note that when  $Rb = Ra = I_3$ , equation (7.10) becomes similar to the pure translation case in (7.9). Also note that equation (7.11) is always under constraint as  $(I_3 - R_a)$  has rank 2, regardless of the number of in-plane rotations, meaning there is no single solution for  $t_x$ .

and the general solution will have exactly one (the number of unknowns minus the rank) arbitrary scale factor  $\zeta$ . So the solution can take the form:

$$t_x(\zeta) = t_o + \zeta * t_n$$

where  $\zeta$  is the unknown scale factor and  $t_o$  is a unique solution in the plane of motion (2-dimensional), since  $(I_3 - R_\alpha)$  has rank 2.  $t_n$  is the normal to the plane of motion (Figure 7.3). In our case, if the plane of motion is the US image plane (the x-y plane),  $t_n$  may equal  $(0, 0, 1)^T$ , which is a unit vector in the z-direction and thus perpendicular to the plane of motion.



### 7.2.3 Rotation about an axis

Assuming that we have  $R_x$ ,  $\lambda_x$ , and  $\lambda_y$ , the next step is to recover either  $\zeta$  in  $t_x(\zeta)$ , or  $t_x$ . By substituting  $R_a$  from equation (1.b) into (1.c) we get the following equation:

$$R_x R_b R_x^T t_x + t_a = R_x t_b + t_x \quad (7.12)$$

In this equation we know everything except  $t_a$ , and  $t_x$ . For general “n” motions, equation (7.12) gives  $3n$  constraints while leaving  $(3n+3)$  unknowns,  $3n$  for  $t_{ai}$  and  $3$  for  $t_x$ , or  $(3n+1)$  unknowns,  $3n$  for  $t_{ai}$  and  $1$  for  $\zeta$ . There are basically two approaches to resolve this imbalance and solve for  $\zeta$  or  $t_x$ . The first approach suggests estimating  $t_{ai}$  for all n motions.  $t_{ai}$  can be recovered by feature/speckle tracking in 6 DOF, which is a straightforward task once we have continuous 3DUS data. However, in case of 2DUS data, the method is reliable to recover the in-plane 3 DOF but it suffers from inevitable drift in recovering the out-of-plane 3 DOF [Hassenpflug-2005]. Section 7.2.4 will capture a snapshot of my recent participation with a new PhD student [Hassan Rivaz], who is working on more reliable out-of-plane motion estimation algorithms [Boctor-2005b]. The second approach, which suggests utilizing a special motion, Figure 7.2, that would group all  $t_{ai}$  in a known relation instead of having to estimate all  $t_{ai}$ . Thus, one can easily recover  $t_x$  or  $\zeta$  in  $t_x(\zeta)$  as follows:

$$t_{a,k} = R_x t_{b,k} + (I - R_x R_{b,k} R_x^T) t_x,$$

The special relation/motion we are proposing here is the following:

$$t_{a,1} = t_{a,2} = \dots t_{a,n}$$

$$R_x^T t_{a,k} = \frac{1}{n} \sum_{k=1}^n t_{b,k} + R_x^T t_x - \frac{1}{n} \sum_{k=1}^n R_{b,k} R_x^T t_x$$

This equation can be solved for either  $t_x$  as shown above or for  $\zeta$  in case of having  $t_x(\zeta)$ .

#### 7.2.4 Out-of-plane motion estimation

The out-of-plane motion is composed of two rotations and one translation. There are several ways to estimate these parameters. As shown in Chapter 6, one can use special phantom to recover the pose between successive 2DUS images. This method, however, does not serve the goal of performing phantomless calibration. A feasible way to perform such calculation would be to use a 3DUS probe to easily estimate these parameters by tracking overlapping volumes. This solution is only applicable to a limited number of US probes. A promising solution for 2DUS probes, is to use an image-based approach, by using the fact that US beam is several millimeters wide in the elevation direction. Each pixel is formed by the back scattered echoes from an approximately ellipsoid called the resolution cell. By moving the US probe out-of-plane, the ellipsoidal resolution cells of pixels in the neighboring scans will overlap, and they should be statistically correlated. By modeling this correlation, we can estimate the out-of-plane offsets between two US images [Prager-2003]. A serious complication of this method is that the theory of correlation holds only for fully developed speckle (FDS). One of the main challenges of this work is to accurately identify the regions of FDS from the non-FDS regions. Appendix D shows a recent collaborative work done by Hassan Rivaz to segment these FDS regions accurately. The out-of-plane motion estimation module is not part of the self-calibration algorithm I present in the coming section.

## 7.3 Methods and System Integration

### 7.3.1 Experimental system

In our experimental prototype (Figure 7.2), we used a SONOLINE Antares US scanner (Siemens Medical Solutions USA, Inc. Ultrasound Division, Issaquah, WA), with a Siemens VF 10-5 linear array probe. The patient was replaced with a tissue mimicking agar phantom. The US probe was held against the phantom in a rigid acrylic holder mounted on an adjustable steady arm. The arm had a dual purpose: to adjust the spatial position of the tracked US probe over the calibration phantom, and to ensure temporal synchronization between the tracker and the US scanner. Multiple optical markers were attached to the probe holder, which then were tracked by an OPTOTRAK device (Northern Digital Inc.).

The tissue mimicking phantom provides realistic images of fully developed speckles. Its construction is based on a recipe by Fenster et al. [Rickey-1995]. Three percent by weight of agar gel (A-7002 Agar, Sigma-Aldrich, St. Louis, MO) was added to distilled water, with three percent by weight 50 $\mu$ m cellulose particles (S-5504 Sigmacell, Sigma-Aldrich), and with seven percent by volume glycerol (W25250, Sigma-Aldrich). The mixture was heated to 92C°, stirred constantly, gradually cooled to 60C°, and then poured into a container mold. We also introduced specular features and structures to mimic bone appearance and to allow for testing algorithmic performance under different echogenicity conditions.

### 7.3.2 Algorithm workflow

The workflow in the real-time self-calibration QC procedure is described in Figure 7.4. The *Acquisition Module* receives the US video signal and tracker readings, from which it prepares synchronized indexed sequences of images and tracking information. The

*Motion Analyzer* sorts out the types of motions in these sequences and sends a control signal for the *Real-time Tracker*, which recovers the  $A$  matrices. Finally, the  $AX=XB$  solver receives corresponding  $A$  and  $B$  data, and recovers the  $X$  calibration matrix. The *Quality Control* unit analyzes the new calibration and compares it with previous runs. In

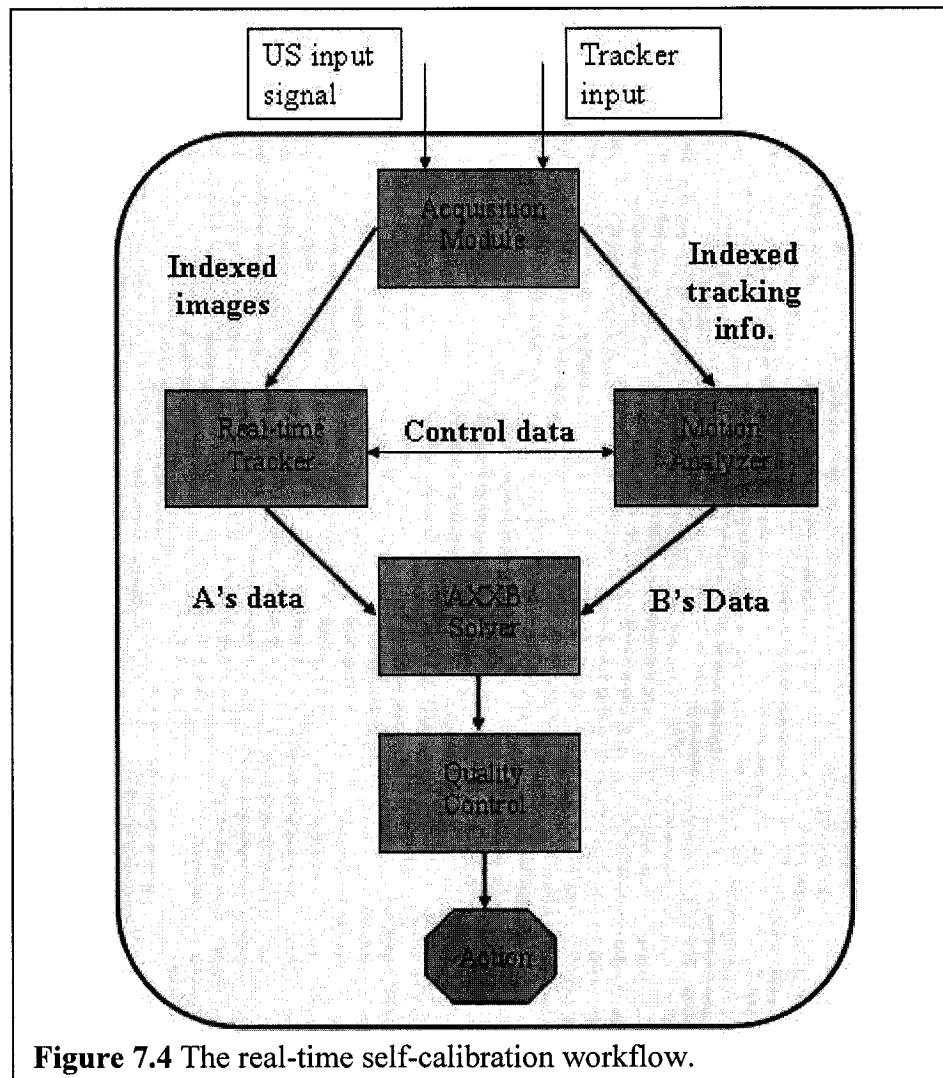


**Figure 7.4** The real-time self-calibration workflow.

case of suspected discrepancy, an appropriate *Action* is initiated to deal with a hazard condition. This action could range from generating a warning message to demanding a

halt of the procedure and full recalibration of the system. The algorithms can be described as follows:

```
Step 1: Capture US and Tracker data  
Step 2: Compute B's  
Step 3: Apply critical motion (CM) test on B's data  
Step 4: if (CM exists in B's)  
        Test this motion by the image tracker and generate A's  
        If (CM exists in A's)  
            Generate A's  
        Else go to step 1  
    Else go to step 1  
Step 5: Run AXXB solver on the pairs of A's and B's  
Step 6: Comparing with previous values;  
        Go to step 1
```

### 7.3.3 Real-time tracker

As mentioned above, the role of the “Real-time Tracker” is to recover the  $A$  matrices, the motion of the US image in construction frame, as it was described in Figure 7.1. It is necessary to compute the relative motion in pairs of ultrasound images for which the absolute (tracked) motion is known. We accomplish this using direct image registration methods similar to those described in [Hager-1998]. Specifically, we introduce an intermediate “warped” image representation  $W$  defined as:

$$W(u, t; p, \alpha) = I(Rot(\alpha)^* u + p)$$

where  $u=(x,y)^T$  is an image location,  $P$  is a translation offset, and  $\alpha$  is an interframe rotation. Let  $W(t; P, \alpha)$  denote the column vector constructed by stacking the value of  $W$  for all possible image locations  $u$ . We then compute an estimate of the offset  $(P_b, \alpha_b)$  between images at time  $t$  and  $t+d$  by iterating the following equation:

$$(p_t^k, \alpha_t^k) = (p_t^{k-1}, \alpha_t^{k-1}) + J^\dagger(W(d+t; p_t^{k-1}, \alpha_t^{k-1}) - W(t; 0, 0))$$

where  $J^\dagger$  denotes the pseudo-inverse of the Jacobian matrix of  $W$  with respect to  $P$  and  $\alpha$ . The values of  $(P_b, \alpha_b)$  is taken from the previous frame.

## 7.4 Experiments and Results

We used the experimental system to collect 5 datasets, altogether containing 20 motions in B-mode with a rectangular view and 8cm depth. One of the datasets contained 4 motions and was obtained under a faulty condition: we purposely flipped lateral polarity of the B-mode image to simulate a common operator error. Table 7.1 shows the rotation and scale reported by the self-calibration QC system.

	<b>Magnitude of rotation (Rodrigues form)</b>	<b>Scale in x and y (mm/pixel)</b>	
<b>Dataset-1</b>	3.163	0.22	0.26
<b>Dataset-2</b>	3.072	0.23	0.26
<b>Dataset-3</b>	2.992	0.23	0.27
<b>Dataset-4</b>	3.008	0.23	0.29
<b>Dataset-5</b>	0.086	0.24	0.27

**Table 7.1** QC system report on rotation and scale.

In testing the image tracker, we used  $d=10$  step size, for which images were matched with

an RMS gray-scale error of less than 2% of signal value, suggesting a registration error of less than 1/10 pixel [Hager-1998].

The heart of the self-calibration QC system, as seen in Figure 7.4, are the real-time image tracker and  $AX=XB$  solver. The image tracker is sensitive to the step  $d$  between registered images, while the  $AX=XB$  solver is sensitive to the number and type of motions used to recover the calibration parameters. The upper graph in Figure 7.5 illustrates the relation between the recovered scale and number of images and the step size  $d$  taken in the image registration algorithm. The “bad” case appears in the upper graph for the first 30 images and the “good” case is in the lower graph. Note that the number of images can be represented by the scanning time, where 1 second corresponds to 33 frames, sweeping over a certain distance covered with the given scanning velocity. The x-axis represents the number of frames used in the  $AX=XB$  solver and the y-axis is the scale ratio in mm/pixel. The upper figure is for  $\lambda_x$ , the lower is for  $\lambda_y$ . Figure 7.5 also shows convergence for the scale ratio under different image registration steps (small  $d$ : 1, 3, and 5; large  $d$ : 10, 20, 30, and 40). Note that as we increase the step size, we also introduce a delay equal to the step size before we start estimating a given parameter. This is because we must wait for the  $d^{th}$  image to arrive.

We have found that steps of larger than 40 frames are not reliable for tracking and predicting speckle pattern motion. At the same time, these kernels are temporarily distant, suggesting that we have to wait for about 2 seconds to detect a faulty condition. Small tracking steps need a few readings to start convergence, due to the small motions they deliver to the  $AX=XB$  solver. Note that the convergence for  $d= 1, 2, \text{ and } 3$  appears after 20 small motions for  $\lambda_y$  and after 30 small motions for  $\lambda_x$ . This is principally due to the type of motion present. The intuition behind this is that we cannot estimate a scaling

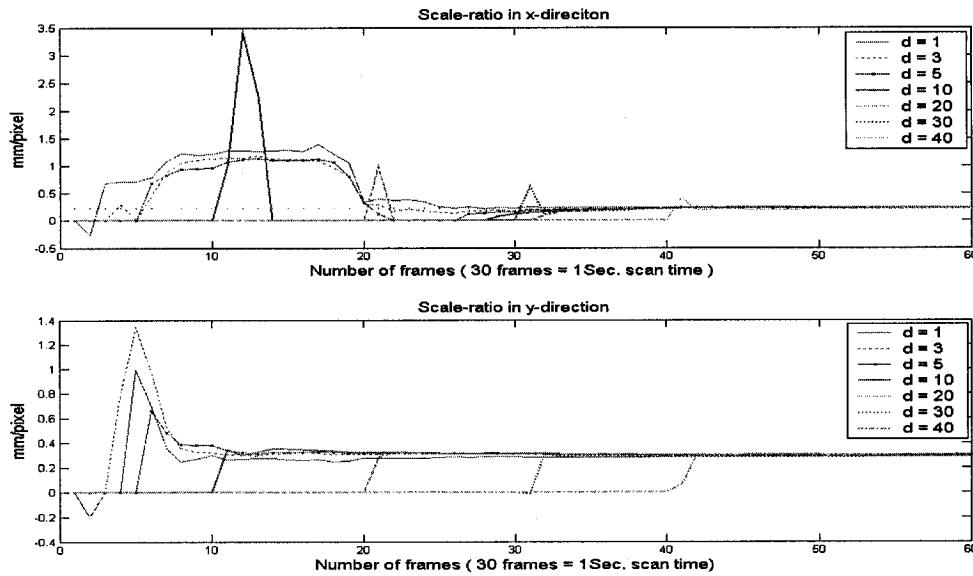


**Figure 7.5** Relation between the recovered scale and number of images & step size.

parameter in a direction normal to the direction of motion. Similarly, favorable results were obtained for the rotation component, as shown in Figure 7.6. We can conclude that given the right motion, a kernel of 10 steps ( $d=10$ ) converges in 10-20 steps, meaning 0.3-0.6 seconds with a total travel of  $\sim 1.5\text{mm}$  (scanning speed @ 3mm/sec.)

## 7.5 Conclusions and Future work

In general, the self-calibration QC system reported the calibration matrix robustly and consistently. It recovered the correct calibration parameters under normal working conditions by monitoring the constancy of the calibration matrix and it did not produce false alarms. It also managed to distinguish a faulty condition by catching an outlier calibration matrix. By far the most significant work item in progress is to extend the self-calibration QC framework to estimate out-of-plane free motion of the US probe, thereby providing full calibration in-vivo, real-time, as the patient is being scanned, which will

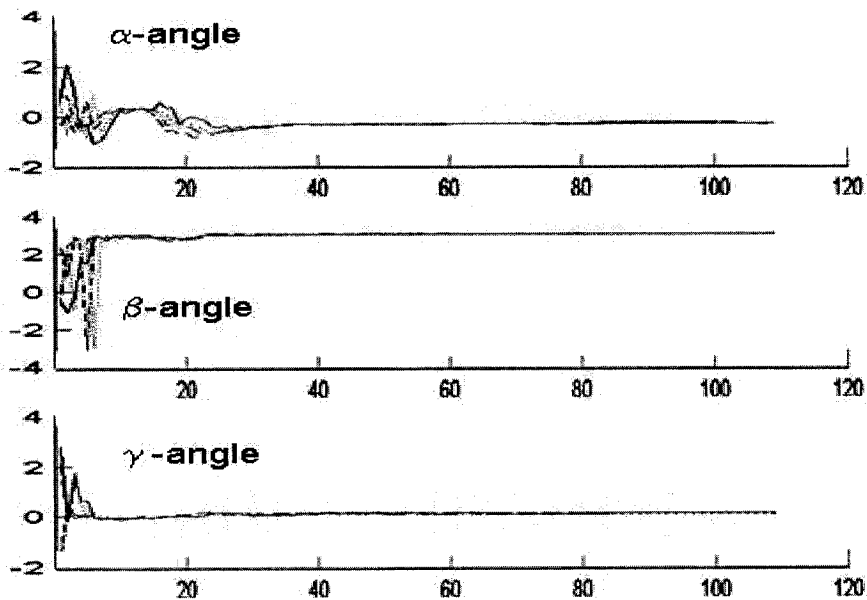


**Figure 7.6** Convergence for the three rotation angles ( $\alpha, \beta, \gamma$ ) under 4 different small steps  $d=(1,2,4,5)$ .

obviate phantom-based calibration. The real-time performance of the self-calibration QC system allows for averaging hundreds of independent calibrations from a single sweep, which in turn promises to retire crosswire-based reconstruction accuracy evaluation and at last free US calibration from any phantom whatsoever. In a future phase of this work I would like to compare the accuracy of our current self-calibration against published off-line calibration methods. Last but not least, the sensitivity and specificity of the self-calibrating QC system should be examined. A clinical-grade QC system must catch all faulty conditions i.e., have a high degree of sensitivity, yet it must not produce false alarms, which would halt the clinical intervention i.e., have high specificity. Altogether, the combined QC and self-calibration system appears to have high practical utility for clinical departments that use and maintain tracked ultrasound systems.

## **Part-III: Chapter 8**

# **Monitoring Ablative Therapy**

### **8.1 Introduction**

Primary and metastatic liver cancer represents a significant source of morbidity and mortality in the United States and worldwide [Nakakura-2000]. Increasing interest has been focused on treatment using thermal ablative approaches, in particular, radiofrequency ablation. These approaches utilize image-guided placement of a probe within the target area in the liver parenchyma. Heat created around an electrode is conducted into the surrounding tissue, causing coagulative necrosis at a temperature between 50°C and 100°C [Buscarini-1997]. Key problems with this approach include: 1) localizing and targeting of the tumor, and 2) monitoring the ablation zone. The first problem has been previously addressed by developing robotic 3DUS systems for guidance of liver ablation and by applying online calibration methods. The second problem, which is the subject of Part-III of this thesis, is monitoring the zone of necrosis during ablative therapy.

Current monitoring approaches often result in either local failure or in excessively large zones of liver ablation. Some ablative devices employ temperature monitoring using thermisters built into the ablation probes. However, these temperatures reading only provide a crude estimate of the zone of ablation. Non-invasive monitoring techniques

include ultrasound imaging, magnetic resonance imaging , computed tomography, X-ray fluoroscopy, and elasticity imaging.

***Ultrasound imaging.*** Conventional ultrasonographic appearance of ablated tumors only reveals hyperechoic areas due to microbubbles and outgassing. Vaezy et al. [Vaezy-2001] suggests that using the right High Intensity Focused Ultrasound (HIFU) exposure intensities and duration leads to increased echogenicity in the B-mode image, which may be used to observe the location of induced ablation. According to Kolen et al. [Kolen-2003], HIFU experiments show that B-mode imaging might be inadequate. The size and shape of the hyperechoid region in the B-mode does not always correspond to the damage seen on the gross-pathology pictures. In this chapter we will show that B-mode imaging tends to overestimate RF ablation compared to gross-pathology ( $p=0.001$ ), which we find to be highly significant.

***MRI imaging.*** Magnetic resonance imaging can monitor temperature changes (MR thermometry), but is expensive and lacks implementation flexibility. MR thermometry provides a low frame rate and requires specifically designed MRI-compatible equipment. [Graham-1999].

***CT and X-ray.*** These technologies are capable of measuring soft tissue mass density changes [Bentzen-1984]. Recently, Salas et al. [Salas-2004] introduced a new method that should aid all thermal ablative techniques. The method requires an X-ray imaging system with a digital detector. During ablation, periodic X-ray exposures are taken and subtracted from the mask, which is an x-ray for the region, before depositing any thermal treatment. The successive subtracted images show the propagation of the change in density indicative of coagulation. This technology was recently adopted by Abla-Tx [Ablatx-web], a private company founded in 2005 to develop a software based algorithm to monitor thermal ablation of tumors.

**Ultrasound elasticity imaging.** Also known as elastography, USEI, first introduced by Ophir [Ophir-1991], has emerged as a potentially useful augmentation to conventional ultrasound imaging. USEI for monitoring ablation [Righetti-1999, Varghese-2002, Varghese-2003, Curiel-2005, Kolen-2003, Boctor-2004e] was made possible by the following observations: (1) different types of tissues may have significant differences in their mechanical properties and (2) the information encoded in the coherent scattering, known as speckles, may be sufficient to calculate these differences following a mechanical stimulus. Elastography is an excellent tool to delineate ablation extension, providing that less aggressive thermal techniques are used. Using HIFU techniques with appropriate power settings to minimize the effects of gas and bubbles help to acquire more coherent ultrasound data and also generate immediate high quality strain images during and after ablation [Righetti-1999, Curiel-2005]. To the best of our knowledge, Bamber et al. and Varghese et al. were the first to use elastography in monitoring RF ablation, which is a more aggressive ablation technique, compared to HIFU and is known to produce more dynamic changes in the US image. Both groups use RITA™ medical ablation devices, a needle-like ablator with number of deployable tines at the tip. As expected, elastography produces excellent results with previously ablated ex-vivo samples [Varghese-2003]. By previously ablated samples, we mean ablating ex-vivo liver first and then embedding the sample in gel and within few hours collecting elastography data. However, the three experiments reported in Kolen's thesis [Kolen-2003] indicated obvious degradation in the resulting strain images, which were shown as overestimation compared to gross-pathology and attenuation images. These degradations [Boctor-2004e] might be attributed to many factors, including decorrelation and shadowing in the US data immediately collected after ablation, freehand data collection, ablator tool shadowing, averaging over a substantial range of induced strain, and algorithms used. Recently, Varghese et al. [Varghese-2004] reported degradation of strain images due to

gas and bubbles generated during ex-vivo ablation when using similar ablation protocols to those used in Kolen's thesis.

Augmenting US with elasticity imaging appears to be the least complicated, cost-effective, and feasible option for monitoring ablation, given the proven success of utilizing US to plan and guide initial ablation. This motivated us to study the extent of the reported degradation by Kolen, if exists, using the Radonics<sup>TM</sup> RF ablation device, which is more aggressive than RITA in producing a larger volume of ablation in a shorter time. We also wanted to study a fast method of collecting 3D strain data, even though it comes with more decorrelation noise. Finally, we wanted to implement a framework that can deal with uncertainties (degradation due to ablation, decorrelation in 3D data, and possible in-vivo tissue motion as reported recently by Ophir's group [Chandrasekhar-2006]) and that still can report an average shape for the ablation zone robustly, as shown in Chapter 9. In the next section, we will present the theoretical background and the state of the art in the elasticity imaging field.

## 8.2 Strain Imaging and Prior Art

The main goal of elasticity imaging is to provide remote and non-invasive representation of the mechanical properties of tissues. The elastic properties of tissues cannot be measured directly, so a mechanical disturbance must be applied, and the resulting response is then evaluated. We can categorize elasticity imaging approaches into static (strain based), dynamic (wave based), and mechanical (stress based) methods [Emelianov-2003]. The strain-based approach images internal motion under static deformation; the dynamic approach images shear wave propagation; and the mechanical approach measures surface stress distribution. The main components of these approaches are as follows: 1) Data capturing during externally or internally applied tissue motion or

deformation, 2) Tissue response evaluation (displacements, strain, or stress), and, if needed, 3) the reconstruction of the elastic modulus based on the theory of elasticity.

The imaging method adopted in this project is the ultrasound strain-based approach known as elastography, first introduced by Ophir et al. [Ophir-1991]. Elastographic imaging techniques have proved that information about mechanical properties can be derived from RF ultrasound images. The objective is to acquire RF US data from a tissue in both rested and stressed states, then to estimate the induced strain distribution by tracking speckle motion (Figure 8.1). The Young's modulus and Poisson's ratio completely describe the elastic properties of an elastic, linear, homogeneous, and isotropic material. Moreover, most soft tissues are incompressible (Poisson's ratio is nearly 0.5) and the Young's modulus can describe the elastic properties. According to Ophir et al. [Ophir-1991], larger compressors cause more uniform axial stress fields which allow strain to provide a first order estimate of the Young's modulus. This explains why most elastographic investigations rely on the estimation of strain.

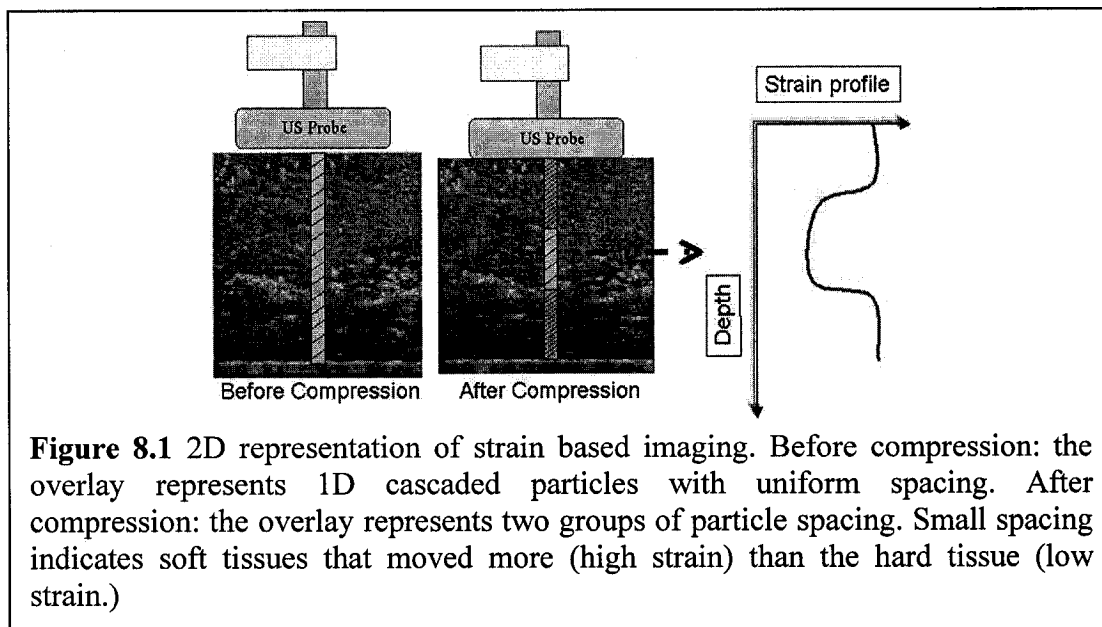


**Figure 8.1** 2D representation of strain based imaging. Before compression: the overlay represents 1D cascaded particles with uniform spacing. After compression: the overlay represents two groups of particle spacing. Small spacing indicates soft tissues that moved more (high strain) than the hard tissue (low strain.)

To extract axial strain images, we start from RF data as input; create the displacement and correlation images; then differentiate the axial displacement field and estimate the axial strain tensor ( $\epsilon_{11}$ ). Obviously, obtaining local strain values with high accuracy depends on precise measurement of local tissue displacement. A significant problem is the loss of similarity (correlation) between the pre- and post-deformed images. During the past few years, several groups have investigated this problem and have devised various strategies for increasing the reliability of the cross-correlation function including:

- 1) Choice of the processing parameters, kernel length and amount of kernel overlap [Bilgen-1997];
- 2) Tracking RF-data instead of envelope-detected data when small displacements are involved [Ramamurthy-1991];
- 3) Temporal stretching that includes adaptive local and global companding [Chaturvedi-1998]; and
- 4) Axial and lateral RF-data interpolation.

In addition to these enhancements for displacement estimation, there has been active research in improving the quality of strain estimation, including:

- 1) A least squares strain estimator (LSQSE) has been suggested [Kallel-1997];
- 2) Multi-step compression [O'Donnell-1994] to increase SNR; and
- 3) Average and median filtering [Doyley-1999].

There is a recent review paper by Ophir et al. which summarizes current research activities for strain estimation algorithms and their various clinical applications [Ophir-2002].

### **8.3 Liver Elasticity Study**

A number of researchers have already studied the elastic properties of liver tissues using both healthy and diseased liver tissue excised from experimental animals [Yeh-2002]. However, research about the mechanical elastic testing and the modeling of liver tissue undergoing different radio frequency treatment protocols is still lacking. In 2003, our

research team<sup>†</sup> began to study the variation of liver elastic properties under thermal ablation. Our study was designed to measure the elasticity, i.e. the elastic modulus and the shear modulus, of recently deceased calf liver undergoing RF ablation. Additionally, pathological studies were carried out to characterize the changes in histology at various stages in the progression of RF ablation. Last year, Varghese et al. [Bharat-2005] published similar elasticity study using an RITA ablation device under different ablation conditions.

### 8.3.1 Materials and methods

Calf liver tissue was used in all of the liver elasticity experiments. Fresh whole liver specimens between 2.2kg and 5.5kg were collected from a local food store. Each specimen was first de-veined, packaged in a plastic airtight bag, and chilled to 5°C. The specimens were then taken to the lab for same day testing. The liver was cut into approximately 15cm x 10cm x 5cm blocks.

Lesions for elasticity testing were induced using an RITA™ Model 1500 Radio Frequency generator with a multi-tined ablator probe (Figure 8.2-Left). A *Windows 95* laptop recorded real-time temperature readings through the ablator probe's built-in thermisters. The liver block was carefully placed and wrapped in aluminum to ensure proper conductivity. A standard adhesive ground pad was placed underneath the aluminum wrapped liver block to draw the electrical current away from the ablator probe. The ablator probe was inserted horizontally so that the probe tip was within 3cm of the liver block's center of mass (Figure 8.2-Right). This offset was required to accommodate the deployment of the ablator probe tines to ensure a spherical RF lesion with its center

---

<sup>†</sup> The project led by Ambert Young (a Stanford student who worked during summer 2003), Michael Awad (a surgical resident in Johns Hopkins) and Emad Boctor.

concentric with the sample block's center of mass. Once the probe was in position the tines were deployed to create a 3cm diameter lesion.

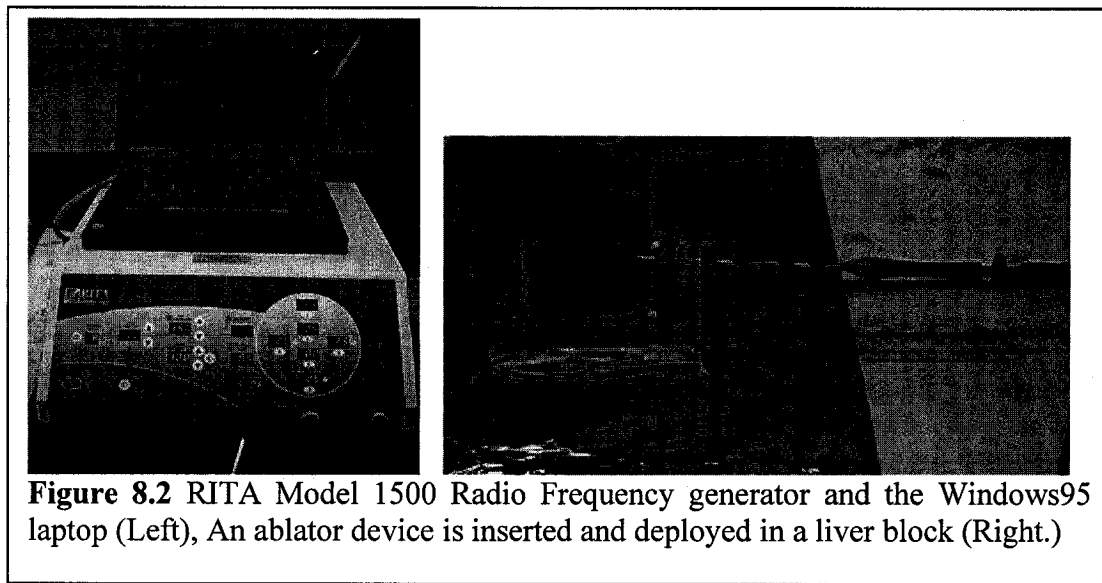


**Figure 8.2** RITA Model 1500 Radio Frequency generator and the Windows95 laptop (Left), An ablator device is inserted and deployed in a liver block (Right.)

A total of seven liver blocks were used to produce the samples for the main elasticity tests. Each block represented a target temperature group from 20°, 50°, 60°, 70°, 80°, 90°, to 100°C. Once the probe was correctly inserted into the block, the RF generator was preset to the target temperature using a maximum output of 100W. The delivery of RF power was continued until the target temperature was reached at which point the target temperature was maintained constant for 10 minutes (Figure 8.3). The probe was then removed and the liver block was allowed to cool to room temperature. The approximate spherical lesion was then segmented and removed from the surrounding tissue using the surgical scalpel. Five cubes were extracted from different lesions with the scalpel to have compression results in groups of five samples per target temperature group (Figure 8.4). The mass of each sample was measured on a Sartorius electronic balance with an accuracy of 0.0001 grams.

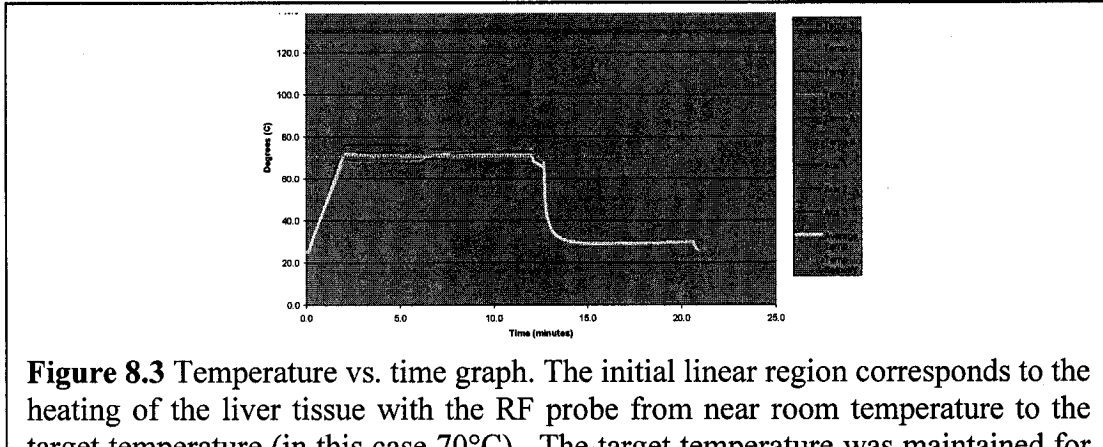


**Figure 8.3** Temperature vs. time graph. The initial linear region corresponds to the heating of the liver tissue with the RF probe from near room temperature to the target temperature (in this case 70°C). The target temperature was maintained for 10 minutes. The RITA RF probe had an array of 5 thermisters and the generator averaged the individual readings and used the average value in a feedback loop to maintain the constant average temperature. After the 10 minute target interval, the RITA generator entered a brief cool down cycle as seen in the graph at the steep drop off point. Similar temperature outputs were obtained for each temperature grouping.

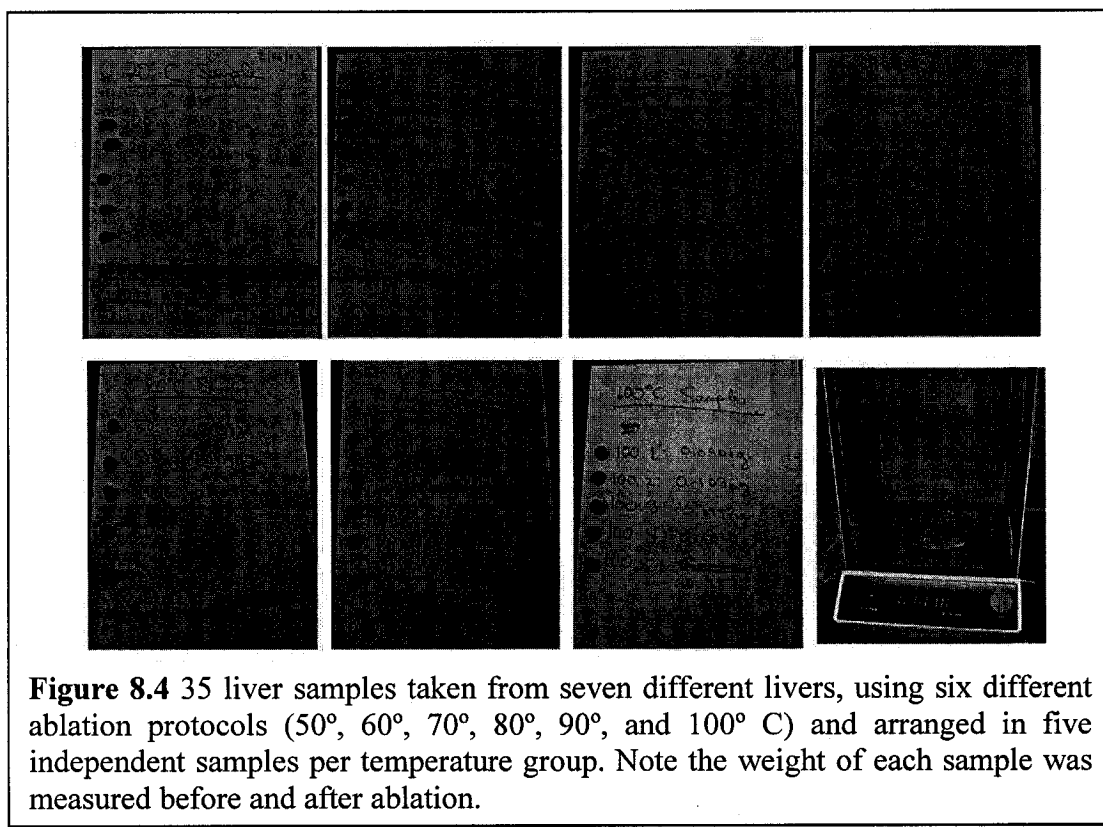


**Figure 8.4** 35 liver samples taken from seven different livers, using six different ablation protocols (50°, 60°, 70°, 80°, 90°, and 100° C) and arranged in five independent samples per temperature group. Note the weight of each sample was measured before and after ablation.

Elasticity testing was performed on a Rheometric Scientific RFS III rheometer connected to a Windows 98 PC for rheometer control and data extraction (Figure 8.5). Specimens were placed in the center of the rheometer tray and the flat ceramic anvil was advanced to near touching. Each sample was zeroed by advancing the compression anvil until the force transducer recorded 1 gram mass. The gap between the position of the anvil and the known displacement to the tray surface was taken to be the starting height in calculating strain values. Each specimen was first subjected to a simple uniaxial compressive test immediately followed by a batch of dynamic shear tests. The uniaxial compressor was set to a maximum strain of 10% at a velocity which depended on the

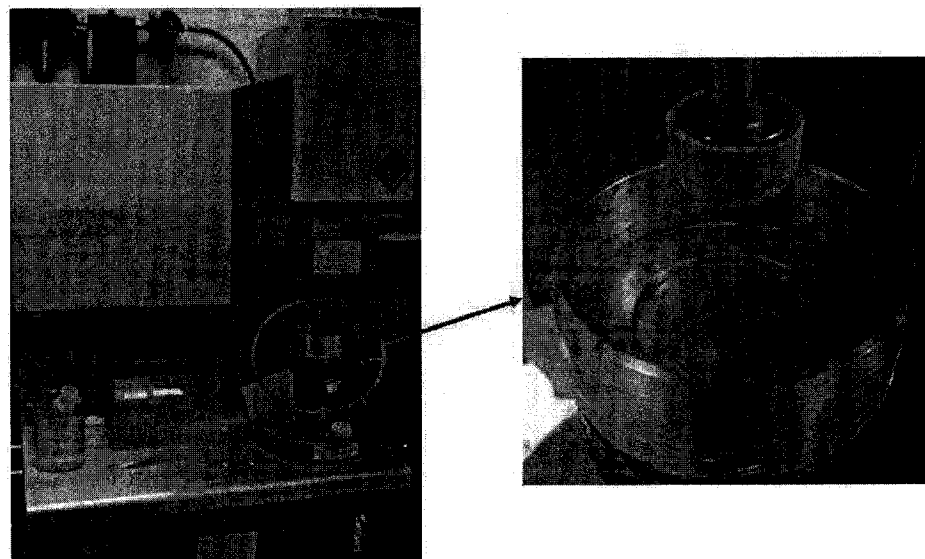


**Figure 8.5** Rheometric Scientific RFS III rheometer and a zoomed picture to demonstrate how specimens were placed in the center of the rheometer tray.

following formula: (maximum strain) \* (sample height) / (duration of compression) where the duration of the compression was set to 20 seconds. Once the sample was compressed to 10% strain, the strain level was maintained for 180 seconds to allow the

sample to equilibrate and to observe the viscoelastic properties of the soft tissue. After the 200 second elapse for the axial compression test, the dynamic shear tests were immediately initiated. The dynamic shear tests included oscillations at variable frequencies at 100, 63, 40, 25, 16, 10, 6, 4, 2.5, 1.6, 1, 0.6, 0.4, 0.25, 0.15, and 0.1 rad/sec.

At the completion of the axial compression and dynamic shear tests, the sample was sealed in a vial of formalin solution (Figure 8.6), embedded in paraffin, and set aside for histological studies. The preserved samples were sent to the pathology lab where slides were cut for the liver samples at each of the temperature groups (20, 50-100°C). For each temperature, a hematoxylin and eosin (H & E) stain and a reticulin stain were cut and photographed.

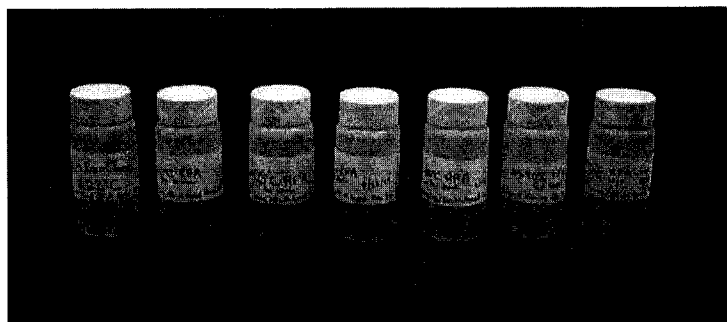


**Figure 8.6** 35 samples kept in formalin solution for histological examinations and arranged from left to right according to temperature, starting from room temperature to 100° C.

#### 8.4 Robotic Strain Imaging System

The liver elasticity experiments described above led us to the second phase of this project by designing and implementing a robotic strain imaging acquisition system, shown in Figure 8.7. We used a Siemens Antares US scanner (Siemens Medical Solutions USA, Inc. Ultrasound Division, Issaquah, WA) with an ultrasound research interface (URI) to

access raw RF data. A Siemens VF 10-5 linear array was used to acquire data. The tracking beams were standard B-mode pulses (6.67MHz center frequency, F/1.5 focal configuration, apodized, pulse repetition frequency (PRF) of 10.6KHz, with a pulse length of 0.3 $\mu$ s). The US system utilizes dynamic focusing in receive such that a constant F/number of 1.5 is maintained. The robot used was a Laparoscopic Assistance Robotic System [Taylor-1995]. The LARS is a kinematically redundant manipulator composed of a translation component with a distal remote center of motion component, which provides three rotations and one controlled insertion motion passing through the RCM point. The LARS end-effector, also shown in Figure 8.7, contained a six degrees-of-freedom force/torque sensor, a translation stage to induce tissue compression with an accuracy of 0.05mm, and a rotation stage to sweep an US volume. As discussed in Chapter 2, we demonstrated improvements in the 3DUS volume quality, repeatability, planning and

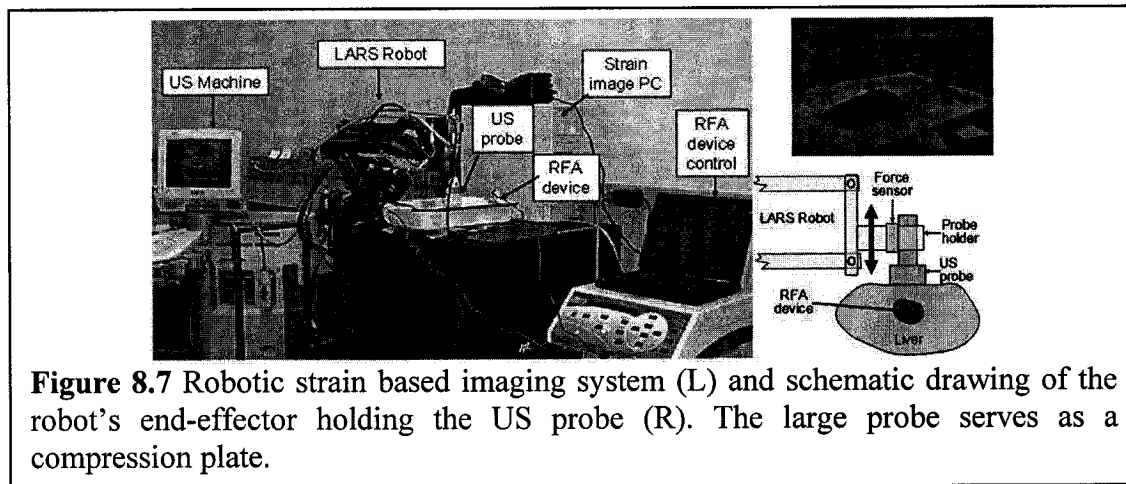


**Figure 8.7** Robotic strain based imaging system (L) and schematic drawing of the robot's end-effector holding the US probe (R). The large probe serves as a compression plate.

targeting with robotic 3DUS vs. freehand scanning [Boctor-2004b]. In this project, the LARS also played a second role by helping generate controlled 3D strain data. A dual processor workstation interfaced to all system components and capable of controlling LARS to generate 3DUS data with controlled pressure.

The thermal ablation system for the first experimental runs was an RFA generator (RITA Medical Systems, Inc., Mountainview, CA) with XL probe. A set of experiments was based on dynamic monitoring of strain in whole fresh bovine liver, ex-vivo. The specimen was soaked in degassed water to remove air pockets, and then was placed into a metal tank to facilitate grounding for the RFA device (Figure 8.7) The protocol of the dynamic study was as follows: (1) System initialization comprised initializing the robot, Antares in URI mode, the dual processor system, and the ablator device. (We fixed the ablator shaft in a stationary pose with respect to the robot and opened up the tips gradually during the study. (2) Alignment comprised setting the robot arm at 0°C such that a part of the ablator shaft is always present in the US image. The 90°C orientation then captures the formed lesion at the tip of the RFA device. (3) Data collection at room temperature, for reference purposes, and at 50°, 75°, and 100°C, for 7 minutes. During the acquisition phase the robot moves in multiple compression steps and records force and displacement measurements (boundary conditions). Displacements have been used to optimize the Time Delay Estimation (TDE) problem while the force data was not utilized in the calculations. The resulting strain images suffered from substantial degradation [Boctor-2004e] due to multiple reasons, including compression non-uniformity, lack of algorithms optimization, and acoustic shadowing by the ablator etc. But as an initial work step, the results were promising and we were able to discern the presence of necrosis at different temperatures. This study, however, was limited and did not allow us to draw conclusions about the feasibility of using 2D or 3D strain in practical and reliable manner.

To the best of our knowledge, Ophir's group [Righetti-1999, Kallel-1999] was the first to use elastography in monitoring HIFU ablation. The work done by Righetti et al. shows excellent correlation between elastography and gross-pathology in identifying induced

thermal therapy. This work, however, did not report use of the aggressive RF ablation techniques. At the time as we started building our system in 2003, there were two research groups (Varghese et al. in U.S. and Bamaber et al. in UK) applied elastography to monitor RF ablation. A. Kolen (Bamber's PhD student) reported on the use of freehand elastography to monitor RF ablation immediately after thermal deposition by using a RITA ablation device in his thesis [Kolen-2003]. He conducted the study on three samples and concluded that elastography did not discern the shape and size of the actual ablation accurately. In his thesis, the registration process between elastography and gross-pathology is not clear, nor is it clear whether the observed overestimation is due to freehand acquisition or is due to degradation from the aggressive RF ablation. At the same time, Varghese et al. [Varghese-2003] reported excellent correlation between elastography and gross-pathology to monitor RF ablation using an RITA ablation device. These excellent results, however, are to be expected as they used large compression pads ensuring uniform stress and acquired elastography data few hours after ablation. These studies motivated us to design an experiment setup to study the feasibility of using elastography to monitor RF ablative therapy immediately, using Radionics RF ablation devices [DeOliviera-2005].

In our setup, we use a Radionics cool-tip ablative device that looks like a needle with no deployable tines at the end. The Radionics device is equipped with an internally-cooled electrode. With tactic internal electrode tip cooling – that avoids desiccation of tissue adjacent to the electrode and rises in impedance– radiofrequency induced coagulation necrosis is greater than that achieved with non-cooled electrodes. These cool-tip devices have two practical features for our experimental setup. First, it has a long active element at the tip that usually produces an oval or ellipsoidal necrosis shape. This feature is important to maximize the similarity between the elastography image and the

corresponding gross-pathology section (Figure 8.8). RITA devices usually produce spherical ablations. Second, we can easily relate the center of ablation in gross-pathology to the obvious needle location in B-mode before or after ablation (Figure 8.8). In case of RITA, there is no central tip location as the ablation comes from a peripheral group of tiny flexible needles.

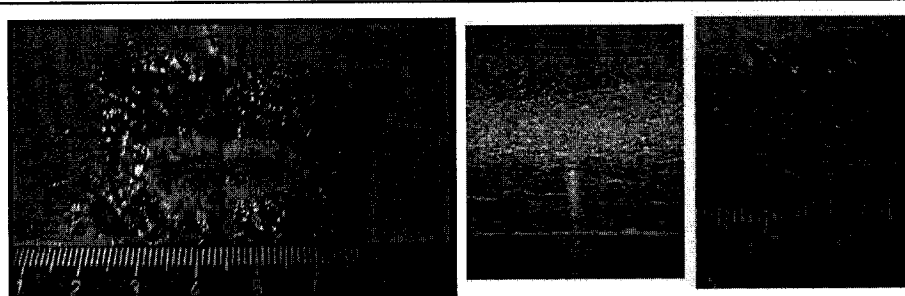


**Figure 8.8** Registration process between gross-pathology and US images. It illustrates the oval/ellipsoidal ablation shape along the needle axis, which tolerates the need of gross-pathology cutting sub-millimeter accuracy (Left), we can see the ablator tip in the B-mode and expect the ablation to build up around it (Right). Also due to cooling cycle induced vibration, the tip can be seen using color Doppler mode during aggressive ablation.

We integrated a compression plate with the US probe holder, as shown in Figure 8.9, to generate consistent uniform stress as recommended by [Ophir-1991]. With a careful calibration procedure to identify the center plane of the US beam in the elevation direction, we placed two small holes in a plane coincides with US beam's plane. These holes can be used to place needle fiducials to help to identify the gross-pathology section that matches the US plane (Figure 8.10). Also, liver samples were embedded in a block of transparent gelatin. The purpose of the gelatin is to give the liver sample more stability and extra support during ablation, imaging and cutting. Using gelatin support it was possible to fix the liver sample in a constant position, to provide a flat surface for the compression plate allowing for a consistent comparative study with identical boundary conditions, and to exhibit similar in-vivo tissue incompressibility due to the gelatin

composition (90% water). The gelatin was made by mixing 10% by weight porcine skin gelatin (Type A, 175 bloom, Sigma Chemical Co) with distilled water. We used a heating disc with a magnetic stirrer to thoroughly stir the mixture at 70°C for 30 minutes. We filled 30-40% of the 10\*10\*10cm<sup>3</sup> mold with the gelatin mixture, and after waiting for few minutes we placed the liver sample; we then poured the gelatin mixture at 40°C to fill the mold.

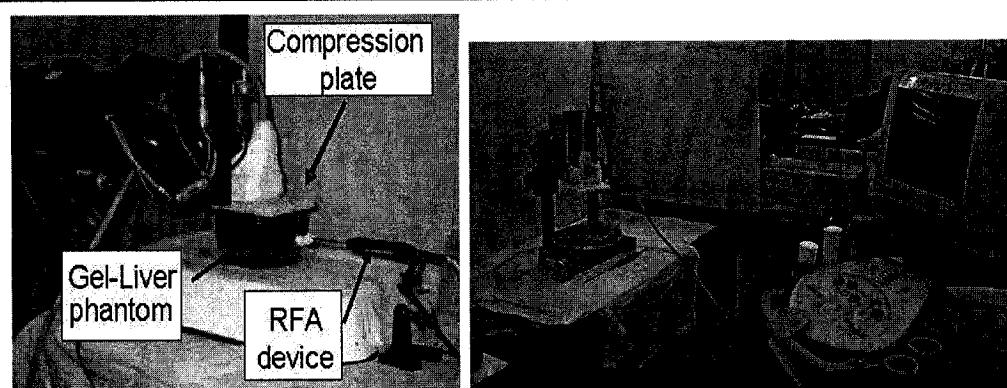


**Figure 8.9** LARS robotic system holding the US probe with a compression plate. It also shows the liver sample embedded in a transparent gelatin phantom, while active ablation is carried on using a Radionics ablation device (Left). To the right, the picture illustrates another setup using passive robotic system and the US Antares unit is shown.

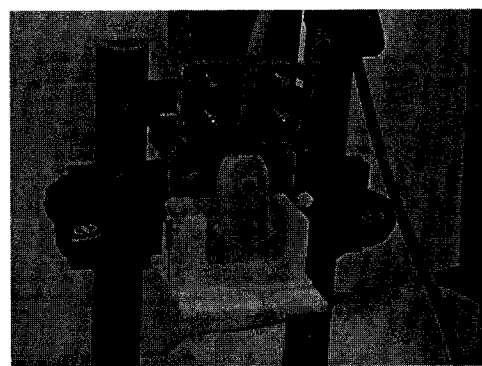
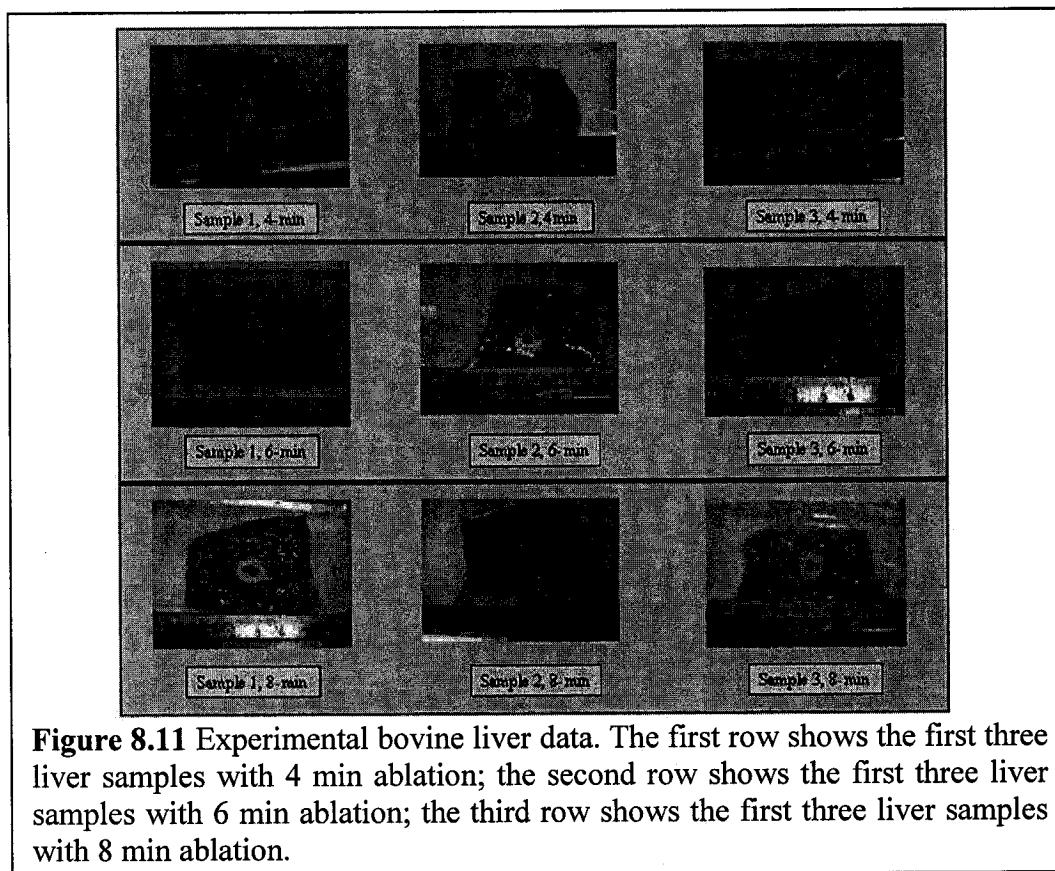


**Figure 8.10** US probe with the compression plate; and it also shows the needle that is used to introduce multiple fiducials in the transparent gelatin on both sides.

Calf liver tissue was used in all of the elasticity experiments. Fresh whole liver specimens between 2.2kg and 5.5kg were collected from a local food store. All specimens were first de-veined, packaged in a plastic airtight bag, and chilled to 5°C. The specimens were then taken to the lab for same day testing. We cut and prepared 18 liver samples from 4 different fresh calf livers. We devised three different ablation protocols with 4mins, 6mins and 8mins heating. The 18 samples were categorized into three groups of 4min, 6min, and 8min each. Figure 8.11 shows the first three samples of each group. Elastography data acquisition started immediately after ablation. We also



acquired 3D elastography data and 2D RF data during the ablation process at every 10 secs. After ablation, the samples were cut and pictured systematically. The offline data

analysis was double-blinded. The author generated the strain without having any gross-pathology information. Two surgical fellows<sup>†</sup> processed the B-mode and gross-pathology independently and blindly from the elastography images.

#### **8.4.1 3D Strain acquisition system**

As we mentioned earlier, our long term objective was to develop and integrate strain imaging in our interventional system with clinical feasibility. One important aspect is rapid generation of 3D strain in a feasible manner. As shown before in Chapter 2, targeting and planning under 3DUS guidance can substantially improved the accuracy compared to 2DUS guidance. We hypothesize that the same is true for strain information. With rapid 3D strain information, clinician could achieve better planning for the subsequent ablation. One can intuitively obtain 3D strain volume from cascading a number of 2D strain images. However, this requires special handling, more scanning time, and depends on an assumption that organ motion is minimal during scanning in order to generate a well registered volume. Obviously, such traditional 3D data collection method does not appear to be clinically feasible for strain. To the best of our knowledge, we were the first to report a patent [Boctor-2004c] that describes a method for generating 3D strain data that has the same rate of generating 3DUS data. The idea capitalizes on the fact that any US beam has an elevation thickness, which means that its resolution cell has a dimension in the elevation direction. In other words, any groups of scatterers extended in the elevation direction can be insonified partially with a moving resolution cell out-of-plane. This actually leads to gradual decorrelation proportional to the moved distance. The idea is to track the US probe --a calibration problem needs to be solved here again, either intrinsic calibration for the resolution cell or external calibration for the

---

<sup>†</sup> Dr. Michelle DeOlivera and her colleague conducted this study at Dr. M. Choti's lab at the medical school in Johns Hopkins.

transformation between US image and attached sensor-- and continuously acquire RF data that would enable us to reconstruct a 3DUS volume and at the same time to generate displacement fields and consequent strain volumes. We suppose that either freehand induced deformation or robotic induced cyclic deformation is enough to generate 1-2% strain. In both cases, we expect that displacement fields in this case should have more decorrelation noise.

We could not implement the previous idea of using overlapped tracked RF US data using the Antares US system, because it was dilcate to synchronize an external tracking device with RF acquisition. Instead, a special passive 4 DOF robotic microstage system was built, as shown in Figure 8.9-right and Figure 8.10. The system enables us to capture US volumes with different scanning mechanisms, including linear translation scan and rotation about an axis. The rotation about an axis motion requires a tedious calibration procedure to align the central point of the US probe to the center of the rotating stage that holds the subject (Figure 8.12). The acquisition of RF data is achieved manually in this offline system. Initially, we intended to prove the feasibility of generating 3D strain and 3DUS at the same rate on a phantom with a spherical inclusion (Figure 8.13). We built this phantom so that the inclusion is isoechoic, not clear in the B-mode. But it is nine times stiffer than the background. We expected more noise and decorrelation due to the offline acquisition. Prager et al. developed a real-time tracked RF acquisition system and worked on the same idea, which was first reported as a short paper on October, 2004 [Lindop-2004].

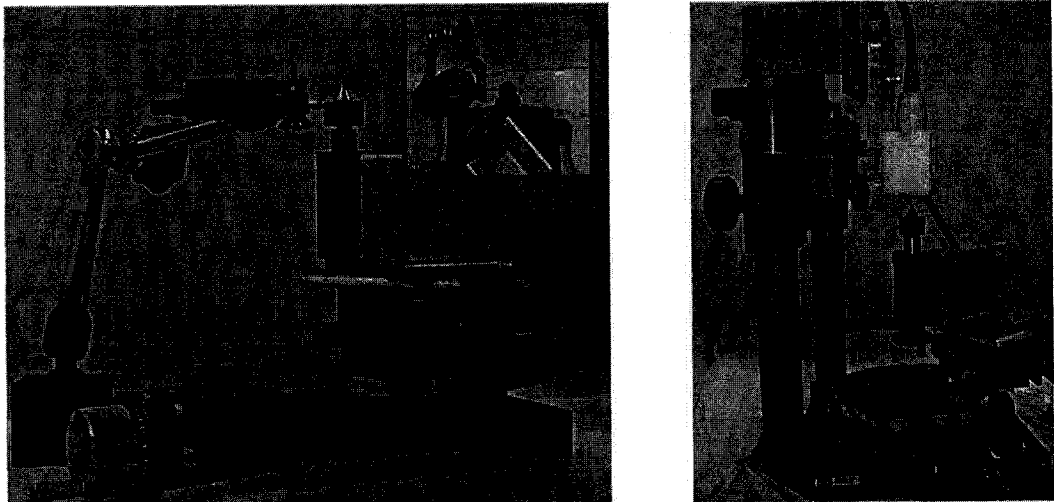


**Figure 8.12** The two steps calibration procedure. First, we locate the pointer at the center of the rotating stage by the help of a micrometer (Left). If the micrometer gives the same reading for the  $360^\circ$  rotation that means that the pointer is in the center of the rotating stage. Second, we adjust the location of the US probe using the 3DOF Cartesian stage and the US image feedback to center the array on the pointer head (Right.)

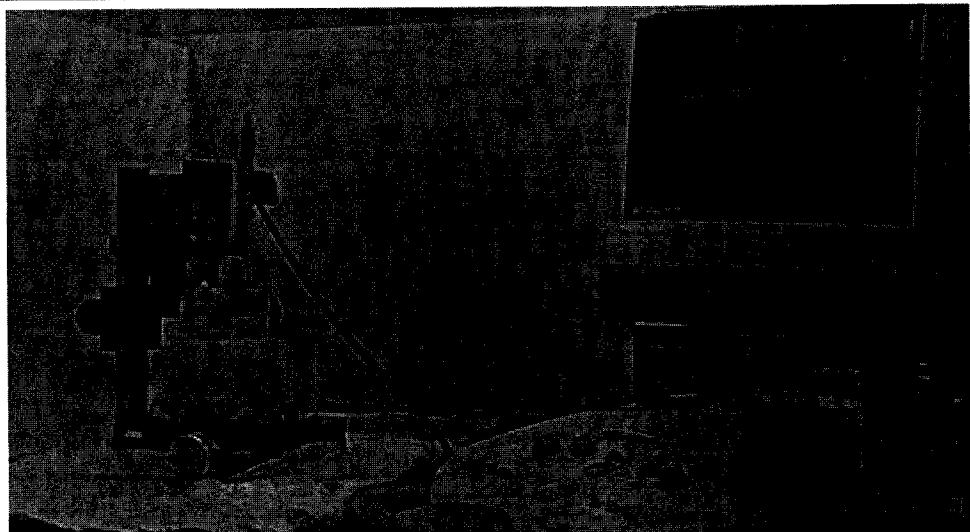
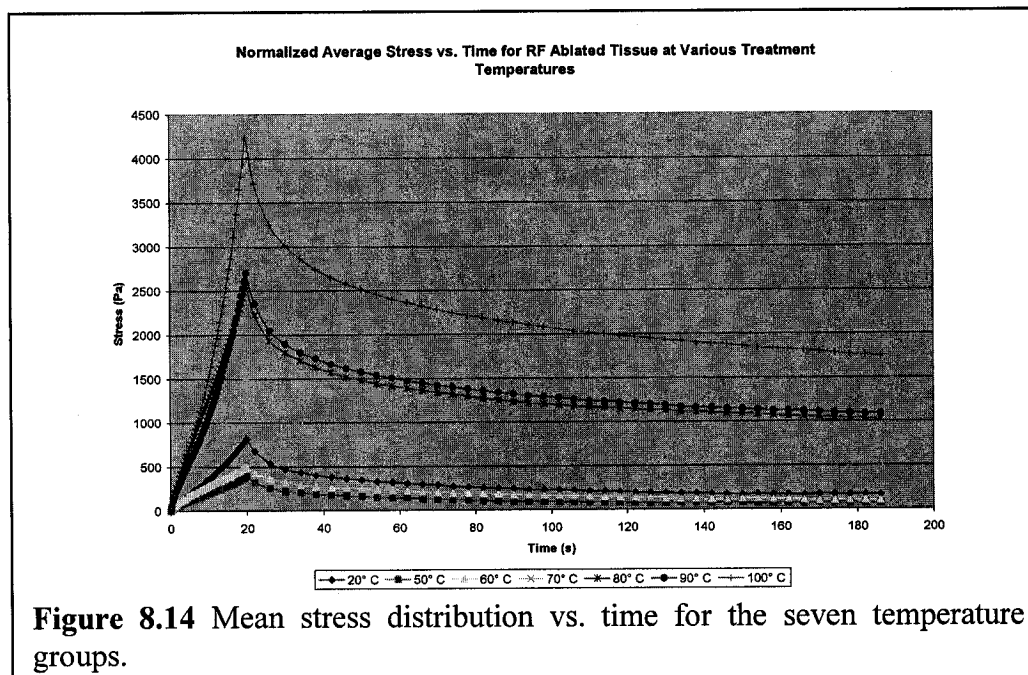


**Figure 8.13** 3D elastography acquisition setup for the  $10\text{ Cm}^3$  phantom with isoechoic spherical inclusion. The B-mode US image does not delineate the location of the enclosed lesion.

## 8.5 Experiments and Results

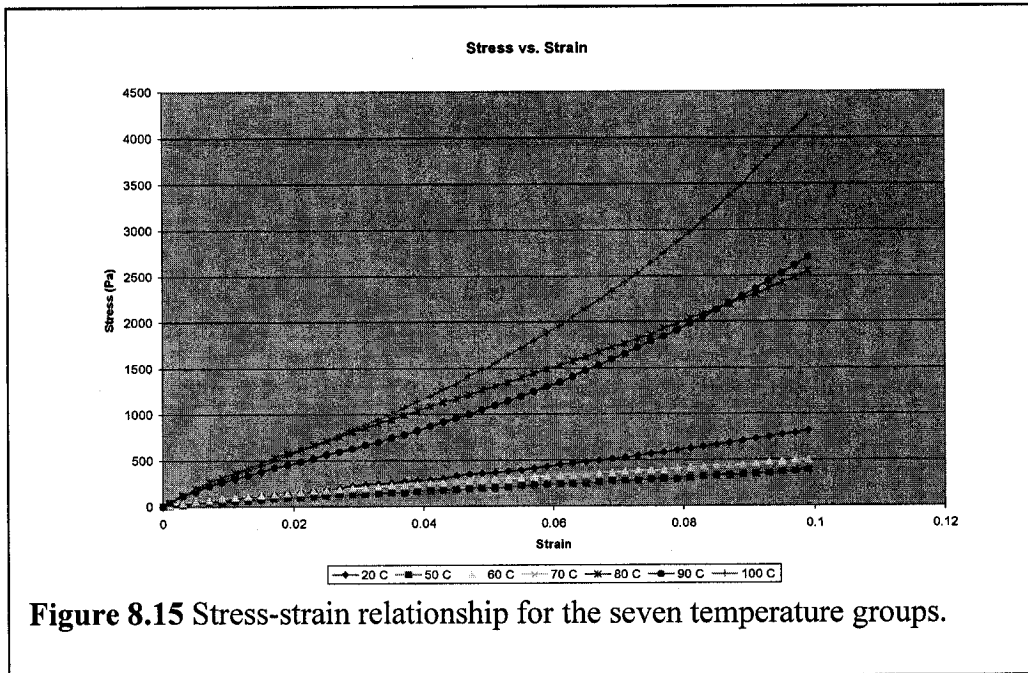
### 8.5.1 Liver elasticity study

Figure 8.14 displays the mean values of the uniaxial compressive tests in stress distribution vs. time. The horizontal axis is the time elapsed and the vertical axis is the calculated stress (in Pa.) Each line pattern corresponds to the average of 5 samples at a single temperature level. The mean stress per unit time increased linearly from room temperature 20°C samples to samples at 100°C. The compression stroke ended at 20 seconds at which point constant 10% strain was maintained for the another 180 seconds. During this 180-second interval, each of the 7 temperature groups demonstrated a non-linear relaxation pattern until the stresses reached a near equilibrium state near the 180-second mark.



**Figure 8.14** Mean stress distribution vs. time for the seven temperature groups.

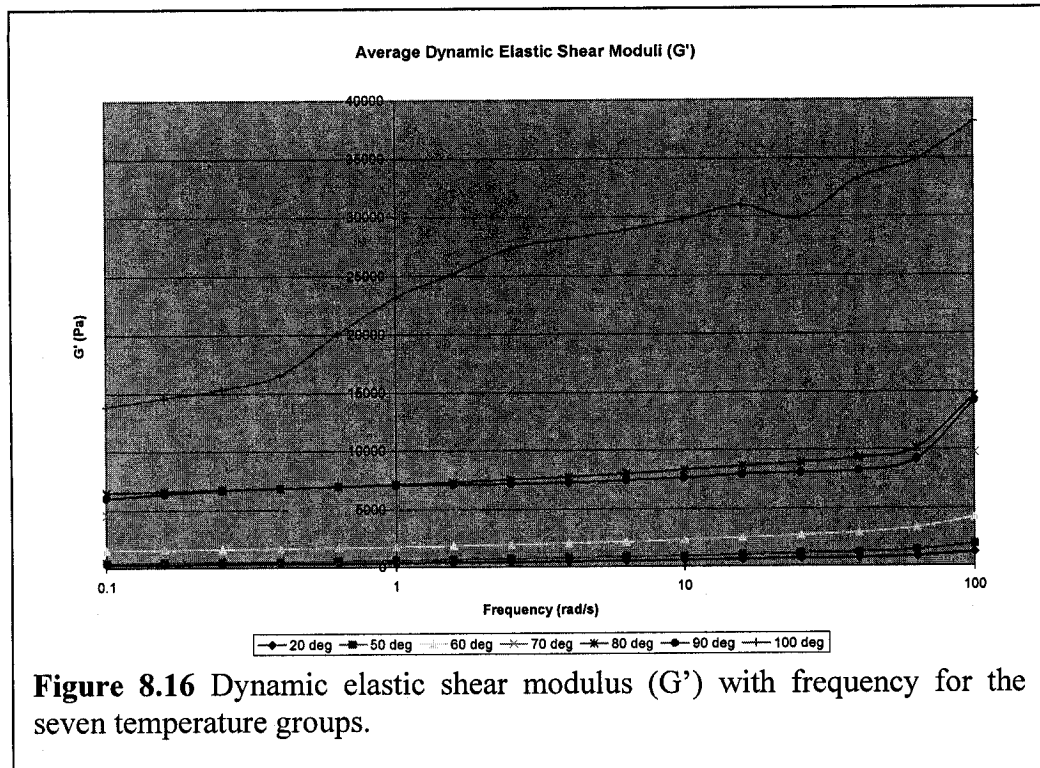
The axial compression stress vs. strain curves are shown in Figure 8.15. These data points were extracted from Figure 8.14 and recalculated to convert strain (on the horizontal axis) based on the average compression velocity and average specimen height. Again, there is a trend of increasing slopes and hence increasing elastic moduli values from 20°C up to 100°C.



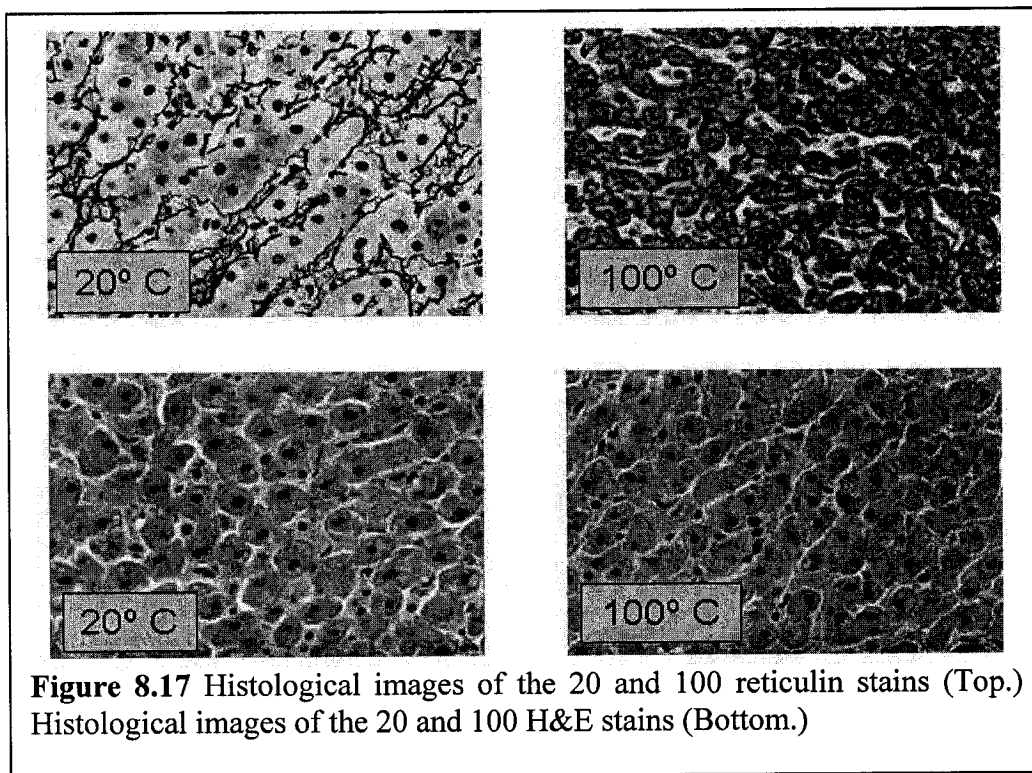
**Figure 8.15** Stress-strain relationship for the seven temperature groups.

Figure 8.16 shows the average dynamic shear modulus vs. the frequency of dynamic oscillations in a logarithmic scale. The shear modulus curve also exhibits a positive correlation with temperature.

Images were taken of the liver samples after an ablation treatment similar to the one shown in Figure 8.11. The color contrast between the afflicted tissue and its surroundings was clearly visible. A trained pathologist stained the two areas with distinct colors and acquired photographs shown in Figure 8.17.



**Figure 8.16** Dynamic elastic shear modulus ( $G'$ ) with frequency for the seven temperature groups.



**Figure 8.17** Histological images of the 20 and 100 reticulin stains (Top.) Histological images of the 20 and 100 H&E stains (Bottom.)

In the reticulin stains images, the disappearance of fibrous networks is the most notable distinction between the two temperature (20°C and 100°C) slides. In H&E stains images, show little change except for the disappearance of red blood cells. This means that one can rely on the change of color in gross-pathology pictures to delineate the actual necrosis and use it as “ground truth”.

### 8.5.2 Monitoring Radionics ablation

Our strain imaging algorithm is based on maximization of normalized cross-correlation between pre- and post- compressed RF signals. Initially, we apply a preprocessing phase to condition the RF signals; this includes band-pass filter and resampling. Next, we apply kernel optimization similar to the work done by Doyley and Kolen [Doyley-1999, Kolen-2003] to choose the optimal kernel size and overlap. While we are running the NCC method to get axial displacement estimates, we are applying cosine-fit interpolation to achieve sub-sample accuracy. Then, we use the algorithm proposed by Kallel et al. [Kallel-1997] to estimate strain using least square approach.

Figure 8.18 shows the resulting 2D strain images for the corresponding gross-pathology pictures shown in Figure 8.11. As mentioned earlier, our liver elasticity study included 18 liver samples, 6 samples each for 4min, 6min, and 8min ablation time. My colleague, Dr. deOlivera, and another surgical resident conducted gross-pathology measurements without having strain imaging results (blinded study). At the same time, I did not have the gross-pathology pictures with rulers during kernel optimization and strain calculations (blinded study). The aim of this double-blinded study is to compare the actual size of the ablated lesion in gross-pathology pictures with both B-mode US and strain images.

Our team decided to drop three samples from the experiment's pool for consistency reasons. The supporting gel for these three dropped samples was broken during the ablation process. For consistency considerations in the statistical study we dropped the samples with broken gel. The third sample of the 4min ablation category shown in both Figure 8.11 and Figure 8.18 is one of the three dropped samples. For this sample,

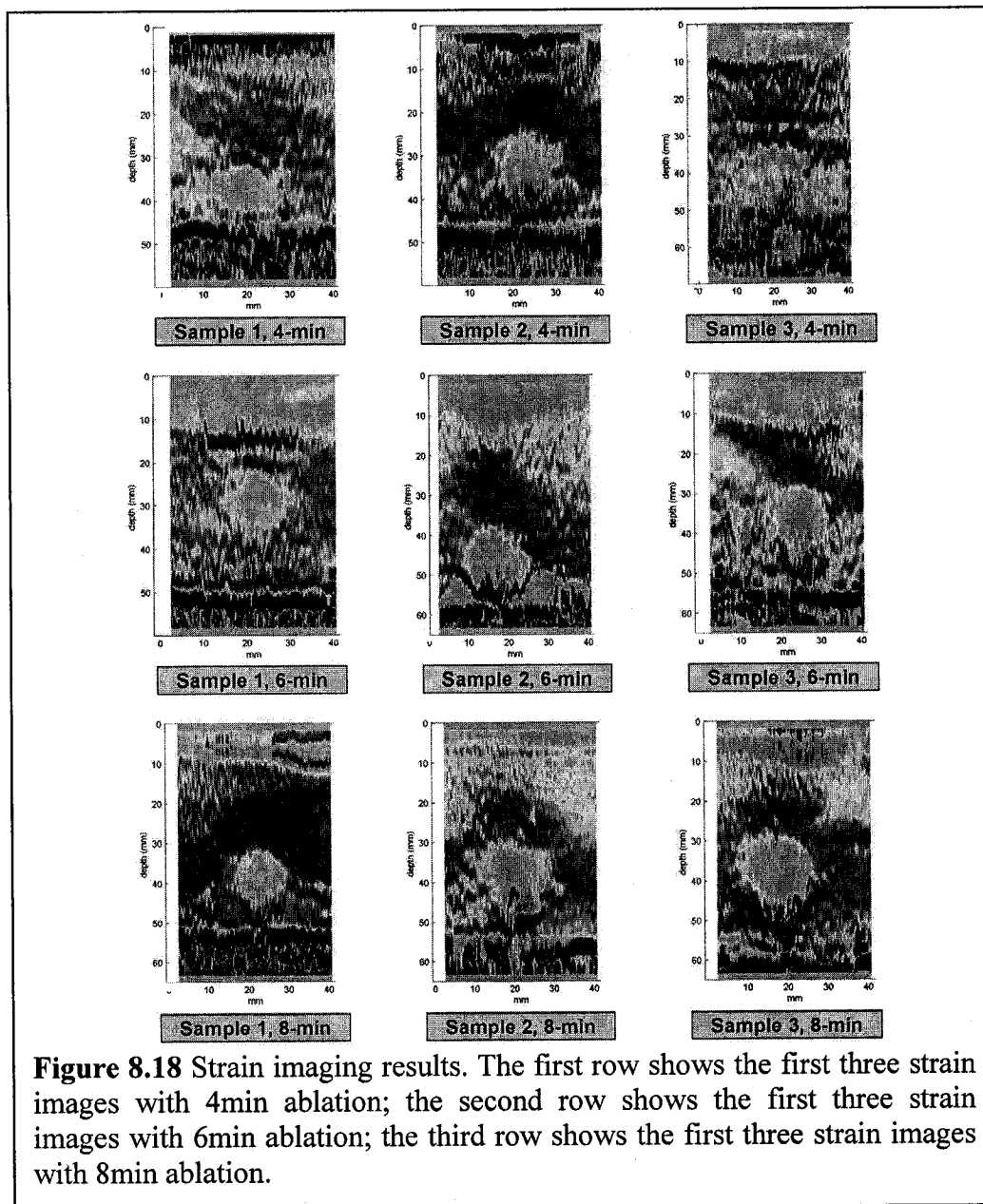


**Figure 8.18** Strain imaging results. The first row shows the first three strain images with 4min ablation; the second row shows the first three strain images with 6min ablation; the third row shows the first three strain images with 8min ablation.

however, we can still delineate at the bottom surface of the liver (Figure 8.18, sample 3 and 4min) an ablation with about 2cm wide and 2cm long. These dimensions are in agreement with the corresponding gross-pathology picture shown in Figure 8.11 (note that the picture is flipped vertically compared to the strain image shown in Figure 8.18.)

Table 8.1 summarizes the measurements done by the two observers for both B-mode ultrasound and strain images for the 15 samples. The measurements were performed by capturing the biggest apparent diameter for the ablation in the image.

Samples	Ultrasound (cm)		Strain (cm)	
	Observer A	Observer B	Observer A	Observer B
1	1.90	2.00	1.50	1.60
2	2.30	2.30	1.90	2.10
3	3.00	3.00	2.30	2.60
4	1.90	2.00	1.60	1.70
5	2.00	1.70	1.50	1.50
6	1.60	1.75	1.40	1.70
7	1.75	1.72	1.40	1.60
8	2.30	1.75	1.50	2.00
9	1.50	1.40	1.40	1.50
10	1.90	2.00	1.70	1.80
11	1.80	1.30	1.10	1.25
12	1.80	1.80	1.50	1.75
13	2.00	1.50	1.50	1.50
14	1.90	1.75	1.70	1.80
15	2.00	1.80	1.50	1.75
mean	<b>1.98</b>	<b>1.85</b>	<b>1.57</b>	<b>1.74</b>

**Table 8.1** Ultrasound and strain measurements for the 15 ablated liver samples.

Before commencing a comparison either between gross-pathology and strain measurements, or between gross-pathology and B-mode, we need to make sure of the observers reliability by conducting intraclass correlation (ICC). In other words, we are trying to test the repeatability of these measurements from one observer to another. Table 8.2 shows that ICC of the observers for both ultrasound and strain measurements are 0.78 and 0.77, respectively with  $p < 0.001$ . This means that we can use one of the two observer measurements and compare them with the gross-pathology dimensions.

	Observer A		Observer B		Correlation	
	Mean(cm)	SD	Mean(cm)	SD	ICC	p
<b>Ultrasound</b>	1.98	0.35	1.85	0.40	<b>0.78</b>	<b>&lt;0.001</b>
<b>Strain</b>	1.57	0.27	1.74	0.32	<b>0.77</b>	<b>&lt;0.001</b>

**Table 8.2** The intra-class correlation study between the observers' measurements.

Since both observers' readings are similar, we choose one of them (observer "A") to compare it with gross-pathology measurements. Table 8.3 summarizes this comparison by listing all gross-pathology, US, and strain data.  $\Delta$ real indicates the deviation from the gross-pathology "ground truth" values (US or strain size – gross-pathology size.)

Regarding US data, this table shows that 13 (86.7%) US measurements are overestimated compared to gross-pathology, where only 2 (13.3%) US measurements are underestimated. The difference in size between US and gross-pathology measurements has a range from -30mm to 70mm, with a mean of 32mm and SD of 26mm. With respect to strain data, Table 8.3 indicates that 5 (33.3%) strain measurements are overestimated, and 8 (53.3%) are underestimated compared to gross-pathology sizes. The difference in

size between strain and gross-pathology measurements has a smaller range from -40mm to 10mm, with a mean of -9mm and SD of 18mm.

US overestimated significantly the measurement of the induced ablation size by both gross-pathology and strain. This difference was tested and considered highly significant ( $p<0.001$ .) The measurements by strain were comparable to those of gross-pathology

Samples	Gross-pathology (cm)	Ultrasound (cm)		Strain(cm)	
		Value	$\Delta$ real	Value	$\Delta$ real
1	1.40	1.90	0.50	1.50	0.10
2	2.00	2.30	0.30	1.90	-0.10
3	2.50	3.00	0.50	2.30	-0.20
4	1.70	1.90	0.20	1.60	-0.10
5	1.40	2.00	0.60	1.50	0.10
6	1.30	1.60	0.30	1.40	0.10
7	1.80	1.75	-0.05	1.40	-0.40
8	1.60	2.30	0.70	1.50	-0.10
9	1.80	1.50	-0.30	1.40	-0.40
10	1.60	1.90	0.30	1.70	0.10
11	1.30	1.80	0.50	1.10	-0.20
12	1.40	1.80	0.40	1.50	0.10
13	1.80	2.00	0.20	1.50	-0.30
14	1.70	1.90	0.20	1.70	0.00
15	1.50	2.00	0.50	1.50	0.00
<b>Mean±SD</b>	<b>1.65±0.31</b>	<b>1.98±0.36</b>	<b>0.32±0.26</b>	<b>1.57±0.27</b>	<b>-0.09±0.18</b>

**Table 8.3** Measurements taken by Observer “A” from gross-pathology, ultrasound, and strain images.

with  $p < 0.253$ . This indicates that we need to repeat this experiments more, in order to get higher significant. At the same time, it proved useful utility of strain imaging to monitor aggressive RF ablation.

### 8.5.3 Initial feasibility of 3D strain acquisition

As shown in Figure 8.13, we collected two 3D datasets of the agar phantom by using a translation and a rotation motion scenario. During the 3D scan, we introduced small perturbations similar to what we normally encounter with freehand scanning (less than 1%). Figure 8.19 shows one of the two datasets, the rotation about an axis volume. The agar phantom we used has a spherical inclusion with isoechoic appearance, which makes it hard to differentiate from the background. But the axial displacement clearly indicates this inclusion.

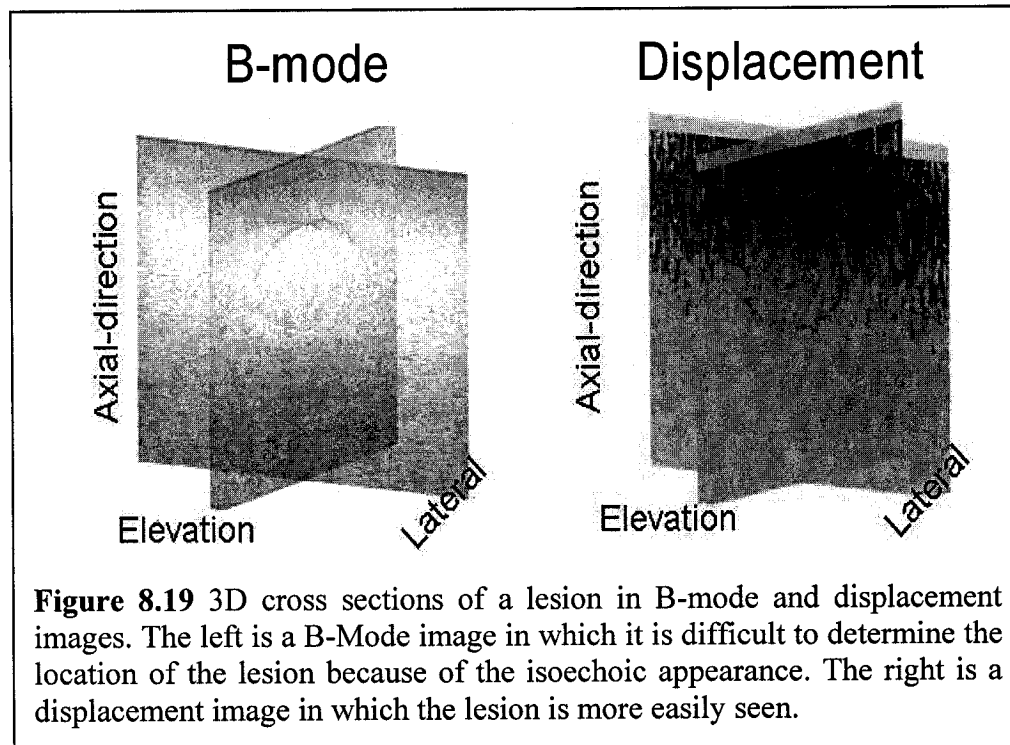


**Figure 8.19** 3D cross sections of a lesion in B-mode and displacement images. The left is a B-Mode image in which it is difficult to determine the location of the lesion because of the isoechoic appearance. The right is a displacement image in which the lesion is more easily seen.

As part of a course project, we conducted a study to test the effect of angular (out-of-plane) separation on the degree of decorrelation. Figure 8.20 depicts how decorrelation on the edges amplifies as we increase the angular separation from 1 to 4 degrees. These angular separation steps ( $1^\circ$ ,  $2^\circ$ ,  $3^\circ$ , and  $4^\circ$ ) correspond to out-of-plane distances at the lateral end-points to 0.33mm, 0.66mm, 1mm, and 1.26mm respectively. This means that real-time performance is possible by acquiring only 45 to 180 images to capture the volume of interest. This can be easily achieved by actuating one rotational DOF, which makes it similar to the current wobbler 3DUS probes in the market.

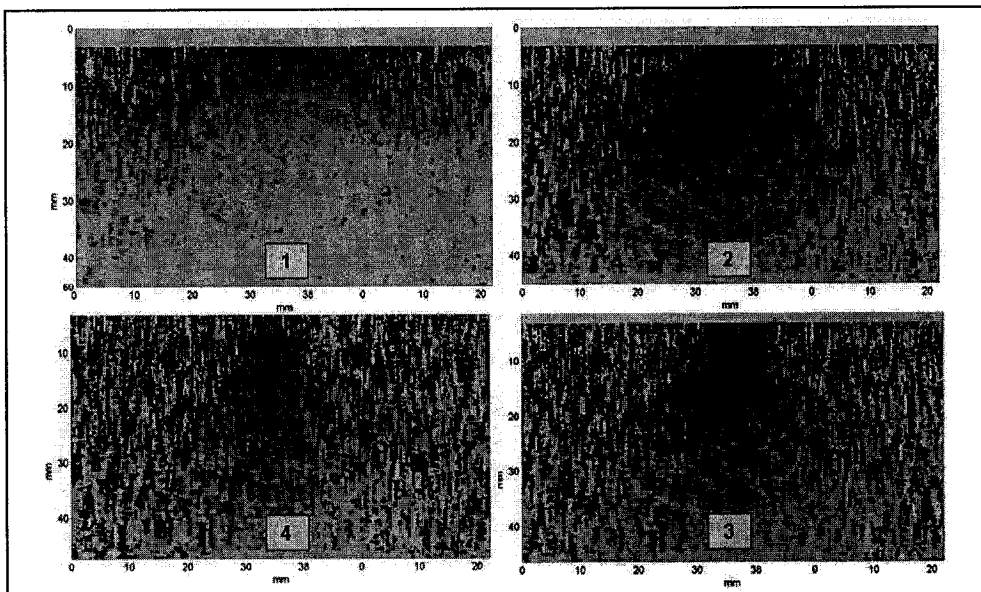


**Figure 8.20** Displacements images (Clockwise from the top-left) for rotational  $1^\circ$ ,  $2^\circ$ ,  $3^\circ$ , and  $4^\circ$  datasets.

## 8.6 Conclusions

The similarity between gross-pathology and strain measurements proves the potential use of elasticity imaging as an enabling technology for immediate monitoring of Radionics<sup>TM</sup> aggressive RF ablation. As indicated before, the statistical significance ( $p < 0.253$ ) can be enhanced by performing more experiments. It also indicates that segmentation of strain

images is not easy to perform, especially with the presence of degradation due to active ablation.

The 3D strain study proved that it is possible to acquire 3D strain data at the same rate of capturing 3DUS volume. However, a drawback to this nice feature is that we get more decorrelation in the RF signals.

Both studies inspired us to find a robust segmentation framework that can delineate an average shape for the deposited ablation from the degraded displacement and strain images or volumes. In Chapter 9, we introduce a new segmentation framework that can potentially be used with various imaging modalities and different clinical applications.

## **Part-III: Chapter 9**

# **Elasticity-based Segmentation**

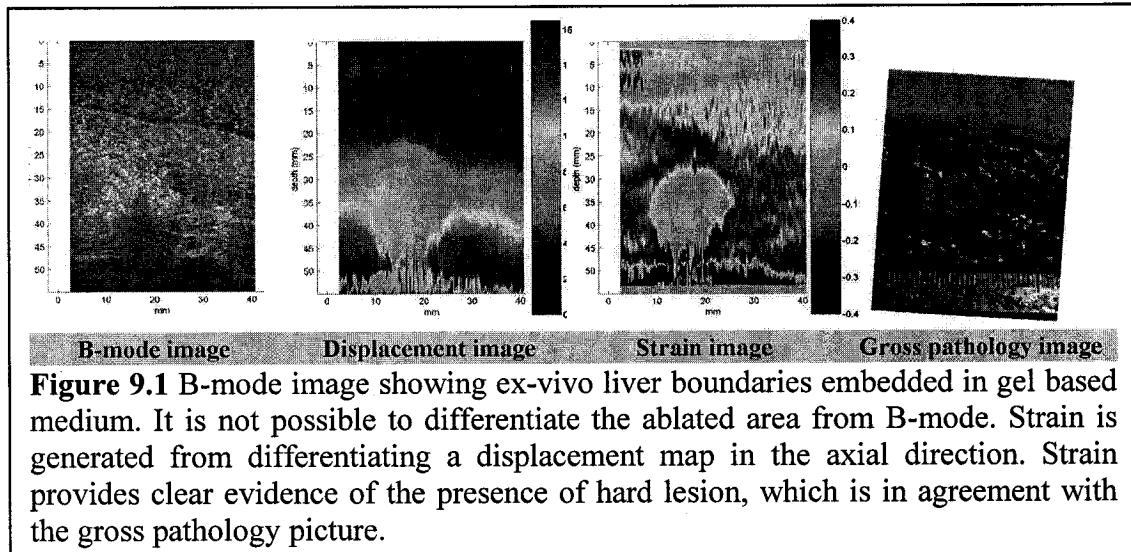
### **9.1 Introduction**

As we mentioned in Chapter 8, monitoring the ablation process in order to document adequacy of margins during treatment is a significant problem. Current approaches often result in either local failure or excessively large zones of liver ablation. Some ablative devices employ temperature monitoring using thermisters built within the ablation probes. However, these temperatures only provide a crude estimate of the zone of ablation. Magnetic resonance imaging can monitor temperature changes, but is expensive, is not widely available, and is difficult to use intraoperatively [Graham-1999]. Ultrasonography is the most common modality for both target imaging for ablation monitoring. However, conventional ultrasonographic appearance of ablated tumors only reveals hyperechoic areas due to microbubbles and outgassing, and cannot adequately visualize the margin of tissue coagulation. Currently, ablation adequacy is only estimated at the time of the procedure; the estimate is primarily based on the probe position and not on the true ablation zone.

Accordingly, ultrasound elasticity imaging, also known as elastography, has emerged as a potentially useful augmentation to conventional ultrasound imaging, as first introduced by Ophir [Ophir-1991]. USEI in monitoring ablation [Righetti-1999, Varghese-2002, Varghese-2003, Curiel-2005, Kolen-2003, Boctor-2004e] was made possible due to the

following observations: (1) different tissues may have significant differences in their mechanical properties and (2) the information encoded in the coherent scattering, a.k.a. speckles, may be sufficient to calculate these differences when following a mechanical stimulus. However, producing a real-time elasticity map using 3D ultrasound data is an exigent task that requires extensive computation and has its own limitations. Despite the fact that strain images have better signal-to-noise and contrast-to-noise (CNR) compared to US images [Varghese-1997, Doyley-1999] (Figure 9.1), these images still suffer from artifacts related to their formation theory or US artifacts. These artifacts can be attributed to decorrelation due to out-of-plane motion, large deformation, shadowing effect, or other causes. Moreover, speckle decorrelation occurs due to the shadowing or attenuating effects underneath the hot ablation zone as seen in the B-mode image (Figure 9.1-left).

Accurate segmentation of strain images is an essential in planning and monitoring



ablations [Righetti-1999, Varghese-2003, Curiel-2005, Kolen-2003, Boctor-2004e]. More generally, our method is directly relevant to a large family of interventions that require targeting, tracking, and monitoring some encapsulated stiff mass suspended in a softer

background. In this paper, we report a generic and rapid approach to segment stiff lesions based on tissue deformation (i.e. displacements), without needing to estimate strain images.

## 9.2 Strain Image Segmentation

Strain imaging holds the promise of playing a significant role in planning and monitoring ablative therapy [Righetti-1999, Varghese-2003, Curiel-2005, Kolen-2003, Boctor-2004e]. However, reliable and rapid semi/automatic segmentation of noisy strain images is needed during ablation intervention. By comparing ablated regions in both gross pathology and strain images to the 18 ex-vivo bovine liver samples, strain imaging - immediately after ablation- tends to overestimate ablation coverage in 44.4% of the time, due to a decorrelation region beneath the ablated lesion [Kolen-2003]. To appreciate this, refer to the strain image in Figure 9.1 that has a strong agreement with gross pathology laterally and an obvious overestimation axially. Ablation coverage in strain images matched corresponding gross pathology images in only 16.7% of the time. Degradation in strain image quality during or immediately after aggressive RF ablation using Radionics<sup>TM</sup> and Rita<sup>TM</sup> devices is possible as reported and noticed earlier in [Kolen-2003, Boctor-2004e, Varghese-2004]. However, obtaining unaffected, consistent, and reliable displacement fields during aggressive ablation, which will result in good quality strain imaging, may possibly be a hard problem to solve. And accurate and reliable segmentation should help the surgeon by monitoring the extent of the applied ablative therapy in 3D, in planning optimal overlap/multiple ablations to cover the original target tumor, and in deciding to terminate the procedure.

One approach to the extraction of ablation boundaries is to apply conventional image segmentation techniques directly to strain images. To get the initial strain images, we start with RF data as input; create the displacement and correlation images; and then differentiate the axial displacement field and estimate the axial strain tensor ( $\epsilon_{11}$ ). Obviously, to have a reliable standalone segmentation module, the inputs (strain images) to this module should meet some expected standards, or have consistent quality. However, obtaining local strain values with high accuracy depends upon precise measurement of local tissue displacement. A significant problem is the loss of similarity (correlation) in the pre- and post-deformed image. During the last few years, several groups have investigated this problem [Kolen-2003] and have came up with various strategies for increasing the reliability of the cross-correlation function including: 1) Choice of the processing parameters, kernel length and amount of kernel overlap [Bilgen-1997]; 2) RF-data tracking instead of envelope-detected data when small displacements are involved [Ramamurthy-1991]; 3) Temporal stretching that includes adaptive local and global companding [Chaturvedi-1998]; and 4) Axial and lateral RF-data interpolation. In addition to these enhancements to displacement estimation, there has been active research on improving the procedure for deriving strain from displacement images including: 1) A least squares strain estimator was suggested [Kallel-1997]; 2) Multi-step compression [O'Donnell-1994] to increase SNR; and 3) Average and median filtering [Doyley-1999].

The following issues, in addition to the perennial problem of decorrelation, must be addressed. ***Displacement estimation:*** The majority of the rapid techniques assume a constant distribution of scatterers before and after a small (<3% axial strain) introduced axial compression. However, this assumption is not valid during ablative therapy proximal to the ablation zone, where vaporization and bubbles affect speckles' appearance and matching. ***Strain estimation:*** The procedure for estimating the axial

strain tensor is based on differentiating the displacement field. However, differentiation also amplifies errors and noise in the displacement measurements. Unfortunately, all current solutions to suppress noise in strain imaging require least squares estimation or average multiple compression steps. Both add a considerable computation cost and/or time delay. **Time performance:** The entire chain (Figure 9.2) of displacement estimation, strain image reconstruction, and strain image segmentation takes far too long for 3D datasets. **Prior knowledge and redundancy:** Clearly, not all displacement and strain measurements are required to locate a lesion. At the same time, in our motivating ablative therapy application, there is well-defined a priori knowledge about the expected shape and size of the ablation. Undoubtedly, utilizing this a priori information effectively

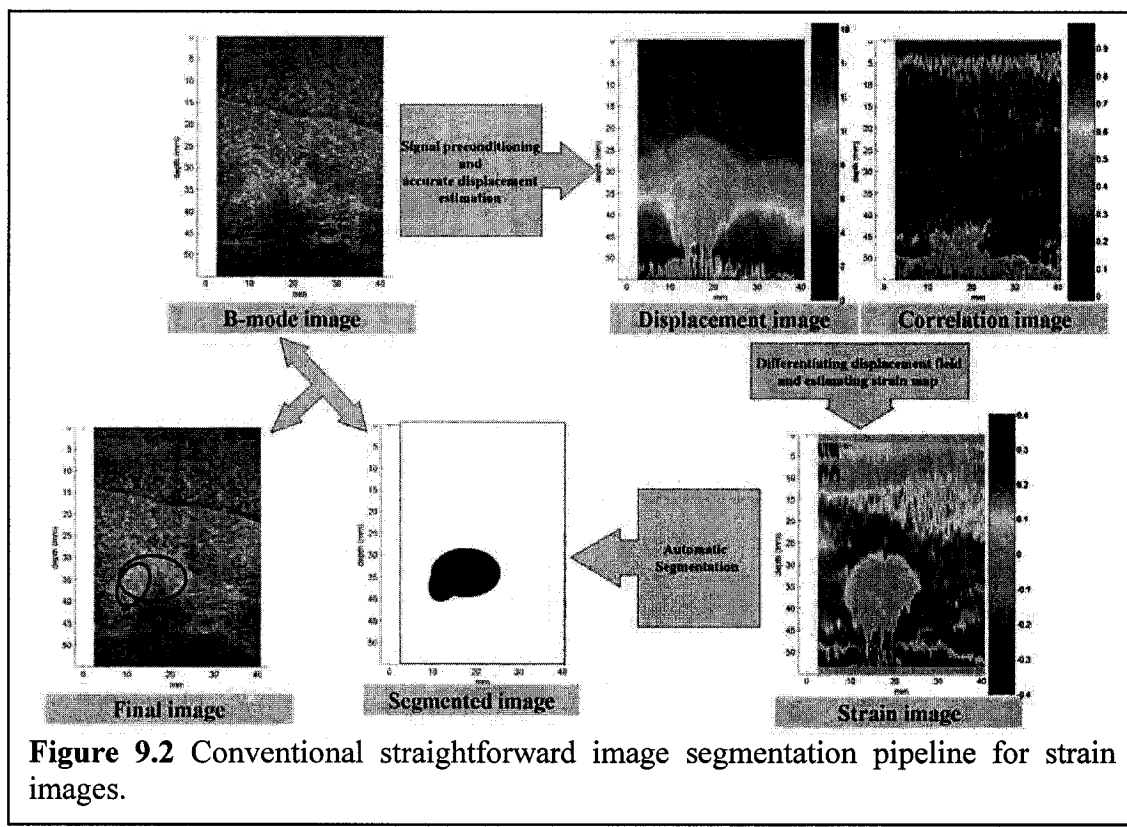


**Figure 9.2** Conventional straightforward image segmentation pipeline for strain images.

should reduce redundant computational cost or time required. **Elasticity Reconstruction:** Segmentation helps in defining the location and boundary of a lesion but fails in reconstructing Young's modulus at the region of interest. It will be favorable, if one can augment the segmentation pipeline to solve the inverse problem with minimal effort.

To address all these issues, we propose a novel framework to segment and track ablated lesions based on tissue deformations and shape priors. No strain estimation is involved in this preliminary investigation. Furthermore, elasticity reconstruction, i.e. to retrieve the Young's modulus, is possible with minimal alteration of the framework.

### 9.3 Elasticity Model based on Tissue Deformations

The key insight into our approach is the integration of prior geometrical knowledge, a physical elasticity model, and direct estimation of tissue deformation. The proposed approach is explained below in Figure 9.3. The process starts from a prior geometrical model in the lower branch of the work-flow. In our example, the ablated lesion is modeled as a simple ellipse. In liver ablation, we have a very reliable initial guess of the location of the lesion, because we know the position of the ablator. Next we solve the forward problem of estimating the theoretical displacement from a geometric mesh representation of the initial model, from the boundary conditions and from an assumed elasticity model. The computational method of choice to solve this forward problem is Finite Element Method (FEM). In the upper branch, we start by calculating the correlation map and then we rapidly estimate the displacement field. The lower and upper branches meet in the shape optimization loop where we iteratively solve the inverse problem in few parameters to optimize our parametric geometric model and locate the region of interest.

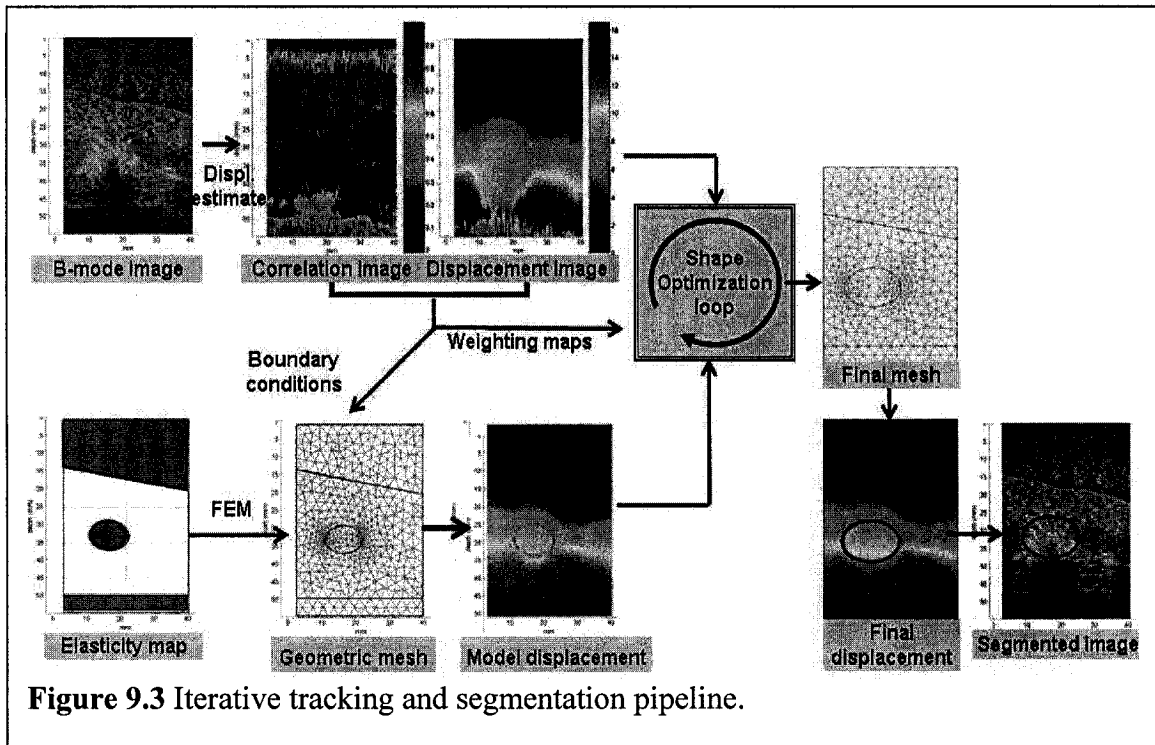
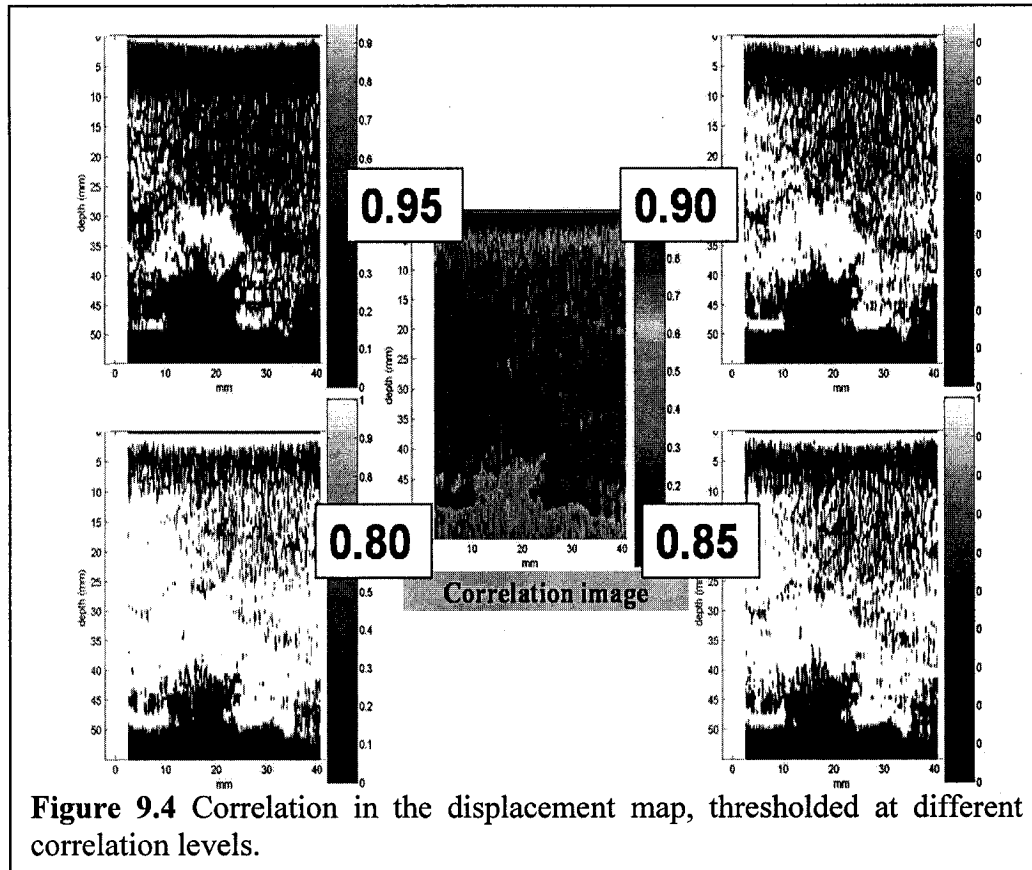


**Figure 9.3** Iterative tracking and segmentation pipeline.

### 9.3.1 Tissue Displacement Estimation

We acquire RF ultrasound data from a tissue in both rest and stressed states, and then estimate the induced deformation distribution by tracking speckle motion. Our implementation is based on maximization of normalized cross-correlation between pre- and post-compressed RF signals, and applying 1D global companding. In the example shown in Figure 9.3, decorrelation was caused by shadowing and attenuation effects underneath the hot ablation zone, as seen in the B-mode image. Fortunately, decorrelation artifacts can be detected from the normalized correlation map associated with the displacement image. Figure 9.4 shows a typical color-coded correlation image, where dark-red indicates perfect correlation (unity) and dark-blue stands for perfect decorrelation (zero). In the same figure, there are four different binary maps based on thresholds 0.95, 0.90, 0.85, and 0.80, all showing the spatial coverage of these correlation regions. The white region associated with correlations greater or equal to 0.95 is small

compared to the region associated with correlations 0.80. Knowing the locations of better correlated regions helps us formulate a better conditioned shape optimization framework as shown in Section 9.3.3.



### 9.3.2 Theoretical Displacement Estimation

To calculate theoretical displacements, a tissue elasticity model needs to be considered. We assume linear elastic, homogeneous and isotropic material. Moreover, liver tissues are mostly filled with water and are incompressible, and hence Poisson's ratio is nearly 0.5. We also apply uniform pressure by the transducer face in a quasi-static form, in which the deformation is considered plane strain. It is a type of deformation where there are no displacements in the z-direction, and the displacements in the x- and y- directions

are functions of x and y only. For the plain strain problem, the assumption is  $\varepsilon_z = \varepsilon_{zx} = \varepsilon_{zy} = 0$ . Given boundary conditions and a finite element mesh, the theoretical displacements  $\mathbf{u} = (u, v)$  can be calculated by solving the following Navier's equations:

$$\rho \frac{\partial^2 u}{\partial t^2} - \nabla \bullet c \nabla u = K \quad (9.1)$$

where  $\rho$  is the material density,  $K$  are the body forces, and  $c$  is a tensor where each entry is a function of  $G$  (shear modulus),  $E$  (Young's modulus), and  $v$  (Poisson's ratio).

### 9.3.3 Shape Optimization

Here we compare observed tissue displacements with simulated displacements using the correlation map as weighting criterion. This weighting method puts high premium on the “most trusted” displacement areas and drives the evaluation of the domain points in the mesh at the corresponding locations. This approach reduces the resources needed for updating the mesh and effectively utilizes the available displacement information with minimal redundancy. Next, in an iterative optimization cycle where lesion location and shape parameters  $S$ , we adjust this hypothetical displacement field until it fits the actual displacement field. When the two fields are sufficiently similar, then the deformed model will yield the contours of the lesion. Thus, this inverse framework is trying to solve a non-linear optimization problem with the objective function:

$$\hat{S} = \arg \min \{ \mathfrak{J}(S) = \sum_{i=1}^N \sum_{j=1}^M W(i, j) \|\hat{u}(i, j) - u(i, j; S)\|^{L1} \} \quad (9.2)$$

where  $\hat{S}$  is the estimated shape parameters,  $\hat{u}$  is estimated tissue motion,  $\mathfrak{J}(S)$  is the objective function,  $N, M$  are the number of rows and columns respectively in the displacement maps, and  $W$  is the correlation map that acts as a weighing function to

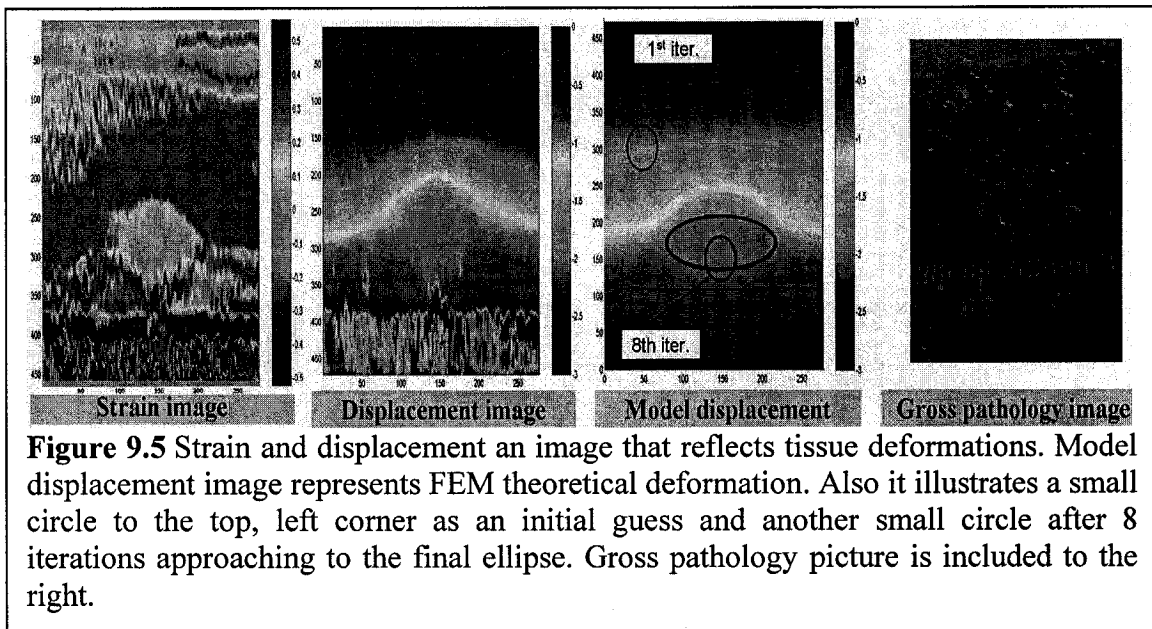
minimize the effects of distrusted tissue displacements. The experimental implementation is currently utilizing a modified version of the simplex search algorithm and LM method.

#### 9.4 Experiments and Results

A thorough simulation study was conducted independently of any US imaging. The study involves running the finite element model to generate a displacement map where we know the ground truth shape parameters coupled to this map. We next use this displacement as the simulated input from tissue deformation. We have 5 parameters to optimize, ellipse location ( $x, y$ ), size ( $a, b$ ), and orientation. We tested the robustness of the method under different conditions and using different optimization schemes. The tests included partitioned optimization by solving  $x, y$  together or separately, then solving for size parameters and orientation. This was performed while applying different objective functions and different search constraints.

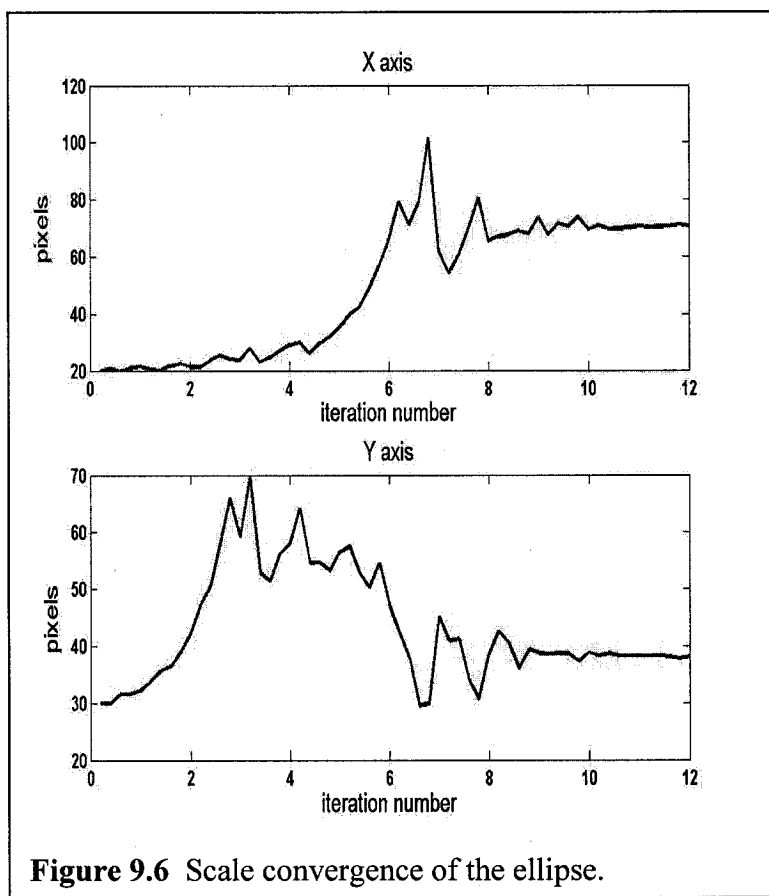
The second study was conducted using a robotic ultrasound acquisition system. We used a Siemens Antares US scanner (Siemens Medical Solutions USA, Inc. Ultrasound Division, Issaquah, WA) with an ultrasound research interface to access raw RF data. A Siemens VF 10-5 linear array was used to acquire data. The tracking beams were standard B-mode pulses (6.67MHz center frequency, F/1.5 focal configuration, apodized, pulse repetition frequency of 10.6KHz, with a pulse length of 0.3 $\mu$ s). We collected data immediately after ablation of 18 ex-vivo fresh bovine liver samples, which were divided into three groups, 4min, 6min, and 8min ablations using a Radionics device. All samples were soaked in degassed water to remove air pockets, and then embedded into gel material to support the liver during ablation and also to maintain the assumed incompressibility of living tissues.

Figure 9.5 reflects the application of our approach on one ex-vivo liver sample, which was ablated for 8min and which serves as a preliminary result. Both strain and axial displacement from tissue deformation are included in the figure. The strain image shows good indication for the ablation zone but the location of the exact boundaries is still not clear. The FEM theoretical axial displacement at the last iteration has a good agreement with the corresponding tissue displacement. Also, we included the initial ellipse at the top-left corner, and in 8 iterations it becomes closer to the final shape, which was estimated in 15 more iterations.



We use two independent ground truths to evaluate the resulting segmentation. The first deals with ellipse location, by relying on the ablator's tip location in the B-mode image before ablation. We have excellent agreement within 1mm laterally. However, it is hard to get a corresponding location axially, due to the unmeasured axial motion of the US probe before collecting strain data. The second ground truth deals with ellipse size, using gross pathology picture to get its accurate measure in the axial direction, our approach

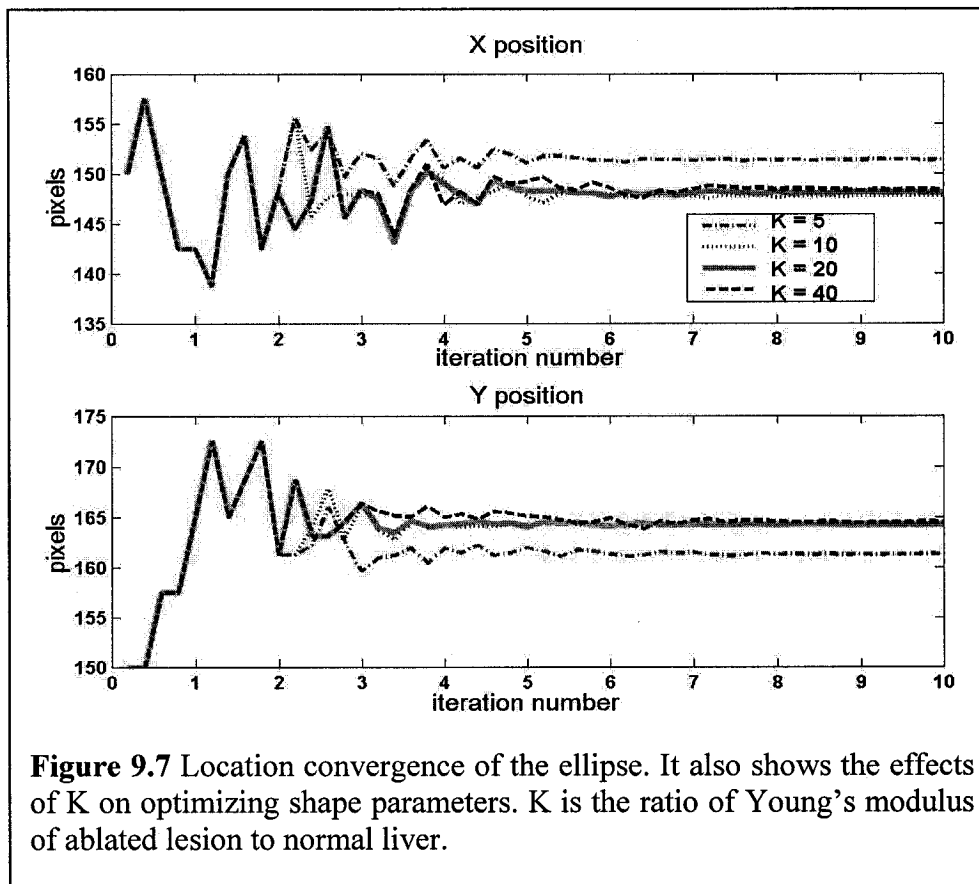
suggests 76.1 pixels (10.49mm) where the pathology picture gives about 11mm. In the lateral direction, however, our approach numbers is 140 pixels (18mm) where pathology is 15mm. This suggests that the axial displacement is very accurate in locating axial features but we that probably need to regularize the objective function with lateral displacement estimation. Figures 9.6 and 9.7 present a convergence study for the scale parameters and for the center location, respectively. In both figures and for all four parameters, 10 iterations were enough to lock on a value with  $10^{-4}$  difference variations.



**Figure 9.6** Scale convergence of the ellipse.

We chose a suggested literature value of 1.5KPa for the Young's modulus of bovine liver, and tested the convergence of the FEM model to the center location using values of the Young's modulus for the ablated tissue, at 7.5, 15, 30, and 60KPa. The results are

shown in Figure 9.7, where the K parameter refers to the ratio of the ablated tissue, at 7.5, 15, 30, and 60KPa. The results are shown in Figure 9.6, where the K parameter refers to the ratio of insensitive to variations for K values in the 10-40 range, in other words, regardless how hard we have cooked the tissue or how poorly estimate its Young's modulus, the model robustly converges. Also when we picked an unreasonable value, such as K=5, the shape optimization algorithm was biased with only 3-5 pixels (0.7mm).



## 9.5 Future work and Conclusions

We have developed and tested a novel shape optimization approach based on tissue deformation and shape priors. The consistent results we collected for the 18 samples will be reported in a detailed journal publication. Extending this framework to 3D is the next

step for this project, which promises to increase the amount of measurements, while reducing the number of unknowns to just 9 parameters for an ellipsoid.

## **Part-III: Chapter 10**

# **Conclusions**

US-guided liver ablation is an ideal setting to make use of tracked ultrasound technologies. Improving real-time guidance for planning, delivery, and monitoring ablative therapies would provide would allow for an effective application of these promising treatment modalities. Image-guided tracked ablation promises to make these procedures more accurate, effective, safe, and ultimately expensive. Having this clinical motivation and the promise embedded in medical robotics and tracking technologies, we have developed multiple embodiments of innovative US-guided interventional systems, with associated testing of their accuracy and functionality through simulations, phantom experiments, animal cadaver tissue studies, and one in-vivo pig experiment.

In the following sections we will summarize the enabling technologies developed and discuss the improvements they enable in targeting accuracy and performance efficacy.

### **10.1 Ultrasound-guided Intervention Systems**

We have developed an experimental test-bed and several system embodiments involving tracked ultrasound, 3D volume compounding, mechanically assisted quantitative ultrasound, elasticity imaging, and placement of percutaneous devices (needles and tissue ablators). We categorized these systems based on the degree of robotic involvement, i.e. using freehand approach, or robotically driven by one arm, or dual-arm. Also we have

developed a programming interface for US-guided intervention, called CISUS, under 3D Slicer medical data visualization package [Gering-2001].

The experimental results on mechanical phantoms and ex-vivo liver samples show accurate targeting (within 4-5 mm) in 3D from the first run, for all system configurations. With regard to the active needle ex-vivo and phantom experiments, there are no substantial differences in accuracy between tracked 3DUS and robotic 3DUS. In fact, with a bit of training with using tracked US probes, one can generate good-quality 3D reconstruction; sufficient to target static or quasi-static objects. Targeting rapidly a moving object is not part of our systems' design specifications and is outside the scope of our research. The driving clinical applications of this dissertation (liver ablation in open surgery scenario and prostate EBRT) do not present with substantial motion artifacts. Robotic US is an important means to provide rapid 3D acquisition from 2D images, i.e. the current mechanical 3DUS wobbler probes, or to ensure US acquisition with repetitive and known boundary conditions for creating elasticity images, as shown in Part-III of this thesis. Furthermore, the use of robotic US has the potential to create steady image of the target by automatically tracking the region of interest and move the US probe to always focus on the target. Appendix-A presents the work undertaken on robotic US servoing in a course project<sup>†</sup>. Similarly, using robots to guide needle insertion is an important addition to these systems, particularly when a moving target is encountered.

From the comparative study and the pig experiment, these interventional systems hold a promise to assist liver interventional procedures as in ablative treatment. Figure 2.22 shows superior performance of the tracked 3DUS over the conventional manual method.

---

<sup>†</sup> This project was undertaken in the spring of 2004, in collaboration with Gregory S. Fischer, with Prof. Taylor as supervising faculty.

However, this performance is mainly attributed to the calibration accuracy of the system and its integration.

## 10.2 Ultrasound Calibration and Online Quality Control

We have made three distinct contributions to the state of the art in ultrasound calibration. First, we have developed novel phantom and insonification sequence for rapid calibration with non-linear optimization:

Second, we have introduced a novel mathematical formulation for real-time calibration performance that obviates non-linear optimization and produces calibration from two motions, i.e. from three ultrasound images:

Third, we observed that the overwhelming majority of intraoperative hazard situations in tracked ultrasound systems are attributed to failure of registration between tracking and imaging coordinate frames. To address this problem, we have developed an in-vivo quality control method of tracked US systems, in order to capture registration failures during the clinical procedure. In effect, we dynamically recalibrate the tracked US system for rotation, scale factor, and in-plane position offset up to a scale factor. We detect any unexpected change in these parameters by capturing discrepancies in the resulting calibration matrix, thereby assuring quality (accuracy and consistency) of the tracked system. No phantom is used for the recalibration. We perform the task of quality control in the background, transparent to the clinical user, while the subject is being scanned.

A unique and fundamentally important “side effect” of this work is that we now calibrate the tracked US system in the actual field of use, instead of using traditional offline calibration on phantoms that may result in up to 5mm depth error when a precalibrated

system is used on patients of various constitutions. For example, different sizes of the urinary bladder alone may cause up to 3mm error in depth measurement, putting the rectum at high risk of being overdosed.

### **10.3 Elasticity-based Segmentation**

First, we conducted a thorough elasticity experiments to study the effect of aggressive RF ablation on liver mechanical properties. Next, we supplanted the above US-based navigation test-bed with USEI and demonstrated its performance on monitoring liver ablation. The similarity between gross-pathology and strain measurements proves the potential use of elasticity imaging as an enabling technology for immediate monitoring of Radonics™ aggressive RF ablation. As indicated before, the statistical significance ( $p<0.253$ ) can be enhanced by performing more experiments and also infers that segmentation of strain images is very difficult to perform, especially in the presence of strain degradation due to active ablation.

The 3D strain study proved the possibility to acquire 3D strain data at the same rate of capturing 3DUS volume. However, this promising feature comes with a price of having to deal with more decorrelation in the RF signal.

A rapid approach to monitor ablative therapy through optimizing shape parameters is introduced. The approach involves the integration of the following components: a biomechanical computational model of the tissue, a correlation approach to estimate/track tissue deformation, and an optimization method to solve the inverse problem and recover the shape parameters in the volume of interest. Successful convergence and reliability studies were conducted on simulated data. Then ex-vivo studies were performed on 18

ex-vivo bovine liver samples previously ablated under ultrasound monitoring in controlled laboratory environment.

Possible extensions to this work include the application of boundary element method and extending this framework to 3D. Another potential extension is to apply this generic segmentation framework with other imaging modalities (most trivially MR) and different clinical applications.

## **Appendix A**

# **Robotic Ultrasound Image Based Servoing**

The goal of this project<sup>†</sup> is to improve the shortcomings of the Active/Active system by augmenting it with the ability to dynamically track a desired target via visual feedback from ultrasound imaging. The problem to be solved is threefold; we must first locate the target in 3D ultrasound space, next move the robot to the desired target, and then track the location of the target in “real-time.” The ultimate goal of such a system will be to implement it in the dual arm system in such a way that the path of the needle being inserted can be updated as it is aligned and inserted.

### **A.1 Approach**

The method of choice, given the hardware constraints available, is to use the “dynamic look-and-move” visual servoing approach. This method involves analyzing the image to determine the center of mass of the target, determining the position error, and feeding the desired trajectory into the LARS robot’s control computer. The RCC manages the low-level PID joint control, which is advantageous because it allows for easier system prototyping, but it does not allow us to directly control the joints.

---

<sup>†</sup> This project was undertaken in the spring of 2004, in collaboration with Gregory S. Fischer, with Prof. Taylor as supervising faculty.

Before we can actually perform feature-extraction based visual servoing, the groundwork must first be laid. The first step is to calibrate the ultrasound probe, as shown in Figure 2.15-B. In order to be able to accurately track an object from the image, we must know which position in the ultrasound image corresponds to the robots frame of reference. There are two basic subsets of this task. The first is to calibrate the US image coordinates to the probe itself. The next part is to relate the location of the probe to the robot base; this is done by determining the kinematics of the robot and the corresponding transformations for all of the joints. The kinematics of the robot allows us to determine the location of the US probe with respect to the robot base and therefore where in the image is an object with respect to the robot's position. Since the image is taken with respect to robot coordinates, error in the image can be transformed from the US image frame to the robot's frame of reference and used in commanding the robot to move so that we may track the moving object.

Once all of the frames of reference and their respective transformations are determined, the following step is to be able to control the robot precisely in as close to a real-time as possible. To control the robot, we have implemented the program in combination with our Modular Robot Control (MRC) library. This allows for high-level control of the robot, and provides a way to send and receive joint positions between our software and the robot. The flow of data in the system is as follows:

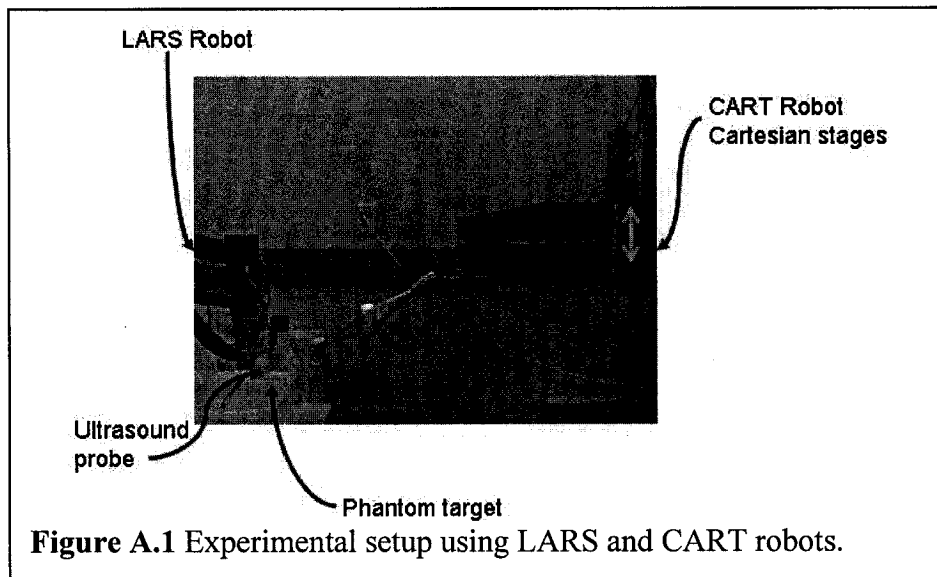
1. Capture US image via Matrox Meteor frame grabber, convert to 640x480 8bit array
2. Condition the image so that processing may be effectively performed on it
3. Determine centroid of target using a center of mass calculation
4. Calculate deviation from desired position in pixels and transform into the robot frame

5. Determine desired robot position based on error and current joint positions
6. Perform filtering/prediction as required and output joint command positions

The two keys to this project are image processing and robot control. Image processing is critical, because in order to be able to follow a feature in the organ such as a tumor, we must be able to automatically identify. This is performed in three discrete steps. The first step, pre-processing the image, primarily concerned with enhancing the image in such a way that it will be ready for the next step. This next step is segmentation of the image, which is a process that involves separating the target from the remainder of the image. For the phantom used in this project, thresholding the image based on its 8 bit grayscale value proved to be sufficient when coupled with a user defined region of interest. Offline experiments with other methods including the Matlab image processing toolbox, the Matrox MIL library, and an active contour model (ACM) algorithm have been performed as well. The ACM appears to be an ideal solution and is quite robust as determining the edge of a target in our trials. Following segmentation, the final step of processing the image is to determine the centroid of the target. This is done using a center of mass calculation on either the thresholded image as done in our online trials, or of the contour produced by the ACM.

As we previously mentioned, the transformations from image coordinates to robot coordinates have been determined and are included in the software. This allows for transforming the error in target position in pixels in US space to the error in robot space in millimeters based on the current robot position. This, combined with the current joint position data, allows us to determine of the desired robot position. When dealing with

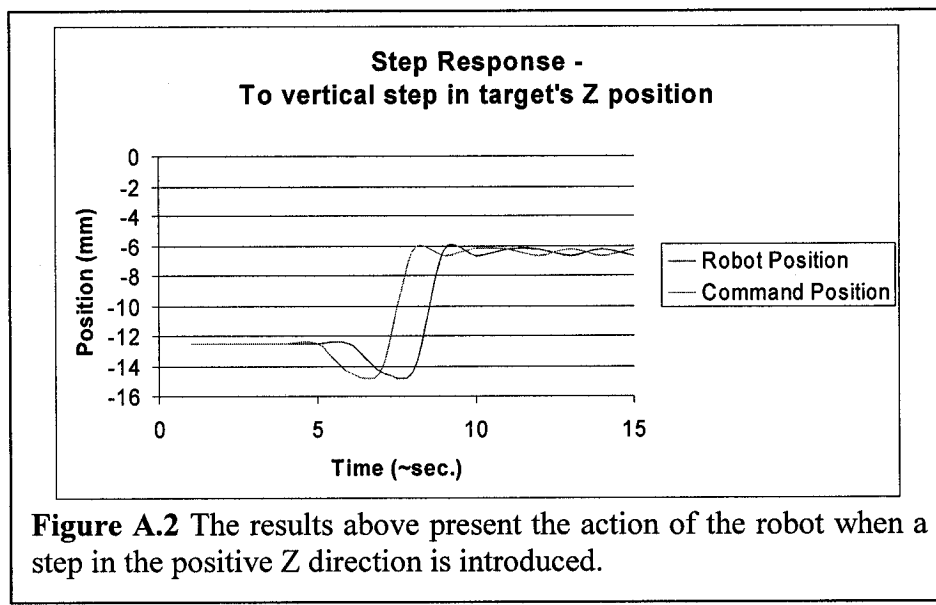
repetitive motion, a further element including smoothing, filtering, and prediction can be incorporated.



## A.2 Experiments and Results

The experimentation performed on this system includes three separate types of trials. The first of these demonstrates the ability of the system to actively track a moving target in real-time using only visual feedback. The experimental setup for this set of experiments is shown in Figure A.1; the CART robot has a  $\frac{1}{4}$ " shaft attached to its Cartesian stage via a passive positioning arm. This robot is capable of moving the target in a water bath in which the LARS is holding the US probe. The plane of the probe is normal to the axis of the shaft, so a single spot is seen on the US image as the target. The CART robot is given a step command and the LARS robot follows. The results of one such step response are shown in Figure A.2. This figure shows a positive step in the target's position in the vertical direction; the software recognizes the step, and then the robot follows. This significant lag between command position and robot position is due to: speed problem

with image capture and analysis, slow motion of the robot, and delays inserted for diagnostic purposes.



The second set of experiments was used to demonstrate the robots ability to follow a contour from a previously performed scan. The phantom used for this was an arc shaped, 3/8" shaft in a water bath. The method for this experiment involved: collecting a 3D ultrasound volume with joint positions for each slice, determining the target in each slice offline, creating a trajectory file, and finally reading in of the trajectory file and commanding the LARS. The plots in the Figure A.3 presents the data obtained from one of these experiments. As in the first experiment, there is a lag as shown in the middle plot showing the displacement along the trajectory.

The last set of experiments dealt with the image processing section of the project. In particular, this experiment focused on the use of the active contour model as a method of segmentation. Figure A.4 shows the use of the ACM on an ultrasound image of the arced shaft phantom.

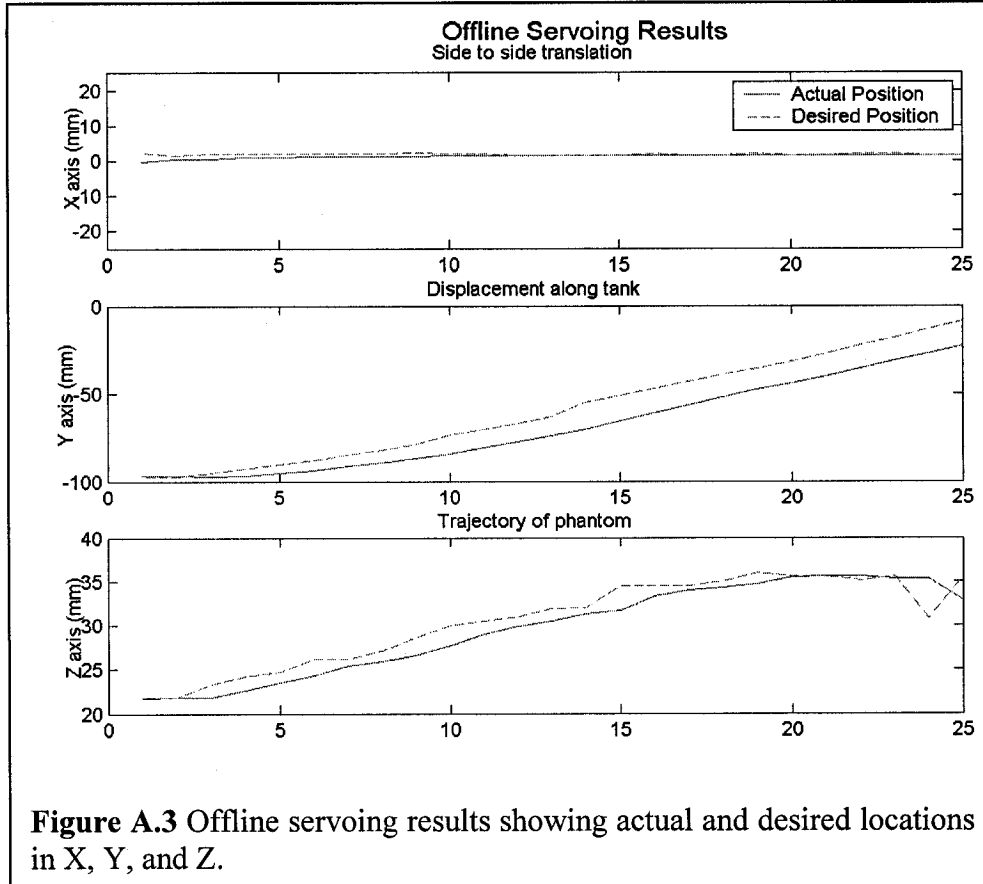


**Figure A.3** Offline servoing results showing actual and desired locations in X, Y, and Z.

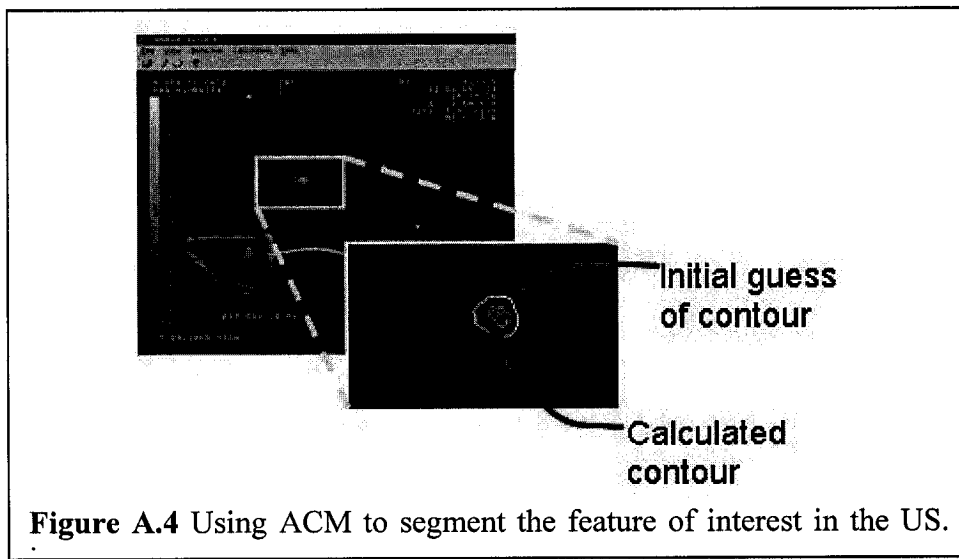


**Figure A.4** Using ACM to segment the feature of interest in the US.

### **A.3 Conclusions**

Visual servoing should improve the effectiveness and accuracy of the Dual-Arm robotic system for US-guided, robotic needle placement by allowing for accurate target tracking despite tissue deformation. This allows for more accurate treatment delivery, increasing treatment effectiveness and decreasing chances of recurrence. The ultimate goal of this project is to be able to guide the needle into the target even though the needle itself and other factors will deflect the tissue significantly.

## Appendix B

# CIS-UltraCal: An Open-Source Ultrasound Calibration Toolkit

The goal of this project<sup>†</sup> is to provide an open-source MATLAB toolkit for ultrasound calibration. It has a convenient graphical user interface which sits on top of an extensive API. Calibration using three phantoms is explicitly supported: the cross-wire phantom, the single-wall phantom, and the Hopkins phantom. Image processing of the Hopkins phantom is automated by making use of techniques from binary morphology, Radon transform and RANSAC. Numerous calibration and termination parameters are exposed. It is also modular, allowing one to use new phantoms.

### B.1 Approach

This toolkit first allows the selection of a set of images and associated tracking data. It next provides an interface for selecting various features within these images. In the case of the Hopkins phantom, we introduce and implement an automatic feature extraction algorithm for the Hopkins phantom that allows for unattended processing of images. Finally, the Levenberg-Marquardt method is used for ultrasound calibration of each of the phantoms. The toolkit also allows for the adjustment of several termination criteria.

---

<sup>†</sup> This project started from my work on cross-wire, single-wall and Hopkins calibration methods. Then, Kishore Kothapalli conducted a qualifying project under supervision of Prof. Hager to segment automatically Hopkins phantom features. Next, I supervised an CIS-II project done by Ryan Kon and Joshua Leven to integrate all the work that has been done in a matlab-based toolkit for US calibration, called CIS-UltraCal [Kon-2005].

- Segment Image
  - Threshold / BW
  - Center of mass
- Search for X-axis
  - radon 180 degrees
  - progressively finer radons (10 degree at 0.5 degree intervals, etc.)
- Search for Y-axis
  - assume y-axis will be approx 90 degrees to x-axis
  - radon +/- 10 degrees of that
  - refine radon
- Find intersection of X- and Y-axes
- Use initial image to determine point positions
  - RANSAC best pair of pixels to determine line based on initial-image intensity
- Find “post”
  - Using final lines as guide, find suspected regions
  - Search areas for “post”
- Sort and order points based on post position
- Return X- and Y-axis points

**Figure B.1** The Hopkins phantom features extraction algorithm.

The Hopkins phantom feature extraction algorithm is summarized in Figure B.1. The algorithm works as follows. First, the initial image is segmented with a simple thresholding function. Each remaining contiguous region of the image is shrunk to its center of mass. Then Radon transforms are used iteratively to determine the principle axis of the Hopkins phantom in the segmented image. Then, the secondary axis is determined by the same method, using a perpendicular angle to the principle axis as an initial guess. Next, the RANSAC algorithm is used to determine the position of the individual points in the image and determine two globally optimal axes. A random pairs of points are chosen to define an axis; a score is calculated based on the intensity in the original ultrasound image at appropriate intervals along that line. Once the two axes are determined, their

intersection is found. Then, knowing the principle axis and the origin, we can find the whereabouts of the orienting post (an additional wire we typically place one unit from the seventh wire on the principle axis), and use that to determine, finally, which is the positive direction for each of the axes. At this point, we know both the position of each point in the image, and which its associated wire in the Hopkins Phantom.

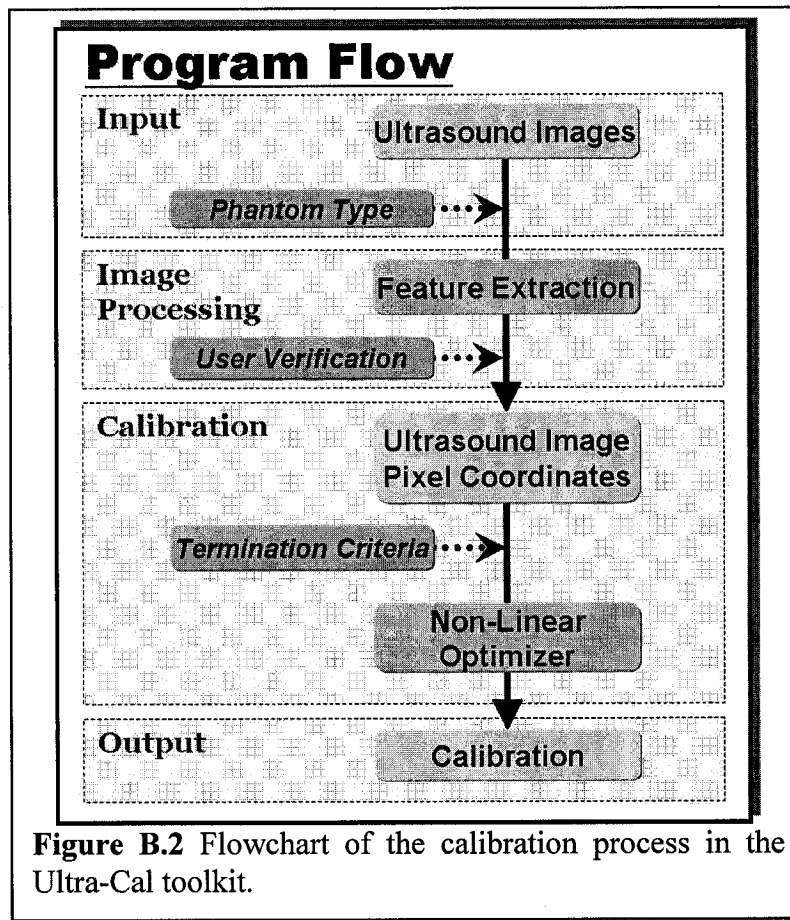


**Figure B.2** Flowchart of the calibration process in the Ultra-Cal toolkit.

## B.2 Interface Design and Implementation

The toolkit is written entirely in MATLAB. The toolkit workflow is illustrated in Figure B.2. It provides both a graphical user interface (Figure B.3) as well as a convenient, highly-modular API. The developers have created interfaces for point and line image feature extraction, as well as a verification interface for the Hopkins Phantom automatic

feature extraction. The Levenberg-Marquardt algorithm is first run on all the data, and then iterated as outliers are removed one by one. Termination is triggered by user-set threshold values of residual error, percentage of outliers, and (in the case of the Hopkins Phantom) reconstruction accuracy. The progress of this iteration is saved to a file which can be used to continue the process at a later time if it is halted.

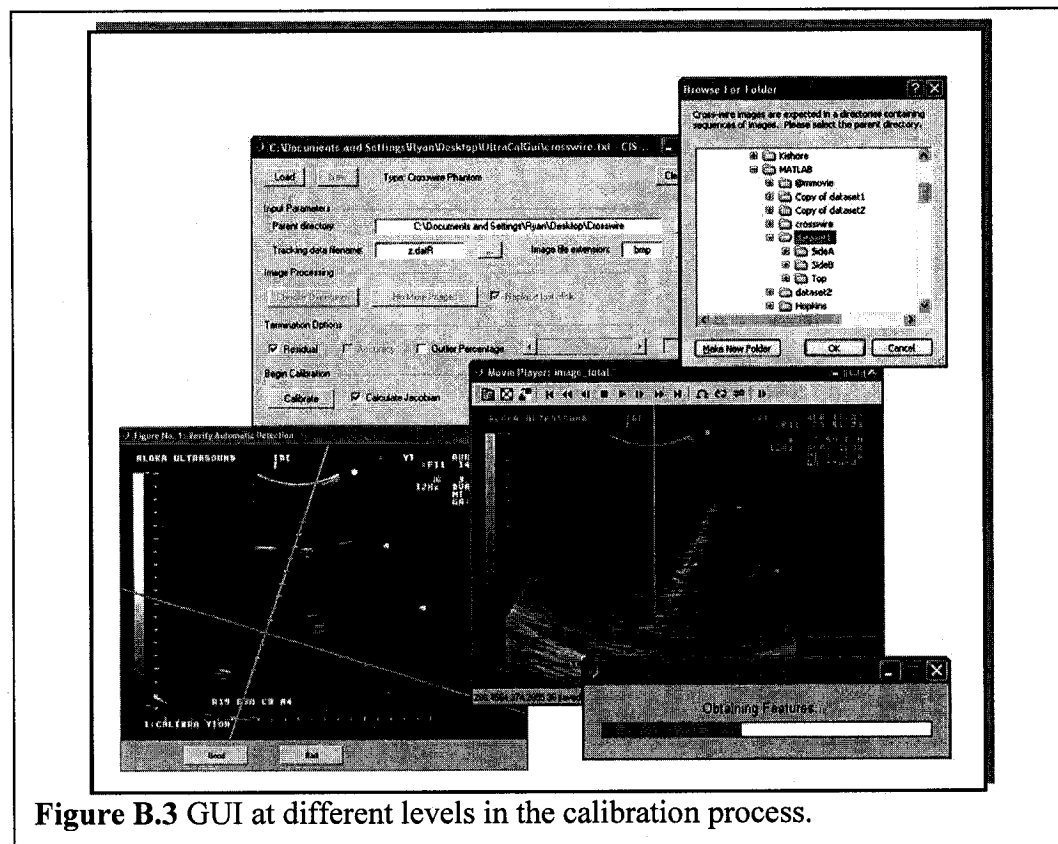


**Figure B.3** GUI at different levels in the calibration process.

## Appendix C

# Error Propagation Analysis of $AX=XB$

As mentioned before, US calibration requires estimating  $X$ , which is a rotation matrix and a displacement vector. Using  $AX=XB$  formulation, we rely on tracking measurements as in  $B$ 's (from a tracking device) and  $A$ 's (from US image.) These measurements are subject to perturbations which will be rendered on the estimation accuracy of  $X$ . In this section, the sensitivity of  $X$  to changes in  $A$ , and  $B$  will be our main concern.

### C.1 Sensitivity Analysis of Linear System

$AX=XB$  is a special case of the Lyapunov equation, and more generally the Sylvester equation:

$$AX - XB = C$$

where  $A$  and  $B$  are square matrices (of possibly different sizes). We refer to the previous equation as the continuous Sylvester equation, which appears frequently in control and stability problems in linear dynamic systems. Deif et al. studied error bounds and sensitivity analysis in linear systems, including Sylvester equation [Deif-1986]. Our goal is to apply this perturbation analysis on  $AX=XB$ , where  $A$ ,  $B$ , and  $X$  are in SE(3) group.

One can convert Sylvester equation [Deif-1986] into an  $Ax=b$  form using Kronecker product calculus:

$$(A \otimes I - I \otimes B^T)x = c$$

where  $x$  and  $c$  are vectors having all the elements in  $X$  and  $C$ , respectively. Starting with  $Ax=b$  problem and adding perturbations to  $A$ ,  $x$ , and  $b$ :

$$(A + \Delta A)(x + \Delta x) = b + \Delta b$$

Multiplying out the terms in the left hand side and canceling the  $Ax=b$  terms (marked terms):

$$\cancel{Ax} + A\Delta x + \Delta Ax + \Delta A\Delta x = \cancel{b} + \Delta b$$

Assuming  $\Delta A\Delta x \approx 0$ :

$$A\Delta x + \Delta Ax \approx \Delta b$$

Solving for  $\Delta x$ :

$$\Delta x \approx A^{-1}(\Delta b - \Delta Ax)$$

Taking the norm and applying the Triangle Inequality:

$$\|\Delta x\| \leq \|A^{-1}\| (\|\Delta b\| + \|\Delta A\| \|x\|)$$

Getting the fraction error by dividing over  $x$ :

$$\frac{\|\Delta x\|}{\|x\|} \leq \|A^{-1}\| \left( \frac{\|\Delta b\|}{\|x\|} + \|\Delta A\| \right)$$

Substituting  $\|x\|$  using the norm of  $Ax=b$ :

$$\|A\|\|x\| \geq \|b\| \Rightarrow \|x\| \geq \frac{\|b\|}{\|A\|}$$

Using this inequality for  $\|x\|$ , and applying it on the previous inequality:

$$\frac{\|\Delta x\|}{\|x\|} \leq \|A^{-1}\| \left( \frac{\|\Delta b\| \|A\|}{\|b\|} + \|\Delta A\| \right)$$

By taking  $\|A\|$  as a common factor we get the following:

$$\frac{\|\Delta x\|}{\|x\|} \leq k \left( \frac{\|\Delta b\|}{\|b\|} + \frac{\|\Delta A\|}{\|A\|} \right), \text{ where } k = \|A^{-1}\| \|A\| \quad (\text{C.1})$$

where  $k$  is the condition number of the  $A$  matrix. Recalling equations C.7 and C.8 from Chapter 7:

$$\begin{pmatrix} I_3 - R_{a1} \otimes R_{b1} \\ I_3 - R_{a2} \otimes R_{b2} \end{pmatrix} \text{vec}(R_x) = 0 \quad (\text{C.2})$$

$$\begin{pmatrix} I_3 - R_{a1} & -D_{a1} \\ I_3 - R_{a2} & -D_{a2} \end{pmatrix} \begin{pmatrix} t_x \\ \lambda_{3*1} \end{pmatrix} = \begin{pmatrix} -R_x t_{b1} \\ -R_x t_{b2} \end{pmatrix} \quad (\text{C.3})$$

As is already known, one can not solve  $X$  uniquely from a single pose. Having the right two motions or three poses, we can solve uniquely for  $X$ . Given the right two motions in equation (C.3) and assuming we have  $R_x$ , we can apply the previous analysis as follows:

$$A = \begin{pmatrix} I_3 - R_{a1} & -D_{a1} \\ I_3 - R_{a2} & -D_{a2} \end{pmatrix}, x = \begin{pmatrix} t_x \\ \lambda_{3*1} \end{pmatrix}, \text{ and } b = \begin{pmatrix} -R_x t_{b1} \\ -R_x t_{b2} \end{pmatrix}$$

In the case of having  $n$  motions, the size of  $A$  will be  $(3n \times 6)$  and the size of  $b$   $(3n \times 1)$ . The system of equations will be over constrained and the condition number can be estimated using Moore-Penrose pseudo inverse, as follows:

$$\frac{\|\Delta x\|}{\|x\|} \leq k \left( \frac{\|\Delta b\|}{\|b\|} + \frac{\|\Delta A\|}{\|A\|} \right), \text{ where } k = \|A^+\| \|A\|$$

where  $A^+$  is the MP pseudo inverse, which can be calculated using the SVD of  $A$ :

$$A^+ = V \begin{bmatrix} D^{-1} & 0 \\ 0 & 0 \end{bmatrix} U^*$$

The use of pseudo inverse in determining the condition number is acceptable, if the following condition is met [Deif-1986]:

$$\|A^+\| \|\Delta A\| < 1$$

This condition is usually guaranteed under slight perturbation  $\Delta A$ . In case of acute perturbation in  $\Delta A$  (large uncertainties in  $R_a$  and  $t_a$ ), the above error bound of  $\Delta x$  might be exaggerated. Instead one should use a tighter bound as described in [Deif-1986]:

$$\begin{aligned} \frac{\|\Delta x\|}{\|x\|} &\leq \hat{k}[(2 + \hat{k}\delta)\alpha + \beta\gamma], \text{ where} \\ \alpha &= \frac{\|\Delta A\|}{\|A\|}, \beta = \frac{\|\Delta b\|}{\|b\|}, \gamma = \frac{\|b\|}{\|A\|\|x\|}, \delta = \frac{\|r\|}{\|A\|\|x\|} \\ k &= \text{cond}(A) = \|A^+\| \|A\|, \hat{k} = \frac{k}{1 - k\alpha}, \|r\| = \|I - AA^+\| \|b\| \end{aligned}$$

Finally, for  $\text{rank}(A) = m = n$  ( $A^{-1}$  exists), the above error bound reduces to formula (C.1). In this case either  $k$  or  $\hat{k}$  can be used. The above perturbation analysis is a general framework for linear system defined in the form  $Ax=b$ . In the next section, we will conduct an error propagation analysis on SE(3) group, utilizing specific algebraic properties for frame and rotation matrices.

## C.2 Error Propagation Analysis of $AX=XB$

In this section, the error propagation analysis of  $AX=XB$  will utilize the fact that all  $A$ 's,  $B$ 's and  $X$  belong to the SE(3) group, which consists of one rotation matrix and a 3D displacement vector.

$$AX = XB$$

$$\begin{bmatrix} R_a & t_a \\ 0 & 0 & 0 & 1 \end{bmatrix} \begin{bmatrix} R_x & t_x \\ 0 & 0 & 0 & 1 \end{bmatrix} = \begin{bmatrix} R_x & t_x \\ 0 & 0 & 0 & 1 \end{bmatrix} \begin{bmatrix} R_b & t_b \\ 0 & 0 & 0 & 1 \end{bmatrix}$$

Multiplying out the terms in the above equation:

$$\begin{aligned} R_a R_x &= R_x R_b \\ R_a t_x + t_a &= R_x t_b + t_x \end{aligned} \tag{C.4}$$

Now, we will define a perturbation in a frame  $F$  as:

$$\Delta F_i = \begin{bmatrix} \Delta R_i & \Delta t_i \\ 0 & 0 & 0 & 1 \end{bmatrix} \in SE(3),$$

where  $\Delta t_i \in \mathbb{R}_3$  is the translation error in 3D

$$\Delta R_i = \Delta R_i(\vec{\alpha}, \|\vec{\alpha}\|) = \exp(\text{skew}(\vec{\alpha})) \in SO(3)$$

where  $\vec{\alpha} \in \mathbb{R}_3$  is a vector representing the axis of rotation, and  $\|\vec{\alpha}\|$  is the angle of rotation in radians. In general, rotations can be represented as  $R = \exp(\hat{n} \theta)$ , where  $\hat{n}$  is a unit vector pointing to the axis of rotation and  $\theta$  is the magnitude of this spin. In our case, we have  $\vec{\alpha} = \hat{n} \theta$ , and by using Taylor's infinite series expansion we get:

$$\Delta R_i(\vec{\alpha}) = \exp(\text{skew}(\vec{\alpha})) = I + \text{skew}(\vec{\alpha}) + \frac{\text{skew}(\vec{\alpha})^2}{2!} + \frac{\text{skew}(\vec{\alpha})^3}{3!} + \dots$$

Assuming small rotation errors allows us to ignore second order terms and higher. This

linearization shows as:

$$\Delta R_i(\vec{\alpha}) = \exp(\text{skew}(\vec{\alpha})) \approx I + \text{skew}(\vec{\alpha}),$$

$$\text{where: } \text{skew}(\vec{\alpha}) = \begin{bmatrix} 0 & -\alpha_3 & \alpha_2 \\ \alpha_3 & 0 & -\alpha_1 \\ -\alpha_2 & \alpha_1 & 0 \end{bmatrix}$$

Each of the measured frames,  $A$ 's and  $B$ 's has an error associated with it.

Our goal is to model the perturbation in  $X$  to changes in  $A$ 's, and  $B$ 's:

$$R_a \Delta R_a \bullet R_x \Delta R_x = R_x \Delta R_x \bullet R_b \Delta R_b \quad (\text{C.5})$$

$$R_a \Delta R_a \bullet (t_x + \Delta t_x) + (t_a + \Delta t_a) = R_x \Delta R_x \bullet (t_b + \Delta t_b) + (t_x + \Delta t_x) \quad (\text{C.6})$$

### Error Propagation on Rotation Equation (C.5).

We will use  $S$  as an abbreviation for “Skew.”  $\alpha_i$ ,  $\beta_i$ , and  $x_i$  will represent the rotation error direction in  $A_i$ ,  $B_i$ , and  $X_i$  respectively. Linearizing the orientation errors:

$$R_a(I + S(\vec{\alpha}))R_x(I + S(\vec{x})) \approx R_x(I + S(\vec{x}))R_b(I + S(\vec{\beta}))$$

Multiplying out the terms:

$$\begin{aligned} R_a R_x + R_a R_x S(\vec{x}) + R_a S(\vec{\alpha}) R_x + R_a S(\vec{\alpha}) R_x S(\vec{x}) &\approx \\ \cancel{R_a R_x} + R_x R_b S(\vec{\beta}) + R_x S(\vec{x}) R_b + R_x S(\vec{x}) R_b S(\vec{\beta}) & \end{aligned}$$

Cancelling out the terms in  $R_a R_x = R_x R_b$  (marked with a circle):

$$\begin{aligned} R_a R_x S(\vec{x}) + R_a S(\vec{\alpha}) R_x + R_a S(\vec{\alpha}) R_x S(\vec{x}) &\approx \\ \cancel{\underline{R_x R_b} S(\vec{\beta})} + \cancel{\underline{R_x S(\vec{x}) R_b}} + \cancel{\underline{R_x S(\vec{x}) R_b S(\vec{\beta})}} & \end{aligned}$$

Substituting  $R_x R_b$  with  $R_a R_x$ , and  $R_x$  with  $R_a R_x R_b^T$  (underlined):

$$R_a R_x S(\vec{x}) + R_a \overset{\curvearrowright}{S(\vec{\alpha})} R_x + R_a \overset{\curvearrowleft}{S(\vec{\alpha})} R_x S(\vec{x}) \approx \\ R_a R_x S(\vec{\beta}) + R_a R_x R_b^T S(\vec{x}) R_b + R_a R_x R_b^T S(\vec{x}) R_b S(\vec{\beta})$$

Using the following facts:

$$\text{cross-product: } \vec{a} \times \vec{v} = skew(\vec{a}) \bullet \vec{v} \\ \text{rotation triple product: } \vec{a} \times (R \bullet \vec{b}) = R \bullet ((R^T \bullet \vec{a}) \times \vec{b}), \text{ consequently} \\ skew(\vec{a}) \bullet R = R \bullet skew(R^T \bullet \vec{a})$$

Applying the previous rule to move  $S(\vec{\alpha})$  one step to the right on the LHS (as shown with the above arrows):

$$R_a R_x S(\vec{x}) + R_a R_x S(R_x^T \vec{\alpha}) + R_a R_x S(R_x^T \vec{\alpha}) S(\vec{x}) \approx \\ R_a R_x S(\vec{\beta}) + R_a R_x R_b^T S(\vec{x}) R_b + R_a R_x R_b^T S(\vec{x}) R_b S(\vec{\beta})$$

Multiplying both sides with  $R_a^T$  and then with  $R_x^T$ :

$$S(\vec{x}) + S(R_x^T \vec{\alpha}) + S(R_x^T \vec{\alpha}) S(\vec{x}) \approx S(\vec{\beta}) + R_b^T S(\vec{x}) R_b + R_b^T S(\vec{x}) R_b S(\vec{\beta})$$

We can neglect the double “Skew” terms from both sides:

$$S(\vec{x}) + S(R_x^T \vec{\alpha}) \approx S(\vec{\beta}) + R_b^T S(\vec{x}) R_b$$

Applying the triple product rule to the last term and using the linearity feature of the *Skew* operator to collect the terms:

$$S(\vec{x} + R_x^T \vec{\alpha}) \approx S(\vec{\beta} + R_b^T \vec{x}) \Rightarrow \vec{x} + R_x^T \vec{\alpha} \approx \vec{\beta} + R_b^T \vec{x}$$

Rearranging the terms and assign a label for motion  $i$ :

$$(I - R_{bi}^T) \vec{x} \approx \vec{\beta} - R_x^T \vec{\alpha} \quad (\text{C.7})$$

Note that  $\vec{x}$  is multiplied by a rank deficient matrix (rank = 2), which makes it impossible to recover  $\vec{x}$  in three directions. This is not surprising, as discussed in Chapter 6 and 7 it is impossible to recover  $R_x$  from a single motion.

### Error Propagation on Displacement Equation (C.6).

Substituting small rotations with 1<sup>st</sup> order *Skew* approximation in equation (C.6):

$$R_a(I + S(\vec{\alpha}))(t_x + \Delta t_x) + (t_a + \Delta t_a) = R_x(I + S(\vec{x}))(t_b + \Delta t_b) + (t_x + \Delta t_x)$$

Multiplying out the terms on both sides:

$$\begin{aligned} & \underbrace{R_a t_x}_{\text{cancel}} + R_a \Delta t_x + R_a S(\vec{\alpha}) t_x + R_a S(\vec{\alpha}) \Delta t_x + \underbrace{t_a}_{\text{cancel}} + \Delta t_a \approx \\ & \underbrace{R_x t_b}_{\text{cancel}} + R_x \Delta t_b + R_x S(\vec{x}) t_b + R_x S(\vec{x}) \Delta t_b + \underbrace{t_x}_{\text{cancel}} + \Delta t_x \end{aligned}$$

Cancel out the terms in the second part of equation (C.2), as marked above:

$$\begin{aligned} & R_a \Delta t_x + R_a S(\vec{\alpha}) t_x + R_a S(\vec{\alpha}) \Delta t_x + \Delta t_a \approx \\ & R_x \Delta t_b + R_x S(\vec{x}) t_b + R_x S(\vec{x}) \Delta t_b + \Delta t_x \end{aligned}$$

Further, we can ignore terms involve second order variations, as in  $S(\vec{\alpha})\Delta t_x = \vec{\alpha} \times \Delta t_x$  and  $S(\vec{x})\Delta t_b = \vec{x} \times \Delta t_b$ :

$$R_a \Delta t_x + R_a S(\vec{\alpha}) t_x + \Delta t_a \approx R_x \Delta t_b + R_x S(\vec{x}) t_b + \Delta t_x$$

Applying the previously used cross-product rule, one can swap the order of multiplied components, as follows:

$$S(\vec{\alpha}) t_x = \vec{\alpha} \times t_x = -t_x \times \vec{\alpha} = -S(t_x) \vec{\alpha} = S(t_x)^T \vec{\alpha}$$

By rearranging the terms on both sides:

$$R_x S(t_b)^T \vec{x} + \Delta t_x - R_a \Delta t_x \approx R_a S(t_x)^T \vec{\alpha} + \Delta t_a - R_x \Delta t_b$$

Rewriting this form for motion  $i$ :

$$R_x S(t_{bi})^T \vec{x} + (I - R_{ai}) \Delta t_x \approx R_{ai} S(t_x)^T \vec{\alpha} + \Delta t_a - R_x \Delta t_b \quad (\text{C.8})$$

Combining (C.7) and (C.8) for  $n$  motions, one can solve for the error bounds on frame  $X$ :

$$\begin{bmatrix} R_x S(t_{b1})^T & (I - R_{a1}) \\ (I - R_{b1}^T) & 0_{3*3} \\ R_x S(t_{b2})^T & (I - R_{a2}) \\ (I - R_{b2}^T) & 0_{3*3} \\ \vdots & \vdots \end{bmatrix} \begin{bmatrix} \vec{x} \\ \Delta t_x \end{bmatrix} \approx \begin{bmatrix} R_{a1} S(t_x)^T & 0_{3*3} & I_{3*3} & -R_x \\ -R_x^T & I_{3*3} & 0_{3*3} & 0_{3*3} \\ R_{a2} S(t_x)^T & 0_{3*3} & I_{3*3} & -R_x \\ -R_x^T & I_{3*3} & 0_{3*3} & 0_{3*3} \\ \vdots & \vdots & \vdots & \vdots \end{bmatrix} \begin{bmatrix} \vec{\alpha} \\ \vec{\beta} \\ \Delta t_a \\ \Delta t_b \end{bmatrix} \quad (\text{C.9})$$

Important observations can be summarized as follows:

- In this analysis we did not depend on matrix and vector norms, as they usually set large error bounds. For this analysis, the main assumption is the first order approximation to linearize the problem and ignoring high order terms.
- Equation (C.9) emphasizes that the error in frame  $X$  depends on both input uncertainties and the type of motion. The key point is to minimize  $(\vec{\alpha}, \vec{\beta}, \Delta t_a, \Delta t_b)$  and also to chose the right motions that can enhance the condition number of the left matrix.
- This observation that error is affected by the type of motion is consistent with the detailed algebraic analysis that is presented in Chapter 7.
- This approach is not easily showing the statistical distribution of the errors in  $X$ . In the next section, we will show how error covariance propagates through the  $AX=XB$  formulation.

### C.3 Covariance Propagation Method

The distribution of a random vector is characterized by its probability density function (pdf). A common assumption is to retain only the first and second moments of the pdf, i.e. the expectation vector and the covariance matrix of a random vector.

$$\text{Expectation of a vector } \vec{x} : \bar{x} = E(\vec{x}) = \int y \cdot \rho_x(y) \cdot dy$$

$$\text{Covariance of a vector } \vec{x} : \sum_{xx} = E((\vec{x} - \bar{x})(\vec{x} - \bar{x})^T)$$

Covariances can be propagated in explicit and implicit functions through the use of Jacobian matrices [Pennec-1995]. We would like to propagate the covariances of  $A$ 's and  $B$ 's through  $AX=XB$  formulation and estimate the covariance of  $X$ . Starting with equation (C.2), it is considered an implicit function of  $R_x$ :

$$f(R_x; R_a, R_b) = 0$$

Assuming we have certain measurements for  $R_b$ 's,  $f$  will be an implicit function of both  $R_x$  and  $R_a$ . By applying the 1<sup>st</sup> order approximation on Taylor's expansion of  $f$ :

$$f(R_x; R_a) = f(\bar{R}_x; \bar{R}_a) + \frac{\partial f}{\partial R_x}(\bar{R}_x; \bar{R}_a) \cdot (R_x - \bar{R}_x) + \frac{\partial f}{\partial R_a}(\bar{R}_x; \bar{R}_a) \cdot (R_a - \bar{R}_a) = 0$$

Based on the implicit function theorem,  $R_x = g(R_a)$  exists around a given point  $(R_x, R_a)$  such as  $f(R_x, R_a) = 0$  if and only if  $\frac{\partial g}{\partial R_x}$  can be inverted at this point, and we will have:

$$\left[ \frac{\partial f}{\partial R_x}(\bar{R}_x; \bar{R}_a) \right] \sum_{xx} \left[ \frac{\partial f}{\partial R_x}(\bar{R}_x; \bar{R}_a) \right]^T = \left[ \frac{\partial f}{\partial R_a}(\bar{R}_x; \bar{R}_a) \right] \sum_{AA} \left[ \frac{\partial f}{\partial R_a}(\bar{R}_x; \bar{R}_a) \right]^T$$

We can not invertible  $\left[ \frac{\partial f}{\partial R_x}(\bar{R}_x; \bar{R}_a) \right]$  from a single motion. At least we need to have

two independent motions to invert this term, as follows:

$$\text{Let } T = \begin{bmatrix} \frac{\partial f}{\partial R_x}(\bar{R}_x; \bar{R}_a) \\ \frac{\partial f}{\partial R_a}(\bar{R}_x; \bar{R}_a) \end{bmatrix}, S = \begin{bmatrix} \frac{\partial f}{\partial R_x}(\bar{R}_x; \bar{R}_a) \\ \frac{\partial f}{\partial R_a}(\bar{R}_x; \bar{R}_a) \end{bmatrix}$$
$$\Sigma_{XX} = (T^T T)^{-1} T^T S \Sigma_{AA} S^T T (T^T T)^{-1}$$

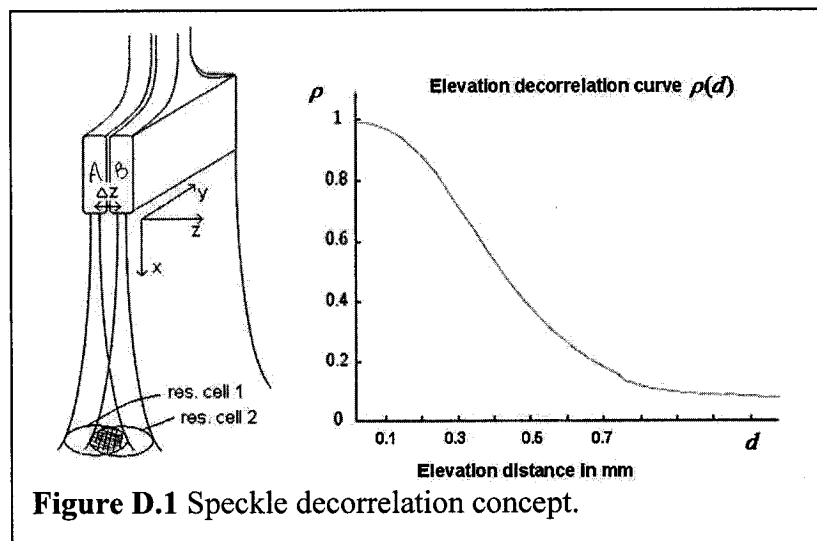
The above equation relates the covariance of  $X$  to that of  $A$ . It is obvious that the type of motion is an important factor in determining the relation between input uncertainties to the output.

In addition to the methods mentioned in this appendix, one can use numerical simulation, similar to the one described in Chapter 6, to check the asymptotic accuracy of the output frame  $X$  under different noise levels.

## Appendix D

# Toward Accurate Out-of-plane Motion Estimation

As mentioned in Chapter 7, image-based approach, known as speckle decorrelation, has the potential to estimate out-of-plane motion. Figure D.1 shows the principle concept of speckle decorrelation approach. By moving an US probe with  $\Delta Z$  distance in the elevation direction, there is considerable overlap between resolution cells from neighboring US scans. This overlap can be observed as a correlation between corresponding patches in these images. Further, the correlation (or decorrelation) depends on the degree of overlap of these resolution cells and reflects the separation of the corresponding patches. One can readily calibrate this dependency and compute



decorrelation coefficient vs. elevation separation, known as decorrelation curve as shown in Figure D.1. Three non-collinear pairs of fully developed speckle (FDS) patches are sufficient to estimate the three out-of-plane degrees of freedom. A serious difficulty for this approach is that the theory of correlation holds only for fully developed speckle. Hence, the main challenge of this approach is to identify accurately the regions of FDS from the non-FDS regions<sup>†</sup>.

## D.1 Approach Introduction

Each pixel in an ultrasound image is formed by the back scattered echoes from an approximately ellipsoid called the resolution cell (Figure D.1). The interference of scatterers in a resolution cell creates the granular appearance of the ultrasound image, called speckle. Although of random appearance, speckle pattern is identical if the same object is scanned from the same direction and under the same focusing and frequency. Diffuse scattering happens if the scatterers in a resolution cell are placed independently and uniformly at random. If each resolution cell in an image patch has many such scatterers, the patch is said to be fully developed speckle (FDS). In contrast, white and dark features in the ultrasound B-mode images are caused by coherent back-scattering of ultrasound pulse.

Speckle detection is useful in segmentation, sensorless 3D freehand US, speckle cancellation and quantitative tissue characterization. In ultrasound compounding, for example, the goal is to cancel the speckles, while in sensorless 3D freehand ultrasound they are utilized to estimate probe movement.

---

<sup>†</sup> The work presented here is published in the IEEE 2006 ultrasonic symposium proceedings.

Assume the effective number of scatterers per resolution cell to be  $\mu$ , and the diffuse and coherent signal energy to be  $2\sigma^2$  and  $s^2$  respectively. Speckles can be classified by  $\mu$  and  $k = s/\sigma$ , with  $\mu > 10$  and  $k < 1$  being FDS. Dutt et al. [Dutt-1994, Dutt-1995] and Prager et al. [Prager-2002] proposed using R and S to estimate  $\mu$  and  $k$  and therefore classify speckles

$$R = SNR = \frac{\langle A^v \rangle}{\sqrt{\langle A^{2v} \rangle - \langle A^v \rangle^2}} \quad (\text{D.1})$$

$$S = \text{Skewness} = \frac{\langle (A^v - \langle A^v \rangle)^3 \rangle}{(\langle A^{2v} \rangle - \langle A^v \rangle^2)^{3/2}} \quad (\text{D.2})$$

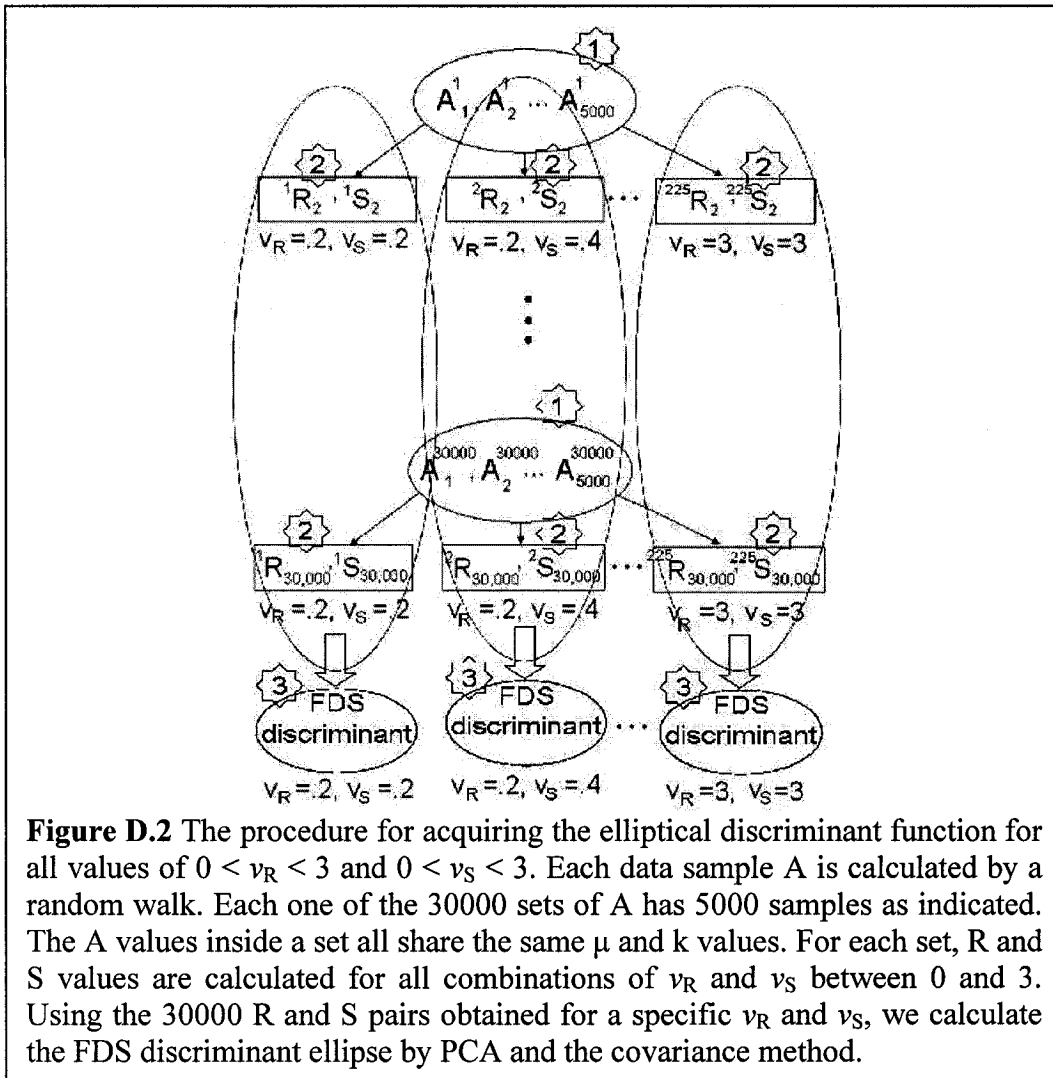
where  $A$  is the amplitude of the ultrasound RF envelope,  $v$  is the signal power and  $\langle \cdot \cdot \cdot \rangle$  denotes mean. Depending on the correlation of data, thousands of sample data are required to reliably calculate R and S [Dutt-1995]. In [Dutt-1995] and [Prager-2002], values of  $v$  that reduce this sample size are sought. Useful variability of clusters of sample data with different  $\mu$  and  $k$  values are maximized in [Prager-2002] to find the optimal  $v$ , a method that is scrutinized by [Martin-Fernandez-2005].

Since R and S are different order moments of sample data, optimal values for  $v$  in R and S are not necessarily the same. We propose using different values of  $v$  in R and S. We follow a similar approach to [Prager-2002] to simulate the B-scan.

## D.2 Simulation Methods

We seek the optimal values of  $v_R$  and  $v_S$  that substitute  $v$  in equations (D.1) and (D.2) respectively. To create the sample data, the sum of  $\mu$  vectors of length  $\sqrt{2}/\mu$  and arbitrary phase (a random walk) is added to a single vector with zero phase and length  $k$ , resulting in a vector  $\mathbf{A}$ , with amplitude  $A$ .

The first step to compare the performance of different values for  $v_R$  and  $v_S$  is to obtain an FDS discriminant function. To this end, we set  $v_R = 0.2, 0.4 \dots 3$  and similarly  $v_S = 0.2, 0.4 \dots 3$ , and for all combinations of  $v_R$  and  $v_S$  ( $15 \times 15 = 225$  cases) acquire an FDS elliptical discrimination function in 3 steps (Figure D.2):



- 1) 30000 sets of 5000 random  $A$  that represent FDS with different parameters  $0 < k < 1$  and  $10 < \mu < 60$  are calculated (each data sample  $A$  itself is obtained by the random walk described above, not shown in Figure D.2).

- 2) For each set, R and S are calculated for all combinations of  $0.2 \leq v_R \leq 3$  and  $0.2 \leq v_S \leq 3$ , resulting in  $30000 \times 225$  samples of R and S.
- 3) Using the 30000 samples of R and S for each  $v_R$  and  $v_S$  combination, 225 elliptical discriminant functions that encompass 95% of R and S values is obtained automatically using PCA and the covariance method.

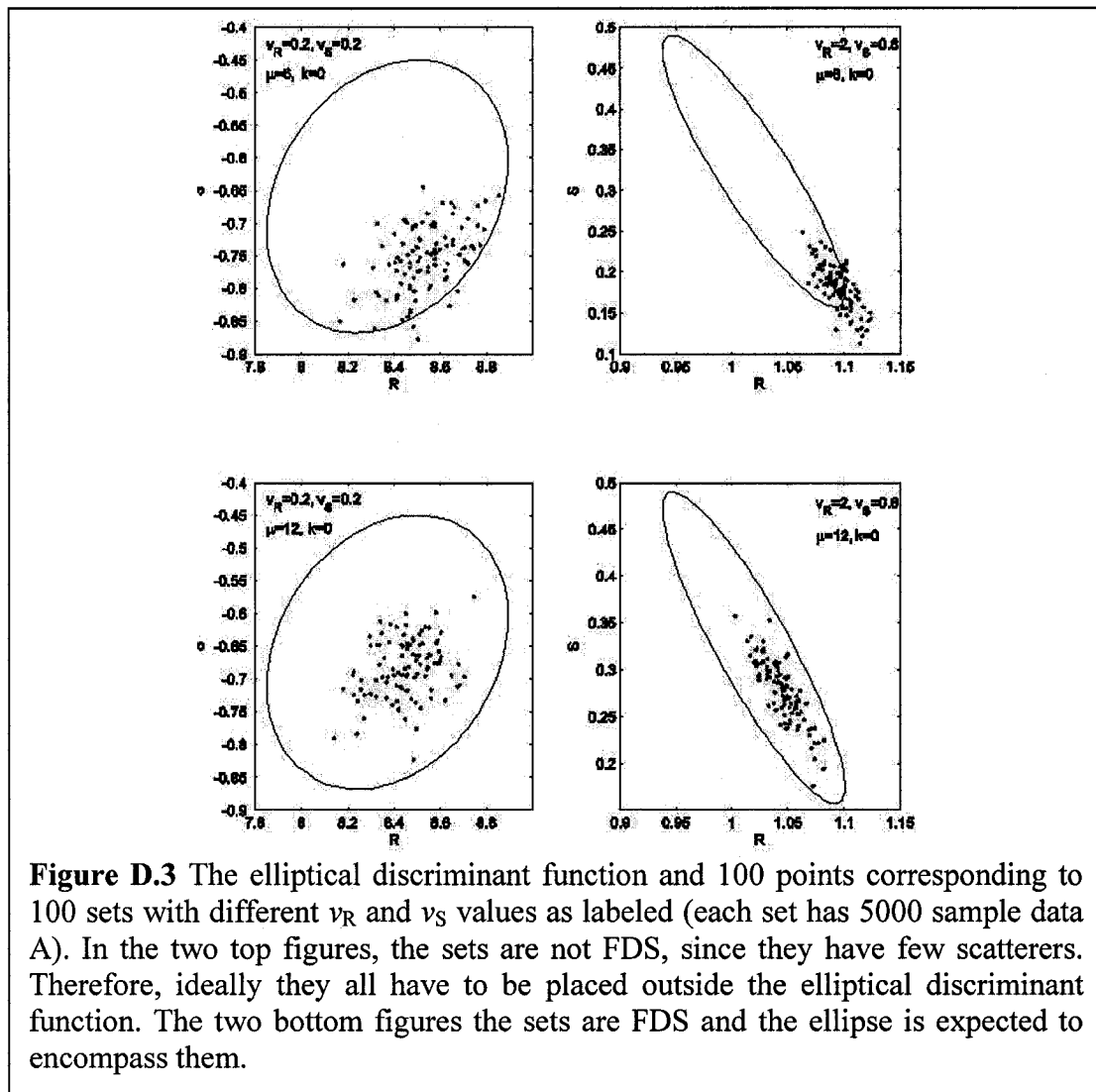
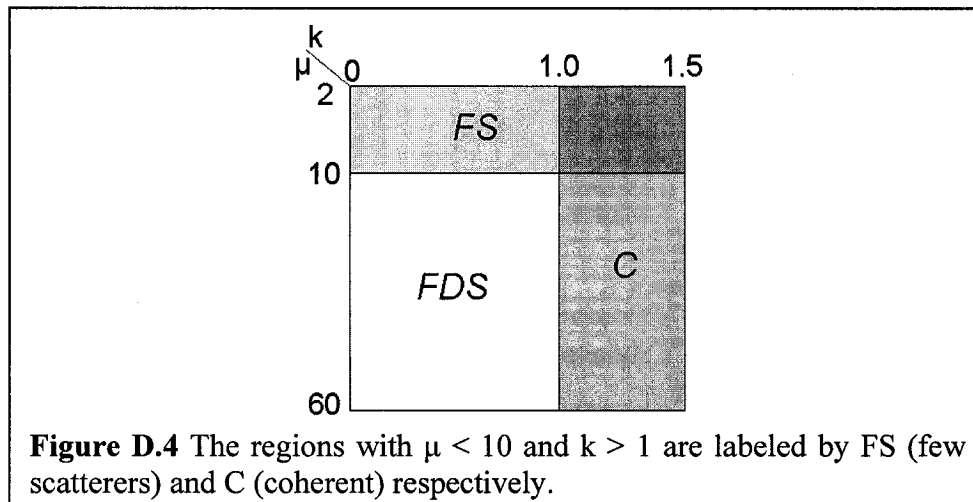


Figure D.3 shows the elliptical discriminant functions for  $v_R = 0.2$  and  $v_S = 0.2$  in the left images and for  $v_R = 2$  and  $v_S = 0.8$  in the right ones. The two top images show 100 (R, S)

points that correspond to 100 sets of data A with  $\mu = 6$  and  $k = 0$  values (few scatterers). These sets have to be categorized as non-FDS, therefore one can say that the pair  $v_R = 2$  and  $v_S = 0.8$  is performing better in this case (minimizing false acceptance). In the two bottom images, same  $v_R$  and  $v_S$  values are used, but for  $\mu = 12$  and  $k = 0$  (many scatterers, FDS). Both left and right discriminant functions categorize all 100 sets correctly (minimizing false rejection). This example shows that different  $v_R$  and  $v_S$  values affect the performance of the discriminant function.

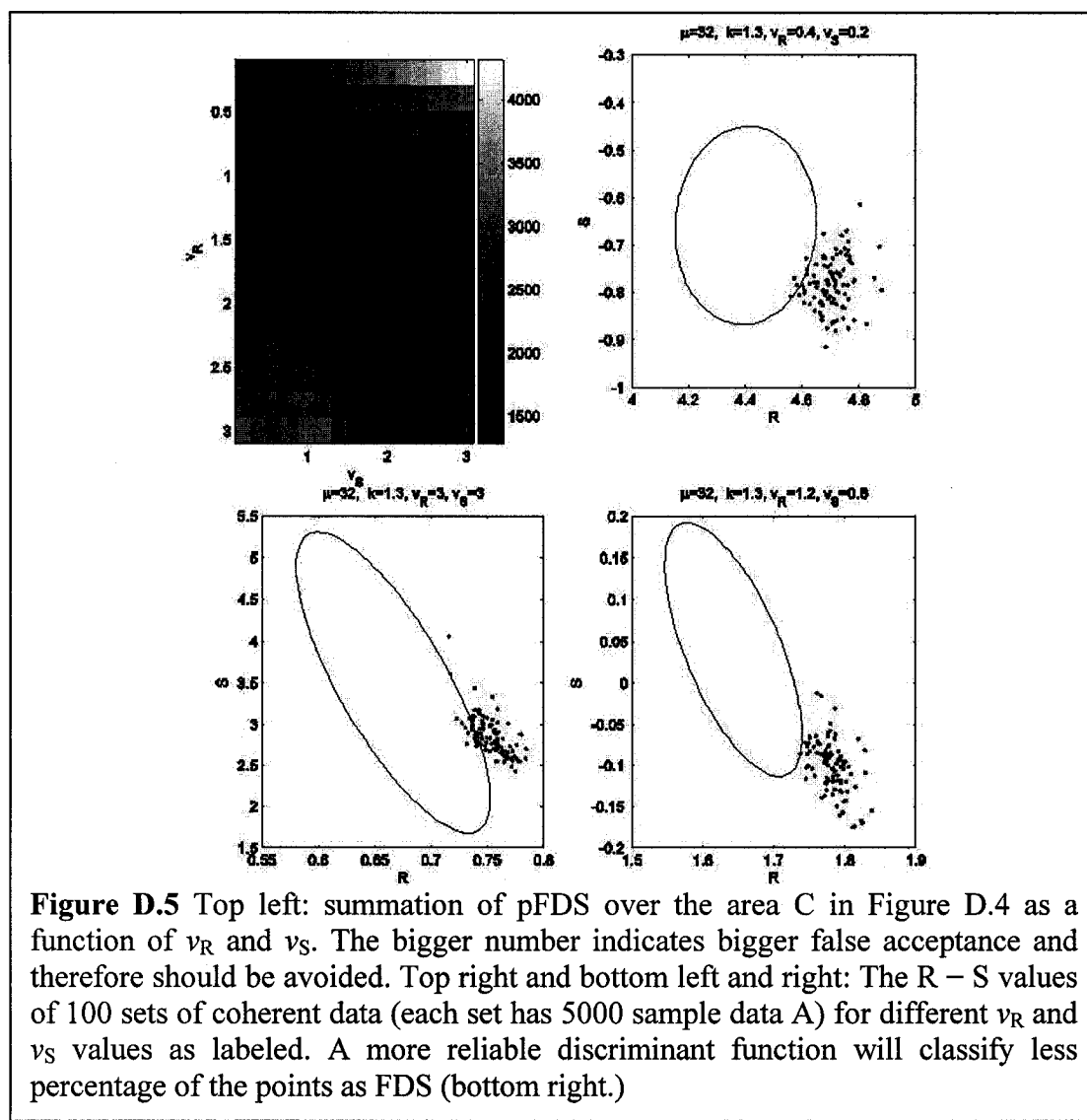
In order to find the optimal  $v_R$  and  $v_S$  values, we obtain the probability that a set with properties  $\mu$  and  $k$  be identified as FDS, i.e. the (R, S) pair calculated for this set falls inside the ellipse. Having such a pseudo pdf (pFDS) for all values of  $\mu$ ,  $k$ ,  $v_R$  and  $v_S$ , it is possible to optimize  $v_R$  and  $v_S$  to achieve a desired probability distribution. Obtaining pFDS, which requires a large number of simulations, is as follows.

- 1) For all combinations of  $k = 0, 0.1, 0.2 \dots 1.5$  (16 values) and  $\mu = 2, 3 \dots 60$  (59 values) in the  $k-\mu$  plane (Figure D.4), generate 100 sets of 5000 random A. The result is  $16 \times 59 \times 100 \times 5000$  random A, with each A being calculated by a random walk.



**Figure D.4** The regions with  $\mu < 10$  and  $k > 1$  are labeled by FS (few scatterers) and C (coherent) respectively.

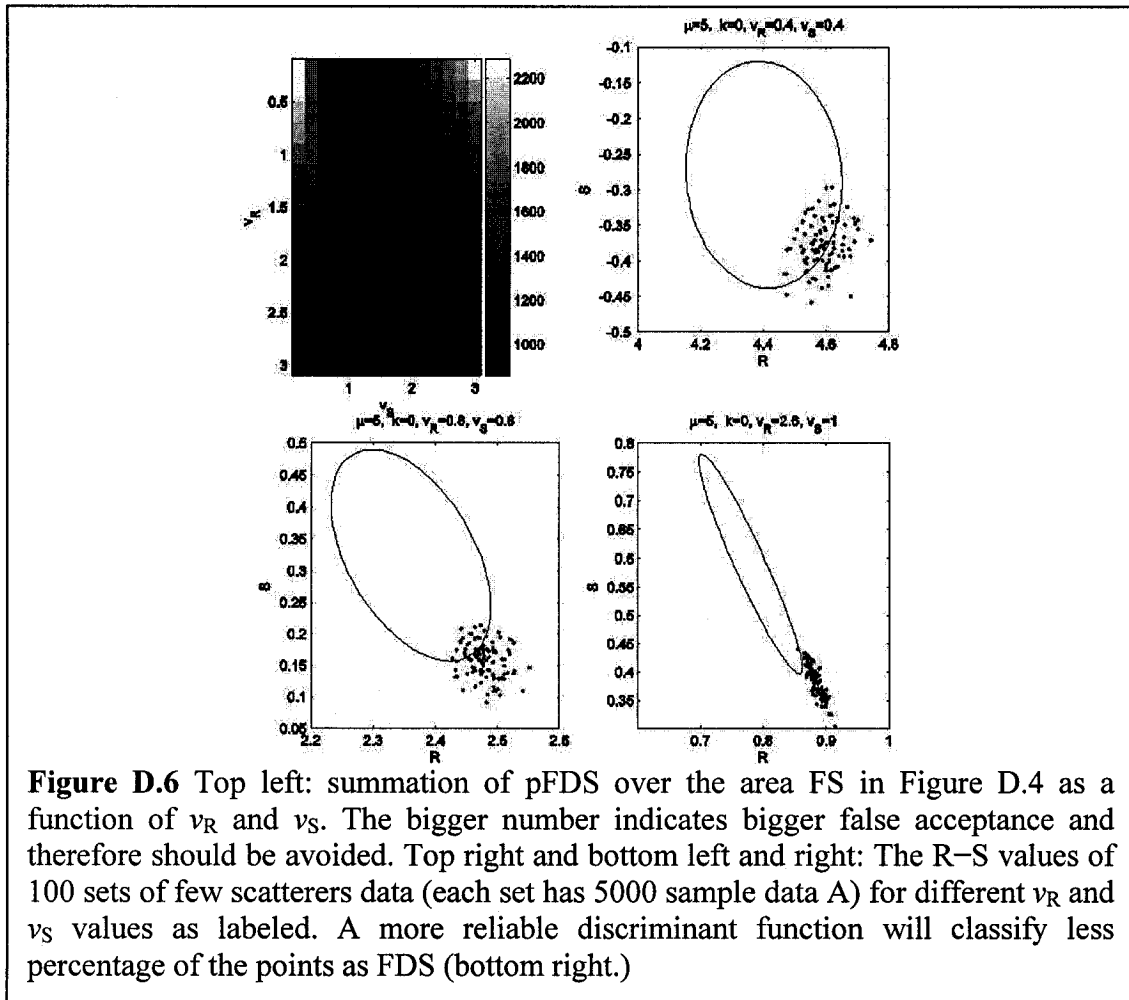
- 2) Calculate R and S of each set for all combinations of vR and vS.
- 3) pFDS = number of the (R, S) pairs that fall inside the FDS discriminant ellipse.
- The resultant pFDS is a function of vR, vS,  $\mu$  and k. Different optimum values for vR and vS can be found depending on the criteria.



### D.3 Optimizing $v_R$ and $v_S$

Using pFDS and depending on the particular application, different optimum values for  $v_R$  and  $v_S$  can be found. We analyze three cases here.

**Minimizing False Acceptance for Coherent Sets.** To minimize false acceptance for the coherent data, one can sum pFDS over the area C in Figure D.4. Figure D.5 top left shows the summation result. Generally speaking, the four corners of the  $v_R$ - $v_S$  plane should be avoided to prevent false acceptance. The FDS discriminant ellipse along with



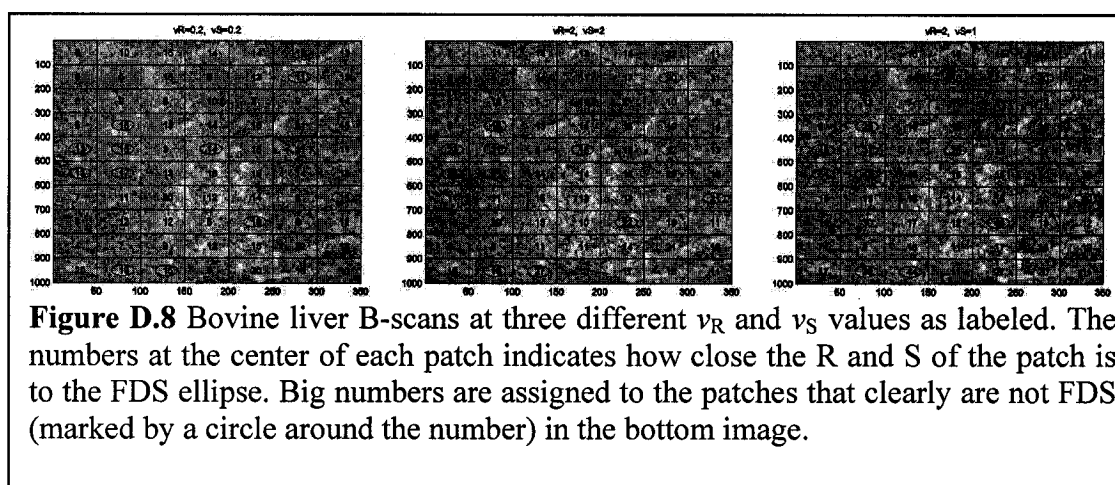
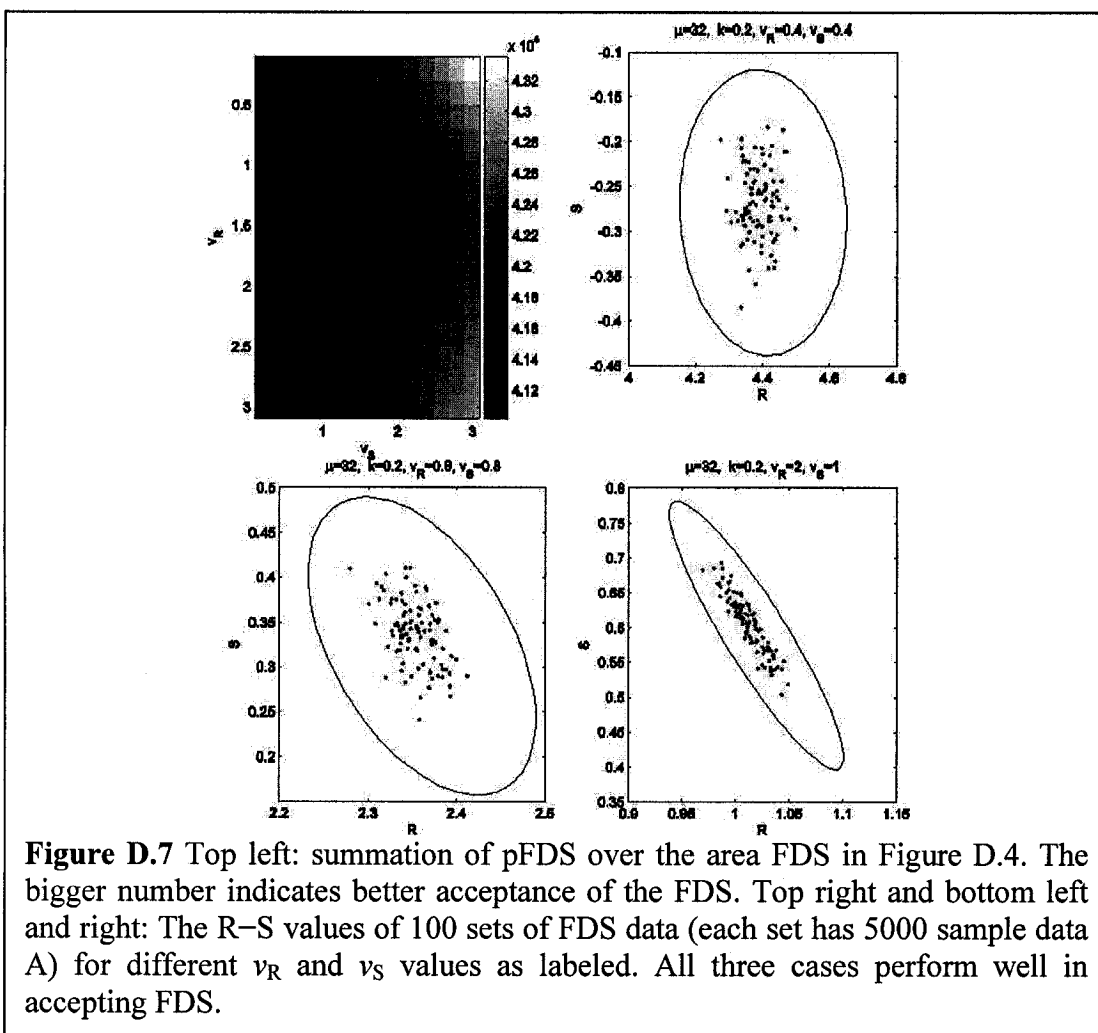
(R, S) of 100 sets of 5000 sample A for three values of  $v_R = 0.4$ ,  $v_S = 0.2$ ,  $v_R = 3$ ,  $v_S = 3$  (bad choices) and  $v_R = 1.2$ ,  $v_S = 0.6$  (good choice) are also shown.

**Minimizing False Acceptance for Few Scatterer Sets.** We sum pFDS over the area FS in Figure D.4 to minimize false acceptance of the sets with low scatterers (Figure D.6 top left). The low values for  $v_R$  and  $v_S$  suffer from high false acceptance (Figure D.6 top right and bottom left). A  $v_R > 2$  and  $v_S < 1.5$  value generates low false acceptance (Figure D.6 bottom right.)

**Minimizing False Rejection for FDS Sets.** To minimize the rejection of FDS sets, we sum pFDS over the area FDS in Figure D.4. Figure D.7 shows the results.

#### D.4 Experimental Results

Based on the results of Figures D.5 and D.6, we conclude that in order to minimize false acceptance of non-FDS sets  $v_S$  has to be approximately half of  $v_R$ . We performed the R–S speckle detection method with different  $v_R$  and  $v_S$  values on bovine liver B-scans. Figure D.8 shows the image divided into patches of  $100 \times 50$  pixels. The R and S values of each patch is calculated. The resultant point in the R – S plane is connected to the center of the FDS discriminant ellipse and the ratio of the length of the line segment to the radius of ellipse at the intersection of the line segment and the ellipse is shown at the center of each patch. A patch with the ratio less than 1 can be considered as a FDS patch. While the three different  $v_R$  and  $v_S$  values give similar results for the patches that are close to FDS, the pair  $v_R = 2$  and  $v_S = 1$  yields larger values for patches that are clearly not FDS (some samples marked by circle).



## D.5 Discussion and Conclusion

This work provides a complete simulation analysis for finding optimum powers to classify speckles. In ultrasound images, one patch includes a variety of backscattering effects: FDS, few scatterers and coherent scatterers. A future research direction would be to consider sets that have a mixture of samples with different  $\mu$  and  $k$  values. This is, however, challenging since the percentage of each set should be relevant to what is observed in real tissue. Therefore the sensitivity of the results to the percentages of data with specific  $\mu$  and  $k$  value should be considered. The attenuation effect is not also considered in this work, which is specifically important for patches that are elongated in the axial direction.

To achieve optimal results in the moment-based speckle classification method discussed in this work, the sample power in  $S$  has to be approximately half of the sample power in  $R$ . The values for  $v_R$  and  $v_S$  have to be selected according to specific concerns: minimizing false acceptance or false rejection or a combination of both. The three optimization criteria analyzed in this work provide a guideline for choosing appropriate values. Proper power selection can result in 50% more reliable classification.

# Bibliography

[**3DSlicer-web**] MIT AI Lab and the Surgical Planning Lab at Brigham & Women's Hospital, <<http://www.slicer.org>>.

[**Ablatx-web**] Abla-tx, Inc., <<http://www.abla-tx.com>>.

[**Abolmaesumi-2002**] Abolmaesumi P, Salcudean SE, Wen-Hong Z, Sorouspour MR, DiMaio SP, "Image Guided Control of a Robot for Medical Ultrasound," IEEE Trans. Rob. & Auto., 18(1) Feb 2002.

[**Andreff-2001**] Andreff N, Horaud R, Espiau B, "Robot Hand-Eye Calibration Using Structure from Motion," International J. of Robotics Research, 20(3), pp 228-248, 2001.

[**Artignan-2004**] Artignan X, Smitsmans MH, Lebesque JV, Jaffray DA, van Her M, Bartelink H, "Online ultrasound image guidance for radiotherapy of prostate cancer: impact of image acquisition on prostate displacement," Int J Radiat Oncol Biol Phys. 2004 Jun 1;59(2):595-601.

[**Bazan-1989**] Russo A, La Rosa C, Cajozzo M, Spallitta I, Demma I, Modica G, Bazan P, "Screening for liver metastases of colorectal carcinoma by the routine use of intraoperative echography," Minerva Chir, 17(44):1893-900, 1989.

[**Bentzen-1984**] Bentzen SM, Overgaard J, Jørgensen J, "Isotherm Mapping in hyperthermia using subtraction x-ray computed tomography," Radiotherapy and Oncology, 2:255-260, 1984.

[**Berman-1999**] Prager RW, Gee A, Berman L, "Stradx: real-time acquisition and visualization of freehand three-dimensional ultrasound," Medical Image Analysis, Volume 3, Number 2, June 1999, pp. 129-140(12).

[**Bharat-2005**] Bharat S, Techavipoo U, Kiss MZ, Liu W, Varghese T, "Monitoring stiffness changes in lesions after radiofrequency ablation at different temperatures and durations of ablation," Ultrasound Med Biol. 2005 Mar; 31(3):415-22.

**[Bilgen-1997]** Bilgen M, Insana MF, "Error Analysis in Acoustic Elastography: II. Strain Estimation and SNR Analysis," J. Acoust. Soc. of Am., 101:1147-1154, 1997.

**[Blackall-2000]** Blackall JM, Rueckert D, Maurer Jr. CR, Penney GP, Hill DLG, Hawkes DJ, "An image registration approach to automated calibration for freehand 3d ultrasound," in Proc. of Medical Image Computing and Computer-Assisted Intervention, 2000.

**[Boctor-1998]** Boctor EM, Saad A, Youssef AB, "Estimation of prostate volume by using 3D ultrasound imagery system," presented in the International Congress of Ultrasonography in collaboration with Hannover University-Germany, April 10-12th, 1998 Cairo, Egypt.

**[Boctor-2001]** Boctor EM, Saad A, Chang DJ, "PC-Based system for calibration, Reconstruction, Processing and Visualization of 3D Ultrasound Data Based on a Magnetic-Field Position and Orientation Sensing System," in ICCS, Lecture Notes in Computer Science, Springer Verlag, 2001, pp. 13-22.

**[Boctor-2003a]** Boctor EM, Fichtinger G, Taylor RH, Choti MA, "Tracked 3D ultrasound in radio-frequency liver ablation," Annual Conference of the International Society for Optical Engineering (SPIE) on Medical Imaging Ultrasonic Imaging and Signal Processing; William F. Walker, Michael F. Insana; Eds., Vol. 5035, p. 174-182, 2003.

**[Boctor-2003b]** Boctor EM, Taylor RH, Fichtinger G, Choti MA, "Robotically assisted intraoperative ultrasound with application to ablative therapy of liver cancer," Annual Conference of the International Society for Optical Engineering (SPIE) on Medical Imaging, Visualization, Image-Guided Procedures, and Display; Robert L. Galloway, Jr.; Eds. Vol. 5029, p. 281-291, 2003.

**[Boctor-2003c]** Boctor EM, Jain A, Choti M, Taylor RH, Fichtinger G, "Rapid calibration method for registration and 3D tracking of ultrasound images using spatial localizer," Proc. SPIE Vol. 5035, p. 521-532, Medical Imaging 2003.

**[Boctor-2003d]** Boctor EM, Webster RJ, Mathieu H, Okamura AM, Fichtinger G, "Virtual remote center of motion control for needle placement robots," Sixth International Conference on Medical Image Computing and Computer-Assisted Intervention, Lecture Notes in Computer Science 2878, pp 157-165, Springer Verlag, 2003.

**[Boctor-2004a]** Boctor EM, Taylor RH, Choti MA, Fichtinger G, "Robotically assisted ablative treatment Guided by freehand 3D ultrasound," Conference

of Computer Assisted Radiology and Surgery (CARS), Chicago; in proceedings, pp 503-508, Elsevier 2004.

**[Boctor-2004b]** Boctor EM, Fischer G, Choti M, Fichtinger G, Taylor R, “*Dual-Armed Robotic System for Intraoperative Ultrasound Guided Hepatic Ablative Therapy: A Prospective Study,*” IEEE 2004 International Conference on Robotics and Automation, in proceedings, pp. 377-382.

**[Boctor-2004c]** Boctor EM, Fichtinger G et al, “*Robotic 5D Ultrasound System,*” Utility patent application 10/895,397 filed 07/22/2004, original ROI was filed on 07/2003.

**[Boctor-2004d]** Boctor EM, Viswanathan A, Choti MA, Taylor RH, Fichtinger G, Hager GD, “*A Novel Closed Form Solution for Ultrasound Calibration,*” In IEEE Int Symp. On Biomedical Imaging, 2004, pp. 527-530.

**[Boctor-2004e]** Boctor EM, Fichtinger G, Yeung A, Awad M, Taylor RH, Choti MA, “*Robotic Strain Imaging for Monitoring Thermal Ablation of Liver Tumors,*” Seventh International Conference on Medical Image Computing and Computer-Assisted Intervention -- MICCAI 2004, Proceedings in Lecture Notes in Computer Science Vol. 3217, pp 81-88, Springer, 2004.

**[Boctor-2004f]** Boctor EM, Viswanathan A, Pieper S, Choti MA, Taylor RH, Kikinis R, Fichtinger G, “*CISUS: An integrated 3D ultrasound system for IGT with modular tracking interface,*” Annual Conference of the International Society for Optical Engineering (SPIE) on Medical Imaging, Volume 5367, pp. 247-256 (2004).

**[Boctor-2004g]** Boctor EM, Webster RJ, Mathieu H, Okamura AM, Fichtinger G, “*Virtual remote center of motion control for needle placement robots,*” Journal of Computer Assisted Surgery, 9(5), pp 175-183, 2004.

**[Boctor-2005a]** Boctor EM, Iordachita I, Choti MA, Hager G, Fichtinger G, “*Bootstrapped ultrasound calibration,*” Stud Health Technol Inform. 2005;119:61-6.

**[Boctor-2005b]** Boctor EM et al, “*Ultrasound Calibration and Real-time Quality Assurance Based on Closed Form Formulation,*” Utility patent application filed 04/15/2005.

**[Booth-2005]** Booth J, Zavgorodni S, “*Modelling the variation in rectal dose due to inter-fraction rectal wall deformation in external beam prostate treatments,*” Phys Med Biol. 2005 Nov 7;50(21):5055-74

- [Brewer-1978]** Brewer JW, “*Kronecker Products and Matrix Calculus in System Theory*,” IEEE Trans. Circuits and systems, 25(9) Sep.1978.
- [Burdette-1997]** Burdette EC, Holupka EJ, Kaplan IR, “*Virtual reality 3D visualization for surgical procedures*,” US Patent 6,256,529: - *Issued*: 7/3/01, *Filed*: 11/24/97.
- [Burdette-1998]** Burdette EC, Komadina B, “*Real-Time Brachytherapy Spatial Registration and Visualization System*,” US Patent 6,129,670: *Issued*: 10/10/00, *Filed*: 5/29/98.
- [Buscarini-1997]** Buscarini L, Rossi S, “*Technology for Radiofrequency Thermal Ablation of Liver Tumors*,” Semin Laparosc Surg. 1997; 4: 96-101.
- [Caratozzolo-1999]** Angelini L, Caratozzolo M, “*Intraoperative echography: the state of the art*,” Ann Ital Chir, 70(2):223-30, March-April 1999.
- [Carr-1996]** Carr J, “*Surface Reconstruction in 3D Medical Imaging*,” Ph.D. thesis, University of Canterbury, Christchurch, New Zealand, 1996.
- [Chandra-2003]** Chandra A, Dong L, Huang E, Kuban DA, O'Neill L, Rosen I, Pollack A, “*Experience of ultrasound-based daily prostate localization*,” Int J Radiat Oncol Biol Phys. 2003 Jun 1;56(2):436-47.
- [Chandrasekhar-2006]** Chandrasekhar R, Krouskop T, Ophir J, “*Elastographic image quality vs tissue motion in vivo*,” Ultrasound in Medicine and Biology, Vol. 32, No. 6, pp. 847-855, 2006.
- [Chaturvedi-1998]** Chaturvedi P, Insana MF, Hall TJ, "2-D local companding for noise reduction in strain imaging," IEEE Trans. Ultrason. Ferroelec. Freq. Control, 45:179-191, 1998.
- [Chen-1991]** Chen H, “*A screw motion approach to uniqueness analysis of head-eye geometry*,” Proc. IEEE Int. Conf. on Computer Vision and Pattern Recognition, Maui, Hawaii, USA, 145-151,(June 1991).
- [Chinzei-2000]** Chinzei K, Hata N, Jolesz A, Kikinis R, “*Surgical Assist Robot for the Active Navigation in the Intraoperative MRI: Hardware Design Issues*,” Proc. 2000 IEEE/RSJ International Conf Intelligent Robots and Systems (IROS 2000), 1: 727-32, 2000.
- [Chirikjian-2002]** Lee S, Fichtinger G, Chirikjian GS, “*Novel Algorithms for Robust Registration of Fiducials in CT and MRI*,” Journal of Medical Physics, Vol. 29, No. 8, pp. 1881-1891, 2002.

- [Choti-2000a]** Nakakura EK, Choti MA, “*Management of hepatocellular carcinoma*,” Oncology 2000;14(7):1085-98; discussion 1098-102.
- [Choti-2000b]** Choti, MA, “*Hepatic radiofrequency ablation*” The Cancer Journal 2000; 6(4): 291-2.
- [Choti-2000c]** Koniaris LG, Chan DY, Magee C, Solomon SB, Anderson JH, Smith DO, De Weese T, Kavoussi LR, Choti MA, “*Focal hepatic ablation using interstitial photon radiation energy*,” J Am Coll Surg. 2000 Aug;191(2):164-74.
- [Choti-2002a]** Choti MA, “*Surgical management of hepatocellular carcinoma: resection and ablation*,” J Vasc Interv Radiol. 2002 Sep;13(9 Suppl):S197-203.
- [Choti-2002b]** Choti MA, Bohlman ME, Solomon SB, “*Robotically Assisted Radiofrequency Ablation of Liver Cancer*,” IHPBA 2002.
- [Chou-1991]** Chou JCK, Kamel M, “*Finding the position and orientation of a sensor on a robot manipulator using quaternions*,” Int. J. Robotics Res. 10(3):240-254. 1991.
- [Chu-2005]** Chu M, Zinchenko Y, Henderson SG, Sharpe MB, “*Robust optimization for intensity modulated radiation therapy treatment planning under uncertainty*,” Phys Med Biol. 2005 Dec 7;50(23):5463-77.
- [Cinquin-1992]** Cinquin P, Troccaz T, Demongeot J, Lavallee S, Champleboux G, Brunie L, Leitner F, Sautot P, Mazier B, Perez A, Djaid M, Fortin T, Chenic M, Chapel A, “*IGOR: Image Guided Operating Robot*,” Innovation et Technol. Biol. Med., vol. 13, pp. 374–394, 1992.
- [CISST-web]** ERC-CISST LAB Johns Hopkins University, <<http://www.cisst.org/resources/software>>.
- [CMS-web]** COMPUTERIZED MEDICAL SYSTEMS (CMS), St. Louis, Missouri, <<http://www.cms-stl.com>>.
- [Cooperberg-2004a]** Cooperberg MR, Lubeck DP, Meng MV, Mehta SS, Carroll PR, “*The changing face of low-risk prostate cancer: trends in clinical presentation and primary management*,” J Clin Oncol. 2004 Jun 1;22(11):2141-9.
- [Cooperberg-2004b]** Cooperberg MR, Broering JM, Latini DM, Litwin MS, Wallace KL, Carroll PR, “*Patterns of practice in the United States: insights from*

*CaPSURE on prostate cancer management,"* Curr Urol Rep. 2004 Jun;5(3):166-72. Review.

**[Cooperberg-2004c]** Cooperberg MR, Broering JM, Litwin MS, Lubeck DP, Mehta SS, Henning JM, Carroll PR, "The contemporary management of prostate cancer in the United States: lessons from the cancer of the prostate strategic urologic research endeavor (CapSURE), a national disease registry," J Urol. 2004 Apr;171(4):1393-401. Review.

**[Corke-1996]** Hutchinson S, Hager GD, Corke P, "A Tutorial Introduction to Visual Servo Control," IEEE Transactions on Robotics and Automation. 1996; 12(5):651-670.

**[Craig-1992]** Craig JJ, "Introduction to Robotics Mechanics and Control," 3rd Edition. Addison Wesley, Reading, MA, 1992.

**[Curiel-2005]** Curiel L, Souchon R, Rouvière O et al, "Elastography for the follow-up high-intensity focused ultrasound prostate cancer treatment," Ultrasound Med Biol. 2005 Nov ;31:1461-8.

**[Daniilidis-1996]** Daniilidis K, Bayro-Corrochano E, "The dual quaternion approach to hand-eye calibration," Proc. IAPR International Conference on Pattern Recognition, pp. 318–322. 1996.

**[Davies-1991]** Davies BL, Hibberd RD, Ng WS, Timoney AG, Wickham JE, "The development of a surgeon robot for prostatectomies," Proc Inst Mech Eng. 1991;205(1):35-8.

**[De Crevoisier-2005]** De Crevoisier R, Tucker SL, Dong L, Mohan R, Cheung R, Cox JD, Kuban DA, "Increased risk of biochemical and local failure in patients with distended rectum on the planning CT for prostate cancer radiotherapy," Int J Radiat Oncol Biol Phys. 2005 Jul;62(4):965-73.

**[Deif-1986]** Deif A, "Sensitivity Analysis in Linear Systems," Berlin, Germany: Springer-Verlag, 1986.

**[DeOliviera-2005]** DeOliviera M, Boctor EM, Awad M, Taylor RH, Fichtinger G, Choti MA, "Robot-assisted 3D strain imaging for monitoring thermal ablation of liver," Annual congress of the Society of American Gastrointestinal Endoscopic Surgeons, pp 240-241, 2005.

**[Detmer-1996]** Detmer PR, Bashein G, Hodges T, Beach KW, Filer EP, Burns DH, Strandness Jr. DE, "3D Ultrasonic Image Feature Localization based on Magnetic Scanhead Tracking: In Vitro Calibration and Validation," Ultrasound in Med. Biol., 23(4):597-609, 1996.

- [Doggett-2000]** Doggett SJ, Burdette EC, “*Intraoperative Treatment Planning for Prostate Brachytherapy*,” Proceedings of the Annual Meeting of the American Brachytherapy Society, Washington, DC, May 2000.
- [Donald-1987]** Donald BR, “*A Search Algorithm for Motion Planning with Six Degrees of Freedom*,” Artificial Intelligence 1987 (31): 295-353.
- [Doyley-1999]** Doyley MM, “*An investigation into methods for improving the clinical usefulness of elasticity imaging*,” 1999. Institute of Cancer research, University of London. Thesis.
- [Dutt-1994]** Dutt V, Greanleaf J, “*Ultrasound echo envelope analysis using a homodyned k distribution signal model*,” Ultrasonic Imaging, vol. 16, pp. 265–287, 1994.
- [Dutt-1995]** Dutt V, Greanleaf J, “*Speckle analysis using signal to noise ratios based on fractional order moments*,” Ultrasonic Imaging, vol. 17, pp. 251–268, 1995.
- [Emelianov-2003]** Emelianov S, “*Elasticity Imaging*,” Short Courses for the 2003 IEEE International Ultrasonics Symposium, Hawaii, 5-8 Oct.
- [Enomoto-2001]** Izumi N, Asahina Y, Noguchi O, Uchihara M, Kanazawa N, Itakura J, Himeno Y, Miyake S, Sakai T, Enomoto N, “*Risk factors for distant recurrence of hepatocellular carcinoma in the liver after complete coagulation by microwave or radiofrequency ablation*,” Cancer. 2001 Mar 1;91(5):949-56.
- [Fenster-2001]** Fenster A, Downey DB, Cardinal NH, “*Three Dimensional Ultrasound Imaging*,” Physics in medicine and biology, vol 46, pp. 67-99, 2001.
- [Fichtinger-2002a]** Fichtinger G, Burdette EC, Tanacs A, Patriciu A, Mazilu D, Whitcomb LL, Stoianovici D, “*Robotically Assisted Prostate Brachytherapy With Transrectal Ultrasound Guidance – Preliminary Experiments*,” (International Journal of Radiation Oncology and Biology, in review).
- [Fichtinger-2002b]** Fichtinger G, Krieger A, Susil RC, Tanacs A, Whitcomb LL, Atalar E, “*Transrectal prostate biopsy inside closed MRI scanner with remote actuation, under real-time image guidance*,” Proceedings to Medical Image Computing and Computer-Assisted Interventions 2002, Lecture Notes in Computer Science, Vol. 2488, Part 1, pp. 91-98, Springer, 2002.

- [Fichtinger-2002c]** Fichtinger G, DeWeese TL, Patriciu A, Tanacs A, Mazilu D, Anderson JH, Masamune K, Taylor RH, Stoianovici D, “*System for robotically assisted prostate biopsy and therapy with intraoperative CT guidance*,” Acad Radiol. 2002 Jan; 9(1):60-74.
- [Fishman-2000]** Kuszyk BS, Boitnott JK, Choti MA, Bluemke DA, Sheth S, Magee CA, Horton KM, Eng J, Fishman EK, “*Local tumor recurrence following hepatic cryoablation: radiologic-histopathologic correlation in a rabbit model*,” Radiology. 2000 Nov;217(2):477-86.
- [Gee-2005]** Gee AH, Houghton NE, Treece GM, Prager RW, “*A mechanical instrument for 3D ultrasound probe calibration*,” Ultrasound Med Biol. 2005 Apr;31(4):505-18.
- [Gering-1999]** Gering D, Nabavi A, Kikinis R, Grimson EL, Hata N, Everett P, Jolesz F, Wells III W, “*An Integrated Visualization System for Surgical Planning and Guidance using Image Fusion and Interventional Imaging*,” Medical Image Computing and Computer-Assisted Intervention (MICCAI), pp. 809-819, 1999.
- [Gering-2001]** Gering DT et al, “*An integrated visualization system for surgical planning and guidance using image fusion and an open MR*,” J Magn Reson Imaging. 2001 Jun;13(6):967-75.
- [Gobbi-2002]** Gobbi DG, Peters TM, “*Interactive intraoperative 3D ultrasound reconstruction and visualization*,” Proceedings to Medical Image Computing and Computer-Assisted Interventions 2002, Lecture Notes in Computer Science, Vol. 2488, Part 2, pp. 156-163, Springer, 2002.
- [Goldberg-2001]** Goldberg RP, Mazilu D, Taylor RH, Stoianovici D, “*A modular robotic system for ultrasound image acquisition*,” Lecture Notes in Computer Science, Volume 2208, pp. 1430-1433, Springer, 2001.
- [Graham-1999]** Graham SJ, Stanisz GJ, Kecojevic A, Bronskill MJ, Henkelman RM, “*Analysis of changes in MRI properties of tissues after heat treatment*,” Magn Reson Med 1999;42(6):1061-71.
- [Hager-1998]** Hager G, Belhumeur P, “*Efficient region tracking with parametric models of geometry and illumination*,” IEEE Transactions of Pattern Analysis and Machine Intelligence, 20(10):1125–1139, 1998.
- [Harms-1993]** Vanderpool HE, Friis EA, Smith BS, Harms KL, “*Prevalence of carpal tunnel syndrome and other work-related musculoskeletal problems in cardiac sonographers*,” Journal of Occupational Medicine, vol. 35, pp. 604-610, June 1993.

- [Harris-1997]** Harris SJ, Arambula-Cosio F, Mei Q, Hibberd RD, Davies BL, Wickham JE, Nathan MS, Kundu B, “*The Probot--an active robot for prostate resection,*” Proc Inst Mech Eng. 1997;211(4):317-25.
- [Hassenpflug-2005]** Hassenpflug P, Prager RW, Treece GM, Gee AH, “*Speckle classification for sensorless freehand 3D ultrasound. Speckle classification for sensorless freehand 3D ultrasound,*” Technical report CUED/F-INFENG/TR 513, Cambridge University Department of Engineering, March 2005.
- [Horaud-1995]** Horaud R, Dornaika F, “*Hand-eye calibration,*” Int. J. Robotics Res. 14(3):195–210. 1995.
- [Horn-1987]** Horn BKP, “*Closed-form solution of absolute orientation using unit quaternions,*” J Opt Soc Am A 1987;4:629–642.
- [Hsu-2006]** Hsu P, Prager RW, Gee AH, Treece GM, “*Rapid, Easy and Reliable Calibration for Freehand 3D Ultrasound,*” Ultrasound in Med. & Biol., Vol. 32, No. 6, pp. 823–835, 2006.
- [ISIS-web]** Imaging Science and Information System, Medical Center, Washington DC, <<http://www.imac.georgetown.edu>>.
- [Jaffray-2002]** Jaffray DA, Siewerdsen JH, Wong JW, Martinez AA, “*Flat-panel cone-beam computed tomography for image-guided radiation therapy,*” Int J Radiat Oncol Biol Phys. 2002 Aug 1;53(5):1337-49.
- [Jani-2005]** Jani AB, Gratzle J, Muresan E, Farrey K, Martel MK, “*Analysis of acute toxicity with use of transabdominal ultrasonography for prostate positioning during intensity-modulated radiotherapy,*” Urology. 2005 Mar;65(3):504-8.
- [Kallel-1997]** Kallel F, Ophir J, “*A least-squares estimator for elastography,*” Ultrasonic Imag., 19:195–208, 1997.
- [Kallel-1999]** Kallel F, Stafford RJ, Price RE, Righetti R, Ophir J, Hazle JD, “*The Feasibility of Elastographic Visualization of HIFU-Induced Thermal Lesions in Soft-Tissue,*” Ultras. Med. and Biol., Vol 25(4), pp.641-647, 1999.
- [Khatib-1987]** Khatib O, “*A Unified Approach for Motion and Force Control of Robot Manipulators: The Operational Space Formulation,*” IEEE Journal of Robotics and Automation, 1987 Feb; RA-3(1):43-53.
- [Kikinis-2003]** Kikinis R et al, “*3D Slicer: Medical Visualization and Processing Environment for Research,*” MIT Artificial Intelligence Lab and the Surgical

Planning Lab at Brigham & Women's Hospital, Accessed 16 January 2003,  
<<http://www.slicer.org>>.

[Kitamura-2002] Kitamura K, Shirato H, Seppenwoolde Y, Onimaru R, Oda M, Fujita K, Shimizu S, Shinohara N, Harabayashi T, Miyasaka K, "Three-dimensional intrafractional movement of prostate measured during real-time tumor-tracking radiotherapy in supine and prone treatment positions," Int J Radiat Oncol Biol Phys. 2002 Aug 1;53(5):1117-23.

[Kolen-2003] Kolen A, "Elasticity imaging for monitoring thermal ablation in liver," 2003, Institute of Cancer research, University of London.Thesis.

[Kon-2005] Kon R, Leven J, Kothapalli K, Boctor EM, Fichtinger G, Hager GD, Taylor RH, "CIS-UltraCal: An Open-Source Ultrasound Calibration Toolkit," SPIE Medical Imaging 2005: Ultrasonic Imaging and Signal Processing, Volume 5750 -- William F. Walker, Stanislav Y. Emelianov, Editors, pp. 516-523, 2005.

[Kumar-2003] Taylor RH, Kumar R et al, "Library of Modular Robots Control," Engineering Research Center Computer Integrated Surgical Systems and Technology (ERC-CISST), <<http://www.cisst.org/resources/software/mrc/>>, Accessed 16 January 2003.

[Kwoh-1988] Kwoh YS, Hou J, Jonckheere EA, Hayati S, "A robot with improved absolute positioning accuracy for CT guided stereotactic brain surgery," IEEE Trans Biomed Eng. 1988 Feb;35(2):153-60.

[Langen-2003] Langen KM, Pouliot J, Anezinos C, et al, "Evaluation of ultrasound-based prostate localization for image-guided radiotherapy," Int J Radiat Oncol Biol Phys. 57(3):635-44, 2003.

[Lattanzi-2000] Lattanzi J, McNeeley S, Donnelly S, Palacio E, Hanlon A, Schultheiss TE, Hanks GE, "Ultrasound-based stereotactic guidance in prostate cancer--quantification of organ motion and set-up errors in external beam radiation therapy," Comput Aided Surg. 2000;5(4):289-95.

[Lavallée-1998] Chassat F, Lavallée S, "Experimental Protocol of Accuracy Evaluation of 6-D Localizers for Computer-Integrated Surgery: Application to Four Optical Localizers," MICCAI1998, Springer-Verlag, Berlin, Heidelberg, 1496:277-284.

[Letourneau-2005] Letourneau D, Wong JW, Oldham M, Gulam M, Watt L, Jaffray DA, Siewerdsen JH, Martinez AA, "Cone-beam-CT guided radiation therapy: technical implementation," Radiother Oncol. 2005 Jun;75(3):279-86.

- [Leven-2005]** Leven J, Burschka D, Kumar R, Zhang G, Blumenkranz S, Dai X, Awad M, Hager GD, Marohn M, Choti M, Hasser C, Taylor RH, “*DaVinci Canvas: A Telerobotic Surgical System with Integrated, Robot-Assisted Laparoscopic Ultrasound Capability*,” MICCAI 2005: 811-818.
- [Li-2002]** Li QH, Zamorano L, Pandya A, Perez R, Gong J, Diaz F, “*The application accuracy of the NeuroMate robot-A quantitative comparison with frameless and frame-based surgical localization systems*,” Comput Aided Surg. 2002;7(2):90-8.
- [Lindop-2004]** Lindop J, Treece GM, Gee AH, Prager RW, “*3D Elastography Using Freehand Ultrasound*,” MICCAI (2) 2004: 1103-1104.
- [Little-2003]** Little DJ, Dong L, Levy LB, Chandra A, Kuban DA, “*Use of portal images and BAT ultrasonography to measure setup error and organ motion for prostate IMRT: implications for treatment margins*. Int J Radiat Oncol Biol Phys,” 2003 Aug 1;56(5):1218-24.
- [Loser-2000]** Loser M, Navab A, “*A new robotic system for visually controlled percutaneous interventions under CT*,” Proceedings to Medical Image Computing and Computer-Assisted Intervention 2000. Lecture Notes in Computer Science, Volume 1935, pp. 887-897, Springer Verlag, 2000.
- [Martin-Fernandez-2005]** Martin-Fernandez M, Alberola-Lopez C, “*On low order moments of the homodyned-k distribution*,” Ultrasonics, vol. 43, pp. 283–290, 2005.
- [Masamune-1995]** Masamune K, Kobayashi E, Masutani Y, Suzuki M, Dohi T, Iseki H, Takakura K, “*Development of an MRI-compatible needle insertion manipulator for stereotactic neurosurgery*,” J Image Guided Surgery, 1995; 1(4):242-8.
- [Masamune-2001]** Masamune K, Fichtinger G, Patriciu A, Susil RC, Taylor RH, Kavoussi LR, Anderson JH, Sakuma I, Dohi T, Stoianovici D, “*System for robotically assisted percutaneous procedures with computed tomography guidance*,” Comput Aided Surg. 2001,6(6):370-383.
- [McGahan-2004]** McGahan JP, Ryu J, Fogata M, “*Ultrasound probe pressure as a source of error in prostate localization for external beam radiotherapy*,” Int. J Radiat Oncol Biol Phys. 2004 Nov 1;60(3):788-93.
- [McNair-2004]** McNair HA, Parker C, Hansen VN, Askew L, Mukherjee R, Nutting C, Norman AR, Dearnaley DP, “*An evaluation of Beam cath in the verification process for prostate cancer radiotherapy*,” Clin Oncol (R Coll Radiol). 2004 Apr;16(2):138-47.

- [Mercier-2005]** Mercier L, Langi T, Lindsesth F, Collins DL, “*A review of calibration techniques for freehand 3-D ultrasound systems*,” Ultrasound in Medicine & Biology, 31(4):449{471, 2005.
- [MISON-web]** MISON (Centre for Medicine and Technology), NORWAY, <<http://www.mison.no>>.
- [Morr-2002]** Morr J, DiPetrillo T, Tsai JS, Engler M, Wazer DE, “*Implementation and utility of a daily ultrasound-based localization system with intensity-modulated radiotherapy for prostate cancer*,” Int J Radiat Oncol Biol Phys. 2002 Aug 1;53(5):1124-9.
- [Muratore-2001]** Muratore DM, Galloway RL, “*Beam Calibration without a Phantom for Creating a 3D Free-hand Ultrasound System*,” Ultrasound in Med. & Biol., Volume 27, No. 11, pp1557-1566, 2001.
- [Nakakura-2000]** Nakakura EK, Choti MA, “*Management of hepatocellular carcinoma*,” Oncology (Huntingt). 2000 Jul;14(7):1085-98; discussion 1098-102. Review.
- [Nederveen-2001]** Nederveen AJ, Lagendijk JJ, Hofman P, “*Feasibility of automatic marker detection with an a-Si flat-panel imager*,” Phys Med Biol. 2001 Apr;46 (4):1219-30.
- [Nederveen-2002]** Nederveen AJ, van der Heide UA, Dehnad H, van Moorselaar RJ, Hofman P, Lagendijk JJ, “*Measurements and clinical consequences of prostate motion during a radiotherapy fraction*,” Int J Radiat Oncol Biol Phys. 2002 May 1;53(1):206-14.
- [Neuromate-web]** Integrated Surgical Systems, Davis, CA, <[www.robodoc.com](http://www.robodoc.com)>.
- [Nikolaou-2005]** Nikolaou K, Flohr T, Stierstorfer K, Becker CR, Reiser MF, “*Flat panel computed tomography of human ex vivo heart and bone specimens: initial experience*,” Eur Radiol. 2005 Feb;15(2):329-33.
- [O'Donnell-1994]** O'Donnell M, Skovoroda AR, Shapo BM, Emelianov SY, “*Internal displacement and strain imaging using ultrasonic speckle tracking*,” IEEE Transactions on Ultrasonics, Ferroelectrics, and Frequency Control, 41:314-325, 1994.
- [Ophir-1991]** Ophir J, Céspedes I, Ponnekanti H, Yazdi Y, Li X, “*Elastography: a method for imaging the elasticity of biological tissues*,” Ultrasonic Imaging, Vol 13 (2), pp. 111-134, 1991.

- [Ophir-2002]** Ophir J, Alam SK, Garra BS, Kallel F, Konofagou EE, Krouskop T, Merritt CRB, Righetti R, Souchon R, Srinivasan S, Varghese T, “*Elastography: Imaging the Elastic Properties of Soft Tissues with Ultrasound*,” Journal of Med Ultrasound, Vol. 29, Winter, pp. 155-171, 2002.
- [Pagoulatos-2001]** Pagoulatos N, Haynor DR, Kim Y, “*A Fast Calibration Method for 3-D Tracking of Ultrasound Images Using a Spatial Localizer*,” *US in Med. Biol.*, 27(9):1219-1229, 2001.
- [Patel-2003]** Patel RR, Orton N, Tome WA, Chappell R, Ritter MA, “*Rectal dose sparing with a balloon catheter and ultrasound localization in conformal radiation therapy for prostate cancer*,” *Radiother Oncol.* 2003 Jun;67(3):285-94.
- [Patriciu-2001]** Patriciu A, Solomon S, Kavoussi LR, Stoianovici D, “*Robotic Kidney and Spine Percutaneous Procedures Using a New Laser-Based CT Registration Method*,” Proceedings to Medical Image Computing and Computer-Assisted Intervention 2001, Lecture Notes in Computer Science Volume 2208, 249-257, Springer Verlag, 2001.
- [Peeters-2005]** Peeters ST, Hoogeman MS, Heemsbergen WD, Slot A, Tabak H, Koper PC, Lebesque JV, “Volume and hormonal effects for acute side effects of rectum and bladder during conformal radiotherapy for prostate cancer,” *Int J Radiat Oncol Biol Phys.* 2005 Nov 15;63(4):1142-52.
- [Pennec-1995]** Pennec X, Thirion JP, “*A Framework for Uncertainty and Validation of 3-D Registration Methods based on Points and Frames*,” *International Journal of Computer Vision* 25(3), 203-229, 1997.
- [Pierrot-1999]** Pierrot F, Dombre E, Degoulange E, Urbain L, Caron P, Boudet S, Gariepy J, Megnien JL, “*Hippocrate: a safe robot arm for medical applications with force feedback*,” *Med Image Anal.* 1999 Sep;3(3):285-300.
- [Prager-1998a]** Prager RW, Gee AH, Berman L, “*Stradx: real-time acquisition and visualization of freehand 3DUS*,” *Medical Imaging Analysis* 3(2), pp129-140, 1998.
- [Prager-1998b]** Prager RW, Rohling R, Gee A, Berman L, “*Rapid calibration for 3D freehand ultrasound*,” *Ultrasound in Medicine and Biology*, vol. 24, no. 6, pp. 855-869, 1998.
- [Prager-2002a]** Prager RW, Gee A, Treece G, Berman L, “*Analysis of speckle in ultrasound images using fractional order statistics and the homodyned k-distribution*,” *Ultrasonics*, vol. 40, pp. 133–137, 2002.

**[Prager-2002b]** Prager RW, Gee AH, Treece GM, Cash CJC, Berman LH, “*Using Image-based Regression to Acquire Freehand 3D Ultrasound*,” CUED/F-INFENG/TR 436, June 2002.

**[Prager-2003]** Peter Hassenpflug, Richard Prager, Graham Treece and Andrew Gee, “*Distance Measurement for Sensorless 3D US*,” Department of Engineering, University of Cambridge, Trumpington Street, Cambridge, UK, CB2 1PZ

**[Ramamurthy-1991]** Ramamurthy BS, Trahey GE, “*Potential and limitations of angle-independent flow detection algorithms using radiofrequency and detected echo signals*,” Ultrasonic Imaging, 13:252-268 1991.

**[Rickey-1995]** Rickey DW, Picot PA, Christopher DC, Fenster A, “*A Wall-less Vessel Phantom for Doppler Ultrasound Studies*,” US in Med. Biol., 21, 1163-1175, 1995.

**[Righetti-1999]** Righetti R, Kallel F, Stafford RJ, Price RE, Krouskop TA, Hazle JD, Ophir J, “*Elastographic Characterization of HIFU-induced lesions in canine livers*,” Ultras. Med & Biol., Vol. 25 (7), pp. 1099-1113, 1999.

**[Rivest-1995]** Betke M, supervised by Rivest R, “*Learning and Vision Algorithms for Robot Navigation*,” Ph.D. dissertation in EECS dept. at the MIT June 1995.

**[Roach-2004]** Roach M, Winter K, Michalski JM, Cox JD, Purdy JA, Bosch W, Lin X, Shipley WS, “*Penile bulb dose and impotence after three-dimension conformal radiotherapy for prostate cancer on RTOG 9406: findings from a prospective, multi-institutional, phase I/II dose escalation study*,” Int J Radiat Oncol Biol Phys. 2004 Dec;60(5):1351-6.

**[Rohling-1997]** Rohling R, Gee A, Berman L, “Three-dimensional spatial compounding of ultrasound images,” Med Image Anal. 1997 Apr;1(3):177-93.

**[Rohling-1998]** Rohling RN, Gee AH, Berman LH, “*Radial Basis Function Interpolation For 3D Ultrasound*,” CUED/F-INFENG/TR 327, July 1998.

**[Rousseau-2002]** Rousseau F, Hellier P, Barillot C, “*A fully automatic calibration procedure for freehand 3D ultrasound*,” In IEEE Int. Symp. on Biomedical Imaging, Washington D.C, Juillet 2002. pp. 985-988.

**[Rovetta-1999]** Rovetta A, “*Tests on reliability of a prostate biopsy telerobotic system*,” Stud Health Technol Inform. 1999;62:302-7.

**[Sakas-1992]** Sakas G, “*InViVo Interactive Visualizer of Large Scalar Voxel Fields*,” Computer Graphic topics, 4(2), pp. 12-13, 1992.

- [Salas-2004]** Salas N, Manns F, Milne PJ, Denham DB, Minhaj AM, Parel J-M, Robinson DS, “*Thermal Analysis of Laser Interstitial Thermography in ex-vivo Fibro-Fatty Tissue using Exponential Functions*,” Phys Med Biol 49(9):1609-1624, 2004.
- [Salcudean-1999]** Salcudean SE et al, “*Robot Assisted Diagnostic Ultrasound – Design and Feasibility Experiments*,” in MICCAI, Lecture Notes in Computer Science, pp-1062-1071, Springer, 1999.
- [Serago-2002]** Serago CF, Chungbin SJ, Buskirk SJ, Ezzell GA, Collie AC, Vora SA, “*Initial experience with ultrasound localization for positioning prostate cancer patients for external beam radiotherapy*,” Int J Radiat Oncol Biol Phys. 2002 Aug 1;53(5):1130-8.
- [Shi-2005]** Shi FH, Wang JH, Liu YC, “*An Approach to Improve Online Hand-Eye Calibration*,” In Proc. of IbPRIA 2005, LNCS 3522, 647-655, (2005).
- [Shiu-1989]** Shiu YC, Ahmad S, “*Calibration of wrist-mounted robotic sensors by solving homogeneous transform equations of the form AX = XB*,” IEEE Trans. Robot. Automat., vol. 5, 16-29, (1989).
- [Siegel-2001]** Siegel T, Moul JW, Spevak M, Alvord WG, Costabile RA, “*The development of erectile dysfunction in men treated for prostate cancer*,” J Urol. 2001 Feb;165(2):430-5.
- [Smith-2003]** Smith WL, Fenster A, “*Analysis of an image-based transducer tracking system for 3D ultrasound*,” Medical Imaging SPIE 2003, Proc. SPIE Vol. 5035, pp. 154-165.
- [Smitsmans-2005]** Smitsmans MH, de Bois J, Sonke JJ, Betgen A, Zijp LJ, Jaffray DA, Lebesque JV, van Herk M, “*Automatic prostate localization on cone-beam CT scans for high precision image-guided radiotherapy*,”
- [Sohn-2005]** Sohn M, Birkner M, Yan D, Alber M, “*Modelling individual geometric variation based on dominant eigenmodes of organ deformation: implementation and evaluation*,”
- [Solomon-2002]** Solomon SB, Patriciu A, Bohlman ME, Kavoussi LR, Stoianovici D, “*Robotically driven interventions: a method of using CT fluoroscopy without radiation exposure to the physician*” Rad. 2002 Oct;225(1):277-82.
- [Souchon-2003a]** Souchon R, Rouviere O, Gelet A, et al, “*Visualization of HIFU lesions using elastography of the human prostate in vivo: Preliminary results*,” Ultrasound Med Biol 2003a;29:1007–1015.

- [Souchon-2003b]** Souchon R, Detti V, Gelet A, Ophir J, Chapelon JY, “*Visualization of high intensity focused ultrasound (HIFU)-induced lesions in the human prostate in vivo using elastography*,” In: Chapelon JY, Lafon C, eds. Third International Symposium on Therapeutic Ultrasound Proceedings 2003b, Lyon, France: INSERM, 2003a:211–216.
- [Stoianovici-1997]** Stoianovici D, Cadeddu JA, Demaree RD, Basile HA, Taylor RH, Whitcomb LL, Sharpe WN, Kavoussi LR, “*An Efficient Needle Injection Technique and Radiological Guidance Method for Percutaneous Procedures*,” Lecture Notes in Computer Science, Volume 1205, pp. 295-298, Springer, 1997.
- [Stoianovici-1998]** Stoianovici D, Whitcomb LL, Anderson JH, Taylor RH, Kavoussi LR, “*A Modular Surgical Robotic System for Image-Guided Percutaneous Procedures, Proceedings to International Conference on Medical Image Computing and Computer-Assisted Intervention*,” Lecture notes in computer science, Volume 1496, pp. 404-410, Springer, 1998.
- [Stoianovici-2001]** Stoianovici D, “*URobotics - Urology Robotics at Johns Hopkins*,” Comp Aid Surg, 2001, (6):360-369.
- [Su-2002]** Su LM, Stoianovici D, Jarrett TW, Patriciu A, Roberts WW, Cadeddu JA, Ramakumar S, Solomon SB, Kavoussi LR, “*Robotic percutaneous access to the kidney: comparison with standard manual access*,” J Endourol. 2002 Sep;16(7):471-5.
- [Susil-2002]** Susil RC, Krieger A, Derbyshire JA, Tanacs A, Whitcomb LL, McVeigh ER, Fichtinger G, Atalar E, “*A System for MRI Guided Diagnostic and Therapeutic Prostate Interventions*,” (accepted by Radiology).
- [Taylor-1994]** Taylor RH, Mittelstadt BD, Paul HA, Hanson W, Kazanzides P, Zuhars JF, Williamson B, Musits BL, Glassman E, Bargar WI, “*An Image-directed Robotic System for Precise Orthopaedic Surgery*,” IEEE Transactions on Robotics and Automation, Vol. 10, Number 3, June 1994, pp 261-275.
- [Taylor-1995]** Taylor RH, Funda J, Eldridge B, Gruben K, LaRose D, Gomory S, Talamini M, Kavoussi LA, Anderson JH, “*A Telerobotic Assistant for Laparoscopic Surgery*,” IEEE EMBS Magazine Special Issue on Robotics in Surgery. 1995. pp. 279-291.
- [Taylor-1996]** Taylor RH, Lavallee S, Burdea GC, Mosges R, “*Computer-Integrated Surgery Technology and Clinical Applications*,” MIT Press, 1996.

- [Taylor-1999]** Taylor RH, Jensen P, Whitcomb LL, Barnes A, Kumar R, Stoianovici D, Gupta P, Wang Z, deJuan E, Kavoussi L, “*A Steady-Hand Robotic System for Microsurgical Augmentation,*” International Journal of Robotics Research, 18(12):1201-1210 December 1999.
- [Taylor-2002]** Taylor RH, Joskowicz L, “*Computer-integrated surgery and medical robotics,*” Standard Handbook of Biomedical Engineering & Design, pp. 29.3-29.45, 2002.
- [Teh-2002]** Teh BS, McGary JE, Dong L, Mai WY, Carpenter LS, Lu HH, Chiu JK, Woo SY, Grant WH, Butler EB, “*The use of rectal balloon during the delivery of intensity modulated radiotherapy (IMRT) for prostate cancer: more than just a prostate gland immobilization device?*” Cancer J, 2002 Nov-Dec;8(6):476-83.
- [Thomas-1998]** Thomas N, Dolores HP, “*Three-Dimensional Ultrasound Imaging,*” Ultrasound in Med. & Biol. Vol. 24, No. 9, pp. 1243-1270, 1998.
- [Trichter-2003]** Trichter F, Ennis RD, “*Prostate localization using transabdominal ultrasound imaging,*” Int J Radiat Oncol Biol Phys. 2003 Aug 1;56(5):1225-33.
- [Tsai-1989]** Tsai RY, Lenz RK, “*A new technique for fully autonomous and efficient 3d robotics hand/eye calibration,*” IEEE Trans. Robot. Automat., vol. 5, 345-358, (1989).
- [Vaezy-2001]** Vaezy S, Shi X, Martin RW, Chi E, Nelson PI, Bailey MR, Crum LA, “*Real-time visualization of high-intensity focused ultrasound treatment using ultrasound imaging,*” Ultrasound Med Biol. 2001 Jan;27(1):33-42.
- [Varghese-1997]** Varghese T, Ophir J, “*A theoretical framework for performance characterization of elastography: The Strain Filter,*” IEEE Trans. Ultrason. Ferroel. Freq. Cont., pp.164-172, 1997.
- [Varghese-2002]** Varghese T, Zagzebski JA, Lee FT, “*Elastographic Imaging of thermal lesions in the liver in-vivo following radiofrequency ablation: Preliminary Results,*” Ultrasound in Medicine and Biology, Vol. 28, No. 11/12, pp. 1467-1473, 2002.
- [Varghese-2003]** Varghese T, Techavipoo U, Liu W, Zagzebski JA, Chen Q, Frank G, Lee FT, “*Elastographic Measurement of the Area and Volume of Thermal Lesions Resulting from Radiofrequency Ablation: Pathologic Correlation,*” AJR Am J Roentgenol. 2003 Sep;181(3):701-7.

**[Varghese-2004]** Varghese T, Techavipoo U, Zagzebski JA, Lee FT Jr, “*Impact of gas bubbles generated during interstitial ablation on elastographic depiction of in vitro thermal lesions,*” J Ultrasound Med. 2004 Apr;23(4):535-44; quiz 545-6.

**[Varian-web]** Varian Medical Systems, Palo Alto, CA, <<http://www.varian.com>>.

**[Varma-2003]** Varma TR, Eldridge PR, Forster A, Fox S, Fletcher N, Steiger M, Littlechild P, Byrne P, Sinnott A, Tyler K, Flintham S, “*Use of the NeuroMate stereotactic robot in a frameless mode for movement disorder surgery,*” Stereotact Funct Neurosurg. 2003;80(1-4):132-5.

**[Vences-2005]** Vences L, Wulf J, Vordermark D, Sauer O, Berlinger K, Roth M, “*Target motion measurement without implanted markers and its validation by comparison with manually obtained data. Med Phys,*” 2005 Nov;32(11):3431-9.

**[Viswanathan-2004]** Viswanathan A, Boctor EM, Taylor RH, Hager GD, Fichtinger G, “*Immediate Ultrasound Calibration from Two Poses and Minimal Image Processing,*” MICCAI 2004, pp 446-454.

**[Wang-1992]** Wang CC, “*Extrinsic calibration of a robot sensor mounted on a robot,*” IEEE Trans. on Robotics and Automation 8(2):161–175. 1992.

**[Wang-2004]** Wang L, Jacob R, Chen L, Ma C, Movsas B, Feigenberg S, Konski A, “*Stereotactic IMRT for prostate cancer: setup accuracy of a new stereotactic body localization system,*” J Appl Clin Med Phys. 2004 Spring;5(2):18-28.

**[Wei-2004]** Wei Z, Wan G, Gardi L, Mills GR, Downey DB, Fenster A, “*Robot-assisted 3D-TRUS guided prostate brachytherapy: system integration and validation,*” Med. Phys. 31(3): 539-548, March 2004.

**[Yang-2005]** Yang J, Mageras GS, Spirou SV, Jackson A, Yorke E, Ling CC, Chui CS, “*A new method of incorporating systematic uncertainties in intensity-modulated radiotherapy optimization. Med Phys,*” 2005 Aug;32(8):2567-79.

**[Yanof-2001]** Yanof J, Haaga J, Klahr P, Bauer C, Nakamoto D, Chaturvedi A, Bruce R, “*CT-integrated robot for interventional procedures: preliminary experiment and computer-human interfaces,*” Comput Aided Surg. 2001;6(6):352-9.

**[Yeh-2002]** Yeh WC, Li PC, Jeng YM, Hsu HC, Kuo PL, Li ML, Yang PM, Lee PH “*Elastic modulus measurements of human liver and correlation with pathology,*” US in Med. Biol. 28(4), 467-474, 2002.

## Emad M. Boctor Mikhail

### Home Address

6232 Green Meadow pkwy, Apt. 'A'  
Baltimore, MD 21209  
Tel (H): (410) 358-4935  
(Cell): (443) 845-6592  
E-mail: [eboctor@ieee.org](mailto:eboctor@ieee.org)

### Office Address

Johns Hopkins University  
3400 N. Charles St.  
New Eng. Build. (B26),  
Baltimore, MD 21218  
Tel : (410) 516-3417

### Education

Ph.D.	<b>Computer Science,</b> Johns Hopkins University, Baltimore MD, USA, 2006
M.Sc.	<b>Computer Science,</b> Johns Hopkins University, Baltimore MD, USA, 2003
MSCS	<b>Engineering Mathematics and Computer Science,</b> University of Louisville, Louisville KY, USA, 1999
M.Eng.	<b>Biomedical Engineering,</b> Cairo University, Giza, Egypt, 1998 Distinction, Valedictorian, highest honors award
B.Sc.	<b>Biomedical Engineering and Systems,</b> Cairo University, Giza, Egypt, 1995 Distinction, Valedictorian, highest honors award

### Professional Summary

- Extensive experience in medical imaging, Instrumentation and robotics research with emphasis on diagnostic ultrasound (US) instrumentation, and US guided interventions.
- Specific expertise in the following areas: computer graphics, signal processing, embedded microprocessor/microcontroller systems, artificial intelligence, real-time programming, parallel computation, finite/boundary element computation methods, elasticity imaging, virtual reality, programmable logic controllers, robotics, and medical imaging.
- Demonstrated ability to initiate and carry out independent and innovative scientific research.
- Participated actively and co-authored three awarded grants and four submitted proposals (in-review.)
- Ability to function effectively as a mentor, team-leader, and a member of fast-paced, multi-disciplinary and culturally-diverse teams.
- Excellent experimental and analytical skills.
- Excellent verbal and written interpersonal communication skills and prolific scientific publisher.

### Languages

English	: Reading, Writing, Listening and Speaking (fluent)
Arabic	: Reading, Writing, Listening and Speaking (native)
Coptic	: Reading and Speaking (basic)

## Publications and Workshops

### **Full papers and peer-reviewed articles:**

- Boctor E.M., DeOliviera M., Ghanem R., Taylor R.H., Choti M., Hager G., Fichtinger G. "Ultrasound Monitoring of Tissue Ablation via Deformation Model and Shape Priors", Ninth International Conference on Medical Image Computing and Computer-Assisted Intervention -- MICCAI 2006 (Accepted)
- Boctor E.M., Iordachita I., Fichtinger G. and Hager G.D. "*Ultrasound Self-Calibration*", Visualization, Image-Guided Procedures, and Display conference in SPIE 2006 -- Honorably mentioned Best Poster Award
- Boctor E.M., Iordachita I., Choti M., Hager G.D., and Fichtinger G. "*Bootstrapped Ultrasound Calibration*", Stud Health Technol Inform. 2005;119:61–6.
- Boctor E.M., Iordachita I., Fichtinger G., and Hager G.D. "*Real-time Quality Control of Tracked Ultrasound*", Eighth International Conference on Medical Image Computing and Computer-Assisted Intervention -- MICCAI 2005, Proceedings in Lecture Notes in Computer Science Vol. 3749, pp 621–627, Springer, 2005.
- Kon R., Leven J., Kothapalli K., Boctor E.M., Fichtinger G., Hager G.D., and Taylor R.H. "*CIS-UltraCal: An Open-Source Ultrasound Calibration Toolkit*", SPIE Medical Imaging 2005: Ultrasonic Imaging and Signal Processing, Volume 5750 -- William F. Walker, Stanislav Y. Emelianov, Editors, pp. 516–523, 2005.
- Viswanathan A., Boctor E.M., Taylor R.H., Hager G.D., and Fichtinger G. "*Immediate Ultrasound Calibration from Two Poses and Minimal Image Processing*", Seventh International Conference on Medical Image Computing and Computer-Assisted Intervention -- MICCAI 2004, Proceedings in Lecture Notes in Computer Science Vol. 3217, pp 446–454, Springer, 2004.
- Boctor E.M., Fichtinger G., Yeung A., Awad M., Taylor R.H., and Choti M.A. "*Robotic Strain Imaging for Monitoring Thermal Ablation of Liver Tumors*", Seventh International Conference on Medical Image Computing and Computer-Assisted Intervention -- MICCAI 2004, Proceedings in Lecture Notes in Computer Science Vol. 3217, pp 81–88, Springer, 2004.
- Boctor E.M., Taylor R.H., Choti M.A., and Fichtinger G. "*Robotically assisted ablative treatment Guided by freehand 3D ultrasound*", Conference of Computer Assisted Radiology and Surgery (CARS), Chicago; in proceedings, pp 503–508, Elsevier 2004.
- Boctor E.M., Fischer G., Choti M.A., Fichtinger G., and Taylor R.H. "*Dual-Armed Robotic System for Intraoperative Ultrasound Guided Hepatic Ablative Therapy: A Prospective Study*", IEEE 2004 International Conference on Robotics and Automation, in proceedings, pp. 377–382.
- Boctor E.M., Viswanathan A., Choti M.A., Taylor R.H., Fichtinger G., and Hager G.D. "*A Novel Closed Form Solution For Ultrasound Calibration*", ISBI 2004, in proceedings, pp 527–530.
- Boctor E.M., Viswanathan A., Pieper S., Choti M.A., Taylor R.H., Kikinis R., and Fichtinger G. "*CISUS: An integrated 3D ultrasound system for IGT with modular tracking interface*", Annual Conference of the International Society for Optical Engineering (SPIE) on Medical Imaging, Volume 5367, pp. 247–256 (2004).
- Boctor E.M., Webster R.J., Mathieu H., Okamura A.M., and Fichtinger G. "*Virtual remote center of motion control for needle placement robots*". Journal of Computer Assisted Surgery, 9(5), pp 175–183, 2004. (Invited paper)
- Boctor E.M., Webster R.J., Mathieu H., Okamura A.M., and Fichtinger G. "*Virtual remote center of motion control for needle placement robots*", Sixth International

- Conference on Medical Image Computing and Computer-Assisted Intervention, Lecture Notes in Computer Science 2878, pp 157–165, Springer Verlag, 2003.
- Boctor E.M., Taylor R.H., Fichtinger G., and Choti M.A. "Robotically assisted intraoperative ultrasound with application to ablative therapy of liver cancer", Annual Conference of the International Society for Optical Engineering (SPIE) on Medical Imaging, Visualization, Image-Guided Procedures, and Display; Robert L. Galloway, Jr.; Eds. Vol. 5029, p. 281–291, 2003.
  - Boctor E.M., Jain A., Choti M.A., Taylor R.H., and Fichtinger G. "Rapid calibration method for registration and 3D tracking of ultrasound images using spatial localizer", Annual Conference of the International Society for Optical Engineering (SPIE) on Medical Imaging -- Ultrasonic Imaging and Signal Processing; William F. Walker, Michael F. Insana; Eds, Vol. 5035, p. 521–532 2003-- Honorably mentioned Best Poster Award
  - Boctor E.M., Fichtinger G., Taylor R.H., and Choti M.A. "Tracked 3D ultrasound in radio-frequency liver ablation", Annual Conference of the International Society for Optical Engineering (SPIE) on Medical Imaging Ultrasonic Imaging and Signal Processing; William F. Walker, Michael F. Insana; Eds., Vol. 5035, p. 174–182, 2003.
  - Boctor E.M., Ali A., Chang D., Kamel K., and Youssef B. "PC-Based System for Calibration, Reconstruction, Processing, and Visualization of 3D Ultrasound Data Based on a Magnetic-Field Position and Orientation Sensing System", International Conference on Computational Science (2) 2001: 13–22.
  - Boctor E.M., and Youssef B. "Statistical Based Automated Ultrasound Imaging Quality Control and Procedure", presented in the Fourth IEEE International Conference on Electronics, Circuits, and Systems ICECS'97, December 15–18, 1997, Cairo, Egypt.
  - Boctor E.M., Youssef B., and Graham J. "Heuristic Based Approach For Extracting Calibration Parameters of Ultrasound Equipment", presented in the ISCA International Conference, June 11–13, 1997, Boston, Massachusetts, USA.
  - Boctor E.M., and Graham J. "Applying Reduction Technique for Solving NxN Puzzle Problem", presented in the ISCA International Conference, June 11–13, 1997, Boston, Massachusetts, USA.

#### **Peer-reviewed abstracts:**

- Rivaz H, Boctor E.M., and Fichtinger G. "Ultrasound Speckle Detection Using Low Order Moments", IEEE International Ultrasonics Symposium, 2006 (Accepted)
- Boctor E.M., lordachita I., Fichtinger G., and Hager G.D. "Ultrasound Self-Calibration and Real-Time Quality Control for Interventions", IEEE International Ultrasonics Symposium, 2005.
- DeOliviera M., Boctor E.M., Awad M., Taylor R.H., Fichtinger G., and Choti M.A. "Robot-assisted 3D strain imaging for monitoring thermal ablation of liver", Annual congress of the Society of American Gastrointestinal Endoscopic Surgeons, pp 240–241, 2005.
- Boctor E.M., Awad M., Fichtinger G., Taylor R.H., and Choti M.A. "Development of a Robotically-Assisted 3D Ultrasound System for Radiofrequency Ablation of Liver Tumors", 6th World Congress of the Hepato-Pancreato-Biliary Association (IHPBA), 2004, Washington.
- Boctor E.M., Ali A. and Youssef B. "Estimation of prostate volume by using 3D ultrasound imagery system", presented in the International Congress of Ultrasonography in collaboration with Hannover University–Germany, April 10–12th, 1998 Cairo, Egypt.

- Boctor E.M. and Youssef B. "Low Cost Image Acquisition System For Ultrasound Equipment", presented in the International Congress of Ultrasonography in collaboration with Hannover University-Germany, April 3-5th, 1997, Cairo, Egypt.
- Boctor E.M., Ali A., and Youssef B. "The Need of Quality Assurance in medical ultrasound", presented in the International Congress of Ultrasonography in collaboration with Hannover University- Germany, April 17-19th, 1996, Cairo, Egypt.

### **Non-peer-reviewed abstracts, posters and workshops:**

- Boctor E.M., Jain A., Fichtinger G., Taylor R. and Choti M.A. "Robotically Assisted Intraoperative Ultrasound with Application to Ablative Therapy of Liver Cancer", CIS Workshop JHU on May 2002.
- Boctor E.M., Kamel K., and Hanna N. "PC Based Freehand 3D Ultrasound System With 6 Degrees of Freedom", Presented in the 4th IEEE EMBS International Summer School on Biomedical Imaging, June 17-24 2000, France.
- Boctor E.M., Ali A. et al. "Low Level Image Processing Routines: Hypercube Algorithms For Image Transformations", Presented in the Speed School Workshop of Using Parallel Programs On The IBM SP2 Supercomputer, January 13, 2000, Louisville KY, USA.
- Boctor E.M., Chang D. and Ali A. "An Innovative, General Purpose PC-Based 3D Ultrasound System. Case Study: Breast Cancer Diagnosis and Treatment", Presented in RESEARCH! LOUISVILLE, November 15-18, 1999, Louisville KY, USA.
- Boctor E.M., Kamel K., and Nakajima S. T. "A Comparative Study Between Standard 2D Ultrasound and 3D Ultrasound of Folliculogenesis in Patients Undergoing Ovulation Induction", Presented in RESEARCH! LOUISVILLE, November 15-18, 1999, Louisville KY, USA.
- Boctor E.M., and Ali A. "Accurate Calibration of Electro-magnetic Tracking Systems and Their Application in Diagnostic Ultrasound Imaging", Presented in The Research Day of Speed School Showcase, 21-22 April 1999, Louisville KY, USA.

### **Invited talks:**

- Philips Research, Briarcliff NY, May 31, 2006
- New Innovation Center at Siemens Ultrasound Headquarter, Mountain view CA, April 11, 2006.
- Siemens Corporate Research, Princeton NJ, Oct. 13, 2005.
- Department of Surgery, Johns Hopkins University, Oct. 7, 2005.
- Georgetown University Medical Center, Department of Radiology, ISIS Center, August 26, 2005.
- Radiation Oncology Department, Johns Hopkins University, August 16, 2005.
- Siemens Corporate Research, Princeton NJ, April 20, 2004.

### **Awards, Honors, and Scholarships**

- 1990-1995, undergraduate scholarship at Cairo University, School of Engineering
- 1996 valedictorian, honor award for my B.SC. Degree from Cairo University, School of Engineering
- 1995-2004, graduate fellowship from Biomedical Engineering Dept. Cairo University, School of Engineering

- 1999 valedictorian, honor award for my M.Sc. degree in Biomedical Engineering from Cairo University, School of Engineering
- 1999–2000, graduate scholarship from Engineering Mathematics and Computer Science (EMCS) Dept. University of Louisville, KY USA
- 2000–2001, research fellowship from the dean of engineering in University of Louisville
- 2000, selected as one of 40 from over 400 students and post-docs to attend Fourth IEEE-EMBS International Summer School on Biomedical Imaging
- 2001–2004, research fellowship from Engineering Research Center (ERC) in Johns Hopkins University
- 2002, best project award from the Computer Science Dept. for the Robotic US research project
- 2003, honorably mentioned best poster award at SPIE Medical Imaging Conference
- 2003, SPIE student fellowship award (\$4000)
- 2003, invited paper to Journal of Computer Aided Surgery for the “Virtual RCM” work presented in MICCAI 2003
- 2004–2006 predoctoral fellowship from Siemens Corporate Research
- 2000–2006, travel grants from IEEE-UFC, IEEE-ISBI, and SPIE
- 2006, honorably mentioned best poster award at SPIE Medical Imaging Conference

### Patents

- Boctor E.M. and Youssef B. *“Original Design: Low Cost Image Capture Card Suitable for Clinical Use”*, filed in the Information and Decision Support Center (IDSC) Cairo Egypt, May 1996.
- Boctor E.M. and Youssef B. *“Automatic Quality Assurance Software Package For Calibrating Ultrasound Equipment Using AIUM Standard”*, filed in the Information and Decision Support Center (IDSC) Cairo Egypt, May 1996.
- Boctor E.M. and Youssef B. *“PC Windows-NT Based 3D Ultrasound System”*, filed in the Information and Decision Support Center (IDSC) Cairo Egypt, May 1999.
- Boctor E.M. and Fichtinger G. et al *“Calibration System for Freehand/Robotically Assisted Volumetric Ultrasonography in Surgery”*, Provisional U.S. patent application #60/472,169 filed 5/21/2003.
- Boctor E.M. and Fichtinger G. et al *“Robotic 5D Ultrasound System”*, Utility patent application 10/895,397 filed 07/22/2004.
- Boctor E.M. and Fichtinger G. *“Ultrasound Strain Imaging in Prostate Therapies”*, Utility patent application filed 05/09/2005.
- Boctor E.M. and Fichtinger G. *“Image Guided Interventions with Interstitial Ultrasound (ISUS) and/or Ultrasonic Transmission (UT) Guidance”*, Utility patent application filed 05/09/2005.
- Boctor E.M., Hager G.D., Fichtinger G. and Viswanathan A. *“Ultrasound Calibration and Real-time Quality Assurance Based on Closed Form Formulation”*, Utility patent application filed 04/15/2005.
- Boctor E.M., Hager G.D., Fichtinger G. *“An Apparatus and Methods for Computing and Processing 3D Ultrasound Elasticity Images”* Provisional U.S. patent application #JHU-REF 4958 filed 04/07/2006.

## Professional and Academic Experience

**Johns Hopkins University**  
Engineering Research Center for  
Computer Integrated Surgical Systems and Technology  
Research Assistant and Doctoral Student

*Baltimore, MD (USA)*

*Sept.01 – Present*

- Collaborated in a multi-institutional (Hopkins, CMU, and MIT), and a multi-disciplinary team on NSF/NIH funded research to develop novel enabling technologies for interventional ultrasound.
- Robot-Assisted Ultrasound-Guided Liver Surgery: Designed, implemented, and validated methods to integrate co-registered robot arms to manipulate the ultrasound probe and the tissue ablator, to treat liver cancer in a minimally invasive manner.
- Ultrasound in Therapy Planning and Monitoring: Proposed and implemented innovative frameworks for strain imaging and speckle tracking to help segment liver cancer and the prostate.
- Ultrasound-guided External Beam Radiation Therapy: Conceptualized and implemented new methods to enhance and segment ultrasound images using novel elasticity and parametric imaging, to register and guide radiation therapy in treating prostate cancer.
- Ultrasound Self-calibration: Invented and developed novel, internationally recognized and awarded, closed-form framework for online ultrasound calibration, and real-time quality control of tracked ultrasound.
- Conceptualized, designed, and co-developed research platform for Computer Integrated Surgery based on 3D Ultrasound (CISUS), and also integrated a general purpose US calibration toolkit (UltraCal).
- Participated in various projects including needle steering research, image overlay project and high frequency US imaging for microsurgery guidance.

**University of Louisville**  
Engineering Mathematics and Computer Science Dept. and  
Regional Information and Technology Institute (RITI), Cairo Campus  
Teaching Assistant and Graduate Fellowship

*Louisville, KY (USA)*

*Jan. 99–July 01*

- Gained substantial mathematical background, computer theory, and programming practice during my MSCS degree:
  - Real-time programming: Implemented real-time program to control a river lock/dam system prototype using *PLC ladder logic* programming.
  - Parallel computations: Designed and implemented low-level image processing toolkit using *C++* and *MPI*/library on a Linux cluster.
  - Computer networking: Developed a simulation package for a number of communication protocols including TCP/IP, and network technologies including ATM and Frame-Relay using *C* and *COMNET* package.
  - Artificial intelligence: Analyzed, designed, tested, and provided a novel framework to solve generic (nXn) puzzle problems with O(n) reduction in time and memory requirements using *Visual C++*.

- **Distributed computing:** Designed and implemented simple chatting with whiteboard program using *Visual C++*.
- **Software engineering:** Designed and developed a travel planning Expert System, starting from *SRS*, *SDS*, implementation, and testing using an assortment of tools including *CLIPS*, *CRC*, and *Rational Rose*.
- **Compiler design:** Implemented simple lexical and syntactical analyzer using *Lex*, *Yacc*, and *Bison*.
- **Image processing:** Conceptualized and implemented novel framework to segment the male bladder in 3DUS data automatically. The method involves mathematical morphology and watershed algorithms.
- **Web programming:** Designed and implemented web-based tele-robotic system, similar to the *Telegarden* system at USC. The arm consists of 3DOF, uses stepper motor actuation and is controlled by a Java based client-server program.
- Developed and programmed various medical image segmentation tools using deformable models, probabilistic region-growing methods, and mathematical morphology. This work addressed different clinical applications including, urinary bladder segmentation and volume estimation, and ovarian follicle segmentation.

### **BIOSYS for Trading and Systems Corporation**

*Cairo, Egypt  
1997-1999*

Co-Founder (50%) and head of a small company with five colleagues, and a starting budget of \$20,000. The annual turn over for the year 1999 was about 120,000 US dollars. Activities for the company included: 1) Software developments (my 3DUS system was acquired by Bahgat group, and MIS systems for pharmacies), 2) Software training (courses in VC, C++, and PowerBuilder), 3) Computer networking (networks and pc assembling), and 4) Medical equipment (Distributor for air abrasion dental system joint ventured with *Scientific and Trading Inc.*)

### **Cairo University**

*Giza, Egypt*

Biomedical Engineering and Systems Dept.

Research Assistant, Instructor, and Teaching Assistant

*Sept. 95- Dec. 98*

- Designed and built a precise mechanical system for electromagnetic field characterization by varying only the three translational degrees of freedom.
- Developed, programmed, and tested a windows-based three dimensional ultrasound system.
- Designed a volume rendering pipeline for 3DUS data using Visual C++ and VolPack library.

### **Cairo Clinical Ultrasound Center**

*Cairo, Egypt*

Research Assistant

*Oct. 94 - July 95*

**BAHGAT Group, Medical Division ([www.bahgat.com](http://www.bahgat.com))**

*Cairo, Egypt*

Part-time Research Engineer

*Oct. 95 - Oct. 98*

- Worked under supervision of Prof. Bakr Youssef (PhD/MD, RDMS) in both places. Dr. Youssef is chief radiologist of the clinical ultrasound center and the head of the medical division of BAHGAT group.
- Developed, programmed, and tested a quality assurance package that automatically reports measurements according to the American Institute of Ultrasound in Medicine (AIUM) standards.
- Designed and developed low-cost (under \$30) ultrasound capture board that acquires single B-mode image in 5–10 seconds.
- Participated in research collaboration with Diasonic/Vingmed Ultrasound (acquired by GE) in the cardiac software implementation.
- Participated in the digital phase design of the low-cost, single board ultrasound machine, including Beamforming and DSC units. My work involves FPGA technology (Altera, Actel and DSP), CVLink86 package (converting C++ code into 86-family machine code), and Design Center (similar to Pcad).

### **Mathematics and Physics Dept.**

*Cairo Univ.  
Summer 1994*

Undergrad research assistant at the Thin Film laboratory, in the area of developing Tin Dioxide thin films appropriate for solar technology. I developed a mathematical nonlinear model that governs various parameters controlling the fabrication of these thin films. I also built a small-signal preamplifier.

### **Advanced Software Development and Application Center (ASDA)**

*Cairo Univ.  
Summer 1993*

Designed and implemented multimedia education projects under system 7 (Apple Macintosh).

### **Siemens Scientific Office**

*Cairo, Egypt  
July (1994, 1993, 1992)*

Trained in troubleshooting, maintenance, and installation of different medical equipment like ECG, Ultrasound, X-ray, Angio equipment, Lithostar, CT as well as S/W testing.

### **Teaching and Mentoring Experience**

#### **Johns Hopkins University Engineering Research Center for Computer Integrated Surgical Systems and Technology**

*Baltimore, MD (USA)  
Sept.01– Present*

- Mentored two high-school students on summer projects, three REU students (two from Hopkins, and one from Stanford), three groups in computer integrated surgery course project, and participated actively with two master degree students (Joshua Leven 2005, and Anand Viswanathan 2004) and one Ph.D. student (Hassan Rivaz).

- Part-time teaching assistant to Prof. Russell Taylor in Computer Integrated Surgery (CIS-I) course.

**University of Louisville**

Engineering Mathematics and Computer Science Dept.

*Louisville, KY (USA)*

*Jan. 99–July 01*

- Awarded participation in "*Future Faculty Preparation Program*" from Sep.00–May01. This was an intense professional training program that covered topics including "Developing a Philosophy of Teaching", "How to Publish Your Ideas", and "Developing a Research Agenda" as well as a group of "College Teaching" courses.
- Taught, tutored, and supervised students in undergraduate classes and labs including, real-time programming, numerical analysis, C/C++, electronics, and Programmable Logic Controller (PLC).

**Cairo University**

Biomedical Engineering and Systems Dept.

*Giza, Egypt*

*Sept. 95–Dec. 98*

- Taught, tutored, and supervised students in undergraduate classes and labs including, Medical Equipment and Clinical Instrumentation, Pattern Recognition, Medical Image Processing, File Structure and Database, Data structure, Compiler Design, Predicate Calculus and Artificial Intelligence, Computer Graphics, and Electronics.
- Mentored undergraduate students on B.Sc. graduation projects. Examples of these projects include a mechanical 3D digitizer system, and a microprocessor embedded multi-channel EMG system.

### Professional Memberships and Activities

- Member of the Egyptian Syndicate of Engineering since graduation (1995–present)
- ISCA "International Society for Computers and Their Applications" member, No. 970028 (1995–1999)
- Member of The Institute of Electrical And Electronics Engineers, IEEE membership No: 41287233 (1998–present)
- Member of the IEEE Engineering in Medicine and Biology (EMB) society.
- Member of the International Society for Optical Engineering (SPIE) (2003–present)
- Member of the Medical Imaging Computing in Computer Assisted Interventions (MICCAI) organization (2004–present)
- Alumni member at Johns Hopkins University, University of Louisville, and Cairo University
- Medical Imaging Computing in Computer Assisted Interventions (MICCAI) reviewer since 2005
- An official Journal of the International Federation of Robotics, Robotica reviewer since 2006
- IEEE Transactions on Ultrasonics, Ferroelectrics, and Frequency Control reviewer since 2006

### Extracurricular activities

- Community service through St. Mary Coptic Christian church in MD since 2001.
- Member of the church board since 2004.